THÈSE

En vue de l'obtention du

DOCTORAT DE L'UNIVERSITÉ DE TOULOUSE

Délivré par : *l'Institut National Polytechnique de Toulouse (INP Toulouse)*

Présentée et soutenue le *21/10/2021* **par :**

Willca Villafana

Numerical Particle-In-Cell studies of Hall thrusters using unstructured grids

---

JURY

Miles Turner	Professor - NCPST/DCU	Rapporteur
Thierry Magin	Professor - VKI	Rapporteur
Anne Bourdon	Professor - CNRS/LPP	Reviewer
Kentaro Hara	Professor - Stanford Univ.	Reviewer
Gwenael Fubiani	Researcher - CNRS/LAPLACE	Reviewer
Benjamin Laurent	Research engineer - SAE	Invited
Bénédicte Cuenot	Professor - CERFACS	Advisor
Olivier Vermorel	Researcher - CERFACS	Co-advisor

École doctorale et spécialité :
MEGEP : Énergétique et transferts
Unité de Recherche :
CERFACS

Contents

List of symbols **14**

List of subscripts **16**

List of acronyms **17**

1 Introduction **25**
1.1 Space propulsion: brief history and current context . . . 25
1.2 Electric based propulsion systems . . . 27
1.2.1 Why is electric propulsion appealing? . . . 27
1.2.2 Kinds of electric propulsion devices . . . 29
1.2.3 Research effort and future of electric propulsion . . . 32
1.3 Hall Thrusters . . . 34
1.3.1 Working concept . . . 34
1.3.2 Hot topics for HTs . . . 37
1.4 Plasma modeling for HTs . . . 45
1.4.1 Fluid models . . . 47
1.4.2 Particle-In-Cell technique . . . 48
1.4.3 Hybrid and Direct Kinetic (DK) methods . . . 50
1.4.4 Summary . . . 50
1.5 Objective and scope of this PhD thesis . . . 51

2 AVIP PIC: code presentation and development **52**
2.1 Overview of AVIP . . . 53
2.1.1 A powerful tool derived from AVBP . . . 53
2.1.2 AVIP for plasma simulations . . . 53
2.2 Numerical implementation . . . 55
2.2.1 Concept and preliminaries . . . 55
2.2.2 Initialization . . . 58
2.2.3 Monte Carlo collisions . . . 59
2.3 Poisson's equation . . . 62
2.3.1 Finite volume method . . . 62
2.3.2 Interpolation scheme . . . 63
2.3.3 Discretization of the Laplacian operator . . . 64
2.3.4 Dielectric interface . . . 69
2.3.5 Solving the linear system . . . 72
2.3.6 Electric field . . . 74
2.4 Particles displacement . . . 74

2.4.1 Solving the equations of motion . . . 74
2.4.2 Transport of particles across the grid . . . 75
2.5 Boundary conditions for particles . . . 77
2.5.1 Classical boundaries . . . 77
2.5.2 Cathode models . . . 78
2.5.3 Secondary electron emission . . . 81
2.6 AVIP PIC performances . . . 84
2.6.1 Code optimization . . . 84
2.6.2 Strong scaling results . . . 87
2.7 Conclusion . . . 91

3 Validation in a 2D $z-\theta$ setup 92
3.1 Description of the model . . . 93
3.1.1 Simulation domain . . . 93
3.1.2 Prescribed axial profiles . . . 94
3.1.3 Cathode model . . . 95
3.2 Benchmarking . . . 96
3.2.1 Strategy and codes details . . . 96
3.2.2 Main plasma parameters . . . 97
3.2.3 Spectral analysis . . . 99
3.3 Application: merging-splitting algorithm . . . 101
3.3.1 Context and objectives . . . 101
3.3.2 Preliminary study on a 1D benchmark discharge . . . 102
3.3.3 Parametric study on the $z-\theta$ benchmark . . . 106
3.3.4 Results and discussion . . . 106
3.3.5 Toward a better use of the merging-splitting algorithm . . . 113
3.4 Conclusion . . . 114

4 Validation in a 2D $r-\theta$ setup 116
4.1 Literature review on plasma wall interactions and the MTSI . . . 117
4.2 Methodology and numerical setup . . . 119
4.2.1 Numerical setup . . . 119
4.2.2 Virtual axial model . . . 121
4.2.3 Ionization . . . 122
4.3 Results for the reference case with the code by CERFACS . . . 122
4.3.1 Simulation timeline . . . 123
4.3.2 Spectral characteristics of the instabilities . . . 125
4.4 Benchmark results . . . 127
4.4.1 Code presentations . . . 127
4.4.2 Code comparisons . . . 129
4.4.3 Comparison of main plasma parameters . . . 131
4.4.4 ECDI-MTSI coupling . . . 131
4.4.5 Statistical convergence . . . 134
4.5 Conclusion and prospective . . . 135

5 3D PIC simulation **136**
5.1 Context . . . 137
5.1.1 Literature review . . . 137
5.1.2 Contribution of our new 3D PIC simulation . . . 138
5.2 Numerical setup . . . 139
5.2.1 Computational domain and grid . . . 139
5.2.2 Charged particles . . . 140
5.2.3 Electromagnetic fields . . . 142
5.3 Transient state . . . 146
5.3.1 1D temporal profiles . . . 146
5.3.2 2D maps . . . 147
5.4 Steady state . . . 151
5.4.1 Main plasma variables . . . 151
5.4.2 Spectral analysis . . . 156
5.5 Comparison with 2D simulation . . . 166
5.5.1 Context and numerical setup . . . 166
5.5.2 Main plasma variables . . . 169
5.5.3 Spectral analysis . . . 173
5.6 Preliminary study on a cylindrical geometry . . . 176
5.7 Scalability analysis and convergence study . . . 180
5.7.1 Scalability analysis . . . 180
5.7.2 Statistical convergence . . . 183
5.8 Conclusion . . . 185

6 Conclusion **188**
6.1 Summary of this thesis . . . 188
6.2 Perspectives . . . 191
6.2.1 Short-term goals . . . 191
6.2.2 Improvement of code performances and efficiency . . . 192
6.2.3 Toward more realistic cases . . . 192

A Unit test case for the dielectric implementation **194**

B Paper draft on axial-azimuthal benchmark **198**

List of Figures

1.1 The rocket at time t, expels at $t + \Delta t$ a mass Δm at a speed $\mathbf{v}_{\text{ex}}$ to accelerate of $\boldsymbol{\Delta}\mathbf{v}$. $\mathbf{x}$ designates the unitary vector of the coordinate system. 26
1.2 Timeline of satellites launched according to their purpose from Harrison et al. [2017]. The dashed line indicates the end of the Cold War. The peak in the late 90's corresponds to the deployment of the Iridium constellation [Garrison et al., 1997]. 28
1.3 Reported thrust and specific impulse of some operational chemical based (left side, black/ white circles) and electric based (bottom side, red/blue/gray symbols) propulsion systems from Liang [2013]. 30
1.4 From Holste et al. [2020], number of satellites in Geosynchronous Earth orbit (GEO) using either arcjets, resistojets, Hall thrusters or ion gridded thrusters between 1981 and 2018. 31
1.5 Illustration of an Ion Gridded Thruster (GIT). (a) operational GIT used for the BepiColombo mission (ESA) currently traveling to Mercury (Credit: QinetiQ). The cathode, in the foreground, is releasing electrons. (b): schematic of a GIT ring cusp configuration. Ions extracted through grid apertures are then neutralized downstream (dashed blue area). 32
1.6 PPS-1350 HTs used for the SMART-I mission (Credits Safran Aircraft Engines). The cathode is visible above the thruster. 33
1.7 (a): Example of a Hall Thruster (Credit PEPL, University of Michigan Ann Arbror). (b): schematic of working principle of a HTs from Liang [2013]. Cathode is at the center. Magnetic coil are in brown. The ceramic covering the channel wall is in white. 34
1.8 (a): Typical magnetic field topology of a HTs [Hofer et al., 2006]. (b): Axial position of ionization and acceleration zones [Boeuf, 2017]. 36
1.9 (a): brand new PPS-1350 (Credits Safran). (b): PPS-1350 severely eroded (Credits Safran). 38
1.10 Left column: Magnetically unshielded / typical configuration. Right column: Magnetically shielded configuration. (a): from Mikellides et al. [2014], topology of the magnetic field in both configurations along with qualitative evolution of the potential and electron temperature at the wall. (b): from Garrigues et al. [2019], 2D spatial distribution of electron temperature (top) and iso-potential lines (bottom) for both configurations. 40
1.11 Comparison of inverse Hall parameter Ω_H^{-1} between experimental measurements (red triangles) made by Meezan et al. [2001] and classical theory (blue circles). Picture taken from [Boeuf, 2017]. 44

1.12 Classification of plasmas according to their electron density and temperature [Bittencourt, 2004, Chapter 1], [Lieberman and Lichtenberg, 2005, Chapter 1]. HT's plasmas are low pressure glowing discharges highlighted in red occurring at a rather cold temperature. 46

2.1 Splitting operators for fluid resolution 55
2.2 PIC cycle executed at every iteration in AVIP PIC 57
2.3 Iso-parametric coordinate system (ξ, η, ζ) in a tetrahedron 58
2.4 Null collision method 61
2.5 Different possible finite volume implementations 62
2.6 Possible control volume for a node centered approach with in (a-b) the Voronoi technique on two meshes and (c) the Median Dual control volume. (b) shows issues with obtuse angles while (c) remains convex 63
2.7 2D example of charge deposition in a triangular (ABC) and quadrilateral (ABCD) cell. P represents the position of the particle. The weighting factor W_{A} for node A is expressed in both cases 64
2.8 Nodal volumes in the example of a triangular mesh. Borders of the nodal volume can coincide with the boundary of the domain Ω. Nodal volume V_i and primal volume V_τ are highlighted with colored areas. One face external face S_f with its area vector is also indicated in orange. 65
2.9 Local face normals of the primal volume V_τ and local nodal vector at vertex i. A normal face vector $\mathbf{S}_f$ is named with the face vertices. G is the centroid of the triangle 66
2.10 Local face normals $\mathbf{n}_{ik}$ and $\mathbf{n}_{ij}$ of the dual volume ∂V_i and local nodal vector at vertex i. G is the centroid of the triangle. 68
2.11 Local face normals $\mathbf{n}_{ik}$ and $\mathbf{n}_{ij}$ of the dual volume ∂V_i at the boundary domain . 68
2.12 Procedure to define a dielectric border in AVIP. (a): continuous problem; a local surface charge density σ over an infinitesimal length dl provides the local charge Q_S. (b): separate discretization of two compatible computational domains for both the dielectric layer and the vacuum. (c): final computational domain after "glueing" both domains; the local surface charge Q_S is concentrated at the interface nodes 70
2.13 The nodal volume of a node i at the vacuum-dielectric interface can be split into V_{vac} and V_{diel}. Their respective boundaries $\partial V_{\mathrm{vac}}$ and $\partial V_{\mathrm{diel}}$ overlap with the dielectric surface S_{diel} (black-yellow dashed line). 71
2.14 Procedure to calculate the surface charge Q_S at each node at the dielectric interface S_{diel} (black dashed line). (a): for any exiting charged particle q crossing the dielectric interface S_{diel}, the face area $S_{\mathrm{A-B}}$ is identified. (b): from the intersection point of q and $S_{\mathrm{A-B}}$, the surfaces to face vertices (here $S_{q-\mathrm{A}}$ and $S_{q-\mathrm{B}}$) are computed. (c): charge q is split linearly between the face vertices and deleted. 72
2.15 The Leap-Frog and Boris schemes de-synchronizes position and velocity. The F function depends on the local position via the electric field and is expressed in Equations (2.54) and (2.55). MCC are the Monte Carlo collisions using data from position $\mathbf{x}^n$ and velocity $\mathbf{v}^{n-1/2}$ 75
2.16 The Verlet scheme has a synchronous position and velocity. It consists of three steps and displacement of particles is performed in two times. MCC are the Monte Carlo collisions using data from position $\mathbf{x}^n$ and velocity $\mathbf{v}^n$ 76

2.17 Working principle of Haselbacher algorithm [Haselbacher et al., 2007] starting from current position $\mathbf{x}_n$ to obtain final position $\mathbf{x}_{n+1}$. Intermediate calculations are denoted with the i subscript and $\prime$ superscript. 76
2.18 Haselbacher algorithm example using notations of Figure 2.17. Crosses indicate intersections of the particle trajectory with cell faces. 77
2.19 The particle orthogonal velocity is reversed at impact. Energy is conserved. . . . 78
2.20 Global electron (blue) and ion (red) currents in a HT, respectively denoted with the e and i subscripts. The anode and the cathode are electrically connected. By convention, all currents are positive. 79
2.21 Cells at the cathode plane are shaded and have a contact node (in red dots) with the cathode boundary (thick line on the right). The local coordinate system at the cathodic boundary is $(\mathbf{x}', \mathbf{y}', \mathbf{z}')$ with $\mathbf{x}'$ normal to the boundary directed to the interior of the domain. It is linked to the global coordinate system $(\mathbf{x}, \mathbf{y}, \mathbf{z})$ by successive eulerian rotations. 80
2.22 Numerical implementation of Barral's law. $\lfloor \sigma_{\text{SEE}} \rfloor$ designates the floor function applied to σ_{SEE}. 83
2.23 Different ways of organizing PIC data in each sub-domain taking the example of 8 particles, characterized by their position $\mathbf{x}$, their velocity $\mathbf{v}$, cell number n_c etc. AVIP retains the (AoSoA) strategy where each sub-domain is split in cell groups G_1, G_2..., each containing structures of particles informations. 85
2.24 Active control of number of particles per cells. In (a) clusters of similar particles are identified and in (b) they are either merged into a bigger particle (left cell) or split into two additional particles (crosses in right cell). 86
2.25 3D simulation domain inspired from the 2D geometry from Joncquieres et al. [2020]; (a) $r - z$ view and (b) $r - \theta$ view. 88
2.26 Time spent per iteration for the different numerical kernels of AVIP, starting with (a) $N_{pcc} = 30$, (b) $N_{pcc} = 60$ and (c) $N_{pcc} = 120$. The average number of nodes per CPU is indicated at the top x axis. In (b) and (c), a minimum of 720 and 1080 processors are required respectively to meet memory requirements. . . 89
2.27 Assessment of modified speed-up $S^\star$ for AVIP using data from Figure 2.26 (a). Solid lines represent AVIP calculations of modified speed-up $S^\star$ distinguishing the Poisson solver (DDM) from the Lagrangian kernel (transport, MCC, sorting, interpolation). Dashed lines represent the theoretical modified speed-up $S^\star_{th}$ for different fractions β benefiting from using more processors than $P_0 = 360$. 90

3.1 $z - \theta$ model implemented in AVIP. A local zoom at the top shows the triangular cells forming the mesh. $x_{B_{max}}$ denotes the position of maximum magnetic field. Top and bottom boundaries are periodic. Left boundary is the anode while the cathode is modeled as an emission plane at $x = x_c$ (blue dashed line). Main fluxes of particles are integrated over the azimuthal direction and denoted by the Γ symbol (red for ions, blue for electrons). The ionization zone is displayed with a blue-cyan color gradient. 94

3.2 Main plasma parameters at steady state for Case 2 at $N_{ppc} = 75$. (a-c-e): 2D maps for CERFACS at 20 µs of ion density n_i, azimuthal electric field E_y and electron axial current $J_{e,x}$. Two zones (I) and (II) can be distinguished when looking at the oscillations in the domain. (b-d-f): mean azimuthally averaged axial profile over 16-20 µs of ion density n_i, axial electric field E_x and total electron temperature T_e. The dashed black line indicates the position of maximum magnetic field $x_{B_{max}}$. 98
3.3 Spectral analysis of azimuthal instabilities. (a-c): numerical dispersion relations computed over 16-20 µs at respectively $x = 0.12L_x$ (zone I) and $x = 0.6L_x$ (zone II). White solid lines represent the theoretical dispersion relation from Equation (3.5). (b-d): normalized main azimuthal wavenumber $k_y\lambda_D$ and pulsation ω/ω_{pi} over the axial location x/L_x for the seven independent codes. The black dashed line represents the location of maximum magnetic field $x_{B_{max}}$. 100
3.4 1D discharge setup from [Turner et al., 2013] using a 2D mesh with a width of Δy. The potential is set at the left boundary while the right one oscillates between $\pm\phi_1$ at the frequency f_1. Particles exit at the left and right boundaries, while the top and bottom boundaries are walls where specular reflections occur. 103
3.5 Mean steady state ion density profile over the last 10 µs of AVIP compared to Case 1 from [Turner et al., 2013]. 103
3.6 Parametric study of $(T_{\mathbf{x}}, T_{\mathbf{v}})$ using the 1D discharge benchmark from [Turner et al., 2013] over the last 10 µs of the simulation. (a): measured discrepancy of final ion density profile with respect to the reference solution as a function of $T_{\mathbf{x}}$ and $T_{\mathbf{v}}$. (b): averaged final number of ions and electrons in steady state and elapsed time for each simulation. 106
3.7 Statistical effects of the merging-splitting algorithm for e^- (left column) and Xe^+ (right column). (a-b): mean number of macroparticles per triangular cell $N_{ppc,fin}$ along the axial direction in the range 16-20 µs. (c-d): mean statistical weight q_f along the axial direction in the range 16-20 µs. In (c-d), the dashed black line represents the statistical weight of Case 3 from Table 3.1 that must be compared to Case F. 108
3.8 Comparison of main plasma parameters averaged over the 16-20 µs range obtained with different parameters of the merging-splitting algorithm: (a) ion density n_i, (b) axial electric field E_x and (c) total electron temperature T_e. 109
3.9 Comparison of spectral analysis over the 16-20 µs range obtained with different parameters of the merging-splitting algorithm: (a) normalized azimuthal wavenumber number $k_y\lambda_D$ and (b) normalized frequency ω/ω_{pi} 111
3.10 Comparison of transients between the reference case and case B. (a): temporal evolution of exiting current density J_m. (b-c): axial profile of electron density n_i for the reference case and case B respectively at $t = 5$ µs. The composition of the total density in blue is detailed according to whether electrons stem from ionization, cathode, merging or splitting. (d-f): axial velocity distribution of electrons along the axial direction at $t = 0.25$ µs for the reference case and case B, respectively. 112

3.11 Comparison of the reference case and the improved splitting-merging case, denoted by MS. (a): transients of exiting current density J_m. The dashed black line indicates when the merging-splitting algorithm is activated. (b): normalized axial profiles of main azimuthal wavenumber k_y and man pulsation ω. (c-d): final azimuthal electric field E_y for the reference case and improved MS case, respectively. 114

4.1 2D radial-azimuthal (z, y) setup. 119
4.2 Virtual axial model used for the 2D radial-azimuthal simulation. The plasma dynamics take place in the $y - z$ plane. 121
4.3 **CERFACS code**: Temporal profiles of ion density n_i and total ion energy E_i (a) and radial $T_{e,z}$ and azimuthal $T_{e,y}$ electron temperatures (b). In (a), the left y axis in blue corresponds to n_i and the right one in orange refers to E_i. Blue arrows in (b) indicate local extrema of $T_{e,z}$ at 11.7 µs (max) and 17.5 µs (min). . 123
4.4 **CERFACS code**: 2D snapshots of azimuthal electric field E_y, radial electron temperature $T_{e,z}$, axial electron current $J_{e,x}$ and radial electron current $J_{e,z}$ at times $t = 0.53$ µs, $t = 0.75$ µs, $t = 11.70$ µs and $t = 17.50$ µs. Local extrema of $T_{e,z}$ shown in Figure 4.3 correspond to times $t = 11.70$ µs and $t = 17.50$ µs. . . . 124
4.5 **CERFACS code**: Spectral analysis of the azimuthal electric field E_y. (a) 2D FFT at linear stage when both ECDI and MTSI start developing. (b) and (c) temporal evolution of the amplitude of the MTSI and ECDI modes in the E_y spectrum. The amplitude has been integrated over k_z components. In (b) the dotted lines mark the linear growth of the modes obtained from a least-square method. 126
4.6 Theoretical growth rates, obtained from Stanford and USASK, using simulation values at the beginning of the linear stage when both ECDI and MTSI start developing for $k_z\lambda_D = 2.19 \times 10^{-2}$, set up by the plasma diffusion toward the walls. Symbols represent PIC measurements for MTSI (diamond) and first ECDI resonance (circle) from Figure 4.5. 127
4.7 **Case A:** Temporal profiles of plasma density (a) up to 3 µs and (b) for the whole simulation time. (c) and (d) Temporal profiles of radial electron temperature on the same time ranges. 132
4.8 Mean radial profiles of ion density (a) and total electron temperature (b), averaged over 25-30 µs. A zoom on the centerline highlights the discrepancies between the codes. On (b) several profiles are superimposed. The shaded gray area indicates the range ±2.5% around the averaged radial profiles of all the groups. 133
4.9 1D azimuthal FFT of the azimuthal electric field E_y, averaged over all radial positions and over three temporal intervals: (a) 5-10 µs, (b) 15-20 µs, (c) 25-30 µs. MTSI and ECDI resonances are indicated by arrows. 133
4.10 Assessment of statistical convergence between 25-30 µs: (a) mean value of ion density for five groups and (b) averaged radial profiles of density for CERFACS's code for various final number of macroparticles per square cells. In (a) error bars for CERFACS indicate the standard deviation around the mean value. The baseline case has around 212 particles per squared cell at steady state. In (b) radial profiles converge from light/green colors towards dark/blue colors. 134

5.1 (a): 3D computational domain from the radial-axial view. The azimuthal direction has a length L_y and is periodic. (b): whole 3D domain 139
5.2 (a): Mesh cut from the radial-axial view. Cells are in yellow and their edges are in black. A local zoom in provides details of the unstructured grid. (b): Radial distribution of the cell size. The dashed-dotted and dotted lines respectively represent the inner and outer channel radial location. 141
5.3 Boundary conditions and ionization layer for the 3D PIC simulation (radial-axial view). The ionization source term profile is given by Equation (5.2) is represented with a blue gradient. The anode is in red and set at the potential $\phi_a = 200\,\mathrm{V}$. The cathode is in blue and uses a quasi-neutral (QN) model. Its potential is $\phi_x = 0\,\mathrm{V}$. The walls are absorbent and the potential is split into two parts. In the upstream channel, in orange, the potential $\phi_{W,1}$ is an affine function that decreases from the anode potential ϕ_a down to 0 V. The other part of the walls, in yellow, has a zero potential $\phi_{W,2}$. 143
5.4 Magnetic field profile in 2D radial-axial view. The profile is uniform in the azimuthal y direction and the magnetic field is only radial 144
5.5 Temporal evolution of space-averaged quantities in the whole domain. (a): ion density n_i. (b): actual cathode electron current I_{cd} and expected cathode electron current $I_d + I_{be} + I_{bi} + I_{we} + I_{wi}$. (c): electron temperature components $T_{e,x}, T_{e,y}$ and $T_{e,z}$. (d): ion temperature components $T_{i,x}, T_{i,y}$ and $T_{i,z}$. The three different phases (I,II,II) are delimited in (a) and (b) with black dashed lines. . . 147
5.6 Timeline of variables of interest in the centered axial-radial $x - z$ plane at $y = L_y/2$. From the first to the fourth row are successively presented the ion density n_i, the ion temperature T_i, the axial electric field E_x and the azimuthal electric field E_y. Each column corresponds to a specific time: $t = 0.50, 1.20, 2.10$ and $7.50\,\mu\mathrm{s}$. 148
5.7 Timeline of variables of interest in the centered axial-azimuthal $x - y$ plane at $z = L_z$. From the first to the last row are successively presented the axial electron current $J_{e,x}$, the radial electron current $J_{e,z}$ and the azimuthal electric field E_y. Each column corresponds to a specific time: $t = 0.20, 1.20, 5.00$ and $7.50\,\mu\mathrm{s}$. The dashed black line represents the channel exit at $x = 0.34L_x = 0.85\,\mathrm{cm}$. 149
5.8 Timeline of variables of interest in the radial-azimuthal $z - y$ plane at $x = 0.12L_x = 3\,\mathrm{mm}$. From the first to the last row are successively presented the axial electron current $J_{e,x}$, the radial electron current $J_{e,z}$ and the azimuthal electric field E_y. Each column corresponds to a specific time: $t = 0.20, 1.20, 5.00$ and $7.50\,\mu\mathrm{s}$. 150
5.9 Radial-azimuthal view at steady state. (a): axial ion speed $v_{i,x}$ with iso-contour of Mach number M. (b): potential ϕ with streamlines of electric field $\mathbf{E}$ in the plane. (c): electron azimuthal current density $J_{e,y}$. (d): axial electron current density $J_{e,x}$ with streamlines of electron velocity $\mathbf{v}_e$ in the plane. (e): total electron temperature T_e with iso-contour of potential ϕ. (f): azimuthal electric field E_y. 151

5.10 **Inside the channel at centerline**. (a) and (b): azimuthally averaged 1D radial profiles at $x = 0.25L_x = 0.625\,\text{cm}$ of plasma density n_i, n_e in (a) and potential ϕ and electron temperature T_e in (b). (c) and (d): azimuthally averaged 1D axial profiles at $z = L_z = 1\,\text{cm}$ (centerline) of plasma density n_i, n_e and electron axial current density $J_{e,x}$ in (c) and axial electric field E_x and electron temperature T_e in (d). The black dashed line in (c) and (d) corresponds to the axial cut position of (a) and (b), i.e, $x = 0.25L_x$. 153
5.11 **Outside the channel and near the outer wall**. (a) and (b): azimuthally averaged 1D radial profiles at $x = 0.45L_x = 1.12\,\text{cm}$ of plasma density n_i, n_e in (a) and potential ϕ and electron temperature T_e in (b). (c) and (d): azimuthally averaged 1D axial profiles at $z = 1.3L_z = 1.3\,\text{cm}$ (near the channel outer wall) of plasma density n_i, n_e and electron axial current density $J_{e,x}$ in (c) and axial electric field E_x and electron temperature T_e in (d). The black dashed line in (c) and (d) corresponds to the axial cut position of (a) and (b), i.e, $x = 0.45L_x$. . . 155
5.12 DMD spectrum obtained over the last microsecond for the azimuthal electric field E_y, the electron axial current density $J_{e,x}$ and the electron radial current density $J_{e,z}$. Two resonances at ω_0 and ω_1 can be observed. 156
5.13 3D clip view of the reconstructed mode $\omega = \omega_0$ of the azimuthal electric field E_y. Shaded grey areas correspond to the part of the domain that is not plotted here, i.e. satisfying both conditions $x > 0.12L_x = 3\,\text{mm}$ and $z > L_z = 1\,\text{cm}$. . . . 157
5.14 2D views of the reconstructed mode $\omega_0 = 2 \times 10^6\,\text{rad}\,\text{s}^{-1}$. (a): axial electron current density $J_{e,x}$ in the axial-azimuthal plane at $z = L_z$ (centerline). (b): axial electron current density $J_{e,x}$ in the radial-azimuthal plane at $x = 0.12L_x$ (inner channel). (c): radial electron current density $J_{e,z}$ in the radial-azimuthal plane at $x = 0.12L_x$. (d): azimuthal electric E_y in the radial-azimuthal plane at $x = 0.12L_x$. 158
5.15 Temporal evolution of azimuthal wavenumbers k_y in the radial azimuthal plane located at $x = 0.12L_x$. Spectrum components have been normalized to the maximum value for each time. 159
5.16 Growth and temporal evolution of the ECDI-ion acoustic instability. (a): temporal evolution of the dimensionless azimuthal wavenumber $k_y\lambda_D$ in the radial-azimuthal plane at $x = 0.12L_x$. The solid red line corresponds to the $k_y\lambda_D$ for which maximum growth rate is achieved for the ion acoustic wave [Lafleur et al., 2016b]. (b): temporal evolution of the dominant azimuthal wavenumber $k_y = 6283\,\text{rad}\,\text{m}^{-1}$ at different axial locations expressed as a fraction of the axial length L_x. The exit channel is located at $x = 0.34L_x$. The dotted lines indicate the linear regression obtained with a least square method during the exponential growth of the instability. (c): comparison of the dimensionless growth rate γ/ω_{pi} (labeled as "exp") measured in the $x = 0.12L_x$ plane with linear theory (blue DR from Cavalier et al. [2013]) and asymptotic ion acoustic DR from Lafleur et al. [2016b] (orange solid line). (d) Axial profile of measured growth rates in its dimensionless and dimensional form γ/ω_{pi} (left y axis) and γ (right y axis). Results are compared with predicted dimensionless values stemming from linear theory by [Cavalier et al., 2013] (dashed line). 163

5.17 Comparison of 2D and 3D PIC results with the theoretical maximum growth rate for the MTSI in 2D [Petronio et al., 2021]. The 2D result is taken from Chapter 4 that was published in [Villafana et al., 2021]. The 3D result is obtained from the radial azimutal mode, i.e. $k_y = 2\pi/L_y$ and $k_z = \pi/L_z$, at $x = 0.12L_x$. 165
5.18 2D axial azimuthal simulation domain compared to 3D results measured at $z = L_z$.167
5.19 Comparison of temporal evolutions of (a) mean ion density n_i and electron temperature components $T_{e,x}$ (axial), $T_{e,y}$ (azimuthal) and $T_{e,z}$ (radial) for the pure 2D simulation (orange lines) and the corresponding axial azimuthal domain at $z = L_z$ from the 3D simulation (blue lines). 169
5.20 Comparison of steady states between the 3D (left column) and 2D (right column) simulations. (a-b): ion density n_i with electron streamlines $\mathbf{v}_e = v_{e,x}\mathbf{x} + v_{e,y}\mathbf{y}$. (c-d): azimuthal electric field E_y. In (c), E_y values have been multiplied by 3 to fit on the same scale as (d). (e-f): electron axial current $J_{e,x}$ with iso-Mach lines. In (e), $J_{e,x}$ values have been multiplied by 10 to fit on the same scale as (f). (g-h): electron radial current $J_{e,z}$. Dashed line indicates maximum of magnetic field. In (g), $J_{e,z}$ values have been multiplied by 2 to fit on the same scale as (h). 171
5.21 Comparison of averaged axial profiles at the steady state between the 2D (orange) and 3D case (blue). (a): ion density n_i. (b): total electron temperature T_e. (c): measured mobility μ_{PIC}. (d): axial electric field E_x. 172
5.22 Comparison of azimuthal electric field E_y in the first moments of the simulation in 3D (left) and 2D (right). The same scale is used for both the 2D and 3D configurations. 173
5.23 Numerical dispersion relation in 3D (left column) and 2D (right column) at two different axial locations at steady state: in the channel at $x = 0.12L_x$ (first row) and in the plume at $x = 0.6L_x$. The modified ion acoustic dispersion relation $\omega_R(\mathbf{k})$ is indicated by the white solid line. In (c-d), the white dashed line corresponds to $\omega_R(\mathbf{k})$ from the channel at $x = 0.12L_x$ normalized with local plasma conditions at $x = 0.6L_x$. In all plots, red dots correspond to the dominant resonance. 174
5.24 Axial evolution of (a) main dimensionless azimuthal wavenumber $k_y\lambda_D$ (solid line) and angular frequency ω/ω_{pi} (dashed line) and (b) Debye length λ_D (solid line) and ion plasma frequency ω_{pi} (dashed line) in 2D and 3D. 175
5.25 $y - v_{i,y}$ phase space of the ions in the near exit region for (a) the 3D simulation and (b) the 2D simulation. Every colored dot represents a particle (warm-yellow colors indicate maximum concentration whereas the black color represents the opposite). 176
5.26 3D view of cylindrical domain investigated. 178
5.27 Magnetic field profile in 2D radial-axial view for the 3D cylindrical geometry. The profile is uniform in the azimuthal θ direction and the magnetic field is only radial. 179
5.28 Comparison of first 3D results of the previous cartesian geometry (top row) with the cylindrical geometry (bottom row). (a-b): total electron temperature T_e in the radial axial plane. (c-d): azimuthal electric field $E_{y,\theta}$ in the centered radial axial plane. (e-f): axial electron current density $J_{e,x}$ in the radial azimuthal plane at $x = 0.12L_x = 3\,\text{mm}$. 179

5.29 Strong scalability analysis for the first 50 iterations using an increasing number of initial particles per cell $N_{ppc,ini}$ (30, 60 and 120). (a-b-c): performances of AVIP PIC modules for the different $N_{ppc,ini}$ values (30, 60 and 120 respectively). (a): the computation with $N_{ppc,ini} = 30$ does not use a coarse grid correction for the Poisson solver MAPHYS as described in Section 2.6.1. (b-c): the computation with $N_{ppc,ini} = 60 - 120$ uses a coarse grid correction. (d): Total CPU cost. The dashed lines represent the CPU cost in the case the coarse grid (CG) correction is turned off. Note that, for now, the CG option was not tested for the $N_{ppc,ini} = 30$ case. (e): Estimated physical time to simulate 10 µs. The dashed lines represent the return time in the case the coarse grid (CG) correction is turned off. 182
5.30 Statistical convergence of 3D PIC simulations using the current ratio I_{cd}/I_M. (a) Temporal evolution of current ratio I_{cd}/I_M with different $N_{ppc,ini}$ for the cartesian geometry. (b) Final current I_{cd}/I_M level at steady state vs the final number of particles per tetrahedral cell for both the cartesian and cylindrical geometries. . 183
5.31 Spectrum of azimuthal electric field E_y obtained the DMD at steady state. The red rectangle highlights higher frequency resonances that disappear as we increase the number of particles per cell. 184

A.1 Schematic of unit test case for the dielectric. The dielectric layers are highlighted in green and delimited by the plasma flow (blue) by the dielectric interface shown in purple. 195
A.2 Comparison of numerical results with analytical ones for the unit test case. (a): 2D map of potential ϕ. (b): 1D profile of ϕ in the x direction. (c): 2D map of electric field E_x. (d): 1D profile of E_x in the x direction. (e): 2D map of electric field E_y. (f): 1D profile of E_y in the x direction. Black dashed and dotted lines at the first row indicate the dielectric layer interface with the plasma flow. . . . 197

List of Tables

2.1 Local vertices coordinates in a tetrahedron. Point A is the origin. 58
2.2 Existing collisions in AVIP PIC. 60
2.3 Parameters for BN-SiO_2 for Barral's law 83

3.1 PIC simulations parameters for the $z - \theta$ setup. 95
3.2 Main codes specificities from [Charoy et al., 2019]. $\star$ and $\star\star$ symbols respectively refer to the pusher and Poisson solvers. $N_{ppc,ini}$ corresponds to the initial number of macroparticles per square cells. 97
3.3 Simulation parameters for Case 1 from [Turner et al., 2013]. 104
3.4 Tested sets $(N_t, T_{\mathbf{x}}, T_{\mathbf{v}})$ of the merging splitting algorithm. For simplicity, $f_t = 10$ for all cases. The reference case is Case 2 from Table 3.1. Cases A to E starts with the same initial conditions as Case 2 while Case F uses the same number of macroparticles as Case 3. 107

4.1 PIC simulations parameters. 120
4.2 Code characteristics. Explicit pusher refers to the standard Leap-frog/Boris algorithm. $\star$ and $\star\star$ symbols respectively refer to the particles (speed, position and weight) and to the fields (potential and electric field). 130

5.1 3D PIC simulation parameters. 145
5.2 Input parameters for the DR solver measured in the radial-azimuthal plane at $x = 0.12L_x$ at 0.5 µs without sheaths. 161
5.3 Simulations parameters for the 2D axial-azimuthal simulation domain that is compared to 3D results measured at $z = L_z$. As a reminder, the 3D case parameters are defined in Table 5.1 168
5.4 Nodes used on Irene cluster at CEA for 3D PIC simulations. This work used the HPC resources of IDRIS/TGCC/CINES under the allocation A0102A06074 made by GENCI. 180

A.1 Parameters of unit test case 196

List of symbols

Bold symbols are vectors. Their components and other scalar quantities are in italic.

Symbol	Description	Unit
Roman letters		
$\mathbf{B}$	Magnetic field vector	G
c_s	Ion speed of sound	$\mathrm{m \cdot s^{-1}}$
$\mathbf{dS}$	Orthogonal and infinitesimal surface vector	$\mathrm{m^2}$
$\mathbf{E}$	Electric field vector	$\mathrm{V \cdot m^{-1}}$
e	Elementary charge	C
f_{sub}	Subcycling frequency	[-]
f_t	Merging-splitting algorithm testing frequency	[-]
g	Earth's gravity field	$\mathrm{m \cdot s^{-2}}$
I	Current	A
i	Imaginary number	[-]
I_{sp}	Specific impulse	s
J	Current density	$\mathrm{A \cdot m^{-2}}$
$\mathbf{k}$	Wave vector	$\mathrm{rad \cdot m^{-1}}$
k_B	Boltzmann constant	$\mathrm{J \cdot K^{-1}}$
K_n	Knudsen number	[-]
L	Length	m
M	Mach number	[-]
m	Mass	s
$\dot{m}$	Mass flow rate	$\mathrm{kg \cdot s^{-1}}$
N_{cell}	Number of cells	[-]
n_d	Problem dimension	[-]
N_{nodes}	Number of nodes	[-]
N_{ppc}	Number of particles per cell	[-]
N_t	Target number of particles in cell	[-]
n_v^f	Number of vertices per cell face	[-]
Q	Total electric charge	C
q	Particle charge	C
q_f	Statistical weight	[-]
$R_1, R_2, ...$	Random number	[-]
r_L	Larmor radius	m
S	Speed-up	[-]
$\mathbf{S}_f$	Normal surface vector at face f	$\mathrm{m^2}$
$\mathbf{S}_{jk}$	Normal surface vector between node j and k	$\mathrm{m^2}$
T	Thrust	s

Symbol	Description	Unit
T_α	Temperature for species α	eV
t	Time	µs
$T_\mathbf{v}$	Tolerance in velocity	[-]
$T_\mathbf{x}$	Tolerance in position	[-]
$\mathbf{u}$	Eulerian velocity vector	$\mathrm{m} \cdot \mathrm{s}^{-1}$
$\mathbf{v}$	Velocity vector	$\mathrm{m} \cdot \mathrm{s}^{-1}$
V_c, V_τ	Cell volume	m^3
V_d	Drift velocity	$\mathrm{m} \cdot \mathrm{s}^{-1}$
V_N	Nodal volume	m^3
v_{th}	Thermal speed	[-]
W_A	Geometric weight for node A	[-]
$\mathbf{x}$	Position vector	m
Greek letters		
β	Fraction of code that can be parallelized	[-]
Δt	Time step	s
Δx	Space step	µm
ϵ_0	Vacuum permittivity	$\mathrm{F} \cdot \mathrm{m}^{-1}$
$\epsilon^\star$	Crossover energy	J
ϵ_r	Relative permittivity	[-]
γ	Wave growth rate	s^{-1}
λ_D	Debye length	µm
μ	Mobility	$\mathrm{V} \cdot \mathrm{s}^{-1}$
ν_m	Neutral-electron collision frequency	s^{-1}
σ	Local surface electric charge	$\mathrm{C} \cdot \mathrm{m}^{-2}$
σ_SEE	SEE yield	[-]
ϕ	Electric potential	V
Ω_{ce}	Cyclotron frequency	$\mathrm{rad} \cdot \mathrm{s}^{-1}$
Ω_H	Hall parameter	[-]
ω_p	Plasma frequency	$\mathrm{rad} \cdot \mathrm{s}^{-1}$
ω_R	Real wave angular frequency	$\mathrm{rad} \cdot \mathrm{s}^{-1}$

List of subscripts

Symbol	Description
a	Toward the anode (current)
b	Toward the plume (current)
cd	Injected from cathode to channel (current)
cp	Injected from cathode to the plume (current)
diel	Related to the dielectric region
e	electron
f	Cell surface f
i	ion
n	neutral
r	Radial direction in Cylindrical geometry
θ	Azimuthal direction in Cylindrical geometry
vac	Related to the vacuum/plasma flow region
w	Toward the wall (current)
x	Axial direction
y	Azimuthal direction in Cartesian geometry
z	Radial direction in Cartesian geometry

List of acronyms

1D	One-dimensional
2D	Two-dimensional
3D	Three-dimensional
BM	Breathing Mode
BN	Boron Nitride
BNSiO2	Boron Nitride-Silicon Dioxide
CE	Current-Equality (cathode model)
CERFACS	Centre Européen de Recherche et de Formation Avancée en Calcul Scientifique. Laboratory, specialized in high performance computing and reactive flows in Toulouse
CG	Conjugate Gradient
CIC	Cloud-In-Cell
CNES	Centre National d'Etude Spatial. The French space agency
COTS	Commercial Off-The-Shelf
CPU	Central Processing Unit
DK	Direct Kinetic
DMD	Dynamic Mode Decomposition
DR	Dispersion Relation
ECDI	Electron Cyclotron Drift Instability
EDI	Electron Drift Instability
EP	Electric Propulsion
ESA	European Space Agency
EVDF	Electron Velocity Distribution Function
FFT	Fast Fourier Transform
GEO	Geostationary-Earth-Orbit
GIT	Gridded-Ion-Thruster
HT	Hall Thruster
IAI	Ion-Acoustic Instability
ICARE	Institut de Combustion Aérothermique Réactivité et Environnement
ITTI	Ion Transit-Time Instability
IVDF	Ion Velocity Distribution Function
LANDMARK	Low temper Ature magNetizeD plasMA benchmaRKs
LAPLACE	LAboratoire PLAsma et Conversion d'Energie. French plasma physics laboratory
LEO	Low-Earth-Orbit

LHS	Left Hand Side
LIF	Laser Induced Fluorescence (for spectroscopy)
LPP	Laboratoire de Physique des Plasmas. A plasma physics laboratory in Paris
LTP	Low-Temperature Plasmas
MCC	Monte Carlo Collisions
MPI	Message Passing Interface
MS	Merging Splitting
MTSI	Modified Two Stream Instability
NASA	National Aeronautics and Space Administration
ONERA	Office national d'études et de recherches aérospatiales. French military laboratory
PEPL	Plasmadynamics & Electric Propulsion Laboratory
PIC	Particle-In-cell
POSEIDON	future Plasma thrusters for LOw earth orbit SatEllIte propulsiON systems
QN	Quasi-Neutral (cathode model)
RHS	Right Hand Side
RMS	Root Mean Square
RNG	Random Number Generator
SAE	Safran Aircraft Engines
SEE	Secondary Electron Emission
Xe	Xenon

Acknowledgments

This Ph.D. work would not have been possible without the support and the multiple interactions I benefited from during those long years. First, I am grateful for the jury members, who accepted to evaluate my work and with whom I had insightful discussions during the defense. In particular, I would like to thank Prof. Hara, with who I had the chance to collaborate during joint journal papers or at the occasion of the France-Stanford program. I have learned a lot from you on a scientific and also professional level.

I am also thankful for my sponsor, Safran Aircraft Engines along with the French government, that not only provided a comfortable financial situation but also, gave me the opportunity to work with Hall thrusters, a formidable high technology device I had dreamt to work with. Stéphane Zurbach and Benjamin Laurent, my two successive industrial advisors, have always been reactive and very supportive with their comments.

I have been lucky to do my Ph.D. at CERFACS, where I have met great people and learned a lot from them. Being at CERFACS was the opportunity to challenge me with the world of HPC. First, I would like to thank Bénédicte and Olivier, my two advisors. Despite they were not experts in plasma physics, they have always tried to guide me with valuable comments and I greatly benefited from their solid research experience in CFD and numerical simulations. Besides, the numerical results would have remained out of reach without the incredible support of the Computer Support Group (CSG) and the COOP team. In particular, I would like to warmly thank Isabelle D'Ast and Gabriel Staffelbach. They both were my last hope when my simulations kept crashing over and over with cryptic error messages. Thank you for rescuing me countless times, teaching me good practices, and making AVIP "magically" work on supercomputers, at home, and outside CERFACS. In addition to the CSG and COOP team, I would like to thank the administrative staff, and in particular, Michèle, Chantal, and Marie, who have made the paperwork easy. Finally, I am grateful I could meet new good friends at CERFACS: Victor, Matthieu, Simon, Julien, ... As I am a slow eater (sorry Thomas!), we have had a lot of time to remake the world at lunch and to escape our daily struggles in our Ph.D. life students. Aurélien, thank you for expanding my Internet and TV culture, it greatly mitigated my constant stress. I will not forget all those very insightful videos at our coffee breaks. Guillaume, I am grateful you came on board the plasma team. You have always been very keen to explain to me IT stuff and I learned a lot from your extensive scientific knowledge in general. Thank you for those good laughs and talks. I am also thinking of the current other plasma team guys: Nico, Lionel, Gabriel. It has always been a pleasure to work with you and I know you will do a great job. Keep it up! I cannot forget Valentin and François, the pioneers of AVIP and plasma physics at CERFACS. Every day I have discovered the good and hard work you left for us. Finally, I would like to acknowledge the essential collaboration of the Hiepacs team that allowed us to benefit from their very performant Poisson solver.

During my Ph.D., I was lucky to closely work with LPP, our partner in Paris. I keep very good memories, either in Paris or in conferences elsewhere in the world, with this amazing

team: Thomas, Antoine, Federico, Alejandro, Anne, Pascal ... I have always been warmly welcomed to visit and interact with you. In moments of doubt, you have guided me out to the light and helped me to define pragmatic configurations that contained interesting and new physics. I have a particular thought for you Anne, you have constantly supported me morally and financially and I will not forget it.

I would like also to thank good old friends who supported me from afar and that helped me to get a picture perspective of the Ph.D. in challenging moments: Umbi, Zoe, Marie, Corentin, Joe, ...

Enfin, j'aurai un dernier mot pour ma famille et mes proches. Je pense à mes frères Kusi, et Auki et ma soeur Nantika, mais aussi à mes parents qui m'ont soutenu tout au long de ces années. Ils ont été mes principaux soutiens et m'ont inculqué une passion pour l'espace et la science. J'ai toujours pu compter sur eux dans les moments difficiles. Enfin, je tiens à remercier Rudy, avec qui j'ai partagé toutes ces années de labeur. Tu m'as constamment remonté le moral et poussé à aller de l'avant pour terminer ce doctorat. Au final, tu as aussi fait le doctorat! Je n'y serais pas arrivé sans toi et je me réjouis de vivre de futures nouvelles aventures pendant de longues années encore.

Résumé

En quelques décennies, l'espace a pris une importance cruciale dans notre société moderne. Avec le déploiement imminent de méga-constellations de satellites, leur nombre va augmenter de manière considérable. Ces futurs satellites seront principalement équipés de systèmes de propulsion électrique, et notamment de propulseurs de Hall.

Cependant les processus gouvernant la physique des plasmas au sein des propulseurs de Hall restent mal compris, ce qui force les industriels à réaliser de coûteuses et laborieuses campagnes expérimentales pour certifier le produit fini.

Pour pallier cette difficulté, la simulation numérique par méthode de Particle-In-Cell (PIC), adaptée à la physique de ce type de plasmas, est un outil précieux. En effet elle permet de décrire des effets cinétiques spécifiques à ces plasmas et qui ne peuvent être représentés avec précision par des méthodes fluides. Du fait du coût des simulations PIC et des phénomènes complexes mis en jeu, les codes existants dans la littérature restent limités à des configurations académiques discrétisées sur des maillages structurés.

Pour surmonter ces défis, le code AVIP PIC est développé au CERFACS avec l'objectif de disposer d'un outil prédictif capable de modéliser des configurations industrielles. Pour ce faire, AVIP PIC travaille avec des maillages non structurés, ce qu'aucun autre code de la communauté ne peut faire actuellement. Cette innovation vient au prix d'une complexification considérable du code et un travail substantiel d'optimisation a d'abord été réalisé dans le cadre de précédents travaux.

Du fait de son caractère novateur, le premier objectif de cette thèse a été de systématiquement valider AVIP PIC. Ainsi, AVIP PIC a d'abord été utilisé pour participer avec succès à un premier benchmark international sur une configuration 2D dans le plan axial-azimutal. Au cours de ce travail tous les groupes ont obtenu des résultats proches avec 5% de différence au plus sur les profiles des principaux paramètres plasma. Une instabilité plasma azimutale, l'instabilité de dérive électronique, a été observée par tous les participants avec des caractéristiques extrêmement similaires. Cette instabilité due à des effets cinétiques, joue très probablement un rôle fondamental dans le transport anormal des électrons au sein du moteur. Fort de ce premier succès, nous avons ensuite utilisé ce cas pour explorer et paramétrer un algorithme de contrôle actif de particules. En empêchant le nombre de particules de devenir trop élevé, cet outil permet de réduire le coût de calcul et sera très utile pour de futures simulations. Toujours dans l'optique de validation du code, nous avons ensuite étudié une configuration simplifiée 2D du plan radial-azimutal du moteur. En effet, la prise en compte de la présence des parois peut considérablement modifier le comportement physique du moteur simulé. En particulier, nous avons mis en évidence une instabilité radiale-azimutale, appelé aussi instabilité modifiée à deux faisceaux, qui est couplée à l'instabilité de dérive électronique citée précédemment. Un travail de benchmark, mené par le CERFACS avec six groupes internationaux, a confirmé ce résultat avec un excellent accord, malgré la grande diversité des codes utilisés.

Fort de notre expérience en 2D, nous avons alors mis au point une simulation 3D reprenant

les éléments géométriques et les conditions plasma des deux cas précédents. Lors de cette étude la forme 3D de l'instabilité de dérive électronique a été identifiée ainsi qu'une possible signature de l'instabilité radiale-azimutale. La comparaison avec les configurations 2D précédentes semble montrer que les simulations 2D tendent à créer un plasma plus chaud et plus dense, ce qui affecte les phénomènes oscillatoires. La structure générale du plasma reste néanmoins similaire. Enfin des outils d'analyse de performances du code ont été développés et se révèleront précieux pour la mise au point de configurations 3D plus avancées.

Abstract

In a few decades, space has become a crucial part of our modern society. With the imminent deployment of mega satellite constellations, their number will increase dramatically. These future satellites will be mainly equipped with electric propulsion systems, and in particular Hall thrusters.

However, the processes governing the plasma physics within Hall thrusters remain poorly understood, which forces manufacturers to carry out costly and laborious experimental campaigns to certify the finished product.

To overcome this difficulty, numerical simulations are essential. They can be based on a Particle-In-Cell (PIC) method, well adapted to the physics of this type of plasma. Indeed, these plasmas present kinetic effects that cannot be accurately described by fluid methods. Due to the cost of PIC simulations and the complex phenomena involved, existing codes in the literature remain limited to academic configurations based on structured meshes. In an effort to overcome these challenges, the AVIP PIC code is developed at CERFACS as a predictive tool capable of modeling industrial configurations. To do this, AVIP PIC works with unstructured meshes, which no other code in the community can currently do. This innovation comes at the cost of a considerable complexity of the code and a substantial optimization work was first done in previous work.

Because of its innovative character, the first objective of this thesis was to systematically validate AVIP PIC. Thus, AVIP PIC was first used to participate successfully in an international benchmark on a 2D configuration in the axial-azimuthal plane. During this work, all groups obtained close results with 5% difference at most on the main plasma parameters profiles. An azimuthal plasma oscillation, the electron drift instability, was also observed by all participants with extremely similar characteristics. This instability due to kinetic effects, most probably plays a fundamental role in the anomalous transport of electrons within the engine. Based on this first success, we then used this case to explore and parameterize an active particle control algorithm. By preventing the number of particles from increasing too much, this tool reduces the computational cost and will be very useful in future simulations. Still in the perspective of code validation, we then studied a simplified 2D configuration in the radial-azimuthal plane of the engine. Indeed, taking into account the presence of the walls can considerably modify the simulated physics of the engine. In particular, we have highlighted a radial-azimuthal instability, also called modified two-stream instability, which is coupled to the electron drift instability mentioned above. A benchmark work, conducted by CERFACS with six international groups, confirmed this result with an excellent agreement, despite the great diversity of the codes involved.

Capitalizing on our experience in 2D, we then developed a 3D simulation based on the same geometrical elements and plasma conditions than in the two previous cases. During this study the 3D electron drift instability was identified as well as a possible signature of the radial-azimuth instability. The comparison with the previous 2D configurations seems to show that

the 2D simulations tend to create a hotter and denser plasma, which affects the oscillatory phenomena. The general structure of the plasma remains nevertheless similar. Finally tools for the analysis of the code performance have been developed which will prove to be valuable for the development of more advanced 3D configurations.

Chapter 1

Introduction

Contents

1.1 Space propulsion: brief history and current context 25
1.2 Electric based propulsion systems 27
1.2.1 Why is electric propulsion appealing? 27
1.2.2 Kinds of electric propulsion devices 29
1.2.3 Research effort and future of electric propulsion 32
1.3 Hall Thrusters 34
1.3.1 Working concept 34
1.3.2 Hot topics for HTs 37
1.4 Plasma modeling for HTs 45
1.4.1 Fluid models 47
1.4.2 Particle-In-Cell technique 48
1.4.3 Hybrid and Direct Kinetic (DK) methods 50
1.4.4 Summary 50
1.5 Objective and scope of this PhD thesis 51

1.1 Space propulsion: brief history and current context

The desire of escaping Earth's gravity was already imagined in the late modern era by artists and writers such as Jules Verne in his novel "Voyage to the Moon" in 1865 [Jules Vernes, 1865], in which adventurers embark on a fictional rocket. First scientific and analytical thinking on how to build such a vehicle was laid out in Russia and in the West during the first years of the 20^{th} century [Hill and Peterson, 1992, Chapter 1]. For rocket scientists, the goal is always the same: accelerate the rocket by expelling at high speed a propellant as shown in Figure 1.1.
In order to understand how a rocket is propelled we shall consider the closed system made of the rocket (payload, structural mass and remaining fuel to be utilized) and the mass of propellant Δm about to be expelled at time t. At time t the total momentum of the system rocket-propellant is given by:

$$\mathbf{P}(t) = (m + \Delta m)\mathbf{v}, \tag{1.1}$$

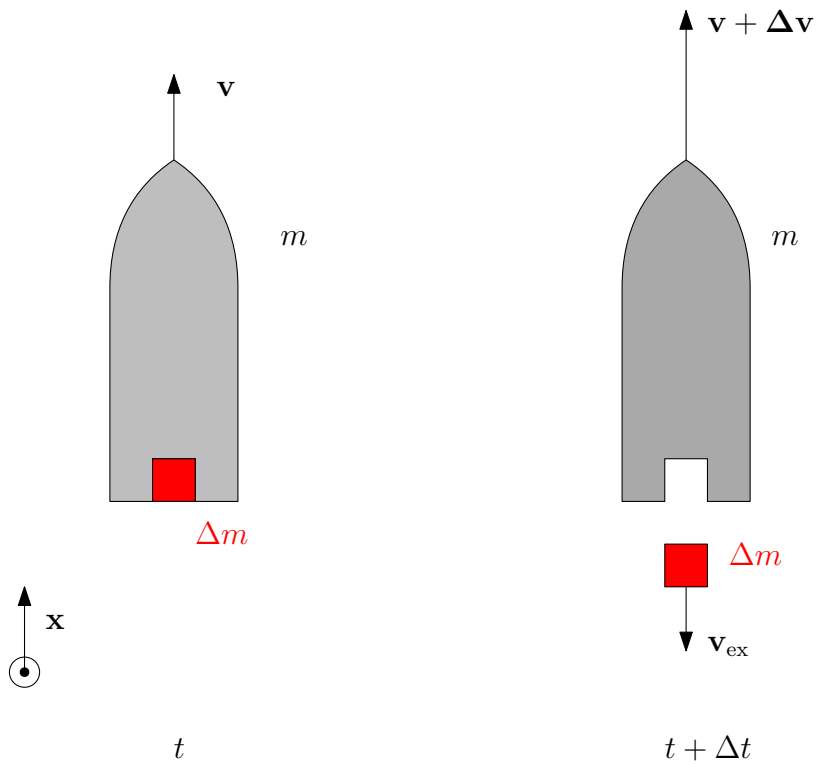

Figure 1.1: The rocket at time t, expels at $t + \Delta t$ a mass Δm at a speed $\mathbf{v}_{\text{ex}}$ to accelerate of $\mathbf{\Delta v}$. $\mathbf{x}$ designates the unitary vector of the coordinate system.

where $\mathbf{v}$ is the speed the system at time t. At time $t + \Delta t$ the propellant has been expelled downwards with an exhaust velocity $\mathbf{v}_{\text{ex}}$ with respect to the rocket. Therefore in the laboratory framework, its net speed is $\mathbf{v} + \mathbf{v}_{\text{ex}}$. In return, the rocket has gained a velocity $\mathbf{\Delta v}$. Thus, at $t + \Delta t$ the total momentum is:

$$\mathbf{P}(t + \Delta t) = m(\mathbf{v} + \mathbf{\Delta v}) + \Delta m(\mathbf{v} + \mathbf{v}_{\text{ex}}). \tag{1.2}$$

The change in momentum must be conserved at all time and in the absence of external forces one can write:

$$\mathbf{0} = \Delta\mathbf{P} = \mathbf{P}(t + \Delta t) - \mathbf{P}(t) = m\mathbf{\Delta v} + \Delta m\mathbf{v}_{\text{ex}} \tag{1.3}$$

Using differential notations and the coordinate system from Figure 1.1, we end up to

$$mdv - \Delta m v_{\text{ex}} = 0, \tag{1.4}$$

which is actually a first order linear differential equation:

$$m\frac{dv}{dt} = \frac{dm}{dt}v_{\text{ex}}, \tag{1.5}$$

The acceleration of the rocket is made possible by the thrust defined as:

$$T = \dot{m}v_{\text{ex}}, \tag{1.6}$$

where $\dot{m} = \frac{dm}{dt}$ is the exiting mass flow rate. Assuming the mass flow rate and the exhaust velocity constant, the famous rocket equation, derived by Russian scientist Tsiolkovsky in 1903

[Tsiolkovsky, 1903], can be retrieved by integrating between instants t_1 and t_2:

$$\Delta v = \int_{t_1}^{t_2} \frac{T}{m(t)} dt = \log\left(\frac{m(t_1)}{m(t_2)}\right) v_{\text{ex}}, \tag{1.7}$$

where $m(t_1)$ and $m(t_2)$ are respectively the mass of the rocket at t_1 and t_2. In a real world, the equation is of course modified when gravity or pressure forces are accounted for. However, the rocket performances, i.e., the achievable Δv, remain optimized with a maximal final mass ratio $m(t_2)/m(t_1)$ and exhaust velocity. The first rockets used chemical reactions to generate thrust from liquid or solid ergols and served first and foremost military purposes. The most emblematic example is perhaps the use of V2 rockets by Nazi Germany capable of virtually reaching 100 km of altitude and hitting targets in a 300 km radius within a few minutes. Considered as unstoppable, these "flying bombs" traumatized the public opinion and left its marks on world's leaders at this time. Therefore, it is not surprising that rocket science constituted an intense research interest during the Cold War, when both the US and the USSR conceived always more powerful and destructive missiles. This race reached a tipping point on October 4, 1957, when the Soviet Union launched into space the first artificial satellites Sputnik 1. Access to space and space supremacy was then considered a top national priority by both superpowers. Numerous technical achievements are reported during this period. Around the immediate neighborhood of the Earth, the first human spaceflight was performed by the USSR in 1961 and the landing on the Moon by Apollo 11 crew in 1969. Deep space exploration in the solar system was also viewed as a mark of power and remarkable missions were carried out: flybys of Venus (1961), Mars (1962), and further planets (Voyager mission from 1979).

From the end of the Cold War, the aerospace sector started to shift and commercial use of space developed as shown in Figure 1.2. This change coincides with the advent of the Internet and all derived economic activities that require telecommunication satellites.
As of today, there are nearly 3000 operational satellites and the space economy is estimated to represent more than USD 350 billion in 2018 according to the [OECD, 2019, Chapter 1]. In recent years, collections of hundreds of small satellites, designated as constellations, gained in popularity for Low and Medium Earth Orbits (LEO-MEO) to expand broadband connectivity and the Internet of the things. Thus, multiple projects such as OneWeb, Starlink or the Kuiper project have announced they intend to deploy thousands of satellites in order to provide worldwide internet access [OECD, 2019, Chapter 6]. Therefore, the number of launches per year is expected to more than quadruple in the near future and its corresponding revenue is to increase by 30% [Euroconsult, 2020]. Such an enthusiasm for small satellites is, at least, made possible by the use of an increasingly popular technology: electric based propulsion system.

1.2 Electric based propulsion systems

1.2.1 Why is electric propulsion appealing?

In order to understand why electric propulsion is appealing for space activities, we shall identify the limitations of chemical based propulsion systems. Basic space mechanics states that escaping Earth's gravity forever requires, at least, $\Delta v = 11.2\,\mathrm{km\,s^{-1}}$ starting from the ground. To reach LEO, a Δv of $9.4\,\mathrm{km\,s^{-1}}$ (250 km of altitude) is necessary. According to Equation (1.7), these values can be reached through a high exhaust velocity or mass ratio. For chemical rockets, the exhaust velocity is obtained by accelerating a hot gas into a nozzle which converts thermal energy, of the combustion chamber, into kinetic energy. The initial thermal energy stems from

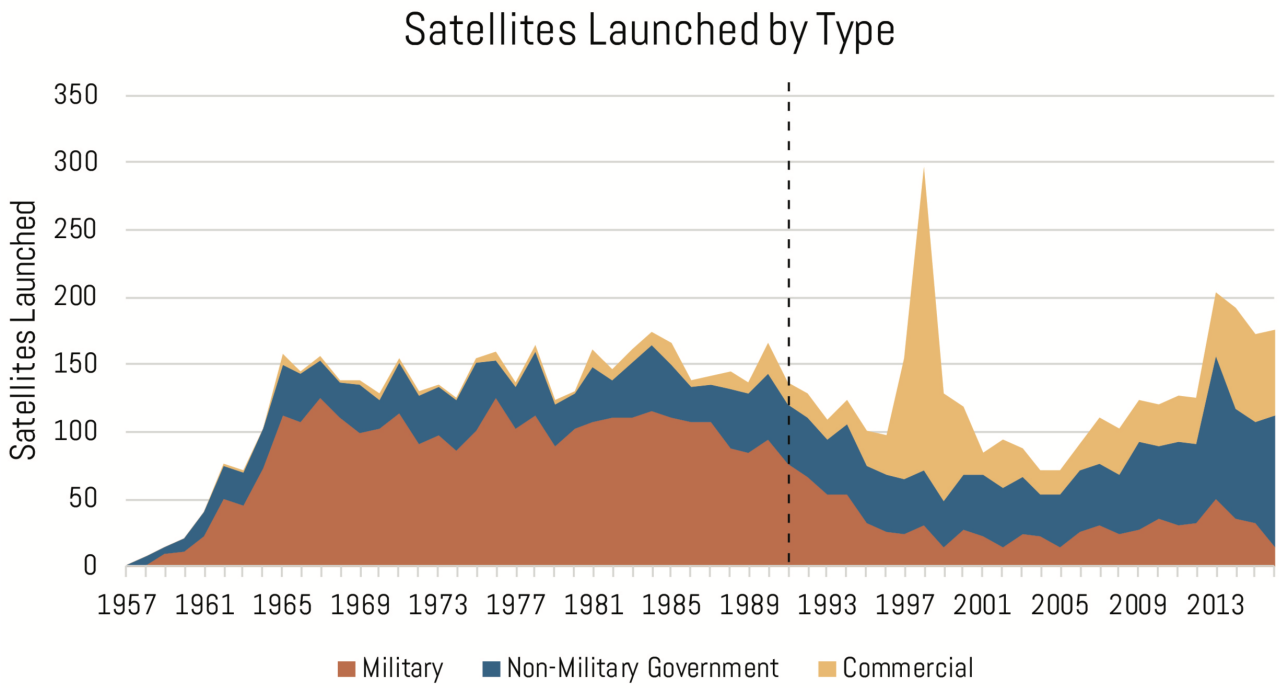

Figure 1.2: Timeline of satellites launched according to their purpose from Harrison et al. [2017]. The dashed line indicates the end of the Cold War. The peak in the late 90's corresponds to the deployment of the Iridium constellation [Garrison et al., 1997].

chemical reactions that release the energy stored in chemical bonds forming fuel molecules. So, the available thermal energy is directly proportional to the embarked mass of fuel. Therefore, the chemical propulsion system cannot exceed $\sim 4\,\mathrm{km\,s^{-1}}$ at best and it is then necessary to optimize the initial mass ratio. The initial mass m_0 of a rocket can be split into two parts: the mass of the embarked fuel m_p and the final mass m_f that will remain when the fuel is exhausted (which includes the payload and the mass of the rocket structure). So, using Equation (1.7), it can be seen the required fuel mass is exponential with the desired Δv:

$$m_p = m_f \left(1 + \exp\left\{\left(\frac{\Delta v}{v_{\mathrm{ex}}}\right)\right\}\right) \tag{1.8}$$

For a typical heavy launcher such as Ariane 5 [CNES, 2020], $m_f \sim 90\,\mathrm{t}$ and assuming $\frac{\Delta v}{v_{\mathrm{ex}}} \sim 3$ for LEO, about 1900 t of fuel would be necessary. The use of multistage rockets, which consists in getting rid of the unnecessary dead weight of boosters when they get exhausted, increases performances but current launchers represent 90% of the final weight. As a result, the use of chemical rockets remains extremely expensive as 1 kg of payload costs $\sim$ USD 15-30K [Aerospace Security, 2020] for LEO; which is why re-usable launchers arouse the interest of space companies and governments nowadays. Overall, the generated thrust $T = \dot{m} v_{\mathrm{ex}}$ is of the order of 10^3 kN and is mostly due to the tremendous mass flow rate $\dot{m} \sim 10 \times 10^3\,\mathrm{kg\,s^{-1}}$.

However, due to low gravity, there are plenty of activities in space that do not require this amount of thrust. Thus, satellites orbiting the Earth must control their attitude and adjust their trajectory during their lifetime, the latter easily ranging over the 15 years. This is especially true for LEO satellites that suffer from remnants of atmospheric drag that could add up over time. It is possible to embark fuel and liquid oxygen and adjust the mass flow rate to achieve

such tasks but the storage of liquid fuel and intricate pumping makes it inconvenient. Besides, the efficiency of chemical-based propulsion systems remains limited. In order to understand this we shall consider another metric, the specific impulse I_{sp} that expresses how much thrust T can be obtained from the propellant weight W_p utilized over the time range $[0; t]$ in the Earth gravity field. It indicates how long one 1 kg of fuel can lift 1 kg on Earth. The specific impulse is expressed as,

$$I_{sp} = \frac{\int_0^t T dt}{W_p} = \frac{\int_0^t \dot{m} v_{\text{ex}} dt}{\int_0^t \dot{m} g dt}, \tag{1.9}$$

where g is the gravitational acceleration. Under the assumptions of constant exhaust velocity and mass flow rate used in this manuscript the equation becomes:

$$I_{sp} = \frac{v_{\text{ex}}}{g}, \tag{1.10}$$

It is expressed in seconds and indicates how long the device can lift one kilogram given one kilogram of propellant, and so the highest value is desirable. Yet, as previously mentioned, the chemical rocket comes up with a limitation on the exhaust velocity, which limits their specific impulse to 300-400 s at most.

Electric propulsion provides a solution to increase the specific impulse. Electric propulsion consists in converting electric energy, stemming from an external source such as a solar panel, into kinetic energy by accelerating an ionized gas, a plasma, via electromagnetic forces. Because the available electric energy does not depend on the fuel mass anymore, the exhaust velocity can be greatly increased. In the example of Hall Thrusters (HTs), a kind of electric propulsion device, the exhaust velocity can reach $20\,\text{km}\,\text{s}^{-1}$, which provides a specific impulse greater than 2000 s. As a result, less fuel needs to be embarked, which reduces launch costs as well. The downside of electric propulsion is that it provides a very limited amount of thrust below 1 N because of a very low mass flow rate of the order of $\sim 10\,\text{mg}\,\text{s}^{-1}$ in the example of HTs. The contrast between chemical based (high T, low I_{sp}) and electrical based (low T, high I_{sp}) propulsion systems is exemplified by Figure 1.3.
However, this amount of thrust is sufficient for maneuvers such as altitude correction or trajectory adjustment. For small satellites, that will represent the bulk of the market over the next 10 years, it is expected that more than 50% [Commission, 2016; Space News, 2017] will be equipped with electric thrusters as they are reliable, cheaper, and more efficient than their chemical counterparts for long-term in-space missions. Overall, chemical propulsion remains irreplaceable to escape Earth's gravity but combined with electric propulsion to rise to final orbit, it could cut costs by 40% [Holste et al., 2020].

Finally, electric propulsion has also demonstrated its capability to carry out space missions further from home. In 2004, the European Space Agency (ESA) launched its first all-electric SMART-I mission propelled by PPS-1350 HTs from Safran Aircraft Engines (SAE), that successfully reached the Moon in around a year [Koppel and Estublier, 2005]. As a comparison, the Apollo mission, using chemical propulsion, needed only four days but burned more than 30 t of fuel to transfer from LEO to the Moon vs 80 kg of fuel for SMART-I.

1.2.2 Kinds of electric propulsion devices

Pioneer concepts of electric propulsion were conceived at the same time as chemical rockets [Choueiri, 2004] but had to wait until the 60's to be tested for the first time in space.

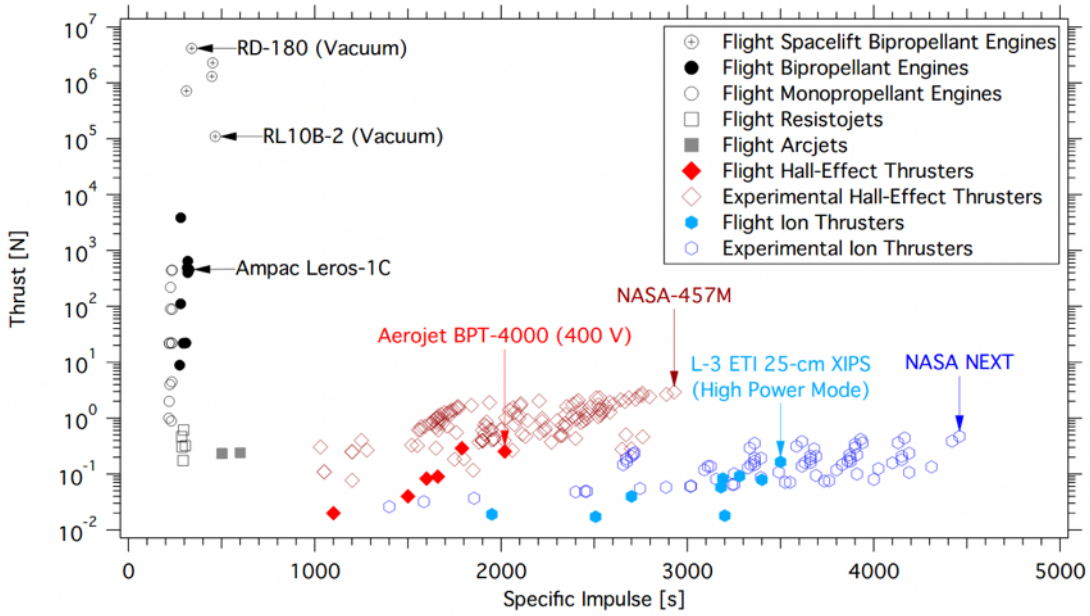

Figure 1.3: Reported thrust and specific impulse of some operational chemical based (left side, black/ white circles) and electric based (bottom side, red/blue/gray symbols) propulsion systems from Liang [2013].

Taking the example of Geosynchronous Earth orbit (GEO), Holste et al. [2020] exemplified the main electric propulsion devices that have been used.
Using the classification from Mazouffre [2016], we distinguish three main categories.

First, we encounter **electrothermal** devices that consist in converting electric energy into thermal energy by heating the propellant. Then, the latter enters a downstream nozzle to accelerate and gain kinetic energy. Arcjets and resistojets are based on this principle and the first telecom satellite, based on electric propulsion *Intelsat V2*, was equipped with a resistojet thruster in 1980. However, the plasma generated by the discharge has a low density and so the $I_{sp} < 700\,\mathrm{s}$ is limited by the initial thermal energy. Since they also generate a low thrust, they will be encountered at the left bottom side of Figure 1.3.

In order to increase the specific impulse, **electrostatic** devices or Gridded Ion Thrusters (GIT) can be considered. An operational GIT is shown in Figure 1.5 (a) and its working principle is presented in Figure 1.5 (b). First, in a parabolic cavity, a plasma is created. This is achieved by either a microwave/Radio-Frequency source (not shown here), or by injecting electrons from an internal cathode. The latter is mostly used in the US and the plasma is confined via a cusp-shaped magnetic field. Then, ions are extracted via a biased accelerator grid to reach tens of $\mathrm{km\,s^{-1}}$. The accelerator grid is protected by a screen grid, which reduces erosion. Downstream, a decelerator grid decreases the velocity of the plasma beam for improved performances. It also prevents cold ions to be backscattered toward the accelerator grid, which could damage it. Finally, an external cathode releases the collected electrons from the parabolic chamber into the plume, that becomes neutral again. Neutralization is essential because otherwise the spacecraft would charge negatively and the exiting beam positively, which would cancel the thrust out. GIT have been first used in 1964 in the SERT-1 mission by the US and has continuously been considered for LEO and even in deep-space mission such as BebiColombo. Their lifetime usually exceeds 20,000h, until the accelerator grid is too eroded.

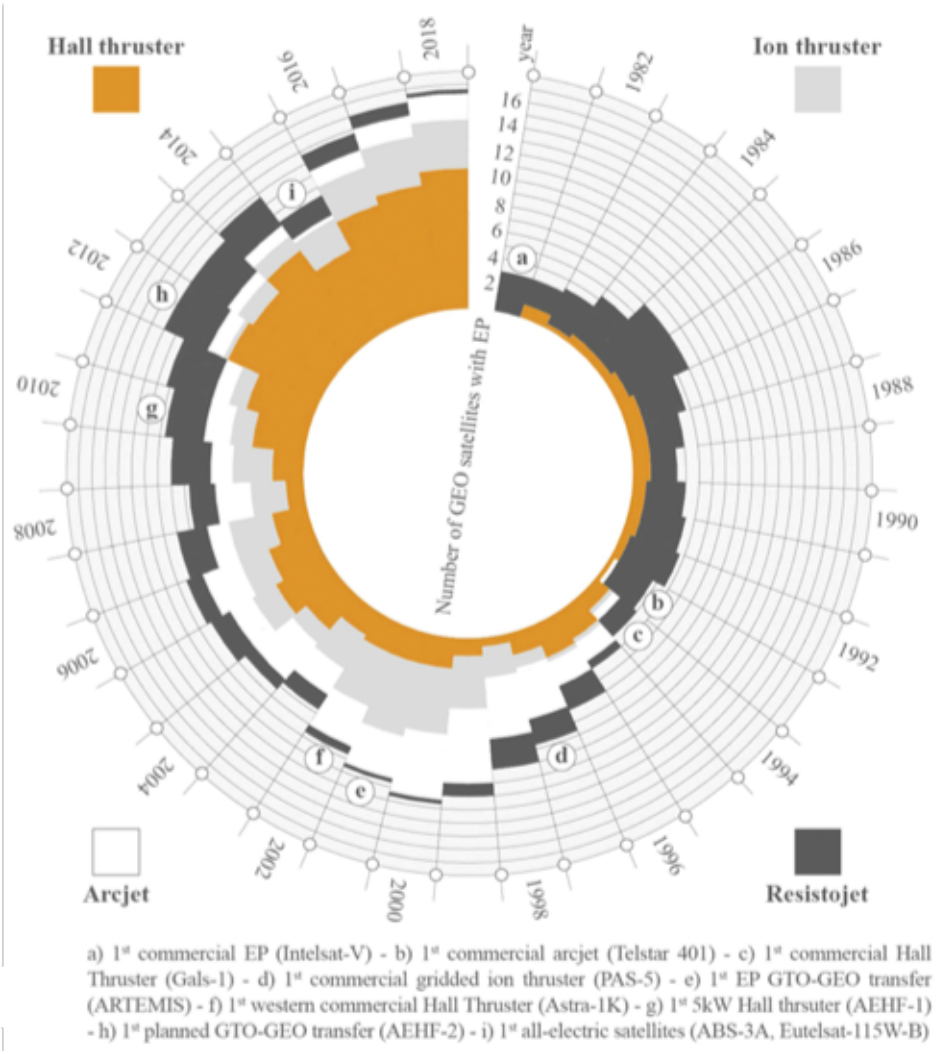

Figure 1.4: From Holste et al. [2020], number of satellites in Geosynchronous Earth orbit (GEO) using either arcjets, resistojets, Hall thrusters or ion gridded thrusters between 1981 and 2018.

The thrust remains below 1 N and the specific impulse is of the order of a couple of thousands seconds. The maximum current that can be extracted is constrained by the dimensions of the aperture grids. Indeed, the latter must be of the size of a Child–Langmuir sheath to enable acceleration of ions [Goebel and Katz, 2008, Chapter 5]. As a consequence, ions are squeezed in tiny volumes until space charge saturation is reached.

In order to allow for higher current densities, which increases the thrust density, there are other options and we can consider **electromagnetic** devices. In contrast to GITs, both electric and magnetic fields play an active role in ionizing and accelerating the plasma discharge into vacuum. The most emblematic and used of this kind of devices is the Hall Thruster (HTs), for which an illustration is given in Figure 1.6. It is a cylindrical cavity in which electrons are trapped by a magnetic barrier allowing the creation of ions that are then accelerated by an electric field. Like in GITs, electrons from the cathode neutralize the exiting beam. A more detailed explanation of HTs' working principles will be given in Section 1.3.1. Taking leverage of pioneer work from Morozov [2003], the USSR launched the first satellite using a HTs in 1971 on Meteor 1-10 [Hendrickx, 2004] and since then the technology gained maturity and has become popular for space activities (see Figure 1.4). In comparison to GITs, HTs present a higher thrust

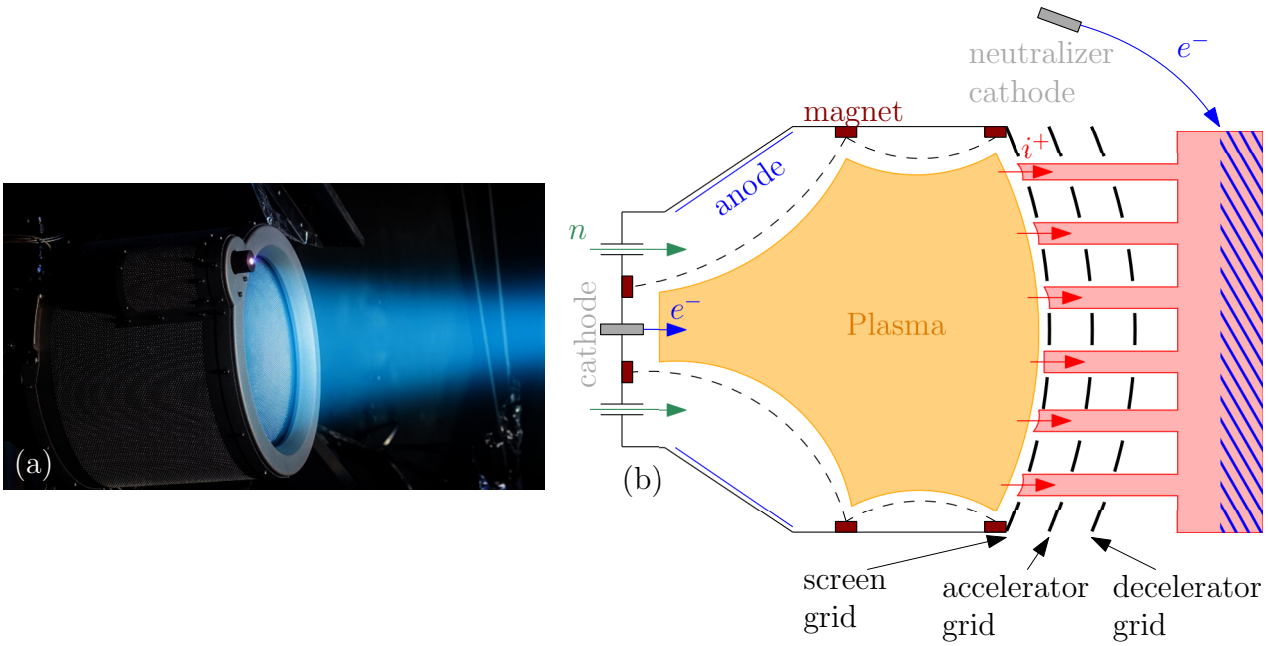

Figure 1.5: Illustration of an Ion Gridded Thruster (GIT). (a) operational GIT used for the BepiColombo mission (ESA) currently traveling to Mercury (Credit: QinetiQ). The cathode, in the foreground, is releasing electrons. (b): schematic of a GIT ring cusp configuration. Ions extracted through grid apertures are then neutralized downstream (dashed blue area).

density and thrust-to-power ratio meaning they are more compact and require a less complex Power processing Unit [Holste et al., 2020]. However, they tend to have a higher divergence beam and suffer more from wall erosion, which decreases their lifespan. The divergence beam is undesirable because, first, it decreases the efficiency of the system, and secondly, it increases the volume occupied by the beam, which may lead to surface contamination with other parts of the spacecraft. As of today, HTs are more popular and are probably better suited for small satellites constellations but GITs are definitely not out of the race since their high I_{sp} and lifetime make them good candidates for in-deep space missions such as Dawn [Rayman et al., 2006], BebiColombo [Sutherland et al., 2019] and Hayabusa-2 [Tsuda et al., 2013].

For a more exhaustive presentation of existing electric propulsion devices and detailed explanations of working principles, the reader can refer to [Hill and Peterson, 1992, Chapter 14] and [Goebel and Katz, 2008].

1.2.3 Research effort and future of electric propulsion

In the distant future, the main challenge of electric propulsion probably lies in its ability to bridge the gap between chemical propulsion (high T, low I_{sp}) and currently available technology (low T, high I_{sp}). Indeed, interplanetary flights will require much shorter travel times but also long-lasting engines to make the trip sustainable for human beings. In the case of electric propulsion, the energy is supplied by solar panels and it is limited to a few kilowatts, which is just enough for the thruster. Using solar panels beyond the Main Asteroid Belt, between Mars and Jupiter, is also unrealistic because the available power would decrease dramatically. Therefore using a nuclear reactor based on fission or fusion is probably an excellent choice [Woodcock et al., 2002; Black and Gunn, 2003]. In this regard, the Variable Specific Impulse Magnetoplasma Rocket (VASIMIR), an electrothermal device, is a technology being researched

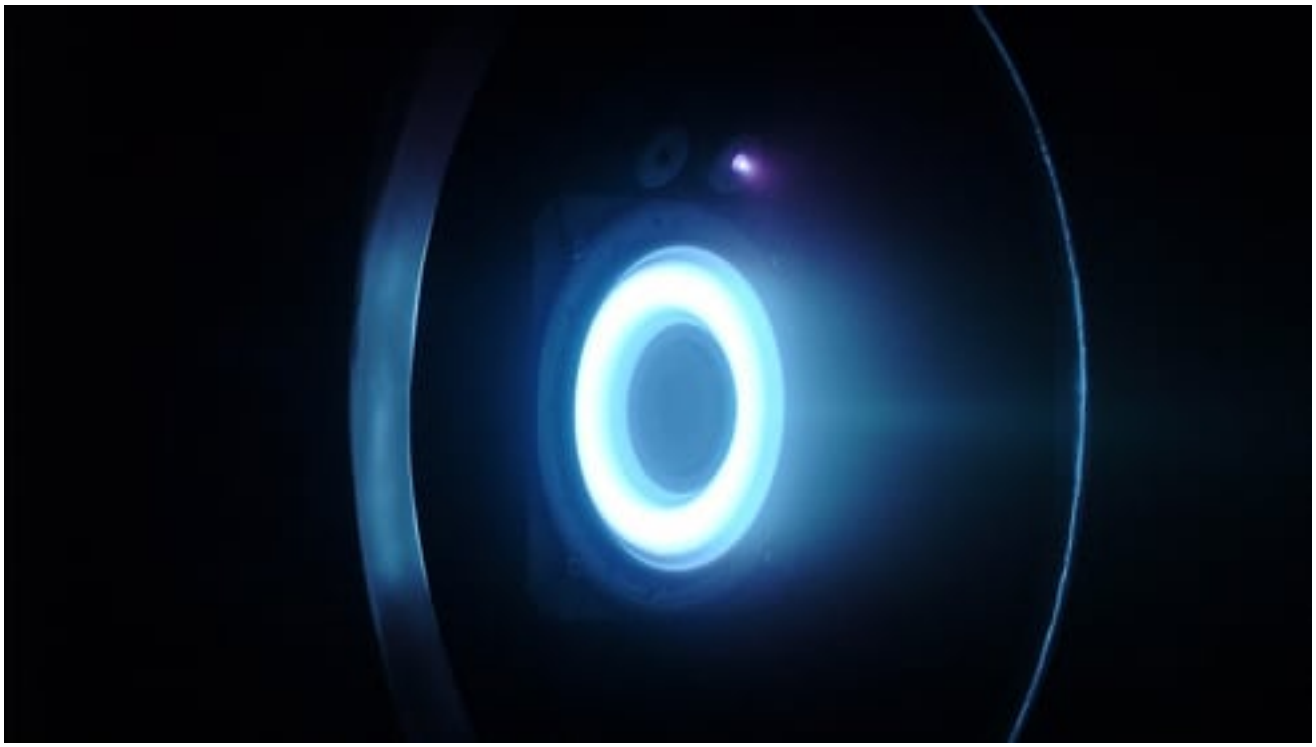

Figure 1.6: PPS-1350 HTs used for the SMART-I mission (Credits Safran Aircraft Engines). The cathode is visible above the thruster.

that could multiply the thrust by 1000 while still ensuring high I_{sp} with more than 100 kW [Giambusso et al., 2020]. More mature technologies, such as HTs and GITs, are also scaling up to operation points of high power levels [Dale et al., 2020]. This constant progress has been made possible by the support from governments and space agencies in Europe [del Amo, 2015], in the US [Schmidt et al., 2018], in Russia [Semenkin, 2007] and in Japan [Komurasaki and Kuninaka, 2007].

France has a long-standing tradition in electric propulsion and can rely on a strong network of research public institutions such as LPP, LAPLACE, CNES, ICARE and ONERA, but also on world-leading companies (Airbus and Safran) and startups (ExoTrail, ThrustMe) [Boniface et al., 2017]. In particular, Safran has been a pioneer in electric propulsion in Europe and is specialized in the conception and production of HTs. It has developed a full range of products from low power PPS X00 ($<$ 1 kW) [Vaudolon et al., 2019], suited for LEO, to high power with PPS 20K (20 kW) [Zurbach et al., 2011], designed for in-deep space missions. However, because of the intricate physics of HTs, the development of new concepts and their commercial certification take years and remain costly. Indeed, performances of new prototypes have to be continuously monitored in vacuum chambers for tens of thousands of hours. At the end of this process, commercial certification is obtained and the product can be sold to customers. Unfortunately, the design is also likely to be modified during the tests and each update will require to start over the long hours of measurements in vacuum chambers. As the small satellite market is expected to expand dramatically and under the pressure of international competitors (Fakel for Russia, Busek for the US), the French aerospace industry needs to overhaul his its strategy to create innovation. Aware of the challenges ahead, the French government reinforced its support for electric propulsion research and in particular for HTs.

Thus, France co-funded the POSEIDON [French National Research Agency, 2016] project

(future Plasma thrusters for LOw earth orbit SatEllIte propulsiON systems) along with Safran that partnered with both LPP in Paris and a newcomer, CERFACS laboratory in Toulouse. LPP has a long-standing experience in cold plasmas, encountered in HTs, whereas CERFACS has world class expertise in massively parallel calculations for Fluid Dynamics and reactive flows. Therefore, POSEIDON gathers proficiencies from different scientific communities to bolster the HT research effort. This is primarily achieved by numerically investigating the system by innovative simulations to get a more precise idea of the plasma dynamics. Ultimately, POSEIDON improves the understanding of HT and facilitates the development of 3D numerical tools suited for industrial configurations. Thus, Safran will be able to guide and speed up its process to develop new thrusters and it will reduce the number of laborious and costly testing. Within this framework, this thesis was performed at CERFACS and has been funded by POSEIDON.

1.3 Hall Thrusters

1.3.1 Working concept

As depicted in Figure 1.7 (a), a Hall Thruster has an annular geometry and performs the following steps that are summarized in Figure 1.7 (b).

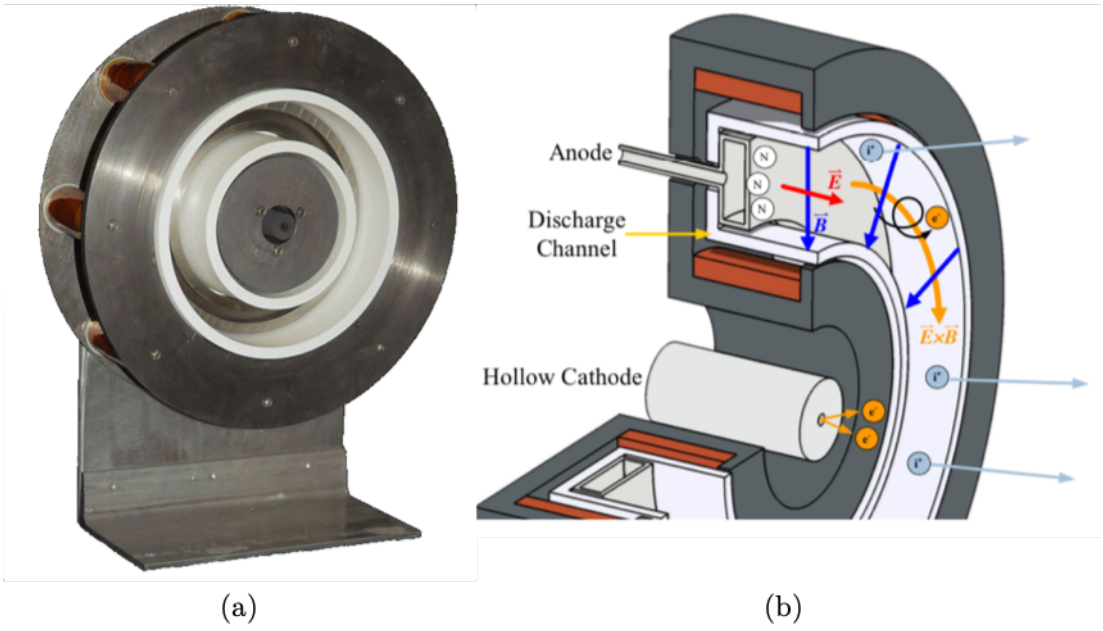

Figure 1.7: (a): Example of a Hall Thruster (Credit PEPL, University of Michigan Ann Arbror). (b): schematic of working principle of a HTs from Liang [2013]. Cathode is at the center. Magnetic coil are in brown. The ceramic covering the channel wall is in white.

Injection of neutral particles

First, a neutral gas is injected through a porous anode located at the back end of the annular channel. The typical mass flow rate is about a few $\mathrm{mg\,s^{-1}}$. The anode is a conductive and metallic piece whose potential is set to a constant value. The neutral gas is usually a noble gas

as it will not react with other components of the thruster.Xenon is the heaviest non-radioactive noble gas so it is usually used as it is safe and optimizes the thrust. Lighter noble elements such as Krypton can also be employed, as in the Starlink constellation for instance, because their cost is much lower.

The neutral gas diffuses in the chamber toward the plume; this zone is cold and un-reactive.

Cathode electron emissions

The cathode, centrally mounted in Figure 1.7, is also a metallic part and biased at a lower potential than the anode. It is heated and releases electrons during this process. The potential drop between the anode and the cathode creates an axial electric field that forces some of these electrons, around $\sim$ 10-20%, to enter the discharge channel.

Magnetic barrier and ionization

At the entrance of the channel, electrons stemming from the cathode experience the effects of an imposed magnetic field, mostly radial in this area. The magnetic field is generated by coils located around the chamber as shown in Figure 1.7. The topology of the magnetic field is a crucial aspect of HTs's design [Garrigues et al., 2003] and is usually designed such that it is maximum at the channel exit, essentially radial and symmetric with respect to the centerline [Morozov and Savelyev, 2000, Chapter 2]. An example of topology is shown in Figure 1.8 (a).

The effect of the magnetic field on charged particles can be assessed by the means of three parameters: the cyclotron frequency Ω_{ce}, the Larmor radius r_L, and the Hall parameter Ω_H. The cyclotron frequency, defined as

$$\Omega_{ce} = \frac{q_\alpha B}{m_\alpha}, \tag{1.11}$$

is the frequency of a particle spinning around magnetic field lines. q_α and m_α are the charge and mass of the particle α and B is the magnitude of the magnetic field. The circular trajectory of a charged particle around the magnetic field lines has a radius called Larmor radius expressed as:

$$r_L = \frac{v_\perp}{\Omega_{ce}}, \tag{1.12}$$

where $v_\perp$ is the velocity component orthogonal to magnetic field lines. Because of their light mass, the Larmor radius of electrons is typically around $\sim$ 0.1 cm [Goebel and Katz, 2008, Chapter 7] which is way below common dimensions of HTs. This means electrons have room to spin around magnetic field lines, i.e., they are magnetized. Under the effect of the axial electric field, their spinning motion drifts in the $\mathbf{E} \times \mathbf{B}$ (i.e., azimuthal) direction. The residence time of electrons in this area is controlled by the Hall parameter defined as:

$$\Omega_H = \frac{\Omega_{ce}}{\nu_m}, \tag{1.13}$$

where ν_m is the collision frequency of electrons and neutral particles. The Hall parameter indicates how long the particle spins around the magnetic field lines before being scattered by collisions. For electrons $\Omega_H \gg 1$, which means they are well confined in the azimuthal direction.

Since their residence time is greatly increased by the magnetic barrier, they eventually collide more often with neutral particles leading to ionization. Ionization generates even more

electrons which sustain or ignite the discharge. The ionization location is shown in Figure 1.8 (b).

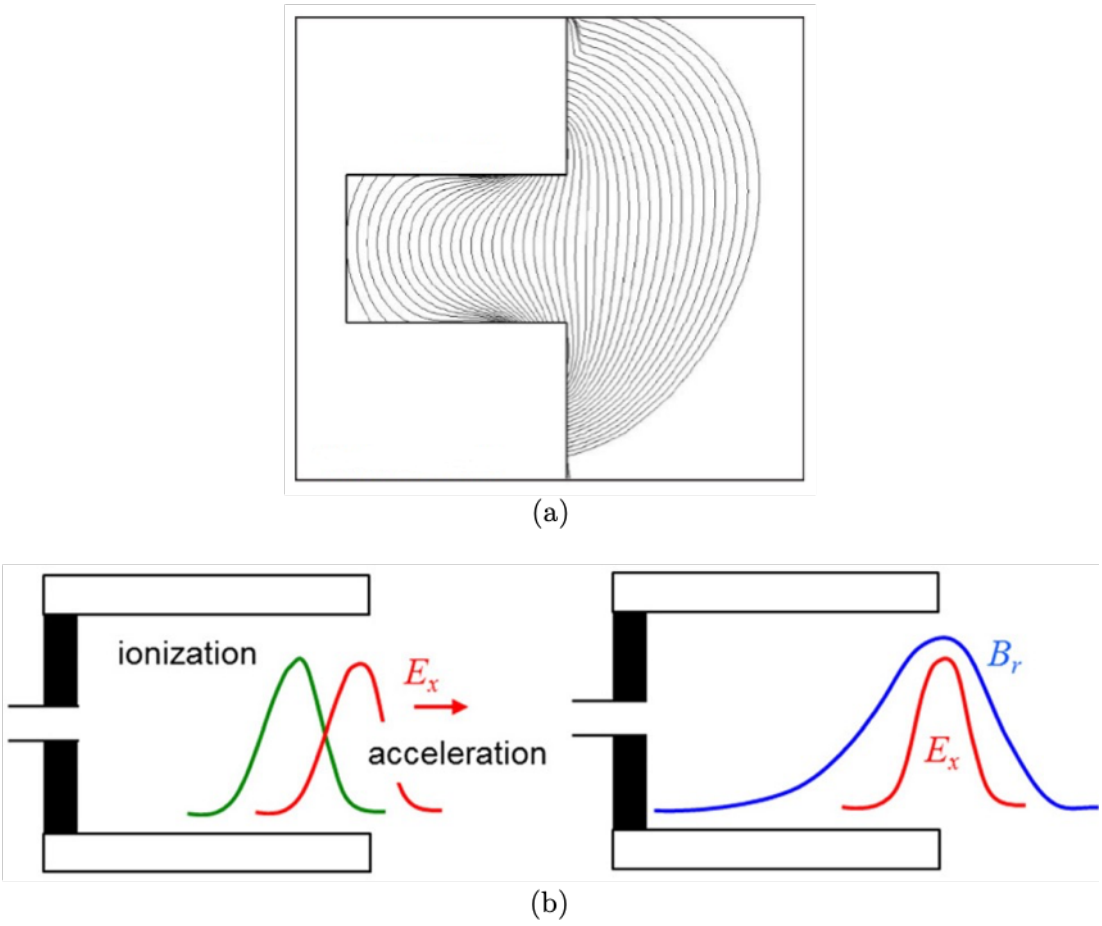

Figure 1.8: (a): Typical magnetic field topology of a HTs [Hofer et al., 2006]. (b): Axial position of ionization and acceleration zones [Boeuf, 2017].

Thrust generation

Once created, ions are immediately accelerated by the axial electric field toward the plume. In contrast to the electrons, they are so much more massive they do not feel the magnetic field. Indeed, their Larmor radius is typically greater than 1 m and $\Omega_H \ll 1$. Ions are therefore accelerated at high speed up to 15-20 $\mathrm{km\,s^{-1}}$, which generates thrust. Since the magnetic field does not create a highly directional beam, a plume divergence appears.

Beam neutralization

The exiting ion beam is by definition positive and is neutralized by electrons stemming from the cathode. This step prevents the spacecraft from being negatively charged which would eventually attract the ion beam back to it, thus canceling the thrust out. Electrons from the cathode are supplied by the anode, that is electrically connected to the cathode. Indeed, in spite of the magnetic field barrier, some electrons end up reaching the anode.

1.3.2 Hot topics for HTs

The working principle of a HT is fairly simple. However, the details of the ongoing physics are still beyond our current understanding.

A primary solution to investigate HTs consists in relying on experimental measurements. This can be done with electrostatic-Langmuir probes [Brown and Jorns, 2019; Tichý et al., 2018; Shastry et al., 2009; Raitses et al., 2005a] that measure plasma parameters such as density or temperature. Unfortunately, this is an invasive technique that can disturb the actual working conditions of HTs. Luckily, we have noninvasive tools to examine some aspects of the plasma. For instance, laser-induced fluorescence (LIF) spectroscopy can assess the velocity distribution function of particles and has been successfully applied to HTs [Dale and Jorns, 2019a; Mazouffre, 2012]. Besides, coherent Thomson scattering [Tsikata and Minea, 2015; Tsikata et al., 2009], measuring fluctuations in the density and electric fields, coupled to a newly developed incoherent Thomson scattering technique [Vincent et al., 2020], assessing thermal electron properties, is hoped to expand spectral analysis of the plasma flow. Unfortunately, all these techniques are unable to monitor the plasma inside the channel and sometimes do not offer enough time and spatial resolution. One way to tackle this challenge, is to rely on simulations that can guide where to perform measurements, and also provide an insight into the channel. To be reliable and efficient, this strategy assumes that simulations are sophisticated enough to make them realistic and comparable to experimental measurements. Therefore, numerical simulations must be equipped with advanced models and account for potential 3D effects, which is a primary goal of this thesis and the POSEIDON project presented in Section 1.2.3.

In the following, a quick overview of current and future challenges is presented and the reader can refer to more exhaustive reviews for more information [Taccogna and Garrigues, 2019; Kaganovich et al., 2020].

Plasma wall interactions

In typical HTs, the walls are usually covered by a ceramic layer, usually, Boron Nitride (BN) or Boron Nitride-Silicon Dioxide (BNSiO2), and are more rarely simply metallic [Choueiri, 2001a]. In all cases, charged particles can hit the walls, which leads to undesired effects.

When an electron hits a wall, it can be either backscattered, elastically or not, or simply absorbed. With the exception of an elastic event, a collision with a wall represents a loss of energy and mass for the plasma flow, which is detrimental for performances. An incident electron with sufficient incoming energy can also tear off other electrons from the material: this event is called Secondary Electron Emission (SEE). Secondary electrons are colder than primary electrons and follow a different velocity distribution function. Besides, the classical plasma wall transition [Chen, 1974, Chapter 8], [Keidar et al., 2001] can be severely modified [Raitses et al., 2005b]. The exact mechanism of electron-collisions is difficult to model [Taccogna, 2003] and in spite of recent progress [Villemant, 2018], simple laws [Vaughan, 1989; Gascon et al., 2003; Sydorenko, 2006; Barral et al., 2003] remain the common way to picture this interaction. Experimental measurements [Barral et al., 2003] showed BN and BNSiO2 minimize SEE but a better understanding of plasma wall interactions, in general, would certainly guide us toward improved and innovative wall material composition.

Because ions are so much more massive than electrons, their impact on the wall can damage the ceramic layer leading to erosion [Cho et al., 2013; Schinder, 2016]. Erosion is visible after a few hundreds of hours of operation as shown in Figure 1.9.
Figure 1.9 (b) shows regular ridges on the ceramic covering the PSS-1350 walls, whose origin

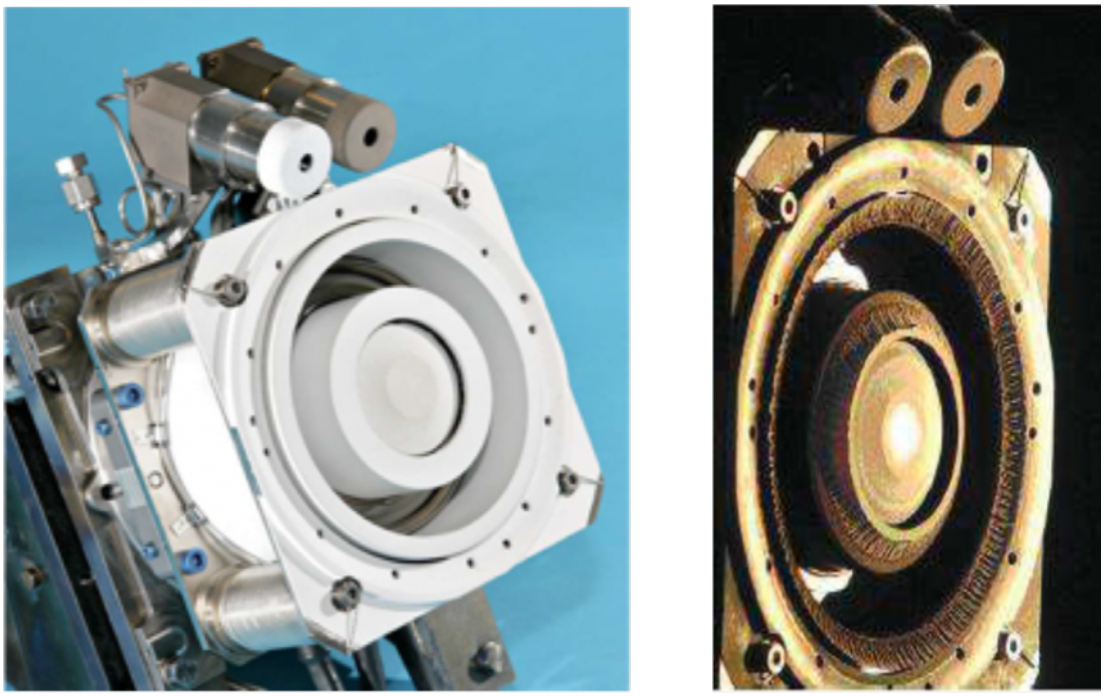

(a) (b)

Figure 1.9: (a): brand new PPS-1350 (Credits Safran). (b): PPS-1350 severely eroded (Credits Safran).

is still unclear [Mazouffre et al., 2003]. This azimuthal pattern is designated as anomalous erosion and is present in other types of HTs [Brown and Walker, 2020]. The modeling of erosion and subsequent numerical simulations remains challenging to perform for two reasons. First, since this is a slow phenomenon, long runtimes are necessary, which is still beyond current capabilities without resorting to numerical artifacts to accelerate the computation. Second, since walls boundaries are changing in time, adaptive meshes are needed. For this kind of scenario, unstructured grids, adding a level of complexity, would be suited for this task.

Erosion first decreases performances of the HTs by chamfering the exit of the HTs, hence enhancing the plume divergence. Finally, it is also a life-limiting factor of a HTs as when the ceramic or metallic wall is completely eroded, the magnetic circuit is exposed to the plasma flow until it breaks down.

Overall, plasma wall interactions remain problematic and even more for the near future. Indeed, HTs must be miniaturized with the rise of small satellites, which increases the surface-to-volume ratio and makes experimental measurements more challenging to conduct. In order to reduce wall losses, a solution could be to remove the central cylinder, which leads to a modified version of a HTs, a cylindrical Hall thruster [Smirnov et al., 2002, 2007]. Another way to minimize plasma wall interactions could be achieved by choosing an adequate magnetic field design.

Magnetic field design

The magnetic field is one of the most crucial aspects of the design of a HTs. One drawback of a typical magnetic field topology shown in Figure 1.8 (a), is that it induces a strong ion

bombardment near the exit because of non-null radial electric field in the acceleration zone. Moreover, this situation is amplified by an important sheath potential drop due to a high electron temperature in this area. This problem can be mitigated by shifting the magnetic barrier slightly outside the thruster. Furthermore, the magnetic field lines are chosen so that they are parallel to the wall as much as possible in the channel. The idea is to keep a layer of cold electrons from the anode close to the wall. The wall is not intercepted by magnetic field lines to complete the shield. This configuration results in bending iso-potential lines to reduce the radial electric field, hence ion bombardment. Figure 1.10 sums up main differences between both configurations.
Promising results were reported in the literature [Mikellides et al., 2014; Hofer et al., 2014; Grimaud et al., 2016] and innovative designs of HTs in the 100 kW range should be equipped with this technology [Jackson et al., 2017; Kaganovich et al., 2020] for deep-space missions. Magnetically shielded configurations are still in development as some erosion is still reported near magnetic poles [Sengupta and Smolyakov, 2020], but thruster performances seem more deteriorated than expected. The latter observation was associated with a greater plume divergence measured in experiments [Conversano et al., 2017]. Furthermore, magnetically shielded HTs are likely to modify non-equilibrium effects taking place in the plasma bulk such as plasma instabilities.

Plasma waves and instabilities

Waves and oscillatory behaviors are common in plasmas in general. In order to understand why they are important, we shall first remind some basic concepts.

Given a scalar quantity Ψ, we can define an *oscillation* as periodic temporal fluctuations affecting Ψ. Perhaps the most fundamental of them is the so-called plasma oscillation for which a light electron oscillates around a heavy and immobile ion because of the electric field. The corresponding pulsation ω_{pe} can be derived as:

$$\omega_{pe} = \sqrt{\frac{n_e e^2}{m_e \epsilon_0}}, \tag{1.14}$$

where n_e is the electron density, e the elementary charge, m_e the electron mass and ϵ_0 the vacuum permittivity. An analogous pulsation ω_{pi} for ions can be defined with the ion mass and ion density.

Following the definition proposed by [Chen, 1974, Chapter 4], a *wave* can be viewed as an oscillation propagating in the medium. The propagation direction is given by the wave vector $\mathbf{k}$. The study of plasma waves can be started by accounting for a small perturbation Ψ_1 in the scalar quantity Ψ expressed as $\Psi = \Psi_0 + \Psi_1$, with $|\Psi_1| \ll |\Psi_0|$, Ψ_0 being the value of Ψ in the quiescent medium. The perturbation Ψ_1 is assumed to follow an exponential law:

$$\Psi_1(\mathbf{x}, t) = |\Psi_1| \exp\left[i(-\omega t + \mathbf{k} \cdot \mathbf{x})\right]. \tag{1.15}$$

With this complex notation, equations governing the plasma can be linearized and ultimately provide the dispersion relation (DR) $\omega = \omega(\mathbf{k})$. This approach, known as linear analysis, is very helpful as it predicts under which conditions a wave will exist and propagate. In the DR, ω is complex valued and so:

$$\omega = \omega_R + i\gamma, \tag{1.16}$$

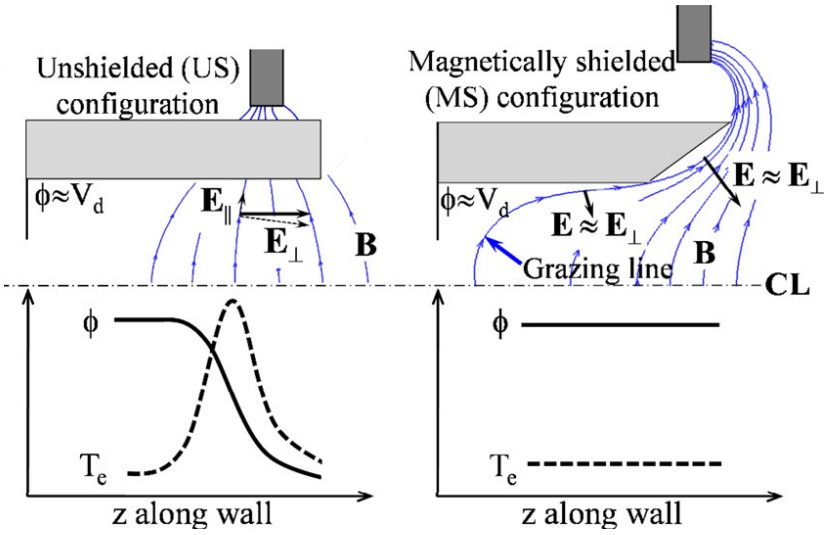

(a)

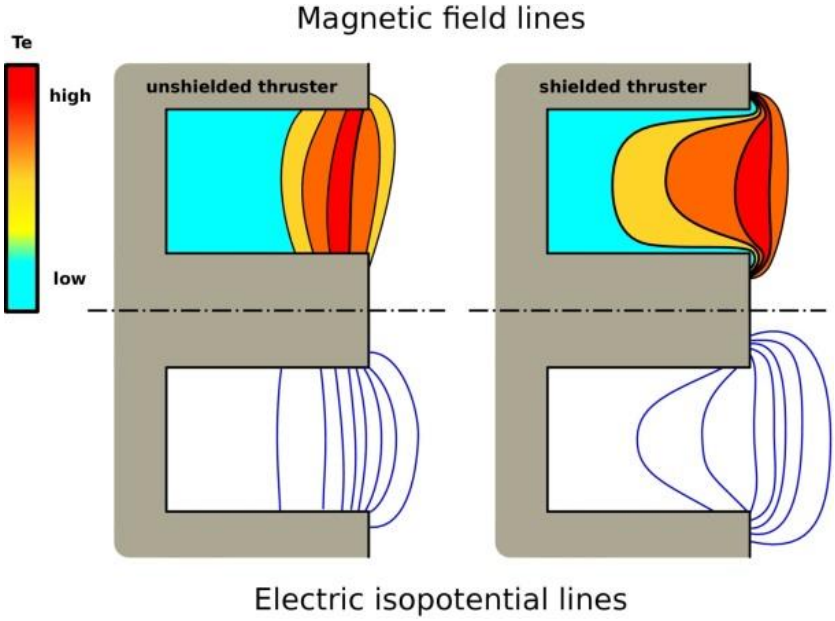

(b)

Figure 1.10: Left column: Magnetically unshielded / typical configuration. Right column: Magnetically shielded configuration. (a): from Mikellides et al. [2014], topology of the magnetic field in both configurations along with qualitative evolution of the potential and electron temperature at the wall. (b): from Garrigues et al. [2019], 2D spatial distribution of electron temperature (top) and iso-potential lines (bottom) for both configurations.

where ω_R is the angular frequency of the wave and γ the growth rate of the wave. If $\gamma < 0$ then the wave will disappear quickly. However, if $\gamma > 0$, then the wave amplitude will grow exponentially, hence giving rise to an *instability*. At some point, the assumption $|\Psi_1| \ll |\Psi_0|$ will break down and linear theory will not suffice to describe what happens next. Some saturation mechanisms stemming from nonlinear effects will eventually balance the exponential growth and a new equilibrium will be established. Describing this intricate state is very challenging

and more advanced models such as nonlinear or quasi-linear theory are needed. For more details about linear, non-linear and quasi-linear theory the reader can refer to the rich existing literature [Stix, 1992; Bakunin, 2018; Jones, 2012; Kadomtsev and Shafranov, 2012; Vedenov, 1963].

In the case of HTs, the system has multiple feedback loops, such as collisions between particles or transfer of energy between the electric field and particles (wave-particle interaction) for instance. As a result, a HT is conducive for the development of a whole range of instabilities that co-exist and interact with each other. Therefore, it becomes delicate to interpret experimental and numerical results and to identify what is going on in spite of recent progress [Smolyakov et al., 2016]. Additionally, plasma instabilities occurring in HTs are multi-scale phenomena in space and time. As an example, we briefly describe three existing instabilities in a HT ranging from the kHz to the MHz scale but the reader should note that many others can take place as well [Choueiri, 2001b].

Breathing Mode

The Breathing Mode (BM) is a low frequency ($\sim 10 - 20\,\mathrm{kHz}$) instability characterized by oscillations of the ionization zone. BM can be explained by a prey-predator model, initially proposed by Fife [1998], and later improved by Hara et al. [2014]; Barral and Ahedo [2009]; Boeuf and Garrigues [1998] that unfolds in three steps. First, the ionization zone, rich in neutral particles, undergoes a strong ionization event. Then, since neutral supplies have been depleted, the ionization rate plummets. Finally, thanks to the constant axial neutral flow rate, the ionization zone is refilled with neutral particles and the process can start over. Recent findings suggest that BM could also happen in the near anode region and be coupled all together with the oscillations from the ionization zone [Dale and Jorns, 2019b,c]. In any case, BM is not a desirable trait as the resulting discharge current oscillations can damage the power supply and performances deteriorate. Some feedback controls have been proposed in the literature [Romadanov et al., 2018; Barral and Miedzik, 2011] but additional research would likely help control more and even prevent the rise of such oscillations.

Ion Transit Time Instability

The Ion Transit Time Instability (ITTI) has a mid-range frequency $\sim 100-500\,\mathrm{kHz}$ and features axial oscillations of the electric field and density. The ITTI was observed experimentally by Esipchuk et al. [1974] and more recently with Laser Induced Fluorescence measurements on the ion velocity distribution function [Vaudolon and Mazouffre, 2015]. Periodically, a wave of axial electric field grows near the anode and then is convected toward the plume. During the process, some ions gain energy from the wave and accelerate, while another population of colder ions appears. A first model was proposed by Barral et al. [2005], but its origin remains unclear . Recent numerical studies can be found in [Charoy, 2020, Chapter 6]. Overall, potential and current discharge oscillations are likely to deteriorate thruster performances, which justifies additional research efforts. Finally, the ITTI seems to interact with higher frequency azimuthal instabilities [Charoy et al., 2021] presented in the following paragraph.

Electron Cyclotron Drift Instability

Electron Cyclotron Drift Instabilities (ECDI) or Electron Drift Instabilities (EDI) refer to azimuthal waves propagating in the MHz range with a typical wavelength of the order of 1 mm. The corresponding dispersion relation can be obtained by assuming an electrostatic perturbation in the electron Vlasov equation coupled with the Poisson equation in the context

of cold ions and partially magnetized plasmas This linear analysis was initially performed for collisionless plasma shocks [Forslund et al., 1970; Lampe et al., 1971b] and it was found the ECDI arises from the overlapping of electron Bernstein waves (Doppler shifted by the $\mathbf{E} \times \mathbf{B}$ drift velocity) and ion acoustic modes [Gary and Sanderson, 1970; Gary, 1970]. In the context of HTs, this electrostatic wave was identified in experiments with coherent Thomson scattering measurements [Tsikata et al., 2009; Tsikata, 2009; Tsikata et al., 2013]. Because of its inherently 3D nature [Tsikata et al., 2010], the full 3D dispersion relation should ideally be solved. Ducrocq et al. [2006] recalls this 3D dispersion relation as:

$$\begin{aligned} 1+k^2\lambda_D^2 + \mathrm{g}\left(\frac{\omega - k_y V_d}{\Omega_{ce}}, \left(k_x^2 + k_y^2\right) r_L^2, k_z^2 \rho^2\right) \\ - \frac{k^2 \lambda_D^2 \omega_{pi}^2}{\left(\omega - k_x v_p\right)^2} = 0, \end{aligned} \tag{1.17}$$

where λ_D is the Debye length, $\omega_p i$ the ion plasma frequency, Ω_{ce} the cyclotron frequency, $V_d = E_x/B_y$, the electron drift velocity, r_L the Larmor radius of electrons, v_p the velocity of the ion beam and k_x, k_y and k_z the axial, azimuthal and radial component of the wavenumber $\mathbf{k}$. $\mathrm{g}(\Omega, X, Y)$ is the Gordeev function [Gordeev G. V., 1952] that can be expressed in two ways:

$$\begin{aligned} \mathrm{g}(\Omega, X, Y) &= i\Omega \int_0^{+\infty} e^{-X[1-\cos(\varphi)] - \frac{1}{2}Y\varphi^2 + i\Omega\varphi} \mathrm{d}\varphi, \\ &= \frac{\Omega}{\sqrt{2Y}} \mathrm{e}^{-X} \sum_{m=-\infty}^{+\infty} \mathrm{Z}\left(\frac{\Omega - m}{\sqrt{2Y}}\right) \mathrm{I}_m(X), \end{aligned} \tag{1.18}$$

where I_m is the modified Bessel function of the first kind and Z the plasma dispersion function. In this relation, we usually aim to find the complex number $\omega = \omega_R + i\gamma$ defined as in Equation (1.16), given the wavenumber $\mathbf{k}$ that is prescribed by the local geometry. Solving ω for $\mathbf{k}$ can be done with a numerical method provided by Cavalier et al. [2013] for instance. However, it is still possible to observe the ECDI in 1D [Lafleur et al., 2016a; Janhunen et al., 2018a; Smolyakov et al., 2020] and 2D [Adam et al., 2004a; Coche and Garrigues, 2014; Taccogna et al., 2019; Croes et al., 2017; Héron and Adam, 2013] numerical simulations. By doing so the original wave-vector $\mathbf{k}$ is artificially constrained in the dispersion relation, one component of $\mathbf{k}$ being 0. [Ducrocq et al., 2006] showed that in 2D, the unstable, i.e. growing, modes were located at multiples of the cyclotron frequency:

$$k_\theta \approx m\frac{\Omega_{ce}}{V_d}, \text{ with } m = 1, 2, ... \tag{1.19}$$

where k_θ is the azimuthal wavenumber and V_d the electron drift velocity.

2D axial-azimuthal simulations agree with this theoretical result but surprisingly showed a transition toward an ion acoustic wave in some cases [Boeuf and Garrigues, 2018; Charoy et al., 2019]. Indeed, a rigorous study of the full 3D dispersion relation [Cavalier et al., 2013] showed that this transition can occur only for a non-zero wave-vector parallel to the magnetic field ($k_\parallel \neq 0$), which is not the case in 1D azimuthal and 2D azimuthal-axial studies. The mechanism responsible for this transition in 2D is not clear but Lampe et al. [1971a, 1972] suggest that an anomalous wave-particle interaction called resonance broadening could "smear out" discrete frequencies from Equation (1.19). There is however no consensus on this matter yet. For 1D azimuthal and 2D radial-azimuthal simulations, for which the axial direction is

not considered, another transition was reported: an inverse energy cascade [Janhunen et al., 2018a,b; Smolyakov et al., 2020; Taccogna et al., 2019]. In this configuration, energy from high k-modes is transferred to low k-modes over time, but this effect is probably due to the absence of convection of the instability into the plume [Taccogna and Garrigues, 2019]. In a 2D radial-azimuthal setup, the inverse cascade analysis can become even more delicate to interpret as interactions with the walls can trigger another kind of instability, the Modified-Two-Stream Instability (MTSI) [Janhunen et al., 2018b; Villafana et al., 2021] depending on the plasma conditions [Petronio et al., 2021]. Finally, saturation following the linear stage is assumed to be related to ion trapping [Lafleur et al., 2016b; Lampe et al., 1971a, 1972] as it was observed in all simulations.

The ECDI is likely to be a fundamental phenomenon of the plasma dynamics of HTs as it is suspected to play a major role in the so-called *anomalous transport* presented in Section 1.3.2. In this thesis, the ECDI was studied in a 2D axial-azimuthal (Chapter 3), 2D radial-azimuthal (Chapter 4) and 3D setup (Chapter 5).

Anomalous transport

A recurrent research topic of HTs concerns the anomalous axial transport of electrons in the near-exhaust channel. The classical theory states that collisions are responsible for the displacement of electrons across the magnetic barrier. We can convince ourselves by considering the simplified electron momentum equation:

$$\frac{\partial}{\partial t}\left(m_e n_e \mathbf{u}_e\right) + \nabla \cdot \left(m_e n_e \mathbf{u}_e \mathbf{u}_e\right) = -e n_e \left(\mathbf{E} + \mathbf{u}_e \times \mathbf{B}\right) - \nabla \cdot \mathbf{\Pi}_e - m_e \nu_m n_e \mathbf{u}_e, \tag{1.20}$$

where n_e is the electron density, $\mathbf{u}_e$ the electron velocity, ν_m the electron-neutral collision frequency and $\mathbf{\Pi}_e$ the pressure tensor. Assuming the flow is at steady state and isothermal and neglecting electrons inertia, the left hand-side of Equation (1.20) can be set to 0 and $\nabla \cdot \mathbf{\Pi}_e = 0$. In such case, the axial velocity $u_{e,z}$ and azimuthal velocity $u_{e,\theta}$ can be expressed as

$$\begin{cases} u_{e,z} = \dfrac{\frac{e}{m_e \nu_m}}{1 + \Omega_{ce}} E_z = \mu_{\text{classical}} E_z & (1.21) \\ u_{e,\theta} = \left| \dfrac{\mathbf{E} \times \mathbf{B}}{\mathbf{B}^2} \right|. & (1.22) \end{cases}$$

In Equation (1.22), we recover the fact that electrons drift azimuthally, which is the Hall current. More importantly, Equation (1.21) indicates that the electron transport in the axial direction should be proportional to the axial electric field with a *mobility* factor $\mu_{\text{classical}}$

$$\mu_{\text{classical}} = \frac{\frac{e}{m_e \nu_m}}{1 + \Omega_H^2}, \tag{1.23}$$

where Ω_H is the Hall parameter from Equation (1.13). For a HT $\Omega_H \gg 1$ so the mobility can be approximated by

$$\mu_{\text{classical}} \approx \frac{1}{\Omega_H B}. \tag{1.24}$$

However this expression of the mobility is unable to explain discrepancies near the channel exit. Indeed, as shown in Figure 1.11 experimental values are several orders of magnitude above the theoretical results.

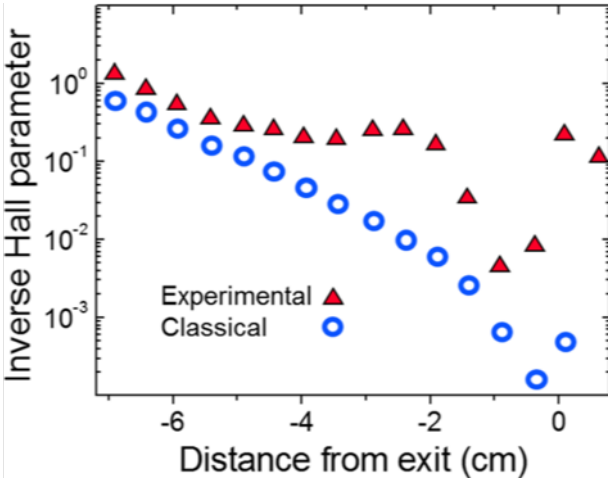

Figure 1.11: Comparison of inverse Hall parameter Ω_H^{-1} between experimental measurements (red triangles) made by Meezan et al. [2001] and classical theory (blue circles). Picture taken from [Boeuf, 2017].

In order to account for this *anomalous* mobility, the common approach is to consider a Bohm collision frequency ν_B [Chen, 1974, Chapter 5] that serves as a semi-empirical law:

$$\nu_B = \alpha_B \Omega_H, \tag{1.25}$$

where α_B is a parameter to be fitted. However, this collision frequency does not refer to real collisions: it is only a fitted parameter to agree with experimental data. Therefore this topic has been actively investigated over the last two decades. Plasma wall interactions via secondary electron emissions [Sydorenko et al., 2006; Raitses et al., 2011] or sheath instabilities [Taccogna et al., 2009] have been considered but it seems their role remains modest [Tavant et al., 2018]. Recently Lafleur et al. [2016a,b] demonstrated that the ECDI, described in Section 1.3.2, was more likely to be responsible for the enhanced cross-field mobility. From kinetic theory, they showed that an *ion-electron friction* force could be added in the momentum electron Equation (1.20):

$$\mathbf{R}_{ei} = \langle \delta E_\theta \delta n_e \rangle_\theta \mathbf{x}, \tag{1.26}$$

where the δ symbol indicates fluctuations of the azimuthal electric field and electron density and $\langle\rangle_\theta$ represents the average operator over the azimuthal domain. When δE_θ and δn_e are in phase, which is the case in the presence of ECDI, this additional force is not zero and an effective mobility μ_{eff} can be derived:

$$\mu_{\text{eff}} = \mu_{\text{classical}} \left(1 - \frac{\Omega_{ce}}{\nu_m} \frac{\langle \delta n_e \delta E_\theta \rangle_\theta}{n_0 E_z} \right), \tag{1.27}$$

where n_0 is the average plasma density over the computational domain. This new force, explored in [Charoy et al., 2020], is promising and perhaps will help us to further explain the anomalous transport.

1.4 Plasma modeling for HTs

Numerical simulations for HTs require to model the plasma dynamics and we shall in this section explain the different existing approaches.

As for all plasmas, the dynamics of the species α present in the discharge (electrons, ions and neutrals) can be described by the velocity distribution function $f_\alpha(\mathbf{x}, \mathbf{v}, t)$. Physically, $f_\alpha \mathbf{dxdv}$ represents the number of particles α that are located at the position $\mathbf{x}$, in the volume $\mathbf{dx}$ and whose velocities lie in the velocity interval $\mathbf{dv}$ around $\mathbf{v}$ at time t. Its variation df_α in the phase space $(\mathbf{x}, \mathbf{v})$ is due to collisions whose contributions are denoted by the collision operator $\mathcal{Q}_\alpha$:

$$df_\alpha = \mathcal{Q}_\alpha, \tag{1.28}$$

The variation df_α can be expressed as a total derivative using the variables $t, \mathbf{x}$ and $\mathbf{v}$:

$$\frac{\partial f_\alpha}{\partial t} + \mathbf{v}_\alpha \cdot \nabla_{\mathbf{x}} f_\alpha + \mathbf{a}_\alpha \cdot \nabla_{\mathbf{v}} f_\alpha = \mathcal{Q}_\alpha, \tag{1.29}$$

where $\mathbf{a}_\alpha$ is the acceleration of the species α. Using second Newton's law, the so called Boltzmann equation is finally obtained:

$$\frac{\partial f_\alpha}{\partial t} + \mathbf{v}_\alpha \cdot \nabla_{\mathbf{x}} f_\alpha + \frac{\mathbf{F}_\alpha}{m_\alpha} \cdot \nabla_{\mathbf{v}} f_\alpha = \mathcal{Q}_\alpha, \tag{1.30}$$

where $\mathbf{F}$ symbolizes the external forces applied at $\mathbf{x}$. For a plasma, it can be reduced to the Lorentz force:

$$\mathbf{F}_\alpha = q_\alpha \left(\mathbf{E} + \mathbf{v}_\alpha \times \mathbf{B} \right), \tag{1.31}$$

where $\mathbf{E}$ and $\mathbf{B}$ are respectively the electric and magnetic fields. Both must satisfy the four Maxwell's equations but the problem for HTs is simpler as the magnetic field is usually assumed to be known as generated by the solely coils although a limited self-induced $\mathbf{B}$ was observed in numerical [Liang et al., 2017] and experimental work [Peterson et al., 2002]. With a static $\mathbf{B}$ field satisfying $\boldsymbol{\nabla} \cdot \mathbf{B} = 0$, we also have $\nabla \times \mathbf{E} = \mathbf{0}$, which means the electric field $\mathbf{E}$ can be derived from a potential ϕ such as $\mathbf{E} = -\boldsymbol{\nabla}\phi$. Therefore, the final Poisson equation in the plasma flow reads:

$$\epsilon_0 \Delta \phi = -e \left(Z n_i - n_e \right), \tag{1.32}$$

where Z is the atomic number of ions. For this work, only singly-ionized particles are considered so $Z = 1$. Overall, plasma dynamics are obtained by solving the coupled system formed by Equation (1.30) and Equation (1.32). Several strategies exist to tackle this problem and the choice of the solving method primarily depends on the kind of plasma we are dealing with. Indeed, as shown in Figure 1.12, it exists a wide variety of plasmas in terms of temperature and density and their description can be obtained by other ways than the brute force resolution of the Boltzmann equation.

A useful metric we can rely on is the Knudsen number K_n. The latter is defined as

$$K_n = \frac{l_m}{L}, \tag{1.33}$$

where l_m is the mean free path and L is the typical dimension of the plasma box. The mean free path is defined as the typical length for which a particle undergoes a collision. At low

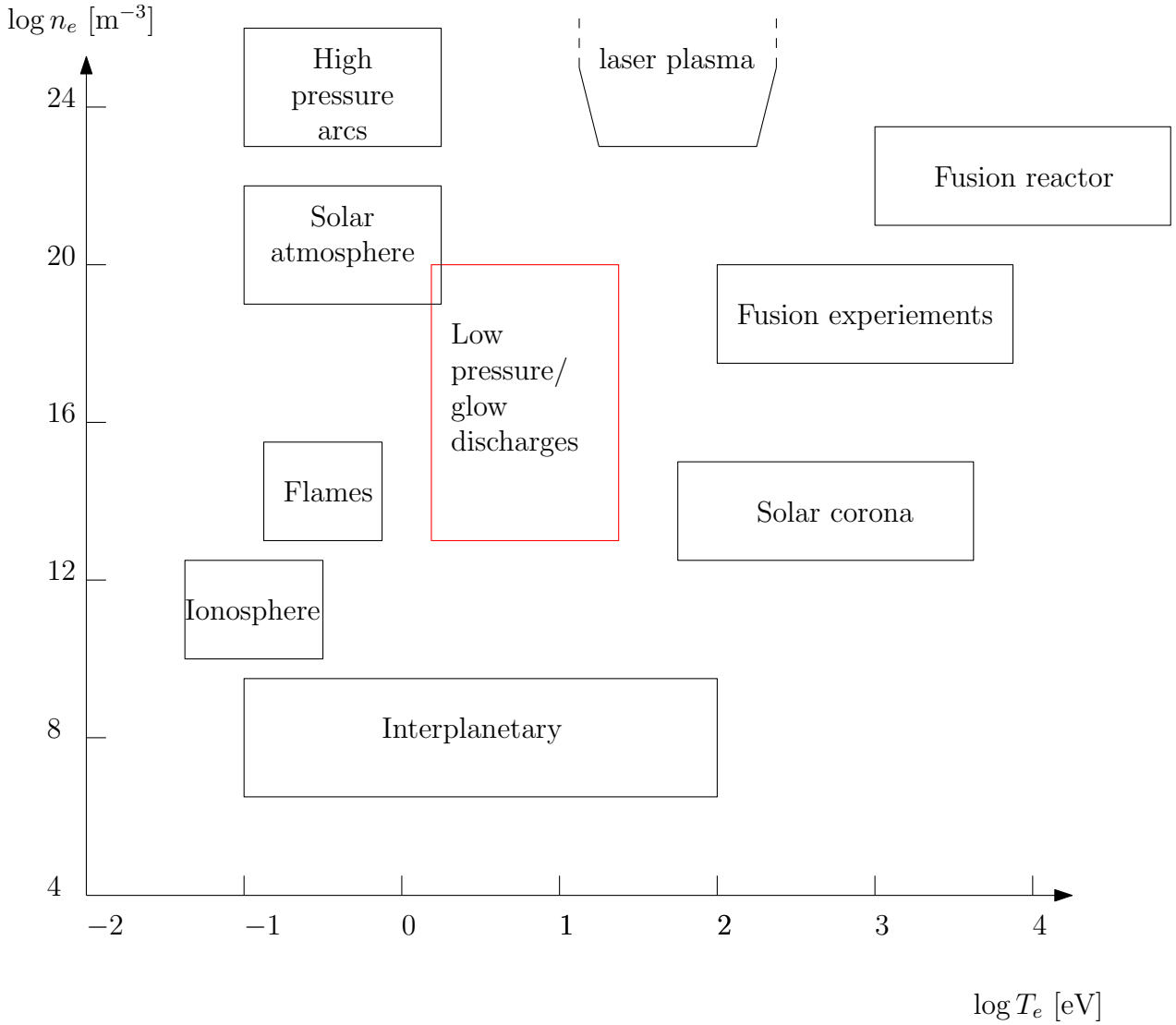

Figure 1.12: Classification of plasmas according to their electron density and temperature [Bittencourt, 2004, Chapter 1], [Lieberman and Lichtenberg, 2005, Chapter 1]. HT's plasmas are low pressure glowing discharges highlighted in red occurring at a rather cold temperature.

density, for $K_n \gtrapprox 0.01$, collisions are scarce and the plasma can be treated as a collection of particles that can be tracked by second Newton's law. Thus, the phase space $(\mathbf{x}, \mathbf{v})$ is discretized by numerical particles. This first approach refers to the **Particle-In-Cell** (PIC) methods, usually combined with a Monte Carlo module to model collisions. When the plasma density is higher, for $K_n \ll 0.01$, collisions occur more often and the plasma can be considered as a *continuum*. For this kind of scenario a **fluid model** is well-suited [Chen, 1974, Chapter 3]. With such an approach, the plasma is described with quantities integrated from the velocity distribution function f such as the density n, the Eulerian velocity $\mathbf{u}$ or temperature T. With this strategy, one can recover a system close to the Navier-Stokes equations as it will be discussed in Section 2.1.2. However, for some plasmas, there are phenomena that cannot be explained by a fluid approach. These phenomena such as Landau damping are called *kinetic effects* [Chen, 1974, Chapter 7] and can only be predicted if we allow a non-Maxwellian velocity distribution function f. In this case, directly solving the Boltzmann equation with a **Direct Kinetic** (DK) method is necessary. Note that if the density remains reasonable, the PIC technique can also

capture kinetic effects and so it is also applicable.

In the particular case of HTs, the Knudsen number K_n is rather low $\sim 0.01 - 0.1$, halfway between a free molecular flow regime and a continuous medium. Therefore, all three modelings or combinations of them, giving rise to **hybrid models**, can be used *a priori*. However, due to their respective limitations, they serve different purposes as it will be seen in the following sections.

1.4.1 Fluid models

A fluid model is obtained by considering integrated quantities extracted from the velocity distribution function. First, Equation (1.30) is multiplied by a generic function $\Psi(\mathbf{x}, t)$ that can be scalar- or vector-valued. Then, an integration over the velocity space leads to the following equation:

$$\iiint_{\mathbf{v}} \frac{\partial f_\alpha}{\partial t}\Psi \mathbf{dv} + \iiint_{\mathbf{v}} \mathbf{v}_\alpha \cdot \nabla_{\mathbf{x}} f_\alpha \Psi \mathbf{dv} + \iiint_{\mathbf{v}} \frac{\mathbf{F}_\alpha}{m_\alpha} \cdot \nabla_{\mathbf{v}} f_\alpha \Psi \mathbf{dv} = \iiint_{\mathbf{v}} \mathcal{Q}_\alpha \Psi \mathbf{dv} \tag{1.34}$$

The averaged quantities $\iiint_{\mathbf{v}} f_\alpha \Psi \mathbf{dv}$ corresponds to the moments of the original distribution function. The first three moments are respectively obtained for $\Psi = 1$, $\Psi = m_\alpha \mathbf{v}$ and $\Psi = \frac{m_\alpha}{2}\mathbf{v}^2$. The integration remains however difficult to conduct in the general case and is highly dependent on the shape of the velocity distribution function f. Assuming the plasma flow is at thermal equilibrium, f becomes a Gaussian function also called Maxwellian distribution,

$$f_\alpha = \frac{n_\alpha}{(\sqrt{\pi} v_{th})^3} \exp\left\{\left(\frac{-\mathbf{v}^2}{v_{th}}\right)\right\} \tag{1.35}$$

where $v_{th} = \sqrt{\frac{2k_B T_\alpha}{m_\alpha}}$ is the thermal velocity of species α and n_α its number density. Under this assumption, the integration can be carried out and in the example of the zeroth moment order, $\Psi = 1$, this leads to

$$\begin{array}{llll} \iiint_{\mathbf{v}} \frac{\partial f_\alpha}{\partial t}\mathbf{dv} & + \iiint_{\mathbf{v}} \mathbf{v}_\alpha \cdot \nabla_{\mathbf{x}} f_\alpha \mathbf{dv} & + \iiint_{\mathbf{v}} \frac{\mathbf{F}_\alpha}{m_\alpha} \cdot \nabla_{\mathbf{v}} f_\alpha \mathbf{dv} & = \iiint_{\mathbf{v}} \mathcal{Q}_\alpha \mathbf{dv} \\ \Longrightarrow \frac{\partial n_\alpha}{\partial t} & + \boldsymbol{\nabla}_{\mathbf{x}}(\mathbf{u}_\alpha n_\alpha) & +0 & = S_{ioniz,\alpha}, \end{array} \tag{1.36}$$

which is the conservation of mass (or equivalently number density) with $n_\alpha = \iiint_{\mathbf{v}} f_\alpha \mathbf{dv}$ and $\mathbf{u}_\alpha = \frac{1}{n_\alpha} \iiint_{\mathbf{v}} f_\alpha \mathbf{v}_\alpha \mathbf{dv}$ the number density and hydrodynamic velocity of species α. $S_{ioniz,\alpha}$ is the net number of particles created by ionization and its precise expression needs additional assumptions that were proposed by Benilov [1996]; Le and Cambier [2016]. With the same procedure, $\Psi = m_\alpha \mathbf{v}$ and $\Psi = \frac{m_\alpha}{2}\mathbf{v}^2$ respectively leads to the momentum conservation equation and the energy conservation equation for species α. Therefore, one ends up with a multi-fluid model in which each species α is described with a set of equations mass, momentum and energy. These sets are coupled with collision source terms which needs to be clarified under several additional assumptions [Benilov, 1996; Le and Cambier, 2016]. Besides, each k moment equation involves a term with the $k+1$ moment. For instance, in Equation (1.36) the mass conservation equation requires to know the mean velocity $\mathbf{u}$ given by the momentum equation, the first moment of the distribution function. Therefore, the system must be equipped with some closure terms in the energy equation to limit the model to three equations.

Unfortunately, this is a difficult exercise as classical closure terms such as the perfect gas law or the Fourier law are not necessarily valid for low pressure plasmas. As of today, there is still no consensus on which closure terms should be used and their modeling has been investigated by the means of theoretical studies [Graille et al., 2009; Hagelaar, 2015; Ahedo and De Pablo, 2007], [Ferziger and Kaper, 1973, Chapter 6] or using numerical measurements from PIC simulations [Boccelli et al., 2020; Joncquieres et al., 2018]. Among the most sophisticated models for HTs,Joncquieres et al. [2020] derived a 10-moment fluid model: one for continuity, three for each velocity component and one for energy, for both ions and electrons [Joncquieres et al., 2020]. Yet, this approach can be numerically costly and is highly constrained by the CFL number in the sheath, which requires a fine discetization [Joncquieres et al., 2018]. Therefore, it is common to consider less moments, by limiting to 2 dimensions in space, get rid of the Poisson equation and assume a quasi neutral plasma everywhere in the simulation domain, and neglecting electron inertia terms in the momentum equation. Under these assumptions, one obtains a so-called Drift-diffusion fluid model, and the electric field is obtained directly by a Navier Stokes-like set of equations [Hagelaar et al., 2002; Barral and Ahedo, 2009]. Simple 1D models are also possible [Ahedo et al., 2001, 2003] to separately simulate the axial and radial directions. With such approximations, the sheath, where quasi-neutrality is not satisfied, is modeled with a dedicated add-on. Besides, all non-linear effects stemming from the electron inertia terms are lost. On that latter point recent works proposed new numerical schemes accounting for the inertia term and improved the transition toward the sheath model [Alvarez-Laguna et al., 2020; Laguna et al., 2020]. With a simplified 1D or 2D fluid model, the simulations can be fairly fast, and can provide a rough approximation of some characteristics of HTs such as the discharge current or the thrust. Thus, this approach is useful for industry but has limited prediction capabilities.

In addition, deriving a fluid model with the assumption that the velocity distribution function is Maxwellian eliminates most *kinetic effects*, which induce important deviations from a Maxwellian. Indeed, it was shown in the literature that both electrons and ions can follow non-Maxwellian velocity distribution functions [Morozov and Savelyev, 2000, Chapter 1], [Goebel and Katz, 2008, Chapter 4] and [Boeuf and Garrigues, 2018]. Observed anomalous electron transport in the axial direction [Meezan et al., 2001] could not be explained by classical theory. Instead, fluid models had to rely on an empirical model using a Bohm collision frequency ν_B [Fife, 1998; Joncquieres, 2019], [Chen, 1974, Chapter 5]. Yet, it seems that the anomalous transport is more likely due to the ECDI creating an additional force [Charoy et al., 2020] that can only grow when kinetic effects are present [Lafleur et al., 2016a,b].

In order to understand better and model those kinetic effects, Particle-In-Cell simulations can be used as numerical experiments.

1.4.2 Particle-In-Cell technique

As already mentioned, the Particle-In-Cell (PIC) technique solves the Boltzmann equation by discretizing the phase space $(\mathbf{x}, \mathbf{v})$ with numerical particles that collide with each other following a Monte Carlo procedure. It is usually combined with a fixed mesh on which particle charges are interpolated with a Cloud-In-Cell method in order to solve the Poisson equation [Birdsall and Langdon, 2004]. Because no approximation is made on the Boltzmann equation, it is accurate and thus, captures all kinetic effects missing in fluid models. Besides, it is robust given that it satisfies conditions that will be presented in Equations (2.5) and (2.6). Finally, the Lagrangian module of PIC codes, handling transport, collision and interpolation of charges on

the grid is easily scalable on supercomputers. Nevertheless the same stability conditions stated in Equations (2.5) and (2.6) along with important memory requirements in order to account for millions of numerical particles make these simulations limited to a few tens of microseconds in a reduced simulation domain. Therefore, they are unable to capture long range and large scale phenomena such as spokes or breathing modes without numerical tricks.

As a result, PIC codes are mainly used in academic configurations over a short time range in order to get physical insights and reliable numerical data to build future fluid models. A good example of how PIC simulations are useful is plasma-wall interactions. Indeed, most boundary conditions are usually straightforward to model in this formalism (see Section 2.5), which allows a detailed study of sheath structures forming at the walls. Thanks to these numerical experiments, Joncquieres et al. [2018] was able to adjust the sheath model for metallic walls in his 10-moment fluid solver. With a similar methodology, Tavant et al. [2019] could derive a non isothermal sheath model following a polytropic law $T_e n_e^{1-\gamma}$, where γ is the polytropic index. Plasma-wall interactions continue to be investigated and the simplest way to do it is to consider 1D-radial simulations [Domínguez-Vázquez et al., 2019; Ahedo and De Pablo, 2007; Taccogna et al., 2007]. In particular it was shown that the sheath structure was very sensitive to the direction of local magnetic field lines [Ahedo, 1997; Chodura, 1982; Moritz et al., 2019] and could also be the place of oscillations due to strong Secondary Electron Emissions (SEE) [Sydorenko et al., 2009; Taccogna et al., 2005]. The latter behavior was also retrieved in a 2D radial-azimuthal configuration by Tavant et al. [2018]; Croes [2017]. Besides, a 2D radial-azimuthal setup can capture multidimensional effects such as the ECDI [Croes et al., 2017; Héron and Adam, 2013] and sometimes the MTSI [Janhunen et al., 2018b; Villafana et al., 2021; Petronio et al., 2021]. This configuration will be considered in Chapter 4.

As mentioned in Section 1.4.1, the ECDI probably plays an important role in the anomalous electron transport [Lafleur et al., 2016a,b] and so the axial direction can be accurately described only if the azimuthal direction is considered as well. Therefore, 2D axial-azimuthal simulations have been extremely popular over the last years [Adam et al., 2004b; Lafleur and Chabert, 2017; Boeuf and Garrigues, 2018; Charoy et al., 2019; Coche and Garrigues, 2014; Taccogna et al., 2019], which helped to derive a new additional force for fluid models [Charoy et al., 2020; Lafleur et al., 2016b]. A particular attention will be paid on the axial-azimuthal plane in Chapter 3.

In a 2D radial-axial setup, the axial electron transport would then be probably underestimated but it can still provide grounds to develop new models for cathodes and account for geometrical effects when the plasma flow exits the channel to go into the plume [Szabo, 2001; Cho et al., 2016]. Furthermore, this plane has to be considered for more realistic comparisons with experimental data [Cho et al., 2015, 2013, 2014; Yokota et al., 2006].

The ideal solution would be to consider 3D simulations that are the only ones which can fully capture the highly coupled multidimensional physics of HTs. Unfortunately, as previously mentioned they become extremely costly and so only a few 3D PIC simulations have been carried out thanks to some necessary simplifications. They either relaxed time and spatial constraints from Equations (2.5) and (2.6) by using artificial small mass ion or large permittivity [Hirakawa and Arakawa, 1995, 1996], or they considered miniaturized HTs by using scaling factors [Taccogna and Minelli, 2018; Minelli and Taccogna, 2017]. Recent progress on a 3D configuration will be reported in Chapter 5.

If PIC simulations remain accurate and reliable, they nevertheless require a substantial amount of numerical particles [Charoy et al., 2019; Villafana et al., 2021]. Even though they do have enough numerical particles to discretize the phase space $(\mathbf{x}, \mathbf{v})$, they still suffer from

statistical noise that is inherent from the method itself.

One way to address this drawback is to consider hybrid or Direct Kinetic simulations.

1.4.3 Hybrid and Direct Kinetic (DK) methods

Hybrid methods consist in combining both fluid and PIC modeling to get the best of them. Because the time step is constrained by fast and light electrons, it is commonplace to model them as a fluid following a near Maxwellian velocity distribution function while heavy species such as ions and neutrals are tracked with the PIC technique. With the exception of [Lam et al., 2015], this approach has been mainly used in radial-axial configurations. In particular, we can cite HPHall, which is perhaps the closest industrial, COTS-level (Commercial off-the-shelf) numerical tool available today. HPHall is based and numerical and semi-empirical parameters and was initially developed by Fife [1998] at MIT in the 90's and later upgraded by Parra et al. [2006]; Hofer et al. [2007] with a HPHall-2 version. Since then, it has inspired many other codes in the literature [Vazquez, 2019; Bareilles et al., 2004; Koo, 2005; Brieda, 2012; Panelli et al., 2021]. In the radial-axial plane, the axisymmetric assumption is usually made, i.e., the solution is assumed independent of the angle θ. This allows to reduce the computational domain to 2D with the rotation axis taken as a boundary. Besides, the mesh is aligned with the imposed magnetic field lines to simplify electron fluid equations, although it may dramatically complicate the final mesh [Araki and Wirz, 2014]. HPHall, and other similar codes, are able to simulate up to around a millisecond in a reasonable time and to retrieve the main outputs of HTs that fairly agree with experimental data. Thus, it allows for quick parametric study for the industry. However, there are some limitations with such hybrid approach. For instance, all deviations from the electron Maxwellian distribution, that do exist at the walls, cannot be accurately predicted. Besides, since the azimuthal direction is averaged, all phenomena such as instabilities (ECDI, Spokes for instance), occurring in this direction cannot be accounted for. The use of semi-empirical parameters can mitigate these effects, but can also represent a limitation for the development of new thrusters for which they must be updated.

Finally, the last existing approach to model HTs is Direct Kinetic method. In contrast to previous hybrid simulations, DK models get entirely rid of the persistent statistical noise due to PIC method. Thus, Hara [2015] proposed a 2D DK code in the axial-azimuthal plane that was able to capture kinetic effects similarly to purely PIC simulations. Later Raisanen [2020] enriched this model by considering the radial axial direction including innovative sheath models but with electrons considered as a fluid. One limitation from DK simulations remains their cost as for each point of the grid, the phase space of the three velocities must be solved, which represents three more grids to solve simultaneously. As a result, only limited results regarding DK models are available as of today.

1.4.4 Summary

Purely fluid models remain the fastest approach, especially if quasi-neutrality is assumed because it avoids solving the costly Poisson equation. Besides the numerical cost will be strictly proportional to the number of points in the grid. The price to pay for speedup will be the loss of important kinetic effects.

Correction of fluid models can be achieved with the help of kinetic simulations such as PIC or DK, that serve as numerical experiments, or by using hybrid PIC-fluid or DK-fluid models. As of today, there is no consensus on which hybrid model is the best but they remain the most

pragmatic approach to get fairly good predictive results to test and design HTs.

If kinetic effects must be taken into account, fully PIC or DK codes are best suited with the price of costly numerical simulations. Besides, PIC codes need to deal with statistical noise while DK codes are confronted with more complex boundary conditions models.

For a more comprehensive overview of Hall thruster modeling, the reader can refer to [Boeuf, 2017; Hara, 2019; Taccogna and Garrigues, 2019; Kaganovich et al., 2020].

1.5 Objective and scope of this PhD thesis

In the near future HTs will be widely used and in spite of an apparent simplicity, there are still many challenges to overcome. In particular, the recent findings on the anomalous transport proved that kinetic effects were absolutely crucial to have an accurate description of the plasma physics. The study of kinetic phenomena and plasma instabilities is usually performed using PIC approaches as they are fairly easy to implement and robust. However, because of a considerable computational cost, these numerical investigations are led in 1D or 2D academic setups. As we have seen in the literature, this approach has definitely provided many insights and has advanced our understanding of HTs but future research needs are arising. Indeed, Cartesian configurations cannot reproduce industrial geometries of real HTs so predictive numerical tools are still out of reach. Furthermore, the physics of HTs is inherently 3D so 1D or 2D configurations inevitably modify the plasma dynamics, which was noticed for plasma instabilities for instance. Therefore this PhD thesis aims to start addressing these shortcomings and advance the numerical modeling of HTs and low temperature plasmas.

Sponsored by Safran, this PhD was led at the European Center for Advanced Research and Training in Scientific Computing (CERFACS in French) and numerical investigations were performed using a massively parallel PIC code, AVIP. As it will be explained in Chapter 2, the development of AVIP was initiated in 2015 and comes in two versions: PIC and full fluid. The first goal of the PhD was to demonstrate the capability of AVIP PIC to describe accurately the plasma dynamics using an unstructured grid formulation. The use of unstructured grids is innovative in our community because it dramatically complicates the code implementation. As of today, all other existing codes rely on either Cartesian or Cylindrical meshes. In order to eliminate possible implementation errors, AVIP-PIC was carefully verified in 2D standard axial-azimuthal and radial-azimuthal setups with the successful participation of CERFACS in international benchmarks. Results are shown and discussed in Chapter 3 and Chapter 4. During this work, new features regarding cathode models and plasma-wall interactions were implemented as well, in particular, a model for secondary electron emissions is now available. Besides, it is now possible to model a dielectric layer in the context of an unstructured framework. Additionally, a substantial effort was made on accelerating simulations by using advanced methods for solving the Poisson equation (see Chapter 2 and Chapter 5) and by tuning an active particle control algorithm (see Section 3.3). A final goal for this PhD has been to advance on more realistic configurations by considering 3D setups. The main physical and numerical aspects of these 3D simulations are discussed in Chapter 5.

Chapter 2

AVIP PIC: code presentation and development

Particle-In-Cell (PIC) codes are a convenient tool to study low temperature and low pressure plasmas in Hall Thrusters (HTs). They are quite straightforward to implement and can describe important kinetic effects present affecting the physics. However, current codes in the literature are all based on structured grids using either a Cartesian [Croes, 2017; Sydorenko, 2006; Minelli and Taccogna, 2017] or a Cylindrical/axisymmetric [Vazquez, 2019] coordinate system. This choice is made because the implementation of the code remains simple. Furthermore, because of the important numerical cost of PIC simulations, the latter are, in their vast majority, focused on 1D and 2D configurations. To our knowledge, only Taccogna and Minelli [2018]; Minelli and Taccogna [2017] a few years ago and Hirakawa and Arakawa [1995, 1996] in the 90's attempted to perform 3D simulations. In this Chapter, an innovative PIC solver, AVIP PIC is presented. Its main strength relies on its capability to deal with unstructured meshes in both 2D and 3D configurations. All required modules to model collisions or plasma wall interactions have been developed in this context and open the path to handle more complex geometries than Cartesian and Cylindrical. Numerical concepts and the subsequent implementations are detailed in this Chapter. The performances of the solver are finally analyzed and discussed on a more realistic 3D case.

Contents

2.1 Overview of AVIP 53
2.1.1 A powerful tool derived from AVBP 53
2.1.2 AVIP for plasma simulations 53
2.2 Numerical implementation 55
2.2.1 Concept and preliminaries 55
2.2.2 Initialization 58
2.2.3 Monte Carlo collisions 59
2.3 Poisson's equation 62
2.3.1 Finite volume method 62
2.3.2 Interpolation scheme 63

2.3.3 Discretization of the Laplacian operator 64
2.3.4 Dielectric interface 69
2.3.5 Solving the linear system 72
2.3.6 Electric field 74
2.4 Particles displacement 74
2.4.1 Solving the equations of motion 74
2.4.2 Transport of particles across the grid 75
2.5 Boundary conditions for particles 77
2.5.1 Classical boundaries 77
2.5.2 Cathode models 78
2.5.3 Secondary electron emission 81
2.6 AVIP PIC performances 84
2.6.1 Code optimization 84
2.6.2 Strong scaling results 87
2.7 Conclusion 91

2.1 Overview of AVIP

2.1.1 A powerful tool derived from AVBP

Historically, AVIP was built from an AVBP fork made in 2015. AVBP is a home made code developed at CERFACS which aims to solve the Navier-Stokes equations for multi-species compressible reactive flows using unstructured and hybrid meshes in 3D. Since its creation in 1997, it has successfully been applied in the domain of combustion [Schonfeld and Rudgyard, 1999; Esclapez et al., 2021; Malé et al., 2021] and aerodynamics [Queguineur et al., 2019] for both academic and industrial geometries. It is designed to be portable on a variety of hardware architectures and has demonstrated excellent computing performances [Gicquel et al., 2011]. It is written in Fortran90 and is parallelized with the Message Passing Interface 1 (MPI-1). Domain decomposition is achieved with the external PARMETIS library [Karypis and Kumar, 2009].

Therefore, AVIP benefits from AVBP features and aims to carry out cold plasma simulations in 3D using unstructured meshes. The latter point is a substantial characteristic since existing plasma codes usually rely on 1D or 2D structured meshes using either a Cartesian [Sydorenko, 2006; Charoy, 2020] or sometimes a Cylindrical/axisymmetric [Vazquez, 2019] coordinates system. To my knowledge, only [Zakari, 2013] used unstructured grids in 2D axisymmetric configurations only.

2.1.2 AVIP for plasma simulations

AVIP fluid

Since AVBP was initially developed for solving Navier-Stokes equations, a natural approach for AVIP is to model the plasma as a fluid. As mentioned in Section 1.4.1 plasma fluid models

are derived from the Boltzmann equation assuming the velocity distribution function is close to a Maxwellian. Then it is possible to integrate the Boltzmann equation with the moments corresponding to the mass, momentum and energy. At CERFACS, Joncquieres et al. [2020] performed such work and was able to get a 10-moments system for electrons and ions, including innovative boundary conditions [Joncquieres et al., 2018]. This is a multi-species fluid model i.e. each species dynamics is governed by an Euler-like set of equations. For each species α (e for electron or i for ion) the set breaks down as follow,

$$\begin{cases} \partial_t n_\alpha + \nabla \cdot (n_\alpha \mathbf{u}_\alpha) = S^0_\alpha \\ \partial_t (n_\alpha \mathbf{u}_\alpha) + \nabla \cdot \left(n_\alpha \mathbf{u}_\alpha \otimes \mathbf{u}_\alpha + k_B T_\alpha n_\alpha \bar{\bar{\mathbf{I}}} \right) = q_\alpha n_\alpha (\mathbf{E} + \mathbf{u}_\alpha \times \mathbf{B}) + \mathbf{S}^1_\alpha \\ \partial_t (\epsilon_\alpha) + \nabla \cdot \left(\left(\frac{1}{2} n_\alpha \mathbf{u}^2_\alpha + \frac{\gamma}{\gamma - 1} k_B T_\alpha n_\alpha \right) \cdot \mathbf{u}_\alpha \right) = q_\alpha n_\alpha \mathbf{E} \cdot \mathbf{u}_\alpha + S^2_\alpha \end{cases} \tag{2.1}$$

In Equation (2.1) each line respectively describes the conservation of mass, momentum and energy of the species α. n is the density, $\mathbf{u}$ the hydrodynamic velocity, q the species Coulombian charge, $\mathbf{E}$ the electric field, $\mathbf{B}$ the magnetic field, T the temperature, k_B the Boltzmann constant and $\gamma = 5/3$ the heat capacity ratio. The total energy per unit mass is denoted by $\epsilon_\alpha = n_\alpha \left(3/2 k_B T_\alpha + \mathbf{u}^2_\alpha / 2\right)$. The $S^0_\alpha, \mathbf{S}^1_\alpha, S^2_\alpha$ terms represent the collisions accounted for in this model. Further details about them can be found in [Joncquieres, 2019]. The treatment of neutral particles is simplified as it is assumed they keep a constant energy and velocity. So only the continuity equation is retained,

$$\partial_t n_n + \nabla \cdot (\mathbf{u}_{0,n} n_n) = S^0_n \tag{2.2}$$

where $\mathbf{u}_{0,n}$ is a constant vector.

Because it is very challenging to solve Equations (2.1) and (2.2) at once in addition to Gauss law Equation (1.32) for the electric field, the computation is split into three steps as shown in Figure 2.1.

In a first step, the electric field is obtained from the Gauss law. The numerical method will be detailed in Section 2.3.3. In a second step, an implicit solver is used to compute the collisions terms $S^0_\alpha, \mathbf{S}^1_\alpha, S^2_\alpha$. Finally, we can use the two first steps as inputs to solve Equations (2.1) and (2.2). The latter are extremely similar to the Euler equations, and so it is possible to adjust existing numerical techniques in AVBP to integrate the final system.

AVIP PIC

AVIP PIC is an explicit PIC (Particle-In-Cell) code that was developed as an alternative to AVIP fluid for performing plasma simulations. In this approach, ions, electrons and neutrals are modeled as point particles described by their position $\mathbf{x}$ and velocity $\mathbf{v}$. Thus, the phase space ($\mathbf{x}$,$\mathbf{v}$) is discretized and we follow the motion of each individual particle α with Newton's second law,

$$m_\alpha \partial_t (\mathbf{v}_\alpha) = q_\alpha (\mathbf{E} + \mathbf{v}_\alpha \times \mathbf{B}) . \tag{2.3}$$

Similarly to AVIP fluid, the electric field $\mathbf{E}$ is obtained from the Poisson's equation (1.32) and the magnetic field $\mathbf{B}$ is an input of the simulation. Note that the hydrodynamic velocity $\mathbf{u}_\alpha$ is related to the particles velocities $\mathbf{v}_\alpha$ by $n_\alpha \mathbf{u}_\alpha = \int (f_\alpha \mathbf{v}_\alpha d\alpha)$, where f_α is the velocity

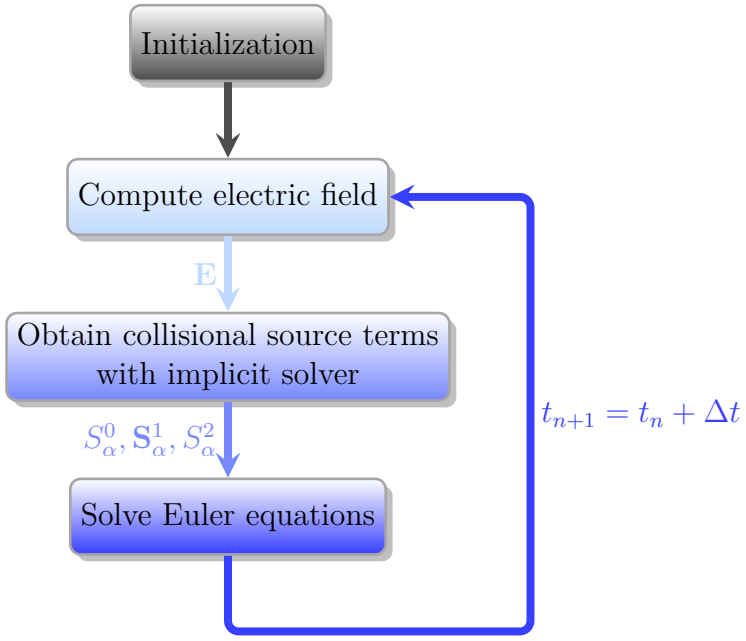

Figure 2.1: Splitting operators for fluid resolution

distribution function. In practice, the number of point particles to follow is too high. Indeed, in HTs, the plasma density is usually $\sim 10^{17} - 10^{18}\mathrm{m}^{-3}$ and the volume occupied by the near plume and channel are at least $> 100\,\mathrm{cm}^3$. So the number of physical particles to track down over a relevant time range would be over 10 billion for one species, which greatly exceeds current computational capabilities. As a result, physical particles for one species (electron, ion, neutral) are packed in macroparticles. Every macroparticle has a statistical weight q_f defined as

$$q_{f,\alpha} = \frac{n_{p,\alpha} V_c}{N_{ppc}} \tag{2.4}$$

where $n_{p,\alpha}$ is the species density, V_c the volume of a cell and N_{ppc} the number of macroparticles in the current cell. Thus, one macroparticle contains q_f physical particles. For the sake of simplicity, a macroparticle will be named as a particle in the following. Moreover electrons, ions and neutrals will respectively denoted by the e, i and n subscripts.

When appropriately used (see section 2.2.1), PIC simulations are precise because they capture the whole physics from the Boltzmann equation, including kinetic effects that are implicitly omitted in fluid models. Thus, in spite of being computationally costly, they can guide the derivation of new fluid models. An example of using PIC measurements to develop AVIP fluid can be found in [Joncquieres et al., 2018].

2.2 Numerical implementation

2.2.1 Concept and preliminaries

AVIP PIC follows a standard approach that is depicted in Section 2.2.1. During each iteration of the calculation, the following modules are activated successively:

1. At the beginning of each iteration, we start by calculating binary collisions between particles. This is done by an optimized Monte Carlo algorithm. Further details are

provided in Section 2.2.3

2. Then charged particles are interpolated onto the meshgrid in order to compute the right hand side of Poisson's equation $-e\left(n_i - n_e\right)/\epsilon_0$ (see Section 2.3.2).

3. Poisson's equation is solved by a linear solver whose implementation is detailed in Section 2.3

4. The electric field $\mathbf{E}$ is interpolated back to every particle

5. Particles' velocities and positions are updated using the equations of motion (see Section 2.4)

6. Finally boundary conditions for particles are applied (see Section 2.5)

Following earlier recommendations [Birdsall, 1991] on accuracy and stability, the PIC simulation must meet constraints on temporal and spatial discretization (Δt, Δx) formulated as

$$\begin{cases} \omega_{p,e}\Delta t < 0.2 & (2.5) \\ \Delta x < 0.5\lambda_D & (2.6) \end{cases}$$

where $\lambda_D = \sqrt{\frac{\epsilon_0 k_B T_e}{n_e e^2}}$ denotes the Debye length and $\omega_{p,e} = \sqrt{\frac{n_e e^2}{m_e \epsilon_0}}$ the plasma frequency. Here, ϵ_0 is the vacuum permittivity, k_B the Boltzmann constant, n_e the electron density, e the elementary charge and m_e the electron mass. The spatial resolution Δx can be defined as $\Delta x = V_c^{1/n_d}$ where n_d is the dimension of the mesh.

In Equation (2.5), the plasma frequency refers to oscillations of electrons around immobile ions. Thus, the time step Δt is chosen such that even the highest frequency phenomena are well discretized.

Equation (2.6) indicates the spatial discretization should capture at least two Debye lengths λ_D. As a reminder, the Debye length is the typical length above which screening of the electric field occurs. For a typical HT, we obtain $\Delta t \sim 0.1-1$ ps and $\Delta x \sim 50$ µm. These are challenging requirements for HT simulations given the typical dimensions of a thruster (a few centimeters) and the physical times to be simulated (a few tens of microseconds)

A third condition concerns the number of macroparticles and plays a key role in the accuracy of PIC simulations. Since they represent groups of particles they inevitably induce numerical discretization errors of the phase space. The error becomes negligible when enough particles per Debye sphere are present [Okuda and Birdsall, 1970] but usually the number of particles per cell N_{ppc} is used instead. indeed, as reported by Birdsall [1991], when the number of macroparticles becomes too low, numerical heating arises as the Debye shielding effect is not well described. This results in creating artificial and supplementary collisions between particles. Above a certain N_{ppc} threshold, using more macroparticles would not change the results significantly and any differences would be due solely to numerical noise inherent to PIC simulations. It is difficult to define precisely when results do not vary "significantly", but in 1D it seems a couple of thousands of particles are necessary [Janhunen et al., 2018a] while in 2D around 200 particles is likely to be enough in axial-azimuthal configurations [Charoy et al., 2019] and in radial-azimuthal setups (see chapter 4).

A specificity of AVIP PIC is that it can handle only 2D and 3D unstructured meshes. Cells can be either rectangles/triangles in 2D and quadrilaterals/tetrahedrons in 3D. The mesh is either generated by the home made package *hip* or the CENTAUR software [Borras et al., 1988].

Since the physics of HTs is intrinsically 3D [Tsikata et al., 2010] and velocities are coupled by the Lorentz force, it is necessary to account for the three velocity components even when the mesh is 2D. In practice, all three $(\mathbf{v}_x, \mathbf{v}_y, \mathbf{v}_z)$ velocities components are updated using the equations of motion (see Section 2.4.1), but the actual displacement of the particle in the 2D domain only rely on the in-plane velocities. AVIP is capable of handling such a 2D3V model: illustrations will be provided in Chapters 3 and 4.

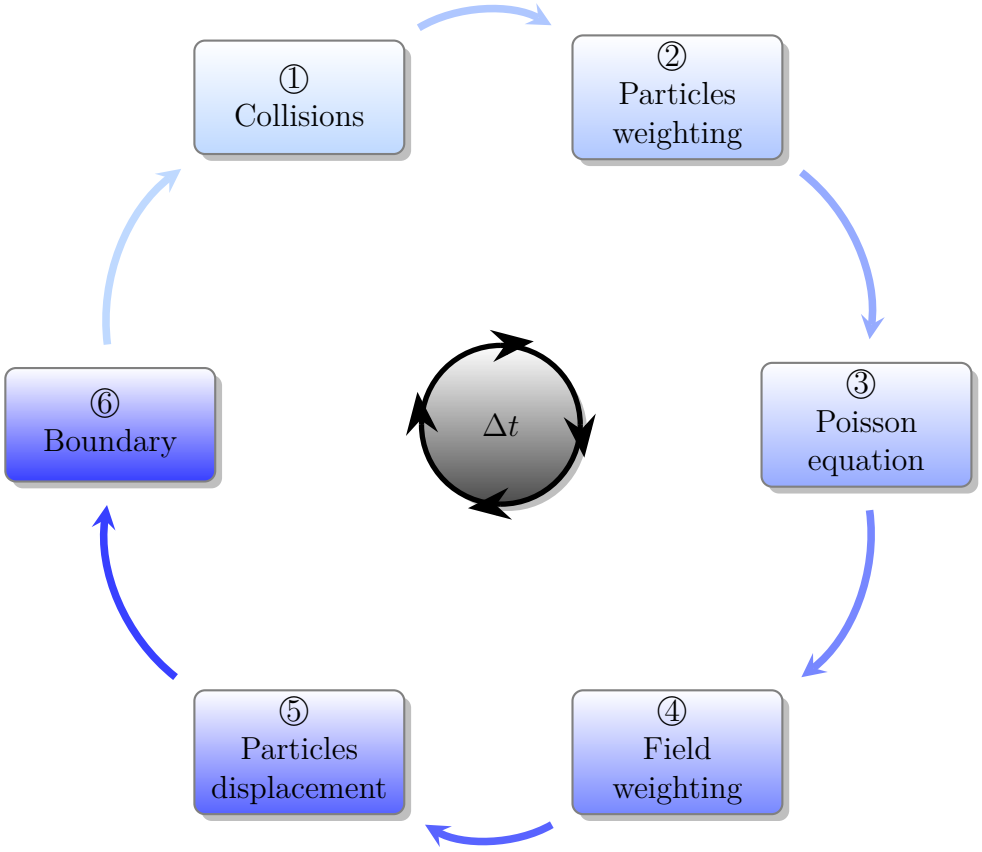

Figure 2.2: PIC cycle executed at every iteration in AVIP PIC

2.2.2 Initialization

AVIP PIC typically starts the simulation by setting a uniform density in the whole domain at thermal equilibrium. Thus, particles are spread uniformly in each cell of the domain. In an unstructured grid, this operation is not trivial because cells/elements can have different shapes. The standard procedure consists in performing iso-parametric transformations that are widely used in finite element methods [Auffray, 2007]. Figure 2.3 shows an example of how uniform distribution of particles is achieved in a tetrahedron element.

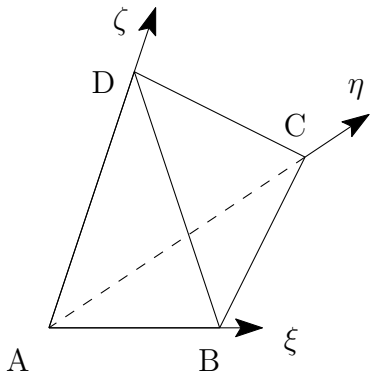

Figure 2.3: Iso-parametric coordinate system (ξ, η, ζ) in a tetrahedron

For each element, one can define a local coordinate system (ξ, η, ζ) where the locations of vertices are summarized in Table 2.1.

Vertex	ξ	η	ζ
A	0	0	0
B	1	0	0
C	0	1	0
D	0	0	1

Table 2.1: Local vertices coordinates in a tetrahedron. Point A is the origin.

With this choice, any particle P (x_ξ, x_η, x_ζ) belonging to the cell can be obtained by a linear combination

$$\mathbf{AP} = x_\xi \mathbf{AB} + x_\eta \mathbf{AC} + x_\zeta \mathbf{AD}, \tag{2.7}$$

where x_ξ, x_η, x_ζ are real numbers between 0 and 1. Since we assume particles are uniformly distributed we can define the first coordinate,

$$x_\xi = R_1 \tag{2.8}$$

where R_1 is a random number between 0 and 1. However, it exists constraints on x_η and x_ζ because the cell is tetrahedral and not cubic. Thus, for the second coordinate, we place ourselves in the (ξ,η) plane and we notice we must be below the straight line whose equation

is given by $\eta = -\xi + 1$. Mathematically this can be formulated as

$$\begin{aligned} & 0 \leq x_\eta \leq -x_\xi + 1 \\ \Longrightarrow & 0 \leq x_\eta \leq 1 - R_1, \text{ from Equation (2.8)} \\ \Longrightarrow & x_\eta = R_2(1 - R_1) \end{aligned} \tag{2.9}$$

where R_2 is a random number between 0 and 1. Finally for the last coordinate we consider the (BCD) plane. We observe the particle P must lie between A and this plane whose equation is $(\zeta + \eta + \xi - 1 = 0)$. Thus we infer,

$$\begin{aligned} & 0 \leq x_\zeta \leq 1 - x_\eta - x_\xi \\ \Longrightarrow & 0 \leq x_\eta \leq 1 - R_1 - R_2(1 - R_1) + 1, \text{ from Equation (2.9)} \\ \Longrightarrow & x_\eta = R_3\left(-R_1 - R_2(1 - R_1)\right) + 1 \end{aligned} \tag{2.10}$$

where R_3 is a random number between 0 and 1. As a final step, we must express the coordinates of P in the canonic coordinate system of domain $(O, \mathbf{x}, \mathbf{y}, \mathbf{z})$ using A (x_A, y_A, z_A), B (x_B, y_B, z_B), C (x_C, y_C, z_C) and D (x_D, y_D, z_D). Thus, we are looking for **OP** and from linear algebra we can write

$$\begin{aligned} & \mathbf{OP} = \mathbf{OA} + \mathbf{AP} \\ \Longleftrightarrow\ & \mathbf{OP} = \mathbf{OA} + x_\xi \mathbf{AB} + x_\eta \mathbf{AC} + x_\xi \mathbf{AD}, \text{ from Equation (2.7)} \\ \Longleftrightarrow\ & \mathbf{OP} = (1 - x_\xi - x_\eta - x_\zeta)\mathbf{OA} + x_\xi \mathbf{OB} + x_\eta \mathbf{OC} + x_\xi \mathbf{OD} \end{aligned} \tag{2.11}$$

Substituting Equations (2.8) to (2.10) into Equation (2.11), we obtain the Cartesian coordinates of P in the current cell with random numbers. In AVIP random numbers are obtained by the built-in Fortan90 function `RANDOM_NUMBER`. The seed of the Random Number Generator is hardcoded so that PIC runs are deterministic which greatly helps for debugging. The same procedure can be implemented for any polygons in 2D and 3D.

In addition to their positions, particles are assigned velocities that are sampled from a Maxwellian since we are at thermal equilibrium. Sampling directly the velocity components v_x, v_y, v_z cannot be done directly with an analytical formula. However, it is possible to generate them thanks to the Box and Muller [1958] method. In the case of a Maxwellian presented in Equation (1.35) this results in [Hagelaar, 2008]

$$\begin{aligned} v_x &= v_{th}\sqrt{-\log R_1}\cos(2\pi R_2) \\ v_y &= v_{th}\sqrt{-\log R_1}\sin(2\pi R_2) \\ v_z &= v_{th}\sqrt{-\log R_3}\cos(2\pi R_4) \end{aligned} \tag{2.12}$$

where R_1, R_2, R_3, R_4 are random numbers between 0 and 1 and $v_{th} = \sqrt{\frac{2k_B T_\alpha}{m_\alpha}}$ is the thermal velocity of species α.

2.2.3 Monte Carlo collisions

At the beginning of each iteration, AVIP PIC models collisions with the Monte Carlo technique. Collisions are binary and only some processes involving neutral particles are considered. Indeed, in HTs, neutral particles are much more numerous than charged particles in the discharge

Name	Threshold	Collision
Electrons		
Elastic scattering	0 eV	$e^- + Xe \rightarrow e^- + Xe$
First excitation	8.315 eV	$e^- + Xe \rightarrow e^- + Xe^*$
First ionization	12.13 eV	$e^- + Xe \rightarrow e^- + Xe^+ + e^-$
Ions		
Elastic scattering	0 eV	$Xe^+ + Xe \rightarrow Xe^+ + Xe$
Charge exchange	0 eV	$Xe^+ + Xe \rightarrow Xe + Xe^+$

Table 2.2: Existing collisions in AVIP PIC.

channel where the density is the highest [Goebel and Katz, 2008]. Therefore, ion-ion, electron-electron and electron-ion collisions are less likely to happen and discarded in AVIP. Table 2.2 sums up the different collisions implemented in AVIP PIC.

The Monte Carlo method needs cross section data that are provided by the LXCat database [2010; 2016]. With a classical Monte Carlo method, for each pair of particles that may collide, the total collision frequency ν_T is computed as

$$\nu_T = n_t \sigma_T(E_p) v_p \tag{2.13}$$

where E_p is the kinetic energy of the incident particle (ion or electron), n_t the local density associated with the target particle (neutral) and v_p is the relative velocity between the incident and target particles. σ_T is the total cross section of all possible collisions i.e. the sum of all cross sections. From Equation (2.13), the total probability to have a collision during the time step Δt for the current incident particle is then given by

$$P_T = 1 - \exp\{(-\Delta t \nu_T)\}. \tag{2.14}$$

A random number R_1 between 0 and 1 is then compared to P_T. If $R_1 < P_T$, then a collision occurs and another random number R_2 determines which collision is chosen. This process is unfortunately very long with a large number of particles because it requires to compute kinetic energies of all particles and look up for the total cross section at every iteration whereas a significant portion of incident particles will not collide at all. As a consequence, the Monte Carlo algorithm is optimized with a variant named the null collision method from Vahedi and Surendra [1995]. Instead of computing each time ν_T, we calculate beforehand the maximum possible total collision frequency regardless of the incident energy of the particle:

$$\nu_m = n_t \max_{E_p} (\sigma_T(E_p) v_p). \tag{2.15}$$

Therefore, the total collision frequency is only computed once for the whole simulation and costly look-up operations are avoided. Note that now ν_m only depends on the local target (neutral) density n_t, whereas Vahedi *et al.* recommended to also find the maximum n_t across the simulation domain. By doing so, we avoid using costly collective MPI communications.

This modification does not affect the accuracy of the algorithm as it will be demonstrated in Section 3.3.2. From Equation (2.15), we infer the maximum collision probability expressed as

$$P_m = 1 - \exp\{(-\nu_m \Delta t)\} \tag{2.16}$$

Thus, the number N_m of particles that have a chance to collide is $N_m = P_m N_p$ where N_p is the number of incident particles. Therefore only a fraction of incident particles has to be tested. Following Mertmann et al. [2011], this is achieved by drawing a random number R_3 and if $R_3 < P_m$ then a collision may happen. A second random number R_4 then decides which kind of collision is selected with the following process:

$$\begin{aligned}
&\text{if} \quad R_4 < \frac{\nu_1}{\nu_m}, && \text{then collision 1 is selected} \\
&\text{if} \quad \frac{\nu_1}{\nu_m} < R_4 < \frac{\nu_1 + \nu_2}{\nu_m}, && \text{then collision 2 is selected} \\
&\qquad \vdots \\
&\text{if} \quad \sum_{j=1}^{N-1} \frac{\nu_j}{\nu_m} < R_4 < \sum_{j=1}^{N} \frac{\nu_j}{\nu_m}, && \text{then collision N is selected} \\
&\text{if} \quad \sum_{j=1}^{N} \frac{\nu_j}{\nu_m} < R_4, && \text{then the null collision is selected}
\end{aligned} \tag{2.17}$$

where ν_j is the collision frequency associated with the jth kind of collision. As shown in Figure 2.4, Equation (2.16) implicitly introduces a fictive collision of frequency ν_0 for which nothing happens: the *null collision* that originally gave the name of the method. In Equation (2.17), the null collision corresponds to the $(N+1)$-th collision.

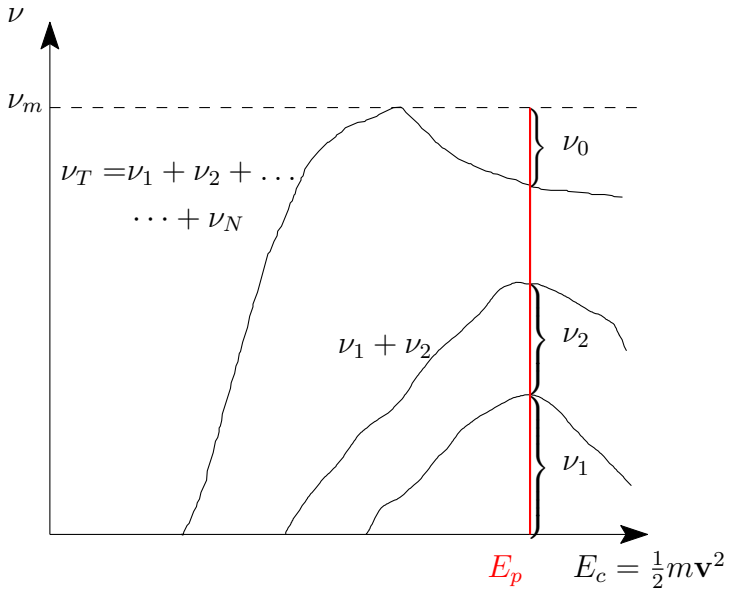

Figure 2.4: Null collision method

2.3 Poisson's equation

2.3.1 Finite volume method

Poisson's equation is treated with a finite volume method, i.e. Equation (1.32) is integrated over a control volume V_{FV} as shown below

$$\int_{V_{FV}} \epsilon_0 \Delta\phi dV = \int_{V_{FV}} -e\left(n_i - n_e\right) \mathrm{d}V \tag{2.18}$$

Then, with the Green-Ostrogradski theorem, we obtain the fluxes exiting the control volume,

$$\oint_{\partial V_{FV}} \epsilon_0 \boldsymbol{\nabla}\phi \cdot \mathbf{dS} = \int_{V_{FV}} -e\left(n_i - n_e\right) \mathrm{d}V \tag{2.19}$$

where **dS** is an orthogonal vector to the surface of the control volume. The goal is to express fluxes on the left hand side and to discretize them. A final linear system is obtained as shown in Equation (2.20).

$$\oint_{\partial V_{FV}} \epsilon_0 \boldsymbol{\nabla}\phi \cdot \mathbf{dS} = \int_{V_{FV}} -e\left(n_i - n_e\right) \mathrm{d}V \iff \mathbf{AX} = \mathbf{B} \tag{2.20}$$

where **A** contains the discretization of the Laplacian operator while **B** contains the net charge deposition onto the grid. **X** is the vector containing the potential and it is accessed by inverting the system with specialized solvers such as PETSc or MAPHYS (see Section 2.3.5).

It exists several choices for the control volume V_{FV} as shown in Figure 2.5.

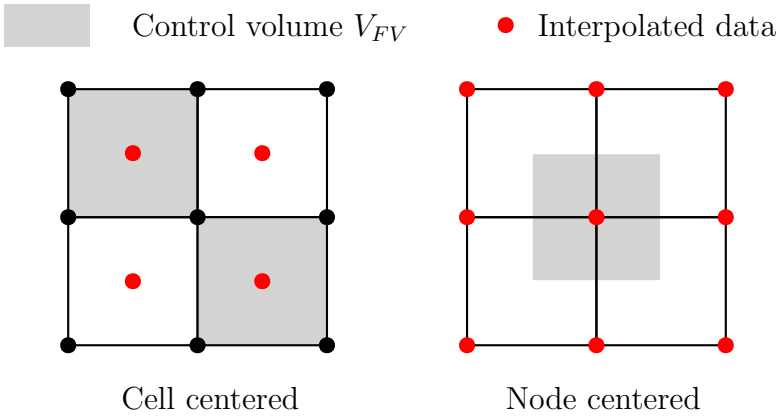

Figure 2.5: Different possible finite volume implementations

- **Cell centered**: the control volumes are the cells of the mesh and interpolated data such as density and potential are at the center of the cells. This is a natural formulation for finite volume methods in the domain of CFD [Crumpton, 1995] and low temperature plasma modeling [Tavant, 2019; Sydorenko, 2006]. However, this strategy has two drawbacks for AVIP. First, the computation of fluxes exiting the control volume can be difficult because the current domain partitioning relies on the cell nodes. Therefore, fluxes may require the knowledge of data in neighboring CPU domains, which is inconvenient. Second, unstructured grids have either the same amount or more cell centers than vertices. Typically a 3D mesh with tetrahedrons has on average six times more cells than vertices, which significantly increases the computational cost.

- **Node centered**: the control volumes are centered on the vertices where data are also stored. Thus, boundary conditions are easier to handle because data are directly available on the edge of the simulation domain and do not require additional interpolations. With a cell centered formulation, an additional interpolation between the cell center and the edge would be needed. Moreover, the node centered approach solves the two aforementioned issues but it complexifies the numerical implementation. Indeed, in addition to work with the cell volume, called *primal* volume, one also needs to define the nodal/*dual* volume. As a result, two metrics must be defined which is performed only once at the beginning of the simulation. Nevertheless, switching from one metric to another tends to slow down the computation time and increases memory consumption and so optimization of the code is crucial.

AVIP retains the node-centered formulation, more suited for our application. The control volume V_{FV} will be then renamed V_N for nodal volume. It exists several methods to construct it [Mishev, 1998; Viozat et al., 2001; Bar, 1992]. The first one is to use Voronoi cells whose vertices are equally distanced from the vertices of the primal cells as shown in Figure 2.6 (a). Unfortunately, for stretched meshes with obtuse angles like in Figure 2.6 (b), the control volume can become twisted which leads to numerical errors [Zakari, 2013].

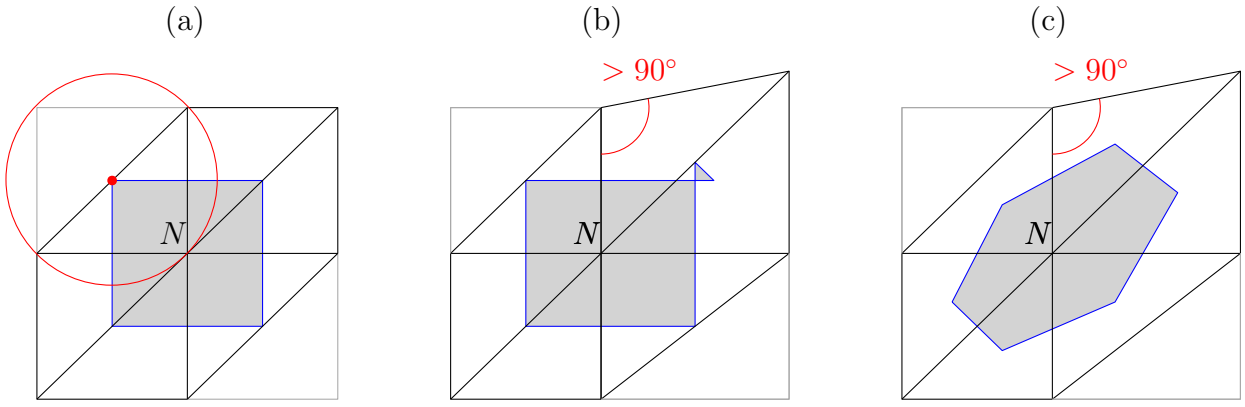

Figure 2.6: Possible control volume for a node centered approach with in (a-b) the Voronoi technique on two meshes and (c) the Median Dual control volume. (b) shows issues with obtuse angles while (c) remains convex

Therefore, we retain the other solution which is to use Median-Dual control volumes. As shown in Figure 2.6 (c), vertices are located at the centroid of the primal volume and the control volume remains convex. Specific use of the nodal volume will be detailed in Section 2.3.3.

2.3.2 Interpolation scheme

In order to solve Equation (2.19), we first need to to discretize the right hand side. At each node N we integrate the density interpolated at the node which gives

$$\int_{V_N} -e\left(n_i - n_e\right) \mathrm{d}V = e\left(N_{i,N} - N_{e,N}\right), \tag{2.21}$$

where $N_{i,N}$ and $N_{e,N}$ are the physical number of charged particles interpolated at node N. Each charged particle is located in a primal cell and it is split with geometrical weighting factors as shown in Figure 2.7.

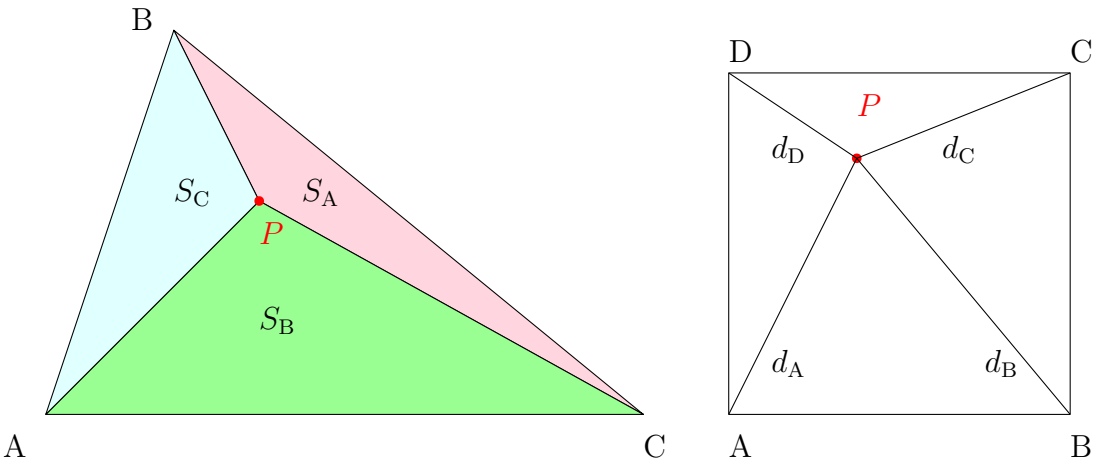

$$W_A = S_A \left(S_A + S_B + S_C\right)^{-1} \qquad W_A = d_A^{-2} \left(d_A^{-2} + d_B^{-2} + d_C^{-2} + d_D^{-2}\right)^{-1}$$

Figure 2.7: 2D example of charge deposition in a triangular (ABC) and quadrilateral (ABCD) cell. P represents the position of the particle. The weighting factor W_A for node A is expressed in both cases

In AVIP, for a triangle or tetrahedron, the charge interpolated on a mesh node depends on the opposite area/volume. For quadrilateral elements in 2D or 3D, the inverse distance weighting interpolation [Shepard, 1968] is used. In order to avoid possible division by 0, we multiply both the numerator and denominator by the product of all squared distances. So at node A we get

$$W_A = \frac{d_B^2 d_C^2 d_D^2}{d_A^2 d_B^2 d_C^2 + d_A^2 d_B^2 d_D^2 + d_A^2 d_C^2 d_D^2 + d_B^2 d_C^2 d_D^2} \tag{2.22}$$

For historical reasons, triangles and tetrahedrons are treated differently than quadrilaterals but the inverse distance weighting interpolation could be used as well. Moreover, this technique is applicable to all element shapes such as pyramids or prisms. The geometrical weighting factor W is used not only to project the charge onto the nodes but also to interpolate a vector field $\mathbf{F}$ such as $\mathbf{E}$ and $\mathbf{B}$ from the nodes onto the particle. In the case of a triangle, this is expressed by

$$\begin{cases} N_A = W_A q_{f,P} \\ \mathbf{F}_p = W_A \mathbf{F}_A + W_B \mathbf{F}_B + W_C \mathbf{F}_C \end{cases} \tag{2.23}$$

where F_p is the interpolated field vector at P and N_A the interpolated number of particles at A using $q_{f,P}$, the statistical weight of P.

2.3.3 Discretization of the Laplacian operator

The left hand side of Equation (2.19) is handled by considering each nodal volume as in Figure 2.8. For now, we assume we are far from dielectrics and ϵ_0 is the vacuum permittivity.

The original integral can be split in two,

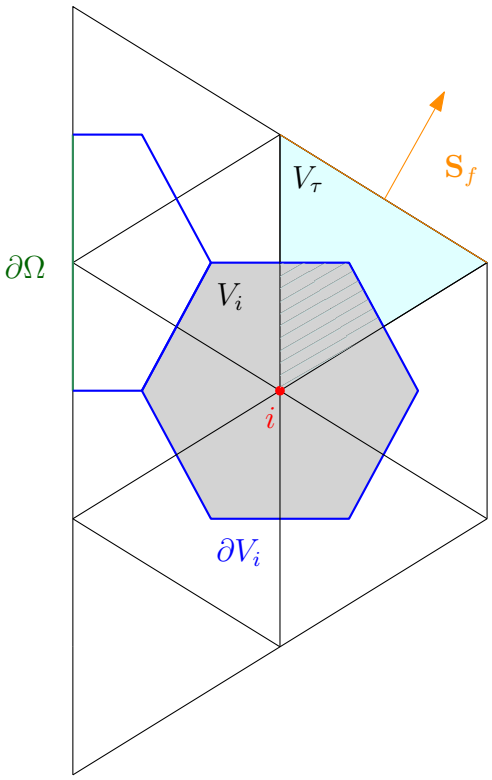

Figure 2.8: Nodal volumes in the example of a triangular mesh. Borders of the nodal volume can coincide with the boundary of the domain Ω. Nodal volume V_i and primal volume V_τ are highlighted with colored areas. One face external face S_f with its area vector is also indicated in orange.

$$\oint_{\partial V_{FV}} \epsilon_0 \boldsymbol{\nabla}\phi \cdot \mathbf{dS} = \underbrace{\int_{\partial V_i \cap \mathring{\Omega}} \epsilon_0 \boldsymbol{\nabla}\phi \cdot \mathbf{dS}}_{I_1} + \underbrace{\int_{\partial V_i \cap \partial\Omega} \epsilon_0 \boldsymbol{\nabla}\phi \cdot \mathbf{dS}}_{I_2} \tag{2.24}$$

where ∂V_i is the surface of the nodal volume V_i, $\mathring{\Omega}$ the interior of the domain Ω without the border $\partial\Omega$. For most of the nodes i, the flux of the potential across ∂V_i corresponds to I_1. For nodes located at the boundary, part of the flux exits at the domain boundary and I_2 is not identically equal to zero. We know shall detail the calculation of both integrals I_1 and I_2 in the following paragraphs.

Treatment of I_1

We can decompose I_1 into elementary fluxes as

$$I_1 = \int_{\partial V_i \cap \mathring{\Omega}} \epsilon_0 \boldsymbol{\nabla}\phi \cdot \mathbf{dS} = \sum_{\tau \ni i} \int_{\partial V_i \cap \tau} \epsilon_0 \boldsymbol{\nabla}\phi \cdot \mathbf{dS} \tag{2.25}$$

where we sum over all the cells containing the node i. In each cell τ we assume $\epsilon_0 \boldsymbol{\nabla}\phi$ to be constant so we can write:

$$I_1 = \sum_{\tau \ni i} \epsilon_0 \boldsymbol{\nabla}\phi_\tau \cdot \int_{\partial V_i \cap \tau} \mathbf{dS} \tag{2.26}$$

The gradient $\boldsymbol{\nabla}\phi_\tau$ is computed with the Green-Gauss formulation,

$$\begin{aligned}\boldsymbol{\nabla}\phi_\tau &= \frac{1}{V_\tau}\int_{V_\tau}\boldsymbol{\nabla}\phi dV \\ &= \frac{1}{V_\tau}\oint_{\partial V_\tau}\phi\mathbf{dS} \\ &= \frac{1}{V_\tau}\sum_{f\in\tau}\phi_f\mathbf{S}_f\end{aligned} \tag{2.27}$$

where V_τ is the primal volume of cell τ and $\mathbf{S}_f$ is the normal vector weighted by the surface area of face f (see Figure 2.8). The value of the potential at each face ϕ_f is assumed to be the average of the potential at the neighboring vertices so Equation (2.27) becomes

$$\frac{1}{V_\tau}\sum_{f\in\tau}\phi_f\mathbf{S}_f = \frac{1}{V_\tau}\sum_{f\in\tau}\left(\frac{1}{n_v^f}\sum_{k\in f}\phi_k\right)\mathbf{S}_f \tag{2.28}$$

where n_v^f is the number of vertices per face. The goal then is to express the normal vector $\mathbf{S}_f$ with vertices instead. To do so, we define nodal vectors as a linear combination of neighboring face normal vectors,

$$\mathbf{S}_k = \sum_{f\ni k} -\frac{n_d}{n_v^f}\mathbf{S}_f \tag{2.29}$$

where n_d is the dimension of the domain (two or three) and n_v^f the number of vertices per face (two in 2D, three for tetrahedrons, four for quadrangles). The situation is depicted in Figure 2.9.

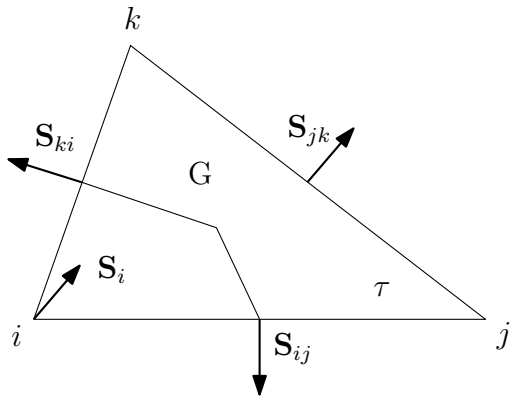

Figure 2.9: Local face normals of the primal volume V_τ and local nodal vector at vertex i. A normal face vector $\mathbf{S}_f$ is named with the face vertices. G is the centroid of the triangle

Equation (2.29) gives nodal vectors as a function of face vectors. Since we seek the contrary we must explicit Equation (2.29) for each element type. For the sake of brevity, the work will only be performed in 2D for triangles. This leads to the following linear system

$$\begin{bmatrix}\mathbf{S}_i\\ \mathbf{S}_j\\ \mathbf{S}_k\end{bmatrix} = \frac{n_d}{n_v^f}\begin{bmatrix}0 & -1 & -1\\ -1 & 0 & -1\\ -1 & -1 & 0\end{bmatrix}\begin{bmatrix}\mathbf{S}_{jk}\\ \mathbf{S}_{ki}\\ \mathbf{S}_{ij}\end{bmatrix} \tag{2.30}$$

The system can be inverted which gives

$$\begin{bmatrix}\mathbf{S}_{jk}\\ \mathbf{S}_{ki}\\ \mathbf{S}_{ij}\end{bmatrix} = \frac{1}{2}\frac{n_v^f}{n_d}\begin{bmatrix}1 & -1 & -1\\ -1 & 1 & -1\\ -1 & -1 & 1\end{bmatrix}\begin{bmatrix}\mathbf{S}_i\\ \mathbf{S}_j\\ \mathbf{S}_k\end{bmatrix} \tag{2.31}$$

As recalled by Lamarque [2007], the sum of nodal vectors is zero:

$$\mathbf{S}_i + \mathbf{S}_j + \mathbf{S}_k = \mathbf{0} \tag{2.32}$$

As a result, face vectors can be expressed by the final system:

$$\begin{bmatrix}\mathbf{S}_{jk}\\ \mathbf{S}_{ki}\\ \mathbf{S}_{ij}\end{bmatrix} = \frac{n_v^f}{n_d}\begin{bmatrix}\mathbf{S}_i\\ \mathbf{S}_j\\ \mathbf{S}_k\end{bmatrix} \tag{2.33}$$

Following notation of Figure 2.9, Equation (2.28) can be reorganized and rewritten as follows

$$\begin{aligned}\frac{1}{V_\tau n_v^f}\sum_{f\in\tau}\phi_f\mathbf{S}_f &= \frac{1}{V_\tau}\left[(\phi_i+\phi_k)\,\mathbf{S}_{ki} + (\phi_k+\phi_j)\,\mathbf{S}_{jk} + (\phi_j+\phi_i)\,\mathbf{S}_{ij}\right]\\ &= \frac{n_v^f}{n_d}\frac{1}{V_\tau n_v^f}\left[(\phi_i+\phi_k)\,\mathbf{S}_j + (\phi_k+\phi_j)\,\mathbf{S}_i + (\phi_j+\phi_i)\,\mathbf{S}_k\right] \text{ from Equation (2.33)}\\ &= \frac{1}{n_d}\frac{1}{V_\tau}\left[\phi_i\,(\mathbf{S}_j+\mathbf{S}_k) + \phi_j\,(\mathbf{S}_i+\mathbf{S}_k) + \phi_k\,(\mathbf{S}_i+\mathbf{S}_j)\right]\\ &= -\frac{1}{n_d}\frac{1}{V_\tau}\left[\phi_i\mathbf{S}_i + \phi_j\mathbf{S}_j + \phi_k\mathbf{S}_k\right] \text{ from Equation (2.32)}\end{aligned} \tag{2.34}$$

The general expression valid for 2D polygons and tetrahedrons is finally given by

$$\frac{1}{V_\tau}\sum_{f\in\tau}\phi_f\mathbf{S}_f = -\frac{1}{n_d}\frac{1}{V_\tau}\sum_{k\in\tau}\phi_k\mathbf{S}_k \tag{2.35}$$

Thus, we have expressed this primal volume gradient with the potential values stored at the vertices k. Going back to Equation (2.26), we shall now express the last integral. We can start discretizing:

$$\int_{\partial V_i\cap\tau}\mathbf{dS} = \sum_{\partial V_i\cap\tau}\mathbf{dS} = \mathbf{n}_{ik} + \mathbf{n}_{ij} \tag{2.36}$$

where $\mathbf{n}_{ik}$ and $\mathbf{n}_{ik}$ are normals weighted by the area as shown in Figure 2.10.

From [Auffray, 2007, p.39-43], it exists a simple relation between normals at the dual volume and the nodal vector $\mathbf{S}_i$ for a triangle,

$$\mathbf{n}_{ik} + \mathbf{n}_{ij} = \frac{\mathbf{S}_i}{2} \tag{2.37}$$

and in the general case, the equation is actually:

$$\int_{\partial V_i\cap\tau}\mathbf{dS} = \frac{\mathbf{S}_i}{n_d} \tag{2.38}$$

Finally, injecting Equations (2.35) and (2.38) into Equation (2.26) allows to discretize the integral I_1 for node i as

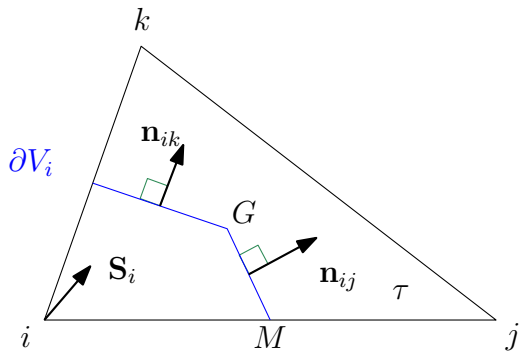

Figure 2.10: Local face normals $\mathbf{n}_{ik}$ and $\mathbf{n}_{ij}$ of the dual volume ∂V_i and local nodal vector at vertex i. G is the centroid of the triangle.

$$I_1 = -\sum_{\tau \ni i} \sum_{k \in \tau} \epsilon_0 \phi_k \frac{\mathbf{S}_k \cdot \mathbf{S}_{i,\tau}}{V_\tau n_d^2} \tag{2.39}$$

where $\mathbf{S}_{i,\tau}$ is the nodal vector defined by Equation (2.29) for node i in the cell τ. Thus, one needs to look at each cell containing i and perform the appropriate scalar products.

Treatment of I_2 and boundary conditions

The strategy to compute I_2 is similar to I_1. We discretize I_2 with the local normal vectors of the problem depicted in Figure 2.11

$$I_2 = \sum_{\substack{f \ni i \\ f \in \partial\Omega}} \epsilon_0 \boldsymbol{\nabla}\phi_f \cdot \int_f \mathbf{dS} = \sum_{\substack{f \ni i \\ f \in \partial\Omega}} \epsilon_0 \boldsymbol{\nabla}\phi_f \cdot \frac{1}{n_v^f} \mathbf{S}_f \tag{2.40}$$

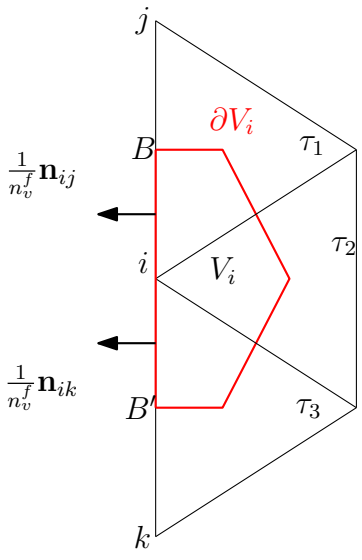

Figure 2.11: Local face normals $\mathbf{n}_{ik}$ and $\mathbf{n}_{ij}$ of the dual volume ∂V_i at the boundary domain

On each face f of $\partial\Omega$ containing i, we need to evaluate the scalar product of the potential gradient at face f with the face local normal $\frac{1}{n_v^f}\mathbf{S}_f$. The local normal around i is a fraction of the total area. In 2D, we take half of the segment ij while in 3D with tetrahedrons we would

take one-third for instance. Three possible cases exist depending on which boundary condition is applied.

Case 1: Periodic boundary condition With a periodic boundary condition, a shadow point i' corresponding to node i exists somewhere on the other side of the domain. In this case, it can therefore be treated as an internal node ($I_2 = 0$) and the full contour of the nodal volume can be calculated as previously.

Case 2: Dirichlet boundary condition A Dirichlet boundary condition sets the potential at node i to a prescribed value: $\phi_i = \phi_0$. As a result, the I_2 integral is never computed and so we implicitly set $\boldsymbol{\nabla}\phi_f = \mathbf{0}$. A necessary modification to the matrix A of Equation (2.20) will be detailed in Section 2.3.5.

Case 3: Neumann boundary condition For a Neumann boundary condition we know beforehand the value of $\boldsymbol{\nabla}\phi_f = \boldsymbol{\nabla}\phi_0$. So, it is unnecessary to discretize the gradient and we just need to compute the scalar product.

2.3.4 Dielectric interface

In Section 2.3.3, the calculation assumed the permittivity in each cell to be constant and equal to its value in vacuum: $\epsilon = \epsilon_0$. Inside a dielectric layer, it can be easily adjusted by substituting ϵ_0 by $\epsilon_0\epsilon_r$, where $\epsilon_r > 1$ is the relative permittivity depending on the material. Commonly, the channel of a HT is covered by a Boron Nitride (BN) layer [Goebel and Katz, 2008, p 325]. The relative permittivity actually depends on the temperature and local oscillations of the electric field but taking the constant value $\epsilon_r = 4$ is reasonable [Laturia et al., 2018]. The dielectric is not conductive but its surface can accumulate over time the electric charge, giving rise to a local charge per surface area σ. At the interface between the dielectric and the vacuum, Maxwell-Gauss equations predict a discontinuity of the normal component of the electric field as,

$$\epsilon_r \mathbf{E}_{\text{diel}} - \mathbf{E}_{\text{vac}} = \frac{\sigma}{\epsilon_0}\mathbf{u}_{\text{vac}\to\text{diel}} \tag{2.41}$$

where $\mathbf{E}_{\text{vac}}$ and $\mathbf{E}_{\text{diel}}$ are respectively the electric field in the vacuum and the dielectric in a neighborhood of the interface. $\mathbf{u}_{\text{vac}\to\text{diel}}$ is the local normal to the interface when going from the vacuum layer to the dielectric as shown in Figure 2.12 (a).

The discretization of the Laplacian operator at the dielectric interface needs a special treatment. The dielectric interface is defined at the nodes as shown in Figure 2.12 (c). This configuration is achieved by building separate meshes with a mesh generator software such as *Centaur* or *hip* at CERFACS. These meshes must be compatible, i.e. nodes and cell faces at the interface can be merged without ambiguity as shown in Figure 2.12 (b).

For a mesh node at the interface, the Green-Ostrogradski theorem cannot be applied directly to the whole nodal volume as in Equation (2.19) because of the discontinuity of the electric field induced by Equation (2.41). Thus, the nodal volume is split in two as shown in Figure 2.13. The Green-Ostrogradski theorem is applied on each volume and the Poisson equation becomes:

$$\oint_{\partial V_{\text{vac}}} \epsilon_0 \boldsymbol{\nabla}\phi \cdot \mathbf{dS} + \oint_{\partial V_{\text{diel}}} \epsilon_0\epsilon_r \boldsymbol{\nabla}\phi \cdot \mathbf{dS} = \int_{V_{vac}} -e\left(n_i - n_e\right) \mathrm{d}V + \int_{V_{diel}} -e\left(n_i - n_e\right) \mathrm{d}V \tag{2.42}$$

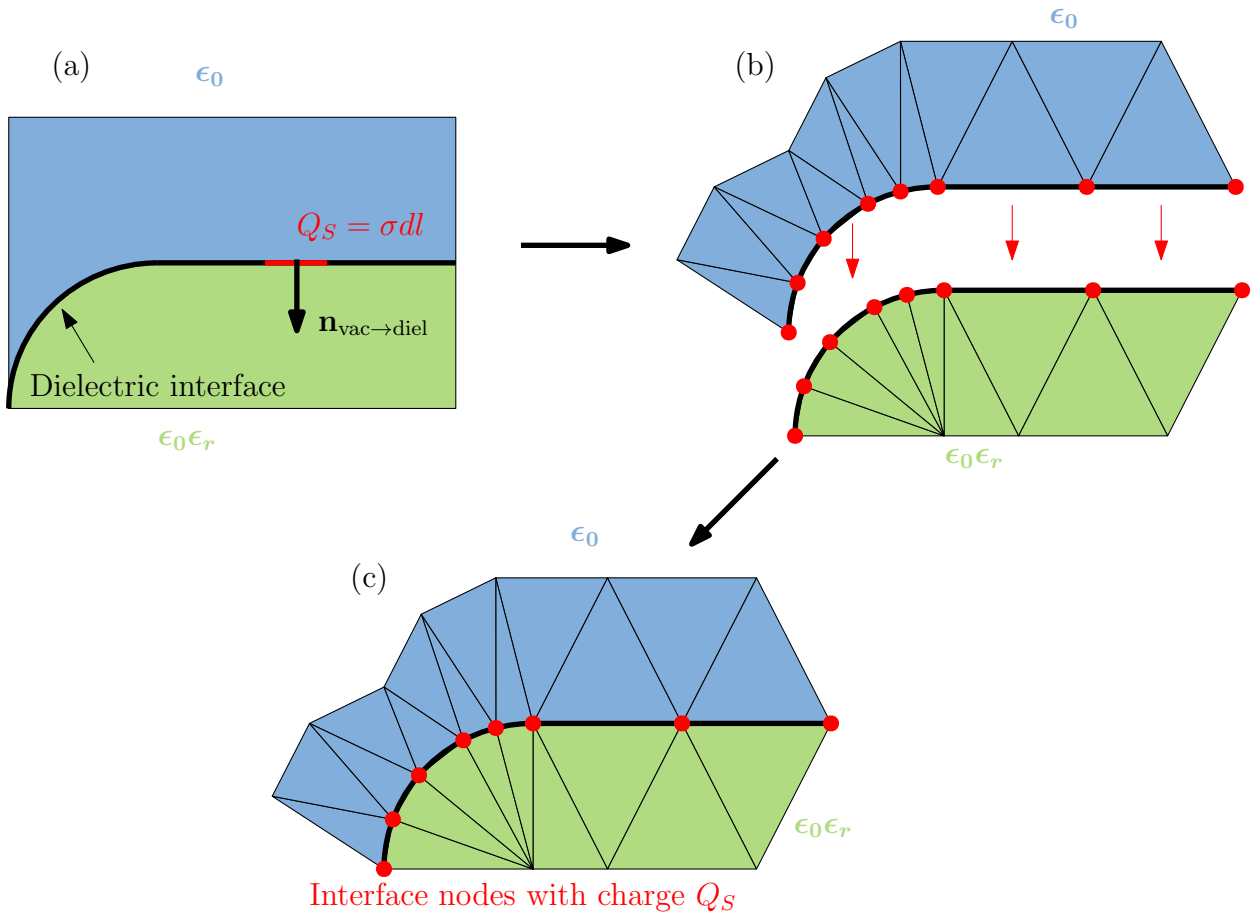

Figure 2.12: Procedure to define a dielectric border in AVIP. (a): continuous problem; a local surface charge density σ over an infinitesimal length dl provides the local charge Q_S. (b): separate discretization of two compatible computational domains for both the dielectric layer and the vacuum. (c): final computational domain after "glueing" both domains; the local surface charge Q_S is concentrated at the interface nodes

The right hand side of the equation can be simplified further by recalling there is no electric charge in the dielectric layer. Thus, it reduces to

$$\oint_{\partial V_{\text{vac}}} \epsilon_0 \boldsymbol{\nabla}\phi \cdot \mathbf{dS} + \oint_{\partial V_{\text{diel}}} \epsilon_0\epsilon_r \boldsymbol{\nabla}\phi \cdot \mathbf{dS} = Q_V \tag{2.43}$$

where $Q_V = e\,(N_{i,N} - N_{e,N})$ represent the electric charge present in the vacuum nodal volume considered. It is computed from Equation (2.21). The fluxes in the vacuum across ∂V_{vac} can be decomposed as

$$\begin{aligned}\oint_{\partial V_{\text{vac}}} \epsilon_0 \boldsymbol{\nabla}\phi \cdot \mathbf{dS} = &\int_{\partial V_{\text{vac}}\cap\mathring{\Omega}} \epsilon_0 \boldsymbol{\nabla}\phi \cdot \mathbf{dS} \\ &+ \int_{\partial V_{\text{vac}}\cap\partial\Omega} \epsilon_0 \boldsymbol{\nabla}\phi \cdot \mathbf{dS} \\ &+ \int_{\partial V_{\text{vac}}\cap S_{\text{diel}}} \epsilon_0 \boldsymbol{\nabla}\phi \cdot \mathbf{dS}_{\text{vac}\to\text{diel}}.\end{aligned} \tag{2.44}$$

The two first integrals on the right hand side are the fluxes already encountered in Equation (2.24). The third integral refers to the flux across the dielectric interface whose surface is

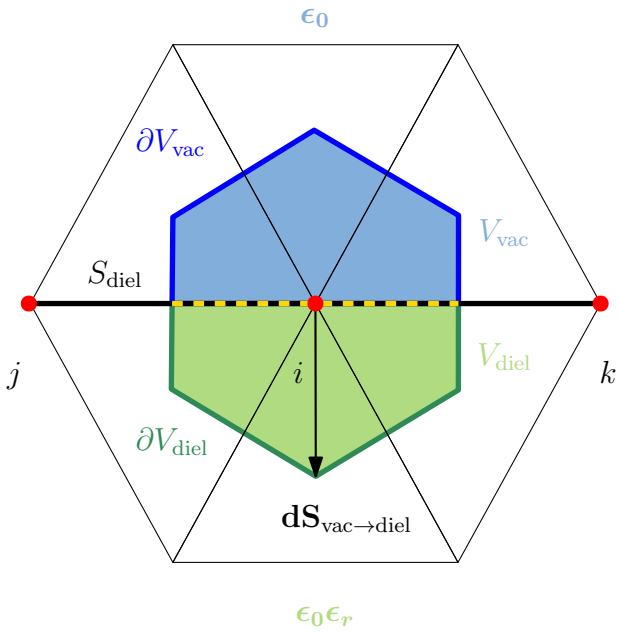

Figure 2.13: The nodal volume of a node i at the vacuum-dielectric interface can be split into V_{vac} and V_{diel}. Their respective boundaries ∂V_{vac} and ∂V_{diel} overlap with the dielectric surface S_{diel} (black-yellow dashed line).

named S_{diel} as shown in Figure 2.13. In the dielectric layer, the fluxes similarly read:

$$\begin{aligned}\oint_{\partial V_{\text{diel}}} \epsilon_0\epsilon_r \boldsymbol{\nabla}\phi \cdot \mathbf{dS} = &\int_{\partial V_{\text{diel}}\cap\mathring{\Omega}} \epsilon_0\epsilon_r \boldsymbol{\nabla}\phi \cdot \mathbf{dS} \\ &+ \int_{\partial V_{\text{diel}}\cap\partial\Omega} \epsilon_0\epsilon_r \boldsymbol{\nabla}\phi \cdot \mathbf{dS} \\ &+ \int_{\partial V_{\text{diel}}\cap S_{\text{diel}}} \epsilon_0\epsilon_r \boldsymbol{\nabla}\phi \cdot \mathbf{dS}_{\text{diel}\to\text{vac}}\end{aligned} \tag{2.45}$$

By symmetry $\partial V_{\text{diel}} \cap S_{\text{diel}} = \partial V_{\text{vac}} \cap S_{\text{diel}}$, and since $\mathbf{dS}_{\text{vac}\to\text{diel}} = -\mathbf{dS}_{\text{diel}\to\text{vac}}$, substituting Equations (2.44) and (2.45) into Equation (2.43) leads to

$$I_1 + I_2 + \int_{\partial V_{\text{vac}}\cap S_{\text{diel}}} (\epsilon_0(\boldsymbol{\nabla}\phi)_{\text{vac}} - (\epsilon_0\epsilon_r(\boldsymbol{\nabla}\phi)_{\text{diel}}) \cdot \mathbf{dS}_{\text{vac}\to\text{diel}} = Q_V \tag{2.46}$$

where $(\boldsymbol{\nabla}\phi)_{\text{vac}} = \mathbf{E}_{\text{vac}}$ and $(\boldsymbol{\nabla}\phi)_{\text{diel}} = \mathbf{E}_{\text{diel}}$. As a reminder, I_1 and I_2 respectively represent the integrated fluxes inside the domain, far from the dielectric surface, and at the computational domain boundaries. Using the jump condition from Equation (2.41), one can get:

$$I_1 + I_2 + \int_{\partial V_{\text{vac}}\cap S_{\text{diel}}} (-\sigma\mathbf{u}_{\text{vac}\to\text{diel}}) \cdot \mathbf{dS}_{\text{vac}\to\text{diel}} = Q_V \tag{2.47}$$

By definition $\mathbf{dS}_{\text{vac}\to\text{diel}} = dS_{\text{vac}\to\text{diel}}\mathbf{n}_{\text{vac}\to\text{diel}}$ which gives

$$I_1 + I_2 - \int_{\partial V_{\text{vac}}\cap S_{\text{diel}}} \sigma \, \mathrm{d}S_{\text{vac}\to\text{diel}} = Q_V \tag{2.48}$$

And finally, we integrate the surface density over the interface to get

$$I_1 + I_2 = Q_V + Q_S \tag{2.49}$$

where Q_S is the total charge accumulated at the surface by the dielectric. Overall, the numerical implementation is extremely similar to what was described in Section 2.3.3 with an additional contribution on the right hand side of the equation. The surface charge Q_S, initially zero, is easily computed by distributing the charge of each particle exiting the domain at the dielectric interface as shown in Figure 2.14. A unit test case is presented in Appendix A.

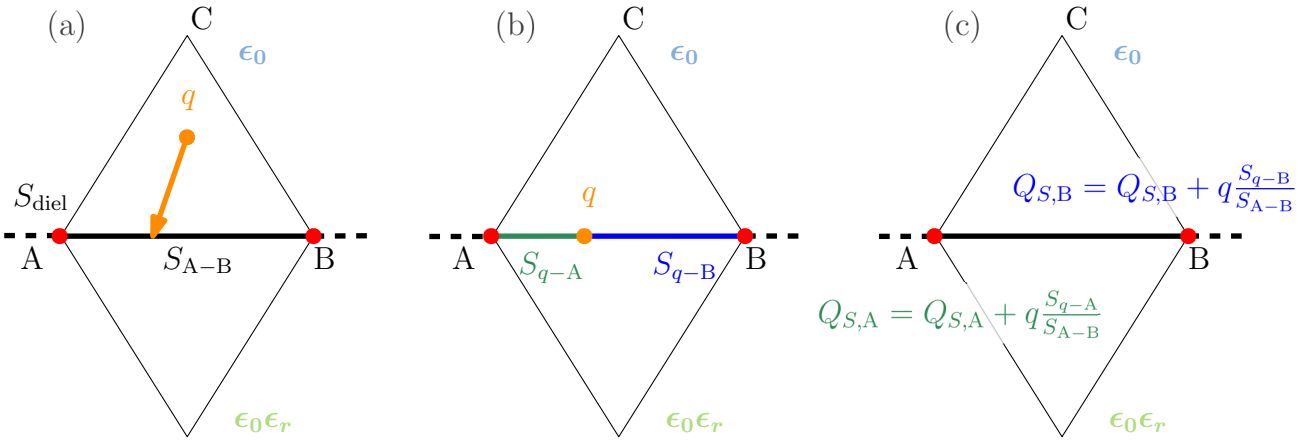

Figure 2.14: Procedure to calculate the surface charge Q_S at each node at the dielectric interface S_{diel} (black dashed line). (a): for any exiting charged particle q crossing the dielectric interface S_{diel}, the face area $S_{\text{A-B}}$ is identified. (b): from the intersection point of q and $S_{\text{A-B}}$, the surfaces to face vertices (here $S_{q-\text{A}}$ and $S_{q-\text{B}}$) are computed. (c): charge q is split linearly between the face vertices and deleted.

2.3.5 Solving the linear system

From the previous section it appears the most general expression of the discretized Poisson equation is given by Equation (2.49). It can be also formulated as a linear system given by:

$$\mathbf{AX} = \mathbf{B} \tag{2.50}$$

where $\mathbf{A}$ is a $M \times M$ matrix which contains the discretization of the Laplacian operator from I_1 and I_2 with N the number of nodes. The unknown potential at the mesh nodes is stored in $\mathbf{X}^\intercal = \begin{bmatrix}\phi_1 & \phi_2 & \cdots \phi_M\end{bmatrix}$ while the net charge deposition is represented by the $\mathbf{B}$ vector. This linear system is challenging to solve because the number of nodes N can be around a few million. Fortunately, matrix $\mathbf{A}$ is sparse and linear solvers can take leverage of that property [Saad, 2003]. The matrix $\mathbf{A}$ is made symmetric for improved numerical properties and we accordingly modify the $\mathbf{B}$ vector. Currently, two external libraries are used in AVIP to solve the linear system: MAPHYS and PETSc.

MAPHYS

MAPHYS stands for MAssively Parallel HYbrid Solver. It is developed by the Hiepacs team [Agullo et al., 2019; Poirel, 2018] in INRIA Bordeaux, France. MAPHYS is open source and uses two numerical methods to invert the sparse matrix $\mathbf{A}$:

- **Direct methods**: direct methods aim to invert exactly $\mathbf{A}$ with Gaussian eliminations or LU decompositions. If accuracy is ensured, the computation cost is estimated to be

$\mathcal{O}(N^2)$ in 3D, which quickly becomes prohibitive. Besides, parallelization is difficult to implement.

- **Iterative methods**: iterative methods provide an approximate solution of the inverted matrix depending on the tolerance defined beforehand by the user. It is more cost-efficient with roughly $\mathcal{O}(N^{7/6}\log(N))$ operations for a 3D domain and less memory demanding. Yet, it might slowly converge to a solution or even diverge depending on the original matrix and its preconditioning.

MAPHYS combines the benefits of both approaches to ensure accuracy at a reasonable computation cost. In each sub-domain a direct method is used while an iterative method computes the system for nodes located on the interface between sub-domains. Subsequently, the $\mathbf{X}$ vector is decomposed in two to differentiate nodes belonging to only one sub-domain (interior nodes I regrouped in $\mathbf{X}_I$), from nodes on the interface Γ between sub-domains, gathered in $\mathbf{X}_\Gamma$. Using the subscript notation Γ and I, Equation (2.50) can be split into the following linear system:

$$\begin{bmatrix} \mathbf{A}_{II} & \mathbf{A}_{I\Gamma} \\ \mathbf{A}_{\Gamma I} & \mathbf{A}_{\Gamma\Gamma} \end{bmatrix} \begin{bmatrix} \mathbf{X}_I \\ \mathbf{X}_\Gamma \end{bmatrix} = \begin{bmatrix} \mathbf{B}_I \\ \mathbf{B}_\Gamma \end{bmatrix} \tag{2.51}$$

Similarly to $\mathbf{X}$, the $\mathbf{B}$ vector distinguishes interior nodes from interface nodes. The $\mathbf{A}$ matrix is decomposed accordingly and $\mathbf{A}_{II}$ has a block-diagonal structure, where each diagonal block corresponds to one sub-domain. We first solve for unknowns located at the interface by eliminating $\mathbf{X}_I$:

$$\underbrace{\mathbf{S}}_{\triangleq \mathbf{A}_{\Gamma\Gamma} - \mathbf{A}_{\Gamma I}\mathbf{A}_{II}^{-1}\mathbf{A}_{I\Gamma}} \mathbf{X}_\Gamma = \underbrace{\mathbf{f}}_{\triangleq \mathbf{B}_\Gamma - \mathbf{A}_{\Gamma I}\mathbf{A}_{II}^{-1}\mathbf{B}_I} \tag{2.52}$$

$\mathbf{S}$ matrix is the *Schur complement matrix*. Equation (2.52) is solved with an iterative method. Since the $\mathbf{S}$ is symmetric definite positive we can use the Conjugate Gradient **??**. We use an additive Schwartz preconditioner to improve performances following Spillane [2014]. Convergence is achieved whenever the residual is below a certain relative threshold δ_{rel},

$$\frac{\|\mathbf{S}\mathbf{X}_\Gamma - \mathbf{f}\|_{L^2}}{\|\mathbf{f}\|_{L^2}} \leq \delta_{\text{rel}} \iff \frac{\|\mathbf{A}\mathbf{X} - \mathbf{B}\|_{L^2}}{\|\mathbf{B}\|_{L^2}} \leq \delta_{\text{rel}} \tag{2.53}$$

Typically, $\delta_{\text{rel}} = 10^{-12}$ for this work. Then, $\mathbf{X}_\Gamma$ is substituted in Equation (2.51) to obtain $\mathbf{X}_I$ with a direct method based on the external solvers MUMPS [Amestoy et al., 2000] and PASTIX [Hénon et al., 2002]. As of today MAPHYS still requires a separate installation and interface [HiePaCS team, 2020] but it should be included in the generalist PETSc package in the near future.

PETSC

PETSc is an open source package containing a wide variety of numerical tools for scientific applications based on partial differential equations [Balay et al., 2019]. In particular, plenty of linear solvers designed for sparse matrix systems are available [Balay et al., 2020]. The Poisson equation is solved with an iterative method, Conjugate Gradient, as the $\mathbf{A}$ is symmetric definite positive. With an unstructured grid, the preconditioner Algebraic Multi-Grid (AMG), is well suited and used. Multi-grid methods consist in successively defining coarser grids on which the error is minimizing with a relaxation technique. High frequencies of the error are gradually

eliminated until the coarsest grid has been reached. The coarsest grid level depends on the mesh and tolerance input by the user. Then the error is reconstructed successively on the previous refined grids. When the original grid is retrieved the error is compared to the tolerance and the "V-shape" procedure is repeated if necessary. Multi-grid methods were originally designed for structured grids and the definition of coarser grids was natural by "skipping" mesh nodes. The algorithm was then generalized to unstructured grids using algebraic structures hence the name Algebraic Multi-Grid methods. For a more comprehensive description of AMG methods, the reader can refer to the rich existing bibliography [Hackbusch, 1985; Trottenberg et al., 2001; Balay et al., 2019]. The Conjugate Gradient is used as a preconditioner as with MAPHYS and the same relative tolerance of 10^{-12} from Equation (2.53) is imposed. Although both PETSc and MAPHYS can be used, MAPHYS tends to scale better at a high number of processors, which is desirable in PIC simulations (see Section 2.6.1).

2.3.6 Electric field

Once the potential is obtained, the electric field $\mathbf{E} = -\boldsymbol{\nabla}\phi$ is calculated. A first solution is to use the inverse distance least-squares gradients technique as in Zakari [2013]. With this approach, the goal is to minimize an error function between the gradient and infinitesimal displacements around the considered node. Yet, according to Mavriplis [2003], it seems the common Green-Gauss approximation presented in Equation (2.27) is a safe choice for most configurations and mesh topologies. Thus, the Green-Gauss formulation is retained for AVIP. With a 2D3V model, the off-plane component of the electric field is directly set by the user and is constant and uniform.

2.4 Particles displacement

2.4.1 Solving the equations of motion

With the newly calculated electric field, AVIP integrates the equation of motions for charged particles with explicit schemes with a constant time step. For unmagnetized particles such as ions a Leap-Frog scheme [Birdsall, 1991] is considered:

$$\begin{cases} \mathbf{v}^{n+1/2} = \mathbf{v}^{n-1/2} + \Delta t \frac{q}{m}\mathbf{E}(\mathbf{x}^n) \\ \mathbf{x}^{n+1} = \mathbf{x}^n + \Delta t \mathbf{v}^{n+1/2} \end{cases} \tag{2.54}$$

Velocity and position are asynchronous and shifted by half a time step as shown in Figure 2.15. The scheme is second order accurate and is stable with the time constraint given in Equation (2.5).

In the presence of magnetic field, electrons are magnetized and the Boris [Boris, 1970] scheme is used. The position is still updated in a similar fashion as in Equation (2.54) but the velocity is computed as follows:

$$\begin{cases} \mathbf{v}^- = \mathbf{v}_{n-1/2} + \frac{q}{m}\frac{\Delta t}{2}\mathbf{E} \\ \mathbf{v}' = \mathbf{v}^- + \frac{q}{m}\frac{\Delta t}{2}\left(\mathbf{v}^- \times \mathbf{B}\right) \\ \mathbf{v}^+ = \mathbf{v}^- + \frac{2\frac{q}{m}\frac{\Delta t}{2}}{1+\left(\frac{q}{m}\frac{\Delta t}{2}\right)^2}\left(\mathbf{v}' \times \mathbf{B}\right) \\ \mathbf{v}_{n+1/2} = \mathbf{v}^+ + \frac{q}{m}\frac{\Delta t}{2}\mathbf{E} \end{cases} \tag{2.55}$$

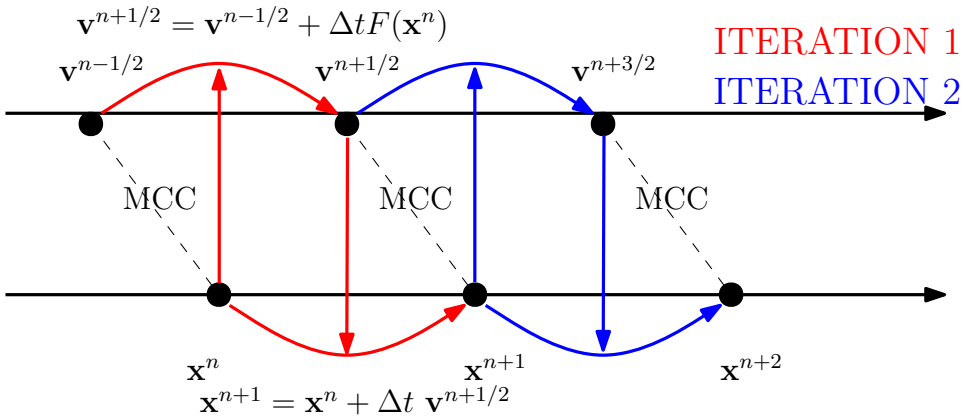

Figure 2.15: The Leap-Frog and Boris schemes de-synchronizes position and velocity. The F function depends on the local position via the electric field and is expressed in Equations (2.54) and (2.55). MCC are the Monte Carlo collisions using data from position $\mathbf{x}^n$ and velocity $\mathbf{v}^{n-1/2}$

Intermediate velocities $\mathbf{v}'$, $\mathbf{v}^+$ and $\mathbf{v}^-$ are introduced to account for the rotation due to the magnetic field. Again, this scheme is second order accurate. The initial temporal shift is introduced at the first iteration for which only half a time step is considered for the pusher while particles are actually displaced with Δt. For both Leap-Frog and Boris schemes, velocity and position must be re-synchronized if diagnostics are needed. Thus, the pusher updates the freshly computed $\mathbf{v}_{n+1/2}$ vector by applying either the Leap-Frog Equation (2.54) or the Boris Equation (2.55) scheme with Δt substituted by $\Delta t/2$. The obtained vector is stored in $\mathbf{v}_{\text{post-proc}} = \mathbf{v}_n$. Such correction is crucial for diagnostics involving the velocity such as temperature and current. Schemes with a non constant time step could be considered to run the simulation faster when time steps as low as $\sim 1 \times 10^{-12}$ s would not be necessary. Thus, the time step could be updated to satisfy the temporal stability condition of Equation (2.5) during transients when the plasma density is low for instance. Unfortunately, the Leap-Frog/Boris schemes cannot adapt to the time step because the temporal shift needs to be constant. However, the Verlet scheme [Sun et al., 2016; Becker et al., 2017; Swope et al., 1982] does not suffer any temporal shift as shown in Figure 2.16. Although it is promising, it can only account for the electric field. So far, no synchronous temporal scheme for magnetized electrons seems to be available in the literature in spite of recent improvements made on the Boris algorithm.

2.4.2 Transport of particles across the grid

Once the velocity of particles is updated they are displaced in the simulation domain. In contrast to structured grids, with unstructured meshes such as those used in AVIP, we cannot deduce easily in which cell the particle will move into. To solve this problem, AVIP relies on the Haselbacher algorithm [Haselbacher et al., 2007], which is schematized in Figure 2.17. Starting from position $\mathbf{x}$, we know the total remaining distance $d_{r,0}$ to travel by the particle i.e. $d_{r,0} = \|\mathbf{v}\|\Delta t$. Here, the velocity $\mathbf{v}$ is the actual velocity for a 3D case while it is the in-plane velocity with a 2D3V model. Then the particle is displaced along the $\mathbf{v}$ direction from one cell face to the next one. This process is repeated until the total distance $d_{r,0}$ has been traveled. Figure 2.18 shows the example of a particle crossing four cell faces. During its journey, the particle can cross several CPU domains and the algorithm is designed to take care of these cases as well.

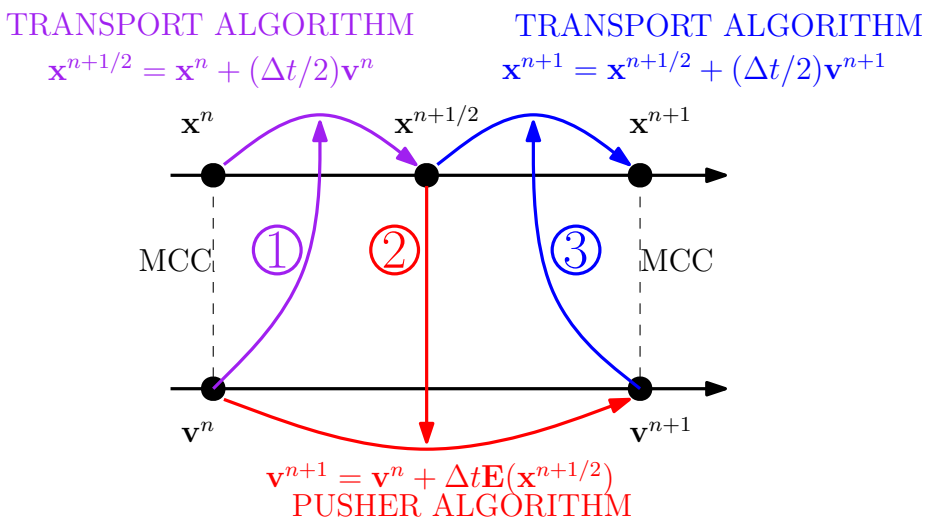

Figure 2.16: The Verlet scheme has a synchronous position and velocity. It consists of three steps and displacement of particles is performed in two times. MCC are the Monte Carlo collisions using data from position $\mathbf{x}^n$ and velocity $\mathbf{v}^n$

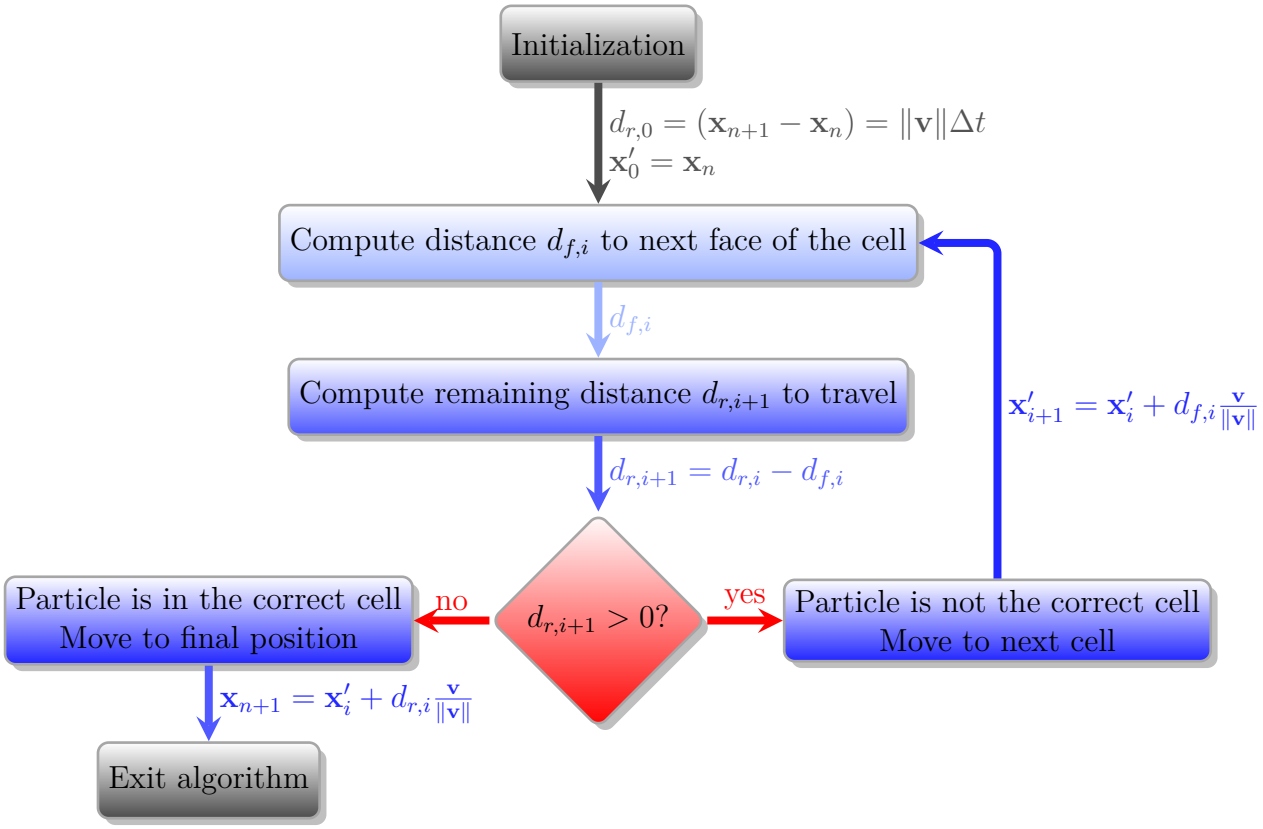

Figure 2.17: Working principle of Haselbacher algorithm [Haselbacher et al., 2007] starting from current position $\mathbf{x}_n$ to obtain final position $\mathbf{x}_{n+1}$. Intermediate calculations are denoted with the i subscript and $\prime$ superscript.

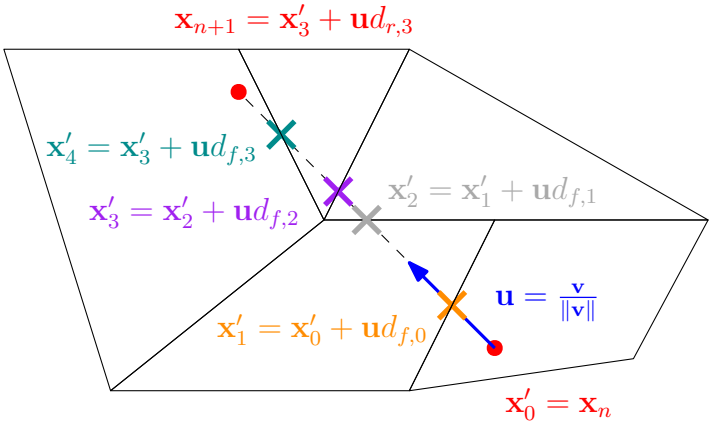

Figure 2.18: Haselbacher algorithm example using notations of Figure 2.17. Crosses indicate intersections of the particle trajectory with cell faces.

2.5 Boundary conditions for particles

In AVIP, boundary conditions are imposed on cells faces that are flagged as such during the pre-processing. They are usually located at the edge of the simulation domain but can also be internal in the presence of a dielectric layer. Thus, each time a cell face is crossed, the Haselbacher algorithm verifies if a boundary condition must be applied in Figure 2.17.

2.5.1 Classical boundaries

"Exit" condition

The first implemented boundary condition is the "exit". If a particle crosses a cell face flagged as "exit", the particle is deleted and removed from the simulation. This is the natural boundary condition for particles lost in the plume downstream of the HT channel. Its use is also appropriate for metallic walls for charged particles: in this case, particles are assumed to be instantaneously absorbed by the conductive wall and they never go back. The "exit condition" gives rise to the sheath.

Periodic condition

The simulation of a full HT with a PIC solver involves a computation cost that is generally prohibitive. Therefore, the azimuthal direction is usually not fully modeled, but only a fraction is considered. Thus, we assume this fraction is representative of the full geometry and periodic boundary conditions are considered. Any particle crossing the boundary will be relocated to the shadow boundary at the correct location, possibly in another CPU domain. In AVIP, every periodic cell face has a mirror at the shadow boundary that is constructed during the mesh generation. Connectivity is stored during the calculation. The velocity of the particle is also adjusted accordingly. In 2D, no velocity correction is necessary. In 3D, in an annular configuration, a particle crossing a periodic boundary $\theta = \theta_0$ will see its velocity $\mathbf{v}$ undergo a rotation of angle $-\theta_0$.

Specular reflexion

Specular reflexion can be useful to model the interaction of neutral particles. The working principle is extremely simple and depicted in Figure 2.19.

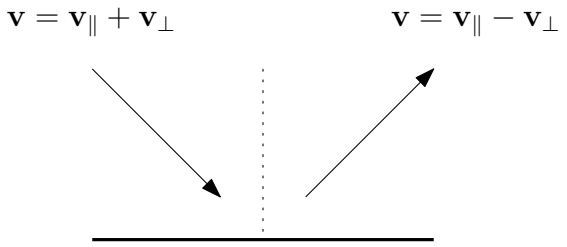

Figure 2.19: The particle orthogonal velocity is reversed at impact. Energy is conserved.

Inelastic collisions

A more realistic modeling of neutral-wall interactions is to account for energy losses to the wall on impact. The model from Song and Yovanovich [1987] was implemented in AVIP but not used for this thesis.

2.5.2 Cathode models

The cathode is a central element of a HT. As stated in Section 1.3, it emits electrons which have two purposes:

1. Some electrons enter the channel to sustain the discharge. Their current is noted I_{cd}
2. The other fraction of electrons go into the plume and neutralize the ion beam, which prevents the thrust to be canceled out. Its current is noted I_{cp}

The total cathodic current is given by

$$I_c = I_{cd} + I_{cp} \tag{2.56}$$

In order to evaluate the total cathodic current I_c to be injected the conservation of current principle must be used. Figure 2.20 lists the different current involved in a HT. Ions and electrons are preliminary created by ionization. Walls can be metallic or covered by a dielectric layer and they absorb charged particles. The exiting electron flux at the walls I_{we} accounts for possible secondary electron emission. The discharge current I_d is the net electron current at the anode: ions, stemming from I_{ai}, neutralize part of the electron flux I_{ae} and subsequent neutral particles are assumed to remain at the anode. The I_{cp} current neutralizes the ion beam current I_{bi} with the help of exiting electrons at the plume I_{be}:

$$I_{bi} = I_{cp} + I_{be} \tag{2.57}$$

Using the notations of Figure 2.20, the current conservation at steady state reads:

$$\begin{cases} I_{e,ioniz} + I_{cd} = I_{we} + I_{ae} + I_{be} \\ I_{i,ioniz} = I_{wi} + I_{ai} + I_{bi} \end{cases} \tag{2.58}$$

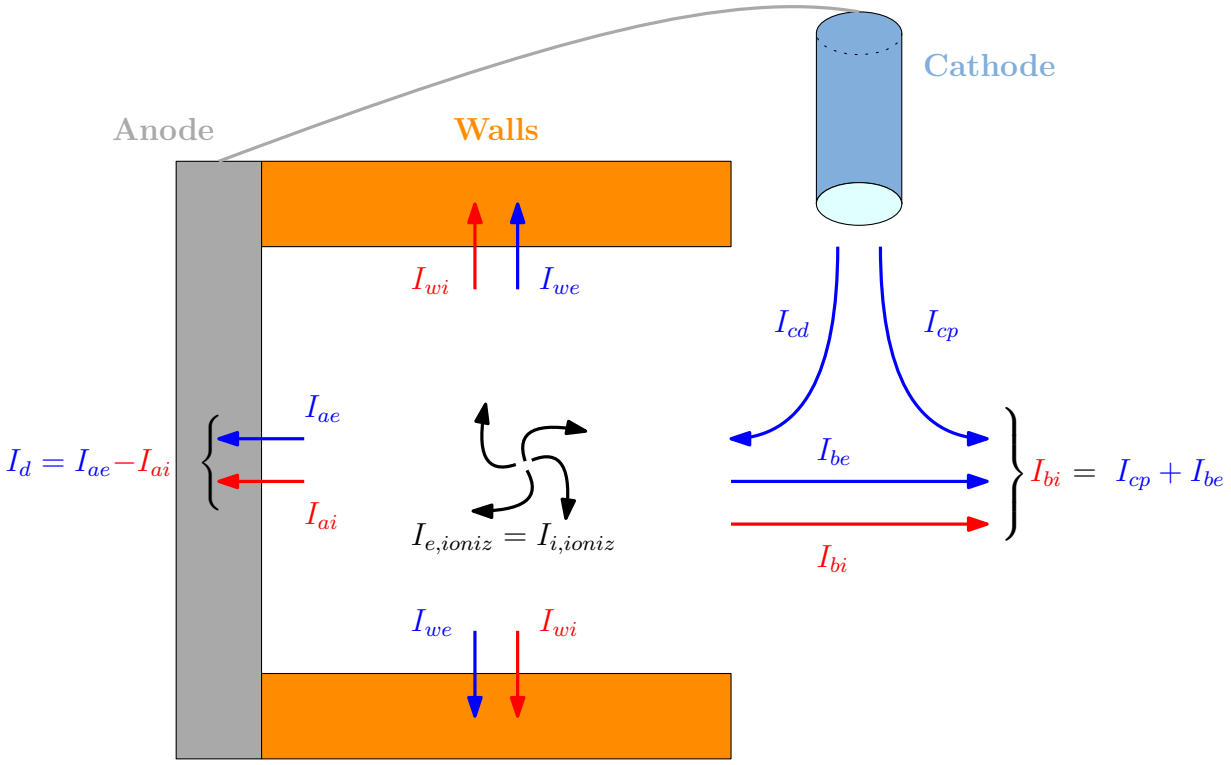

Figure 2.20: Global electron (blue) and ion (red) currents in a HT, respectively denoted with the e and i subscripts. The anode and the cathode are electrically connected. By convention, all currents are positive.

Since $I_{i,ioniz} = I_{e,ioniz}$, we can substract the electron equation with the ion one in Equation (2.58) which leads to

$$I_{cd} = I_{we} - I_{wi} + \underbrace{I_{ae} - I_{ai}}_{I_d} + \underbrace{I_{be} - I_{bi}}_{-I_{cp}} \tag{2.59}$$

In a HT, at steady state, dielectric walls ensure $I_{we} = I_{wi}$, and we get

$$I_c = I_d \tag{2.60}$$

In order to limit the size of the simulation domain, the far plume, downstream the cathode, can be discarded [Szabo, 2001; Charoy, 2020]. Thus, the right side of the domain is simply a plane from which the I_{cd} current is injected. I_{cp} cannot be accessed but can still be accounted for when calculating the current to be injected I_{cd}. Going back to Equation (2.59) we get,

$$I_{cd} = I_{we} - I_{wi} + I_d + I_{be} - I_{bi} \tag{2.61}$$

Here, currents toward the walls are voluntarily left out because in the case of metallic walls they might not cancel each other out. This equation must be satisfied at steady state. As presented in [Szabo, 2001], there are two methods to satisfy this equality: the current equality or the quasi neutrality.

Current equality (CE)

The first solution is simply to compute the currents on the right hand side of Equation (2.61) at each time step Δt. Thus we obtain I_{cd}. Then the number of electrons to inject at the current

iteration is given by

$$N_{e,inj} = \Delta t \frac{I_{cd}}{e} \tag{2.62}$$

This method was the first one implemented in AVIP and has already been used in the literature [Boeuf and Garrigues, 2018; Cho et al., 2015]. However, Charoy [2020]; Szabo [2001] pointed out this approach was flawed during the transient and in presence of oscillations because Equation (2.60) is strictly true at steady state only. In practice, the plasma starves for electrons and the system is unbalanced. They also noted the system becomes very sensitive to changes in the numerical setup.

Quasi neutrality (QN)

Another way to inject the correct number of electrons at the cathode is to ensure the quasi-neutrality is verified at the cathode plane. Thus, we must count the number of electrons and ions at the cathode plane and balance the charge. In AVIP, cells in contact with the cathode plane are identified during the pre-processing as shown in Figure 2.21. Both ions and

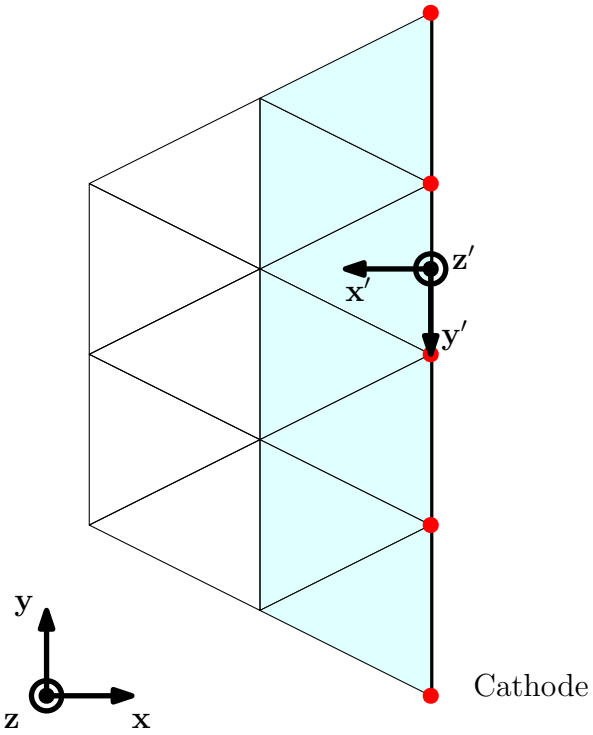

Figure 2.21: Cells at the cathode plane are shaded and have a contact node (in red dots) with the cathode boundary (thick line on the right). The local coordinate system at the cathodic boundary is $(\mathbf{x}', \mathbf{y}', \mathbf{z}')$ with $\mathbf{x}'$ normal to the boundary directed to the interior of the domain. It is linked to the global coordinate system $(\mathbf{x}, \mathbf{y}, \mathbf{z})$ by successive eulerian rotations.

electrons located in these cells are counted during the displacement of the particles to minimize computational cost. The total net number of electrons to inject at the cathode is given by $N_{e,inj}$, expressed as:

$$\begin{cases} \text{if } \sum_j^{N_{\text{cell}}} N_e - N_i > 0, \text{ then } N_{e,inj} = \sum_j^{N_{\text{cell}}} N_e - N_i \\ \text{else } N_{e,inj} = 0 \end{cases} \tag{2.63}$$

where N_{cell} is the number of cells in contact with the cathode and N_e and N_i are respectively the number of electrons and ions in each cell. In other words, we inject electrons only if some are missing to ensure quasi-neutrality from the cathode. More importantly, numerical simulations from Charoy [2020]; Szabo [2001] showed Equation (2.61) was satisfied and much less sensitive to changes in the numerical setup in contrast to the current equality (CE) approach. Simulations of Chapter 5 will be based on the quasi-neutral method.

Position and velocity

For both the current equality or the quasi-neutrality method, the procedure to define the location and velocity of cathodic electrons is the same. Particles are injected uniformly along the cathode boundary. It is possible to shift the injection location by a short distance of the order of $\sim 1\,\text{mm}$ [Boeuf and Garrigues, 2018; Charoy, 2020] to prevent newly introduced particles to exit immediately. With the CE method, the risk of such a situation is to have electrons unable to leave the vicinity of the cathode boundary, while new ones are constantly supplied. Cho et al. [2016] showed a potential barrier could eventually forms, which disconnects the cathode from the discharge. The QN approach seems more robust because if too many electrons are already counted in cathode cells, less particles will be injected. Besides, with a sufficiently high injection temperature, cathodic electrons can escape the boundary more easily [Cho et al., 2016]. With an unstructured grid, it is difficult to shift an injected particle by a pre-defined length because it can change cell. Thus, AVIP relies on an injection temperature high enough to prevent cathodic electrons to agglutinate. Numerical results are available in Chapter 5. Assigning the velocity of new particles is straightforward. First, we assume electrons emitted by the cathode are at thermal equilibrium with a temperature T_{inj}. Then, using the local coordinate system $(\mathbf{x}', \mathbf{y}', \mathbf{z}')$, the tangential components of the velocity $\mathbf{v}'_y$ and $\mathbf{v}'_z$ are sampled from a Maxwellian distribution (Equation (2.12)). The normal component $\mathbf{v}'_x$ is sampled from a half Maxwellian distribution as explained by Hagelaar [2008]. In practice we get:

$$\begin{aligned} v'_x &= v_{th}\sqrt{-\log R_1} \\ v'_y &= v_{th}\sqrt{-\log R_2}\sin\left(2\pi R_3\right) \\ v'_z &= v_{th}\sqrt{-\log R_2}\cos\left(2\pi R_3\right) \end{aligned} \tag{2.64}$$

where R_1, R_2, R_3 are random numbers between 0 and 1 and $v_{th} = \sqrt{\frac{2k_B T_{inj}}{m_e}}$ is the thermal velocity of electrons. Finally, we apply eulerian rotations to get the actual velocity $\mathbf{v}$: $(\mathbf{v}'_x, \mathbf{v}'_y, \mathbf{v}'_z) \rightarrow (\mathbf{v}_x, \mathbf{v}_y, \mathbf{v}_z)$.

2.5.3 Secondary electron emission

In a HT, electrons hitting the dielectric layer covering the walls can exhibit a more complex behavior than being simply absorbed (see "exit" condition Section 2.5.1) or specularly reflected (Section 2.5.1). Villemant [2018] identified three other possible interactions with the walls:

1. **Elastic collisions**: the incident electron, whose energy is E_0, is elastically back-scattered. This means its energy after impact is conserved. In contrast to specular reflections from Section 2.5.1, the outgoing direction of the electron is not necessarily $(\mathbf{v}_\parallel, -\mathbf{v}_\perp)$ and is anisotropic in space. A significant proportion can be even reflected back in the incident direction [Villemant et al., 2017].

2. **Inelastic collisions**: the incident electron loses part of its energy on impact.

3. **True secondary electron emission (SEE)**: when an incident electron hits the wall with enough energy, it can rip electrons from the dielectric layer that are then released into the plasma flow. This is a "true secondary electron emission" in contrast to elastic and inelastic collisions because there is an actual production of particles.

Although it would be ideal to model these three interactions, it is in practice challenging to achieve because of its computational cost. Indeed, the accurate way to do so is to rely on probabilistic and Monte Carlo calculations [Furman and Pivi, 2002; Pierron et al., 2017; De Lara et al., 2006]. However, these calculations rely on empirical parameters that require a careful study for each wall material [Taccogna, 2003]. Once the model is set up, it provides interesting insights on sheath mechanisms [Ahedo and De Pablo, 2007; Domínguez-Vázquez et al., 2019] but since Monte Carlo calculations are extremely costly, it is unrealistic to use this approach in 2D or 3D.

Analytical models can circumvent this limitation. Among the most ambitious ones, we can cite Sydorenko [2006], who attempted to account for three kind of interactions [Sydorenko, 2006]. However, the lack of experimental data for elastic and inelastic collisions makes his results uncertain. For the sake of simplicity, we can discard inelastic collisions and focus on SEE and elastic collisions only. That was performed by Villemant [2018] in his thesis who sought to implement a fast and more accurate method to take both elastic collisions and SEE into account. That was achieved by tabulating spatial velocity distributions after impact with the help of the Single Large-Angle Backscattering (SLAB) model [Jablonski, 2013; Salvat et al., 2021].

As a first implementation effort into AVIP, we did not seek to distinguish the three kinds of interactions but rather in having qualitative results first. In this context, we can focus on analytical models that assume elastic and inelastic collisions are negligible and only SEE are present. Vaughan [1989] proposed such a model from experimental data with only two parameters: the energy and incidence angle of primary (or incident) electrons. The model provides the total yield of secondary electrons that is assumed to be equal to the SEE yield. Croes [2017] suggested the effects of the incidence angle were moderate on HTs simulations, so an even simpler model [Gascon et al., 2003; Barral et al., 2003], also based on experimental data, could be sufficient. This model has been implemented into AVIP and will be described below.

Like the Vaughan model, the Barral model does not distinguish elastic, inelastic and SEE. It is a linear-saturated law that provides the SEE yield σ_{SEE} after impact:

$$\sigma_{\text{SEE}} = \begin{cases} \sigma_{\text{SEE},0} + (1 - \sigma_{\text{SEE},0})\frac{\epsilon}{\epsilon^\star} & \text{if } \epsilon \leq \epsilon_{\max} \\ \sigma_{\text{SEE,max}} & \text{if } \epsilon \geq \epsilon_{\max} \end{cases} \tag{2.65}$$

where $\epsilon = 1/2 m_e \|\mathbf{v}_e\|^2$ is the kinetic energy of the primary electron, $\epsilon^\star$ the crossover energy, $\sigma_{\text{SEE},0}$ the asymptotic yield at zero energy, $\sigma_{\text{SEE,max}}$ the saturated emission yield starting from a certain threshold $\epsilon = \epsilon_{\max}$. The parameters $\epsilon^\star$, $\sigma_{\text{SEE},0}$ and $\sigma_{\text{SEE,max}}$ depend on the wall material. They were measured for boron nitride [Barral et al., 2003; Dawson, 1966] and their respective values are presented in Table 2.3. The $\epsilon_{\max}$ threshold can be deduced by solving the equation $\sigma_{\text{SEE}} = \sigma_{\text{SEE,max}}$.

The numerical implementation of the model is detailed in Figure 2.22. Depending on the value of σ_{SEE}, one or more secondary electrons can be emitted and three outcomes are possible.

Parameter	Value	Unit
$\epsilon^\star$	53	eV
$\sigma_{\mathrm{SEE},0}$	0.45	-
$\sigma_{\mathrm{SEE,max}}$	2.9	-

Table 2.3: Parameters for BN-SiO_2 for Barral's law

Given the values from Table 2.3, we notice $\sigma_{\mathrm{SEE}} = \sigma_{\mathrm{SEE,max}} = 2.9$ for $\epsilon = \epsilon_{\mathrm{max}} = 236\,\mathrm{eV}$, an energy hardly reached for a primary electron. Thus, most of the time only one or no secondary electron is emitted.

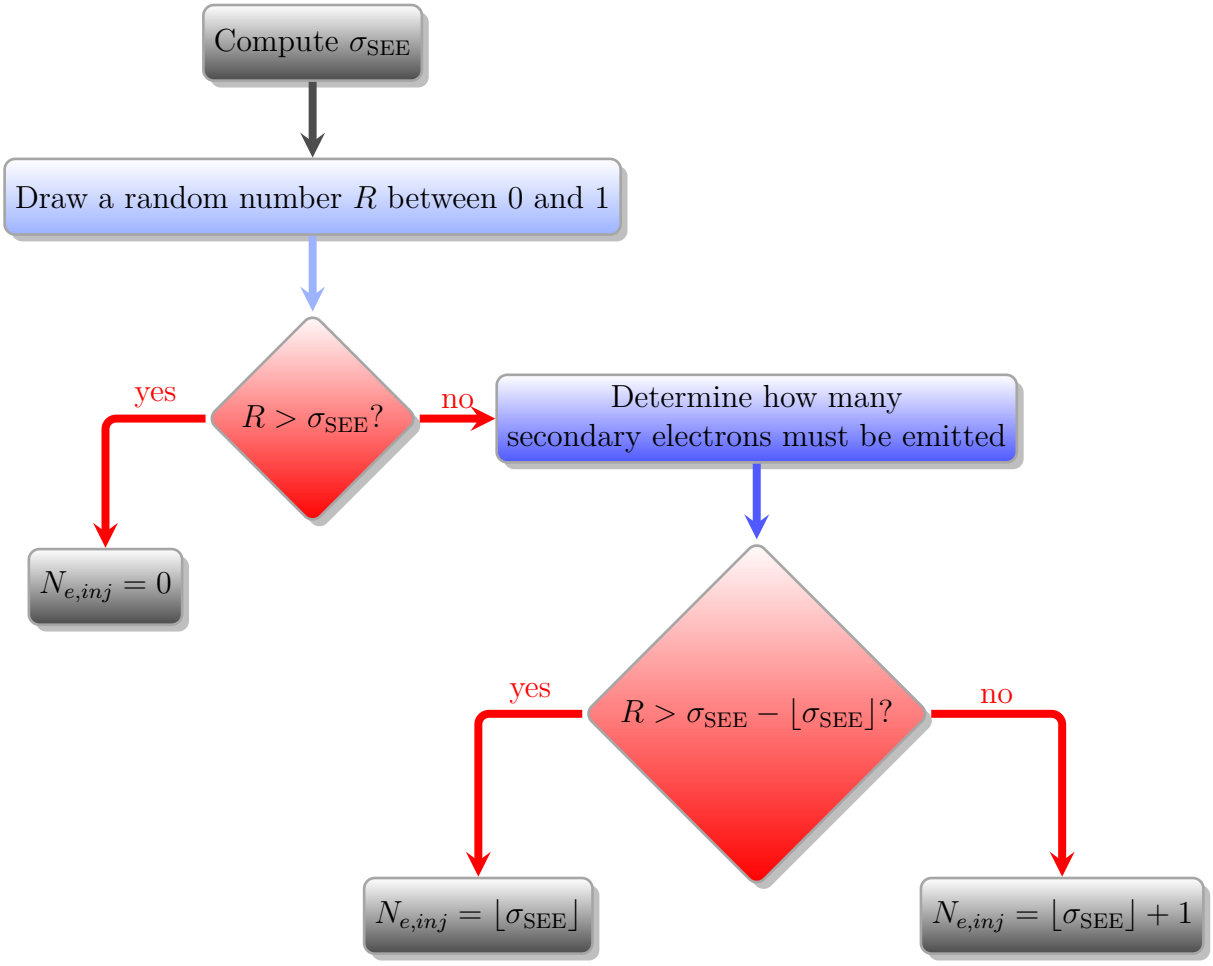

Figure 2.22: Numerical implementation of Barral's law. $\lfloor\sigma_{\mathrm{SEE}}\rfloor$ designates the floor function applied to σ_{SEE}.

True secondary electrons are emitted near thermal equilibrium according to experiments [Villemant, 2018]. So, once the number of electrons to be emitted has been computed, their velocity is assigned by sampling from a half Maxwellian distribution. Thus Equation (2.64) is applied here at the wall boundaries. Typically the wall temperature is of the order of a few thousand Ks and is assumed constant during the simulation.

2.6 AVIP PIC performances

Since AVIP aims to simulate 3D realistic geometries of HT, optimizing computing time is crucial. For a PIC code, the computational cost can be split into two main categories: solving the Poisson equation and managing the particles (Lagrangian solver).

2.6.1 Code optimization

Poisson solver's optimization

As mentioned in Section 2.3.5, the computational time to solve the Poisson equation depends on the number of nodes. Thus, domain decomposition is based on the external library PARMETIS [Karypis and Kumar, 2009] velocities up the code as long as MPI communications remain moderate. For each configuration, there is an optimal number of sub-domains (and therefore of processors) to be used to minimize the total cost of solving the Poisson equation. This question should be investigated before running the simulation. Besides, MAPHYS offers the option to activate a coarse grid correction [Poirel, 2018] following the Generalized Eigenvalue in the Overlap (GENEO) procedure [Spillane, 2014; Spillane et al., 2014].

When this option is ON, MAPHYS will first define a coarse space depending on the matrix preconditioning that is imposed by the user. This coarse space is not a coarser grid as in AMG and the original linear system is transformed to another one whose size is smaller. Then, a designated sub-communicator solves the coarse system, transforms the subsequent solution back to the original space and communicates it to all other sub-communicators. This intermediate solution helps the Conjugate Gradient (CG) to converge to the final solution. The efficiency of the coarse grid correction depends on the matrix preconditioning. Indeed, a small preconditioning value speeds up the CG convergence but increases the size of the coarse grid to solve by the designated sub-communicator. Besides, Poirel [2018] noticed that the this trade-off depended on the geometry of the simulation domain. Finally, one drawback of the coarse grid correction is that it tends to overburden the designated sub-communicator memory because the coarse linear system to solve is proportional to the number of sub-domains. Therefore, the available memory to the sub-communicator should be taken into account as well. As a conclusion, the use of the coarse grid correction is case and hardware dependent and it should be investigated for each setup.

Lagrangian solver

The Lagrangian solver refers to the computation of Monte Carlo collisions, charge interpolation onto the grid, interpolation of the Eulerian electric field on the particles, displacement of particles and management of particles at boundary conditions. In a typical 3D configuration, billions of electrons, ions and neutral macroparticles are required and stored in memory for each sub-domain. Different ways of organized the data exist and are presented below and schematized in Figure 2.23.

A natural solution of data management consists in using an array of structures (AoS): a dedicated structure "particle" contains all information such as the position $\mathbf{x}$, or statistical weight q_f. Although intuitive, this data management becomes inefficient for PIC simulations because data might be not contiguously stored in the RAM. Since cache memory is limited, the machine needs to constantly look up for particles in the RAM-memory, load them in the

cache memory and repeat this process unnecessarily numerous times before having all the data of the same type it needs to continue the computation.

Thus, a structure of arrays (SoA) could be another solution: for each sub-domain all particles characteristics are stored in common arrays. Yet, those arrays are very long and take time to be read and loaded. Besides, this approach has the disadvantage of being less intuitive and readable.

As a result, AVIP relies on an array of structures of arrays (AoSoA): each sub-domain is split into cell groups as a second level domain decomposition. For each cell group, a structure contains all the information of particles belonging to the cell group. Therefore, arrays to read remain short, which speeds up the code. In order to ensure a contiguous data storage in memory, after each particle displacement or injection, particles are sorted out according to the Quicksort dual-pivot algorithm [Bowers, 2001]. This greatly helps AVIP during the interpolation operations and it accelerates the calculations of Monte Carlo collisions.

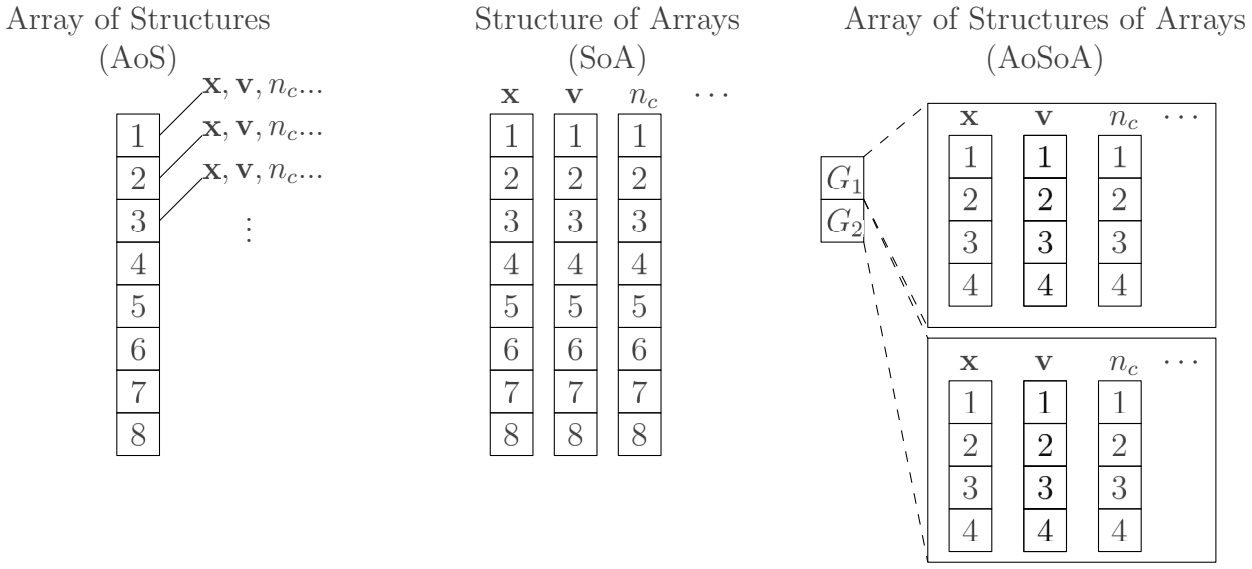

Figure 2.23: Different ways of organizing PIC data in each sub-domain taking the example of 8 particles, characterized by their position $\mathbf{x}$, their velocity $\mathbf{v}$, cell number n_c etc. AVIP retains the (AoSoA) strategy where each sub-domain is split in cell groups $G_1, G_2...$, each containing structures of particles informations.

Another aspect affecting the performances of the code is the presence of transients. During transients such as ignition of the HT, the number of particles can locally increase significantly, which can eventually overflow the processor memory in a specific sub-domain. AVIP can restore load balancing at the restart by taking into account the spatial distribution of particles. Besides, AVIP can also take leverage of the different characteristic time scales inherent for each species α. Thus a subcycling technique [Adam et al., 1982] has also been implemented to avoid unnecessary calculations for heavy particles such as ions and neutrals. Briefly, the subcycling technique consists in updating the position and velocity of heavy particles every f_s iterations, where f_s is an integer chosen beforehand. The idea is that during a time step, heavy particles do not really move as the time step is primarily constrained by the plasma frequency to capture the dynamics of electrons. Therefore, updating $\mathbf{x}$ and $\mathbf{v}$ every f_s iterations can be sufficient and speed up the code. Typically a value of $f_s = 5$ was found to be a correct choice for AVIP [Charoy et al., 2019].

A final optimization has been investigated during this PhD thesis. AVIP has the possibility to actively control the number of particles in each cell of the domain. For a given cell, if the number of particles is below or above a threshold prescribed by the user, an attempt will be made to respectively split or merge them. Merging unnecessary small particles can greatly speed up the code. Splitting particles reduces numerical noise by repopulating regions where the plasma expands, especially in the plume. The merging-spiltting algorithm is based on the work of Luu et al. [2016]; Martin and Cambier [2012]. For each species α (ion, electron, neutral), three parameters must be defined by the user at the beginning of the simulation:

1. The target number of macroparticles per cell N_t
2. The tolerance in position $T_{\mathbf{x}}$
3. The tolerance in velocity $T_{\mathbf{v}}$

The two tolerances $T_{\mathbf{x}}$ and $T_{\mathbf{v}}$ are dimensionless and used to identify groups of particles within the current cells that are similar in terms of position x_i and velocity v_i as shown in Figure 2.24. The particles are considered to be sufficiently similar if they meet all of the following conditions:

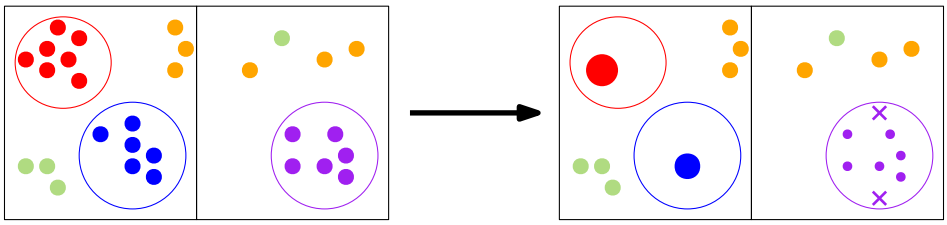

(a) (b)

Figure 2.24: Active control of number of particles per cells. In (a) clusters of similar particles are identified and in (b) they are either merged into a bigger particle (left cell) or split into two additional particles (crosses in right cell).

$$\text{for } i = 1, ..., n_d \begin{cases} \sigma_{x_i}/V_c^{1/n_d} < T_{\mathbf{x}} \\ \sigma_{v_i}/\bar{v}_i < T_{\mathbf{v}} \end{cases} \tag{2.66}$$

where n_d is the dimension of the domain, σ_{x_i} the standard deviation for the positions x_i of the considered particles and σ_{v_i} the standard deviation for the velocities v_i. These standard deviations are respectively compared to the typical size V_c^{1/n_d} of the cell for the positions x_i, and to the mean velocity $\bar{v}_i$ for the v_i component of the velocity. When particles are merged, the final particle is assigned the following statistical weight $q_{f,m}$, position $\mathbf{x}_m$ and velocity $\mathbf{v}_m$:

$$\begin{cases} q_{f,m} = \sum_j^n q_{f,j} \\ \mathbf{x}_m = \frac{1}{n} \sum_j^n \mathbf{x}_j \\ \mathbf{v}_m = \frac{1}{n} \sum_j^n \mathbf{v}_j, \end{cases} \tag{2.67}$$

where n is the local number of macroparticles in the current cluster. Thus, during this process, the mass m, momentum $m\mathbf{v}$ of the cluster are conserved, but not the energy $1/2m\|\mathbf{v}\|^2$. However, according to Luu et al. [2016], the error should remain negligible as long as $T_{\mathbf{x}}$ and $T_{\mathbf{v}}$ are chosen wisely.

For splitting, two particles are systematically generated and they are assigned the following statistical weight $q_{f,s}$, position $\mathbf{x}_s$ and velocity $\mathbf{v}_s$:

$$\begin{cases} q_{f,s} = \frac{1}{2}\frac{2}{n+2}\sum_j^n q_{f,j} \\ \mathbf{x}_s = \frac{1}{n}\sum_j^n \mathbf{x}_j + \sigma_{\mathbf{x}} \\ \mathbf{v}_s = \frac{1}{n}\sum_j^n \mathbf{v}_j + \sigma_{\mathbf{v}}, \end{cases} \tag{2.68}$$

where $\sigma_{\mathbf{x}}$ and $\sigma_{\mathbf{v}}$ are the standard deviations whose components for each spatial dimension $i = 1, 2, ..n_d$ are σ_{x_i} and σ_{v_i} from Equation (2.66). In order to conserve the mass during the splitting process, a portion of weight $q_{j,f}$ is taken out from the original particles j:

$$q_{j,f} \leftarrow \frac{n}{n+2} q_{j,f}. \tag{2.69}$$

In contrast to the merging process, both the momentum and energy are conserved.

The target number of particles N_t will determine the frequency at which the merging-splitting algorithm will be applied but there is no guarantee that the number of particles will be reduced or increased: if $T_{\mathbf{x}}$ and $T_{\mathbf{v}}$ are set too low, for example, the algorithm will not find any cluster to merge or divide and will have no effect. Therefore, it is important to choose with great care $T_{\mathbf{x}}$ and $T_{\mathbf{v}}$ as they determine which particles can be considered as similar enough to be merged or split. A parametric study will be conducted in Section 3.3 regarding this matter.

Merging particles can be essential in regions where Monte Carlo collisions occur at a high rate because numerous macroparticles can be introduced. Obviously, in the ionization zone, the number of numerical particles increases because matter is created. However, this increase is also due to the other collisions from Table 2.2. Indeed, in contrast to other PIC codes, the statistical weight of the incident particle and the neutral $\mathrm{X_e}$ particle are not necessarily the same. For instance, let's assume an electron with a statistical weight $q_{e,f}$ elastically collide with a Xe particle whose weight is $q_{n,f} > q_{e,f}$. Equation (2.70) describes the ongoing process and also indicates a new Xe macroparticle with a weight $q_{n,f} - q_{e,f}$ must be introduced:

$$\underbrace{\mathrm{e^-}}_{q_{e,f}} + \underbrace{\mathrm{Xe}}_{q_{n,f}} \rightarrow \underbrace{\mathrm{e^-}}_{q_{e,f}} + \underbrace{\mathrm{Xe}}_{q_{e,f}} + \underbrace{\mathrm{Xe}}_{q_{n,f}-q_{e,f}} \tag{2.70}$$

In simplified 2D geometries, the creation of additional particles by collisions might be supportable, but can seriously deteriorate performances in 3D.

2.6.2 Strong scaling results

AVIP's performances have recently been evaluated [Agullo et al., 2021] in a 3D setup representative of a SPT-100 HT [Morozov and Savelyev, 2000] (15 mm high and 34 mm long). The simulation domain is depicted in Figure 2.25. The mesh is made of 27 million tetrahedral elements (around 5 million nodes). The cell size is relatively homogeneous with a minimum of $50\mu m$ near the ceramic walls and around $80\mu m$ elsewhere. Since we are interested in to profiling here, boundary conditions are simplified to simple exit conditions (see Section 2.5.1) except in the θ direction where periodic boundary conditions are used. The anode and cathode are respectively set to 200 V and 0 V. The plasma is initialized with a Maxwellian cloud of ions $\mathrm{Xe^+}$, electrons $\mathrm{e^-}$ and neutral Xe.

The first 50 iterations are simulated for different numbers of processors ranging from 360 to 7200 on the Occigen supercomputer hosted by CINES in Montpellier (France). The number of

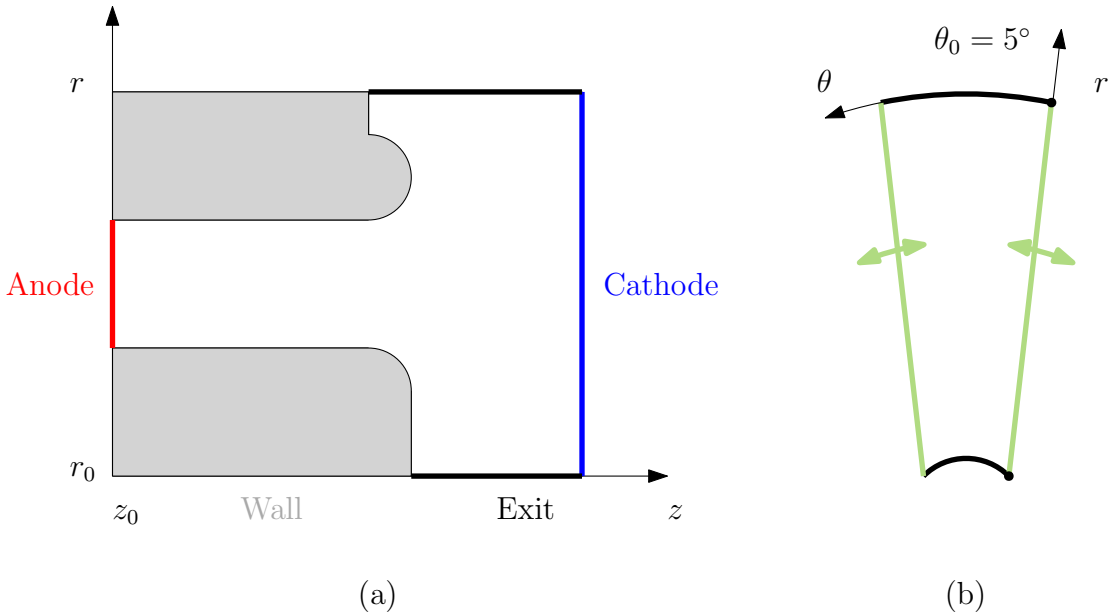

Figure 2.25: 3D simulation domain inspired from the 2D geometry from Joncquieres et al. [2020]; (a) $r - z$ view and (b) $r - \theta$ view.

initial particles per cell N_{pcc} for each species α is also varied ($N_{pcc} = 30, 60$ and 120). Therefore the total number of particles in the domain ranged from 2.43×10^9 ($N_{pcc} = 30$) to 9.72 ($N_{pcc} = 120$). Each run was repeated three times to discard any outliers. Finally, both MAPHYS and PETSc were tested as a Poisson solver. MAPHYS is used with grid coarse correction mentioned in Section 2.3.5 and is denoted as DDM for Domain Decompostion Method. PETSc equipped with the Algebraic Multi-Grid method is designated by AMG. Figure 2.26 sums up all results. In Figure 2.26 (a), it can be observed that subroutines from the Lagrangian solver scale very well with an increased number of CPUs. At a low number of CPUs, both MAPHYS and PETSc benefit from using more CPUs but they eventually slow down the computation. Indeed, the MPI communication costs eventually outweigh the size reduction of the matrix system to be solved by each CPU. The optimum regime for MAPHYS (DDM) is located at around 3,000 nodes/CPU while the efficiency of PETSc (AMG) is reduced much earlier at around 10,000 nodes/CPU. It can be noticed that PETSc is faster with a low number of CPUs, but since most of the time is consumed in Lagrangian numerical kernels (transport, interpolation and MCC), benefits are minimal in comparison with MAPHYS. Finally, in Figure 2.26 (a), it appears that using more than 2,500 CPUs does not really speed up the code.

When the number of numerical particles is increased in Figure 2.26 (b-c), the computational time due to Lagrangian numerical kernels is logically increased. Poisson's solvers are not affected because their cost depends on the mesh size and not on the number of particles. It also shows that with a significant number of particles, it might be interesting to use more CPUs than in case (a).

These observations highlight trends but do not constitute general rules. The optimum spot for AVIP is not always located at around 3,000 nodes/CPUs because the geometry of the simulation domain and the hardware architecture will also affect performances of the MPI communications and of the Poisson solvers. For instance, Poirel [2018] remarked that MAPHYS was overall slower in geometries with an aspect ratio near one such as cuboids. For all the simulations carried out in this work, it appeared that MAPHYS was the most efficient solver

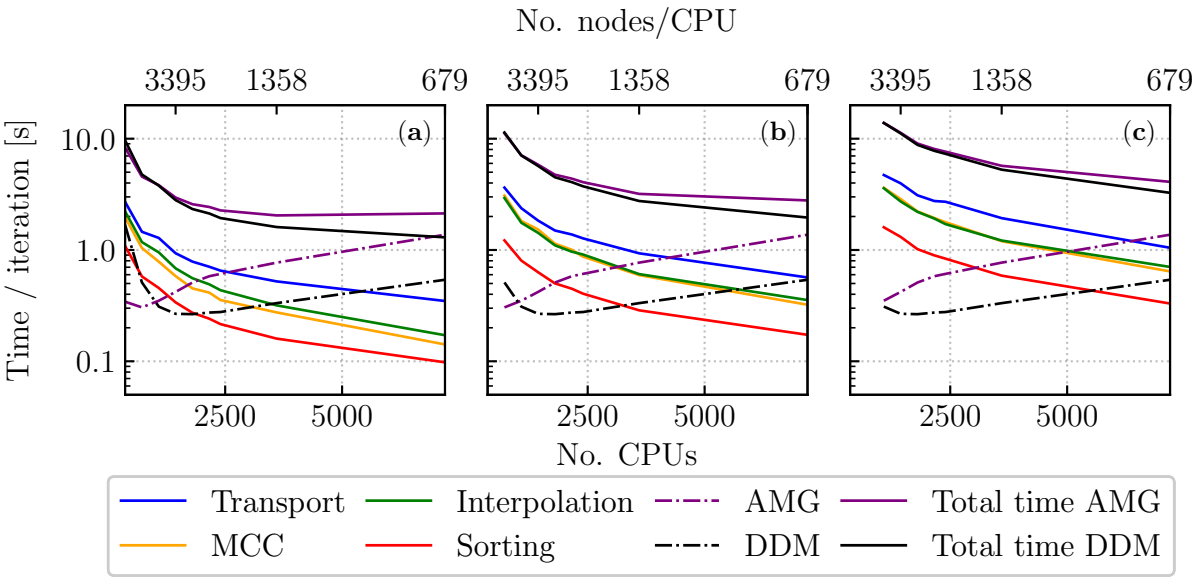

Figure 2.26: Time spent per iteration for the different numerical kernels of AVIP, starting with (a) $N_{pcc} = 30$, (b) $N_{pcc} = 60$ and (c) $N_{pcc} = 120$. The average number of nodes per CPU is indicated at the top x axis. In (b) and (c), a minimum of 720 and 1080 processors are required respectively to meet memory requirements.

and it was therefore systematically used.

A final interesting metric to consider is the speed-up. Given a fixed problem size, the speed-up S is an estimate of how much a code can accelerate when more processors are used. Its definition is:

$$S(P) = \frac{t_1}{t_P} \tag{2.71}$$

where t_1 is the best elapsed time when the code is serial while t_P is the elapsed time when P processors are used. The theoretical speed-up can be assessed with Amdhal's law [Amdahl, 1967] which reads:

$$S_{th}(P) = \frac{1}{1 - \beta + \frac{\beta}{P}} \tag{2.72}$$

where β is the fraction of code that benefits from the parallelization of the code. When $\beta = 1$, the code is perfectly parallel and $S_{th}(P) = P$, which means the code is P times faster with P cores. However, as pointed by Moreland and Oldfield [2015], this formula seems unfit for large codes such as AVIP because above ~ 100 processors, the predicted speed up is approximately constant as S_{th} tends to the limit $S_{th} \to (1 - \beta)^{-1}$ whereas AVIP clearly still gains from employing more processors from Figure 2.26. Another difficulty for large parallel code is to accurately compute the speed-up because it requires to know the serial time t_1, which is impossible to obtain in practice because of memory constraints for instance.

Several solutions are proposed in [Moreland and Oldfield, 2015] to properly evaluate the strong scalability. Yet, they require to evaluate *minimal cost* per mesh node, which consists in minimizing the quantity $C_{/u} = Pt_P N^{-1}$ by testing different meshes of size N. For the purpose of our discussion, we did not test several meshes but instead we computed a modified speed-up $S^\star$ as follows:

$$S^\star(P) = \frac{t_{P_0}}{t_P} \tag{2.73}$$

where t_{P_0} is the elapsed time when P_0 processors are used, which becomes the new reference instead of the serial time. This time t_{P_0} can be split in two: $t_{P_0} = (1-\beta)t_{P_0} + \beta t_{P_0}$ where $(1-\beta)t_{P_0}$ is the fraction of time that will not be reduced when using more processors than P_0 in contrast to βt_{P_0}. Therefore, if we assume the scaling of the parallelizable component is linear, it can be expected the elapsed time with $P > P_0$ processors will be:

$$T_P = (1-\beta)T_{P_0} + \frac{\beta T_{P_0}}{\frac{P}{P_0}} \tag{2.74}$$

Thus, a very similar law to Amdhal's one can be derived:

$$S^\star_{th}(P) = \frac{t_{P_0}}{t_P} = \frac{(1-\beta)t_{P_0} + \beta t_{P_0}}{(1-\beta)t_{P_0} + \frac{\beta t_{P_0}}{\frac{P}{P_0}}} = \frac{1}{(1-\beta) + \frac{\beta}{\frac{P}{P_0}}} \tag{2.75}$$

Although it is not as rigorous as what proposed Moreland and Oldfield [2015], interesting conclusions can be drawn as depicted in Figure 2.27. If AVIP was perfectly parallel starting

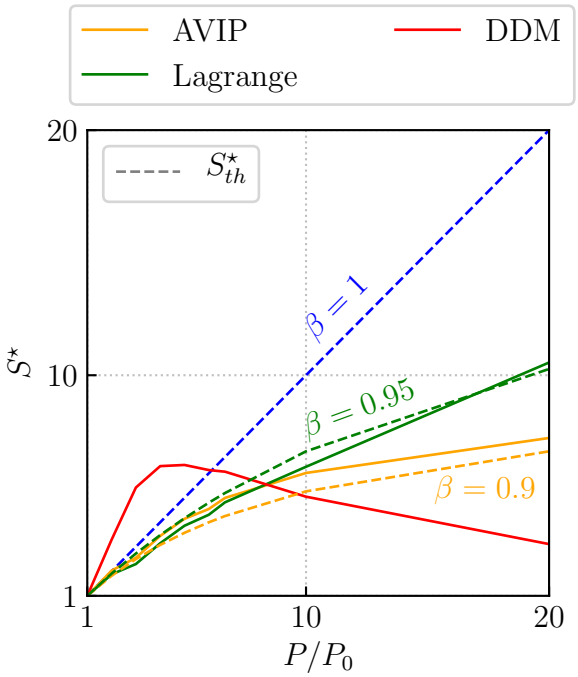

Figure 2.27: Assessment of modified speed-up $S^\star$ for AVIP using data from Figure 2.26 (a). Solid lines represent AVIP calculations of modified speed-up $S^\star$ distinguishing the Poisson solver (DDM) from the Lagrangian kernel (transport, MCC, sorting, interpolation). Dashed lines represent the theoretical modified speed-up $S^\star_{th}$ for different fractions β benefiting from using more processors than $P_0 = 360$.

from $P_0 = 360$ processors, then using $P > P_0$ processors would speed up the code by a factor $S^\star_{th} = P/P_0$, which is represented by the blue dashed line. The Lagrangian kernel exhibits an excellent strong scalability. More than 95% of the workload of the reference point P_0

benefits from additional parallelization and better performances are difficult to obtain. AVIP also shows excellent performances whit a fraction $\beta > 90\%$. AVIP is less scalable than the Lagrangian kernel essentially because of the Poisson solver (DDM here). Indeed, for $P > 3P_0$, the Poisson solver becomes slower with an increased number of CPUs because of prohibitive collective communications, which echoes previous observations on Figure 2.26. What is revealed by Figure 2.27 is that the Poisson solver actually outperforms a perfectly parallel AVIP in the for P values in the $[P_0, \sim P_0]$ interval. The *supralinear* behavior of the Poisson solver can be actually explained by two factors. First, although each sub-domain is shrunk by a factor P/P_0, the factorization of matrix A of the linear system is sped up by a factor greater than P/P_0. Besides, the Conjugate Gradient (CG) used to solve the potential between the sub-domains has also a cost that is inherently supralinear with the domain size. Those benefits are nevertheless overthrown by the cost of collective communications when sub-domains become too numerous.

2.7 Conclusion

AVIP is a plasma solver that offers the possibility to either use a fluid model or follow a Lagrangian approach by the means of PIC simulations.

In this Chapter the numerical implementation of the PIC version, AVIP PIC, was presented. AVIP PIC has all the tools to perform accurate simulations including kinetic effects. Both neutrals and charged particles (electrons and ions) can be included altogether. Note that ions can be doubly charged or more if necessary. Furthermore, collisions are self consistently modeled with a Monte Carlo module while the electric field is obtained from the Poisson equation. The main strength of AVIP is its capability to work with unstructured grids, which dramatically complicates the coding with respect to all other existing PIC codes in the community. For instance, the displacement of particles is achieved by calculating the successive intersections of the particle with cell faces along the velocity vector. In contrast, in a structured grid based PIC code, the final cell can be immediately deduced as the cell spacing is regular. In spite of being more complicated, AVIP has been highly optimized. An innovative Poisson solver, MAPHYS, has been coupled with the code and a coarse grid correction method has been tested with success on AVIP PIC to improve the speed-up. Regarding the numerical cost of the Lagrangian solver (particles transport, interpolation, collisions), the code shows an excellent strong scaling, which paves the way for more ambitious simulations in 3D (see Chapter 5. In particular, an active particle control algorithm has been implemented and is very promising to overcome important variations of the number of particles. For instance, in the case of strong oscillatory events, that exist in instabilities such as the breathing mode, the sudden surge of macroparticles and the associated memory footprint can be greatly mitigated.

In the two next chapters, AVIP PIC and its features will be tested in international benchmarks to verify its implementation.

Chapter 3

Validation in a 2D $z - \theta$ setup

In order to validate AVIP PIC, it is important to verify its results. As a first approach, this can be done by making a comparison with academic setups, which leads to analytical results. However, in advanced cases, no analytical formulas are available and so we can confront the numerical results with either experiments or other PIC codes. Unfortunately, in spite of the use of noninvasive techniques, such as collective Thomson scattering measurements [Tsikata et al., 2009; Tsikata, 2009; Tsikata et al., 2013], experimental data remain challenging to obtain for HTs, and so benchmarking with other codes constitutes a more pragmatic solution. With this in mind, we first used the 1D benchmark from Turner et al. [2013] to test and verify key AVIP PIC's modules such as the Poisson solver implementation or the calculations of Monte Carlo collisions (see Section 3.3.2). This benchmark is extremely helpful because it is quick to set up and run. However, it remains limited because it does not reproduce all the characteristics and specificities of a HT: first of all, no magnetic field is present unlike an HT; secondly, it is inherently 1D whereas many multidimensional phenomena can occur in HTs [Tsikata et al., 2010]. Thus, within the framework of the LANDMARK project [2018], a 2D axial-azimuthal setup inspired from Boeuf and Garrigues [2018] was also used as a benchmark. Seven independent PIC codes were thus compared. Published results [Charoy et al., 2019] demonstrated AVIP PIC could successfully retrieve the Electron Cyclotron Drift Instability (ECDI), a crucial plasma instability responsible for electron anomalous transport across the magnetic barrier (see Section 1.3.2). This test case also provides a basis to develop and test new numerical methods. Thus, we used the 2D axial azimuthal simulation to investigate to the behavior of the merging-splitting algorithm. A careful parametric study on the algorithm parameters was carried out in order to evaluate their respective effects on the simulation and in particular with regard to the development of instabilities.

In this chapter, the axial-azimuthal setup is first presented in Section 3.1. Benchmark results are detailed in Section 3.2. Finally the parametric study on the merging-splitting algorithm is performed in Section 3.3.

Contents

3.1 Description of the model 93

3.1.1 Simulation domain 93

3.1.2 Prescribed axial profiles 94

3.1.3 Cathode model 95
3.2 Benchmarking 96
3.2.1 Strategy and codes details 96
3.2.2 Main plasma parameters 97
3.2.3 Spectral analysis 99
3.3 Application: merging-splitting algorithm 101
3.3.1 Context and objectives 101
3.3.2 Preliminary study on a 1D benchmark discharge 102
3.3.3 Parametric study on the $z-\theta$ benchmark 106
3.3.4 Results and discussion 106
3.3.5 Toward a better use of the merging-splitting algorithm 113
3.4 Conclusion 114

3.1 Description of the model

By considering the axial-azimuthal direction we can study the impact of the ECDI on anomalous transport. Since this phenomena is rather complex, the present 2D model makes simplifying assumptions that are described in the following subsections.

3.1.1 Simulation domain

The axial-azimuthal domain is modeled as a rectangle and no curvature effects are taken into account. As shown in Figure 3.1, the axial and azimuthal directions are respectively denoted by x and y and their lengths are L_x and L_y. Mesh cells are isosceles right angle triangles made of squares cut in half along the diagonal. This cell shape was found to lead to no distinguishable differences in comparison with regular square cells. The typical cell size is $\Delta x = \Delta y = 50\,\mu\text{m}$. A 2D3V model is used so unmagnetized ions are pushed with the Leap-Frog scheme from Equation (2.54) while electrons rely on the Boris algorithm from Equation (2.55) with a time step $\Delta t = 5 \times 10^{-12}\,\text{s}$. Both Δx and Δt satisfy accuracy conditions given by Equations (2.5) and (2.6). In order to speed up the simulations, the subcycling technique [Adam et al., 1982] is used. In the present case, it was found updating positions and speeds of ions every $f_{sub} = 5$ iterations accelerated the code by 40% without noticeable impact on the accuracy.

The top and bottom boundaries are periodic while the anode boundary uses the "exit" condition presented in Section 2.5.1 and is set at a constant potential $\phi_0 = 200\,\text{V}$. At the right boundary, $x = L_x$, particles leaving the domain are also deleted and removed from the simulation ("exit" condition). A special treatment regarding the Poisson's equation and the modeling of the cathode is detailed hereafter in Section 3.1.3. The simulation starts with uniform density $n_0 = 5 \times 10^{-16}\,\text{m}^{-3}$ of electrons and ions, assumed at thermal equilibrium at temperatures $T_{e,0}$ and $T_{i,0}$, respectively. Thus, positions and speeds are determined as explained in Section 2.2.2. For the benchmark, the initial number of macroparticles $N_{ppc,ini}$ per square cell was varied to assess the statistical convergence. The simulation is run until $20\,\mu\text{s}$ and diagnostics are averaged over 5000 iterations before being output. Global parameters used for this chapter are summed up in Table 3.1.

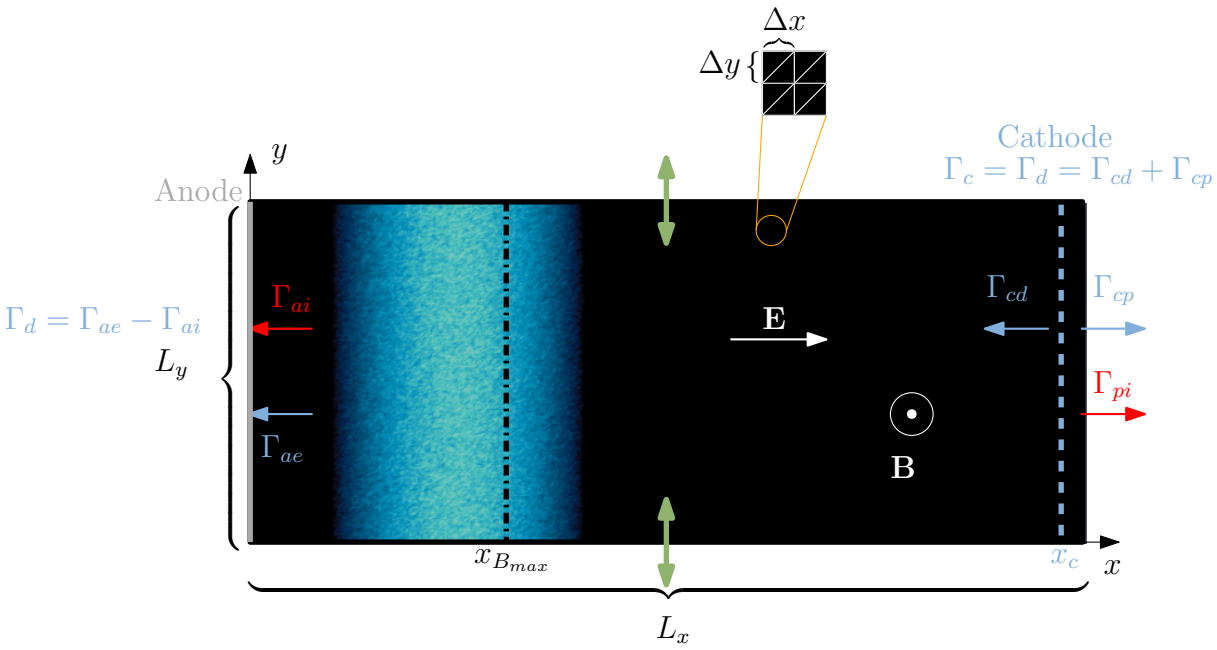

Figure 3.1: $z - \theta$ model implemented in AVIP. A local zoom at the top shows the triangular cells forming the mesh. $x_{B_{max}}$ denotes the position of maximum magnetic field. Top and bottom boundaries are periodic. Left boundary is the anode while the cathode is modeled as an emission plane at $x = x_c$ (blue dashed line). Main fluxes of particles are integrated over the azimuthal direction and denoted by the Γ symbol (red for ions, blue for electrons). The ionization zone is displayed with a blue-cyan color gradient.

3.1.2 Prescribed axial profiles

Radial magnetic field

The magnetic field is constant directed along the off plane, radial direction. It is uniform in the azimuthal direction but its axial profile is a piecewise gaussian function given by:

$$\mathbf{B}(x) = \left[a_k \exp\left(-\frac{(x - x_{B_{\max}})^2}{2\sigma_k^2} \right) + b_k \right] \mathbf{u}_z \tag{3.1}$$

where $k = 1$ for $x \leq x_{B_{max}}$ and $k = 2$ for $x > x_{B_{max}}$. We set $\sigma_1 = \sigma_2 = 0.625\,\text{cm}$. The four coefficients a_k and b_k are chosen such that $B(x = 0) = 6\,\text{mT}$, $B(x = L_x) = 1\,\text{mT}$, $B(x = x_{B_{max}}) = 10\,\text{mT}$ and by satisfying the continuity at $x = x_{B_{max}}$.

Ionization

In this model, neither neutral particles nor collisions are taken into account. Instead, an artificial and constant source term mimics the ionization process. It is uniform in the azimuthal direction and its axial profile is:

$$S(x) = \begin{cases} S_0 \cos\left(\pi \frac{x - x_m}{x_2 - x_1}\right) & \text{for } x_1 \leqslant x \leqslant x_2 \\ 0 & \text{for } x < x_1 \text{ or } x > x_2 \end{cases} \tag{3.2}$$

where $x_1 = 0.25\,\text{cm}$, $x_2 = 1\,\text{cm}$ and $x_m = (x_1 + x_2)/2$. Its 2D profile is shown in Figure 3.1. The strength of the source term S_0 is set such that the current density is $J_m = e \int_0^{L_y} S(y)dy =$

Parameters	Symbol	Value	Unit
Computational domain and grid			
Cell size	$\Delta x = \Delta y$	50	µm
Axial length	L_x	2.50	cm
Azimuthal length	L_y	1.28	cm
Number of square cells	N_{cell}	500×256	
Initial conditions			
Plasma density	n_0	5×10^{16}	m^{-3}
Ion temperature	$T_{i,0}$	0.5	eV
Electron temperature	$T_{e,0}$	10	eV
Number of particles/square cell	$N_{ppc,ini}$	75/150/300	
Computational/Physical parameters			
Discharge voltage	ϕ_0	200	V
Location of maximum magnetic field	$x_{B_{max}}$	0.75	cm
Time step	Δt	5×10^{-12}	s
Subcycling frequency	f_{sub}	5	iterations
Average time range	N_a	$5000\Delta t$	s
Final time	t_{max}	20	µs

Table 3.1: PIC simulations parameters for the $z - \theta$ setup.

$400\,\mathrm{A} \cdot \mathrm{m}^{-2}$, which gives $S_0 = 5.23 \times 10^{23}\,\mathrm{m}^{-3} \cdot \mathrm{s}^{-1}$. As detailed in [Boeuf and Garrigues, 2018; Charoy et al., 2019], for each iteration the number of $(\mathrm{X}_e^+, \mathrm{e}^-)$ pairs to be injected is given by $\Delta t L_y \int_0^{L_y} S(y)dy$. Particle positions are picked according to the profile from Equation (3.2) i.e.

$$\begin{cases} x_i = \arcsin\left(2R_1 - 1\right) \frac{x_2 - x_1}{\pi} + x_M \\ y_i = R_2 L_y, \end{cases} \tag{3.3}$$

where R_1 and R_2 are random numbers between 0 and 1. Finally, velocities are sampled from a Maxwellian distribution using Equation (2.12).

3.1.3 Cathode model

For the benchmark

The right hand side boundary is used to define the cathode. For the benchmark [Charoy et al., 2019], the cathode is modeled as an emission line located inside the domain at $x_c = 2.4\,\mathrm{cm} < L_x$, 1 mm before the right side of the domain $x = L_x$. When the Poisson equation is solved, a

Dirichlet boundary condition $\phi = 0\,\mathrm{V}$ is set at $x = L_x$. In order to keep consistency with the actual location of the cathode, the calculated potential $U(x, y)$ is shifted as,

$$\phi(x, y) = U(x, y) - \frac{x}{x_c}\overline{U}_c \tag{3.4}$$

where $\overline{U}_c = \frac{1}{L_y}\int_0^{L_y} U\,(x_c, y)\,dy$ is the azimuthal average of the calculated potential at $x = x_c$, the cathode position. By doing so the resulting potential ϕ has a y average of $0\,\mathrm{V}$ at the cathode location.

The cathode model is based on an adapted version of the current equality condition described in Section 2.5.2. Because the cathode is inside the domain there is no need to evaluate $I_{cd} = e\Gamma_{cd}$ as in Equation (2.61). Instead, Equation (2.60) is directly used and at each time step, the discharge and cathodic currents are strictly equal. Injected electrons are sampled from a Maxwellian distribution and uniformly distributed along the emission line.

Other possibility

The previous cathode model was originally designed to avoid any artificial sheath that would form if the emission line was strictly located at $x = L_x$. By doing so, the model also implicitly assumes that $I_{cd} = I_{cb}$, which is not necessarily true. As it was already mentioned in Section 2.5.2, a cathode using a quasi-neutrality model is more realistic and can be defined at the domain boundary. This cathode model will be applied in the 2D simulations of Chapter 5.

3.2 Benchmarking

3.2.1 Strategy and codes details

For this benchmark, seven different groups from international institutions worked together for over a year to converge on the aforementioned numerical setup, plasma diagnostics and results analysis. A detailed description of each code can be found in [Charoy et al., 2019] and in Appendix B and they greatly differ in key features as shown in Table 3.2. Indeed, the different codes use various solutions and strategies to complete the PIC loop from Section 2.2.1. For instance, in contrast to the other codes, RUB uses an implicit pusher along with a GPU architecture to conduct their calculations. Thus, such a choice radically changes how the code is parallelized and the way the speed of particles is updated, which could definitely lead to distinct results from the other explicit, CPU-based codes. Another difference, that is of paramount importance for CERFACS, is the nature of the considered grid for the computational domain. Indeed, all present codes, except AVIP PIC, rely on a Cartesian, structured grid. This choice greatly simplifies how the metric and connectivity of the cells is defined since neighbors of a given cell are naturally known. For instance, right next to cell (i, j), there is cell $(i+1, j)$. In the present unstructured grid by AVIP PIC, the cells are not square (see Figure 3.1) and neightbors are not known *a priori*, which drastically complicate the metric. As a result, the parallelization and data management must be carefully designed beforehand (see Figure 2.23) to overcome this challenge. Overall, the implementation of AVIP PIC greatly differs from the other codes, assuming a structured grid, and this can be source of differences in results. Finally, we shall also realize that these runs were conducted with different supercomputers, with different compilers, different precision points and all of them represent multiple reasons to get different outcomes in the end.

	LPP	LAPLACE	CERFACS	RUB	USASK	TAMU	PPPL
Algorithms							
Pusher solver ($\star$)	Explicit	Explicit	Explicit	Implicit	Explicit	Explicit	Explicit
Poisson solver ($\star\star$)	Hypre	Pardiso	Maphys	FFT Thomas	FFT	Hypre	Hypre
Floating-point precision	Double	Single* Double**	Double	Single* Double**	Double	Double	Double
Code acceleration							
Architecture	CPU	CPU	CPU	GPU	CPU	CPU	CPU
Parallelization	MPI	MPI OpenMP	MPI	CUDA	MPI	MPI	MPI OpenMP
Decomposition	Domain	Particle	Domain	Both	Domain	Particle	Particle
Language	Fortran	Fortran	Fortran	C+ Cuda C	Fortran	C++	C
Simulation times in days (elapsed time)							
Case 1 ($N_{ppc,ini} = 150$)	8	5	7	14	21	15	2.5
(No. CPU/GPU)	(360)	(108)	(360)	(1)	(32)	(300)	(224)
Case 2 ($N_{ppc,ini} = 75$)	5	3	4	9	11	11	2.5
(No. CPU/GPU)	(360)	(108)	(360)	(1)	(32)	(200)	(112)
Case 3 ($N_{ppc,ini} = 300$)	14	6	13	14	20	22	2.5
(No. CPU/GPU)	(360)	(180)	(360)	(2)	(64)	(400)	(448)

Table 3.2: Main codes specificities from [Charoy et al., 2019]. $\star$ and $\star\star$ symbols respectively refer to the pusher and Poisson solvers. $N_{ppc,ini}$ corresponds to the initial number of macroparticles per square cells.

The simulation takes around $\sim 16\,\mu s$ to reach a steady state. During the transient the mean density increases from n_0 to $\sim 3.6 n_0 = 1.8 \times 10^{17}\,m^{-3}$ before stabilizing. In Charoy et al. [2019], we showed that for this benchmark statistical convergence was achieved from $N_{ppc,ini} = 75$ (Case 2) with a final number of particle per cell $N_{ppc,fin} \approx 275$. Thus, we will focus in the following on the results of Case 2.

3.2.2 Main plasma parameters

At steady state, the main plasma parameters for Case 2 are presented in Figure 3.2.

On the left hand side, 2D maps for the CERFACS simulation at $20\,\mu s$ provide an overview of the ongoing physics. First, Figure 3.2 (a) shows that the plasma density is mainly localized at the position of the ionization profile, its peak being upstream of the position of the maximum magnetic field $x_{B_{max}}$. Electrons are convected in the azimuthal direction under the effect of the $\mathbf{E} \times \mathbf{B}$ drift but with short-wavelength oscillations that are clearly visible in the zone (I) in Figure 3.2 (c). Downstream $x = x_{B_{max}}$, the oscillations seem to transition toward longer wavelengths. Around $x = x_{B_{max}}$, the axial electronic current exhibits the long-wavelength azimuthal pattern with a strong magnitude $\|\mathbf{J}_{e,x}\|$ in Figure 3.2 (e). Oscillations of regions (I) and (II) will be further discussed in Section 3.2.3. In Figure 3.2 (e), one can also notice the effects the cathode at $x = x_c$. Indeed, if we approach the emission line from the left, we see that $J_{e,x}$ and once we cross $x = x_c$, $J_{e,x}$ abruptly goes from positive to negative. This means

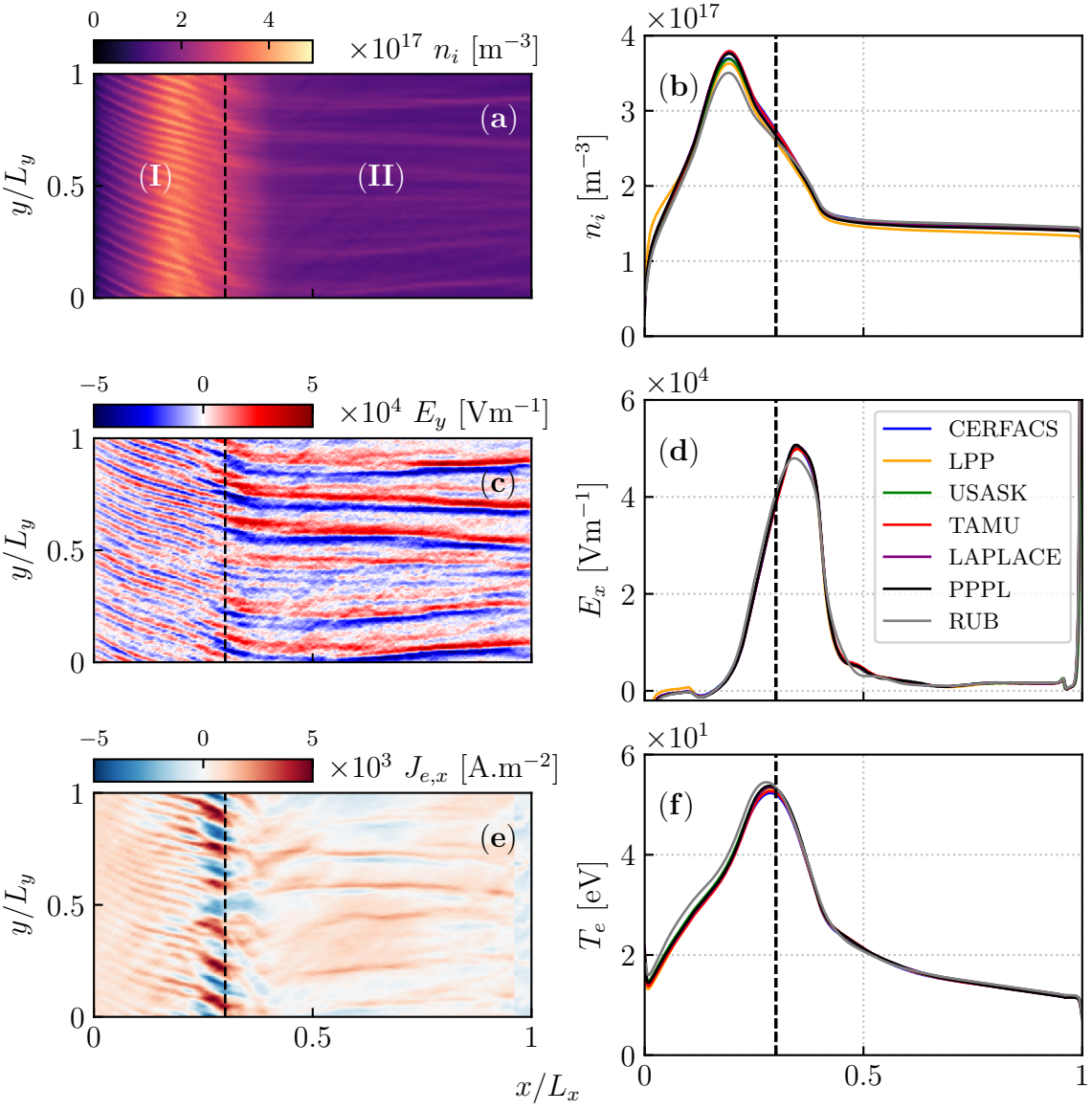

Figure 3.2: Main plasma parameters at steady state for Case 2 at $N_{ppc} = 75$. (a-c-e): 2D maps for CERFACS at 20 µs of ion density n_i, azimuthal electric field E_y and electron axial current $J_{e,x}$. Two zones (I) and (II) can be distinguished when looking at the oscillations in the domain. (b-d-f): mean azimuthally averaged axial profile over 16-20 µs of ion density n_i, axial electric field E_x and total electron temperature T_e. The dashed black line indicates the position of maximum magnetic field $x_{B_{max}}$.

electrons go toward the anode at the left of the emission line while they go toward the cathode at the right of $x = x_c$. Thus, the directions of electron fluxes depicted in Figure 3.1 are coherent with the numerical results.

On the right hand side of Figure 3.2, azimuthally averaged axial profiles of the last 4 µs compare results between the codes presented in Table 3.1. The average over the azimuthal direction removes the oscillation effects while the time average over 16-20 µs mitigates the influence of numerical noise. Thus, it is much easier to quantitatively compare numerical results generated by the independent codes. Overall, it appears that all 1D profiles are extremely close

within a 5% difference interval. Figure 3.2 (b) confirms that the plasma density is mainly located upstream of $x = x_{B_{max}}$. Figure 3.2 (d) shows the axial electric field reaches a maximum value right downstream of $x = x_{B_{max}}$. Finally, from Figure 3.2 (f), we see that the electrons reach a maximum temperature $T_{e,max}$ also around the transition region between zone (I) and (II). Besides, $T_{e,max}$ occurs where the current $J_{e,x}$ is most intense according to Figure 3.2 (e), which suggests Joule heating $\mathbf{J} \cdot \mathbf{E}$ is important in this area.

3.2.3 Spectral analysis

Observed oscillations in Figure 3.2 (a-c-e) can be further explored by a spectral analysis. In 2D, coherently to earlier theoretical works [Lashmore-Davies and Martin, 1973; Lampe et al., 1971b], Ducrocq et al. [2006] found that the ECDI grows at discrete azimuthal wavenumbers $k_y \approx m\Omega_{ce}/v_0$, with $m = 1, 2, ...$, where Ω_{ce} is the electron cyclotron frequency and v_0 the electron drift velocity. According to linear theory, the ECDI can transition to an ion acoustic like instability [Gary and Sanderson, 1970; Cavalier et al., 2013]. From quasi-linear theory, Lafleur et al. [2016a,b] derived a good approximation of the dispersion relation of the ion acoustic mode, expressed as:

$$\omega_R \approx \mathbf{k} \cdot \mathbf{u}_i \pm \frac{kc_s}{\sqrt{1 + k^2\lambda_d^2}}, \tag{3.5}$$

where $\boldsymbol{v}_i$ is the ion beam velocity and $c_s = (\gamma T_e/m_i)^{1/2}$ is the ion sound with the heat capacity ratio γ. According to Lafleur et al. [2016b], this expression remains a good approximation as long as $k_\parallel \lambda_D$ is not too small, where $k_\parallel$ is the wave vector component parallel to $\mathbf{B}$ (k_z in the current notation). Yet, in 2D simulations neglecting $k_\parallel$ [Charoy et al., 2019; Boeuf and Garrigues, 2018], the transition to the ion acoustic mode has also been observed. In earlier theoretical studies, Lampe et al. [1971a, 1972] found that anomalous wave-particle interactions, called resonance broadening, could smooth cyclotron resonances out, which may be responsible for the ion acoustic transition.

For the present work, the numerical dispersion relation has been obtained at two axial locations. In Figure 3.3 (a), the normalized 2D Fast Fourier Transform (FFT) computed over 16-20 µs characterizes the azimuthal instability in zone (I) at $x = 0.12L_x$. The analytical dispersion relation from Equation (3.5) has also been included assuming $\mathbf{k}\cdot\mathbf{v}_i \approx= k_y\mathbf{u}_y\cdot v_i\mathbf{u}_x = 0$ i.e. assuming that the instability essentially propagates in a perpendicular direction to the ion beam. The numerical dispersion relation exhibits a continuous feature and fits well with the theoretical result, which suggests the transition to the ion acoustic mode has been achieved in the upstream region of the simulation domain.

In Figure 3.3 (c), the same analysis performed in region (II) leads to different conclusions. The numerical dispersion relation seems more discrete and the instability does not correspond to a modified ion acoustic mode. Its nature is still the subject of active research [Hara and Tsikata, 2020]. Convection of the ion acoustic mode from zone (I) to zone (II), where the magnetic field is weaker, probably participates in modifying the original ion acoustic mode.

Figure 3.3 (b) and (d) respectively show the evolution of the main azimuthal wavenumber and pulsation over the axial location for all codes. Transition from zone (I) to zone (II) is clear and the azimuthal wavenumber is approximately divided by more half. This means the wavelength is multiplied by roughly two which is consistent with what was observed in Figure 3.2 (c). Besides, most of the groups, with the exception of LAPLACE, sees a sharp increase of $k_y\lambda_D$ before dramatically decreasing from $x = x_{B_{max}}$.

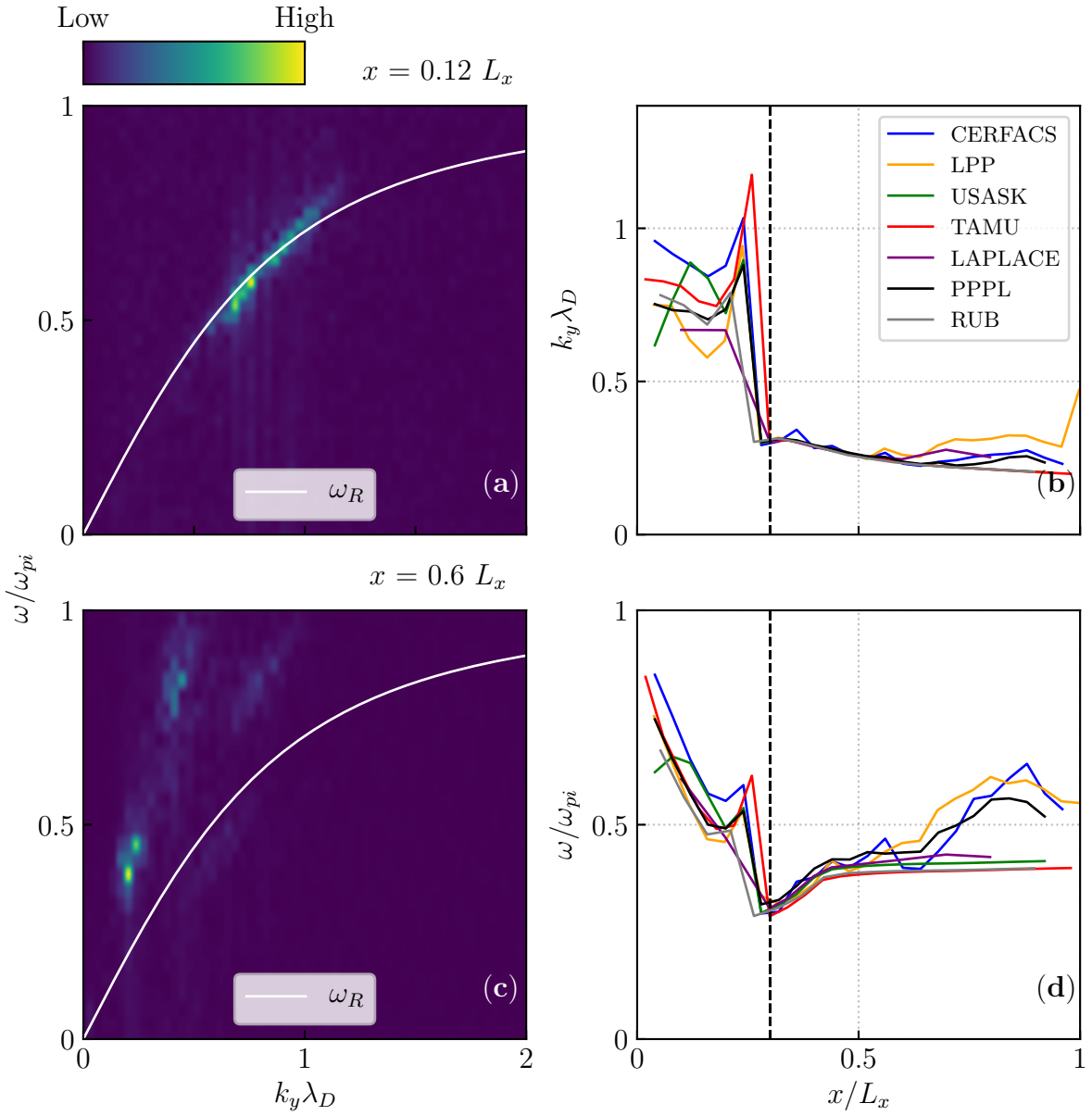

Figure 3.3: Spectral analysis of azimuthal instabilities. (a-c): numerical dispersion relations computed over 16-20 µs at respectively $x = 0.12L_x$ (zone I) and $x = 0.6L_x$ (zone II). White solid lines represent the theoretical dispersion relation from Equation (3.5). (b-d): normalized main azimuthal wavenumber $k_y\lambda_D$ and pulsation ω/ω_{pi} over the axial location x/L_x for the seven independent codes. The black dashed line represents the location of maximum magnetic field $x_{B_{max}}$.

In Figure 3.3 (d), the frequency starts decreasing at first and reaches a minimum value. Then, in zone (II), it increases again before stabilizing at a lower level than in zone (I) for USASK, TAMU, LAPLACE and RUB. For CERFACS, LPP and PPPL, the pulsation continues to rise around the plume and cathode locations. This behavior could not be explained during this study.

Finally, from Figure 3.3 (b) and (d), we can roughly estimate the phase velocity from $v_\varphi \approx k_y/\omega$. From zone (I) to zone (II) ω/ω_{pi} is divided by ~ 2 and $k_y\lambda_D$ by a lesser factor. Thus, in ad-

dition to exhibit a lower wavelength, the waves are traveling faster in zone (II) than in zone (I).

As a conclusion, all the codes describes a similar physics, characterized by the presence of two zones. We first distinguish zone (I), in the channel, that presents a short azimuthal wavelength. The latter transitions into zone (II) where the wavelength increases in the plume. In all codes, the numerical dispersion relation closely fits a modified ion acoustic wave dispersion relation,. The latter is believed to be the asymptotic behavior of a previous instability, the ECDI, that is likely to play an important role in the anomalous transport [Lafleur et al., 2016b]. The plasma structure is also very similar to axial profiles that are close with a 5% interval. Although all groups considered the same setup and initial conditions, all codes differed greatly in their implementation and used different supercomputers and compilers. These differences could have prevented such a good agreement between the groups. Nevertheless, a high enough spatial and temporal resolution (following Equation (2.5) and equation (2.6)) combined with a statically converged phase space (with $N_{ppc,ini} \geq 150$) were sufficient to make these differences negligible with respect to the present physics here.

3.3 Application: merging-splitting algorithm

3.3.1 Context and objectives

The merging-splitting algorithm presented in Section 2.6.1 can be very useful in large simulations but is delicate to manipulate. Indeed, there are four parameters to set: the target number of particles per cell N_t, the tolerances in position and speed $T_{\mathbf{x}}$ and $T_{\mathbf{v}}$ and finally, the frequency f_t at which the merging-splitting algorithm will be applied.

In order to decide which parameters can be acceptable for a HT configuration, the previous 2D axial-azimuthal configuration is a good test case to perform a parametric study. Indeed, it is fairly quick to run, well understood without the merging splitting algorithm and it captures typical features, such as the ECDI, that exist in a HT. The present parametric study will serve as a basis for future runs that will need the use of the merging-splitting algorithm. As stated in Section 2.6.1, this will be the case for real situations where the number of macroparticles can greatly vary. For instance, during ignition of the thruster, the number of particles can greatly increase locally. With a domain decomposition approach such as in AVIP PIC, this can be problematic because processors taking care of the ionization zone can dramatically slow down the simulation or even exhaust the available CPU memory. Another example of application of the merging splitting concerns large spatial instabilities such as the breathing mode (BM). As explained in Section 1.3.2, the BM is characterized by significant temporal oscillations of the plasma and neutral density. Capturing each of these peaks can be very challenging as the number of macroparticles can rapidly increase, hence slowing down the computation or causing out-of-memory errors.

In order to have a good guess for the four $(N_t, T_{\mathbf{x}}, T_{\mathbf{v}}, f_t)$ parameters we can first guide our thinking upon the literature and experience.

The N_t parameter should be chosen such that the described physics is the same as if the algorithm has not been used, but at a lesser cost. Ideally, the statistical convergence should still be ensured but one can also make a compromise between accuracy and simulation time. From 2D HTs benchmarks [Charoy et al., 2019; Villafana et al., 2021], it seems statistical convergence is achieved from ~ 200 particles per square cell at steady state, so this threshold should be kept in mind when performing merging-splitting in 2D. In 3D, this value should probably be

updated as it will be demonstrated in Chapter 5.

As a reminder, the tolerances $T_{\mathbf{x}}$ and $T_{\mathbf{v}}$ are chosen by the user and serve as a dimensionless threshold in Equation (2.66) to decide if particles are similar in terms of position and speed. $T_{\mathbf{x}}$ and $T_{\mathbf{v}}$ can be difficult to relate to a measurable physical quantity in the general case but we can give an example to grasp a more intuitive sense of them. We can clarify their meaning by considering a hypothetical simple 1D case. In this scenario, $n_d = 1$ and V_c^{1/n_d} reduces to the spatial step, i.e., $V_c^{1/n_d} = \Delta x$ inEquation (2.66). Therefore, if we choose a space threshold $T_{\mathbf{x}} = 1$, this would indicate we require particles to satisfy $\sigma_{x_i} < \Delta_x$, which means we want particles being scattered over a typical length of Δx at most. In the general case, we can view $T_{\mathbf{x}} = 1$ as a constraint to only consider particles that are located in a volume of size V_c. For the speed threshold $T_{\mathbf{v}}$, a similar interpretation can be done with the local mean speed. In the literature, Luu et al. [2016] suggests that using $T_{\mathbf{x}} \sim 1$ and $T_{\mathbf{v}} \sim 0.02$ are a good first guess to capture an accurate physics while reducing the number of particles. However, these values are case-dependent and should be checked every time.

The final parameter f_t, expressed a number of iterations, describes how often the algorithm will be applied. This parameter is also important as it dictates that the algorithm will be triggered every f_t, which might affect performances if f_t is too low.

Determining adequate values for all four parameters is challenging because a four dimensional space parameters must be explored. Thus, for a given setup we need to do two things. First we should test as many sets $(N_t, T_{\mathbf{x}}, T_{\mathbf{v}}, f_t)$ as possible. Then, the collected results can be compared to the same simulation for which the merging-splitting algorithm is turned off. It is then expected to obtain a series of sets $(N_t, T_{\mathbf{x}}, T_{\mathbf{v}}, f_t)$ for which numerical results are deemed unchanged in spite of the use the algorithm. *A priori*, this laborious effort would need to carry out for each new configurations, which is inconvenient. However, one can reasonably assume that for a system exhibiting the same kind of physics, as a HT, a common set $(N_t, T_{\mathbf{x}}, T_{\mathbf{v}}, f_t)$ must exist. Therefore, in this section, we propose to identify reasonable values of the four parameters $(N_t, T_{\mathbf{x}}, T_{\mathbf{v}}, f_t)$ and to assess the effects of the merging-splitting algorithm on a HT simulation setup. Before diving straight into the previous axial-azimuthal configuration we can first start with a simplified 1D setup to have a quick good sense of acceptable choices.

3.3.2 Preliminary study on a 1D benchmark discharge

Description of the simulation

In order to have a quick overview of the algorithm behavior, we can start the investigation with a simple 1D discharge that was benchmarked by Turner et al. [2013]. As already mentioned in Section 2.2.1, AVIP cannot handle 1D meshes but since the physics essentially occurs in one direction, we can still consider a thin 2D mesh as shown in Figure 3.4. As in Section 3.1.1, the simulation domain is made of square cell sliced into two isosceles right angle triangles. The domain is initially filled with a uniform density of electrons e^- and ions He^+ at thermal equilibrium. Neutral particles of helium are not present but instead a constant density n_n at temperature T_n is imposed during the whole simulation. For this pseudo 2D case, ions and electrons particles can exit at the left and right boundaries and are specularly reflected at top and bottom boundaries as described in Section 2.5.1. Since no magnetic field is present, the Leap-Frog algorithm is used to update the velocities of particles.

The left boundary is set to a potential $\phi = 0\,\mathrm{V}$ while the right one oscillates between $\pm\phi_1$ at the frequency f_1. During the simulation, the plasma is excited by the varying right potential and ionization (modeled self-consistently by the Monte Carlo module from Section 2.2.3) occurs

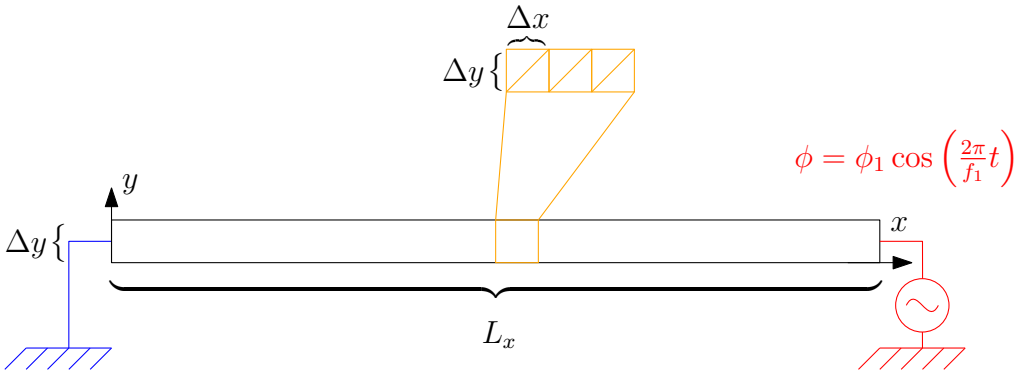

Figure 3.4: 1D discharge setup from [Turner et al., 2013] using a 2D mesh with a width of Δy. The potential is set at the left boundary while the right one oscillates between $\pm\phi_1$ at the frequency f_1. Particles exit at the left and right boundaries, while the top and bottom boundaries are walls where specular reflections occur.

in the center of the domain. In Turner et al. [2013], four simulations were run and, each of them tested different initial densities, spatial resolution and voltage frequency at the right side of the domain. In this benchmark, the main physical quantity that was compared between the different participants was final ion density profile at steady state. Overall, this meticulous work on the four configurations represent a standard benchmark for the low temperature plasma community. AVIP PIC was validated on the four cases and as an example, we present in Figure 3.5 the comparison on Case 1 of AVIP PIC and published results.Parameters for Case 1 are given in Table 3.3. We can see that AVIP PIC closely fits results from [Turner et al., 2013].

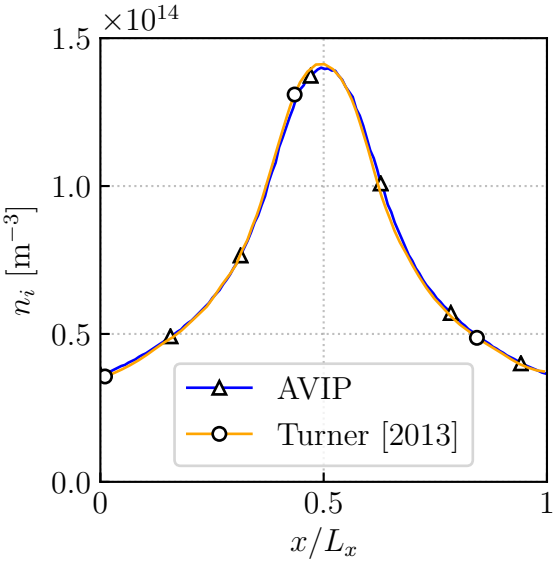

Figure 3.5: Mean steady state ion density profile over the last 10 µs of AVIP compared to Case 1 from [Turner et al., 2013].

Parameters	Symbol	Value	Unit
Computational domain and grid			
Cell size	$\Delta x = \Delta y$	523	µm
Width	Δy	523	µm
Length	L_x	6.7	cm
Number of cells	N_{cell}	128×2	
Initial conditions			
Plasma density	n_0	2.56×10^{14}	m^{-3}
Ion temperature	$T_{i,0}$	300	K
Electron temperature	$T_{e,0}$	30000	K
Number of particles/ triangular cell	$N_{ppc,ini}$	256	
Physical parameters			
Left potential	ϕ_0	0	V
Right potential amplitude	ϕ_1	450	V
Right potential frequency	f_1	13.56	MHz
Computational parameters			
Time step	Δt	1.8436×10^{-10}	s
Average time range	N_a	$12800\Delta t$	s
Final time	t_{max}	94.40	µs

Table 3.3: Simulation parameters for Case 1 from [Turner et al., 2013].

Parametrical study

Since the pseudo 1D simulation takes around 30 min to complete with AVIP, multiple sets of $(T_{\mathbf{x}}, T_{\mathbf{v}})$ have been tested while keeping a target number of particles $N_t = 100$, which is enough here to ensure a statistical convergence, and a testing frequency $f_t = 10$. In this study the goal is to quickly identify good candidates of $(T_{\mathbf{x}}, T_{\mathbf{v}})$ that can be used in a HT simulation.

In Figure 3.6 (a), twenty sets of $(T_{\mathbf{x}}, T_{\mathbf{v}})$ have been tested and are represented by dots. For each of these sets, the simulation is run using parameters specified in Table 3.3. Their respective final ion profiles are averaged over the last 10 µs of the simulation. For all cases, the final n_i profile had the same shape as the reference case but possibly shifted to higher values. In order to easily compare them with the reference case shown in Figure 3.5, their error with respect to the reference case is measured using a L_2 norm. From Figure 3.6 (a), several trends appear. First, when $T_{\mathbf{v}}$ increases, the simulation will eventually accumulate errors and diverge from the correct solution. The point from which divergence occurs depends on the value of $T_{\mathbf{x}}$: the higher it is, the lower the tipping point $T_{\mathbf{v}}$ will be. Besides, it is remarkable to observe

that divergence can occur rather quickly. For instance, using $T_{\mathbf{x}} = 0.1$ and $T_{\mathbf{v}} = 10^{-1}$ leads to a correct solution whereas setting $T_{\mathbf{x}} = 0.1$ and $T_{\mathbf{v}} = 1.5 \times 10^{-1}$ ends up to a completely erroneous solution. Overall, two zones (1 and 3) provide accurate results.

It is interesting to assess the effects of the algorithm on the statistics at steady state and the elapsed time for each simulation. In Figure 3.6 (b), the reference case takes approximately 30 min to complete and ends up with about 35,000 particles in the computational domain. In the center of the domain, there are ~ 140 ion particles per cell and less than 40 at the extremities. For successful sets of $(T_{\mathbf{x}}, T_{\mathbf{v}})$, the effects of the merging splitting algorithm are spectacular. Particles have been aggressively merged at the beginning of the simulation and their numbers have been divided by around 100 at final time. Obviously, the criteria $N_t = 100$ particles per cell is not satisfied in any cell of the domain, but it did not prevent the n_i profile from being correct. At steady state, the algorithm attempts to split particles to comply with the $N_t = 100$ requirement but it fails to do so because particles are too different given the constraints $T_{\mathbf{x}}$ and $T_{\mathbf{v}}$. More importantly, the elapsed time has dramatically reduced by a factor ~ 2.7. On the other hand, for zones 2 and 4, the final number of particles is either close or higher than the reference case. Therefore their respective simulation time is around 30 min as well. The criteria N_t is satisfied but since their final n_i profiles are off, it suggests particles with too many differences in position and speed have been merged and split.

Overall, thanks to this quick study, it seems recommendations from [Luu et al., 2016] are reasonable for plasma simulations. The 1D discharge benchmark have a rather simple physics comparing to 2D or 3D simulations of HT that involve the magnetic field. In the present case, only the final ion profiles could be compared. However, in a HT simulation, other features such as plasma instability must be preserved in spite of using the algorithm. With so few particles at the final time, the velocity distribution function (VDF) may be not well discretized. As a consequence, small variations in the VDF, that would give rise to kinetic effects and micro-structures, could be severely modified or even lost. In HT, the ECDI characteristics could then be erroneous. Therefore, it is necessary to conduct a similar parametric study using a HT simulation and verify if and how it can describe a more complex physics. From what was learned in this section, $T_{\mathbf{x}} = 0.1$ and $T_{\mathbf{v}} \sim 10^{-2}$ are probably good candidates to start with in the next parametric study.

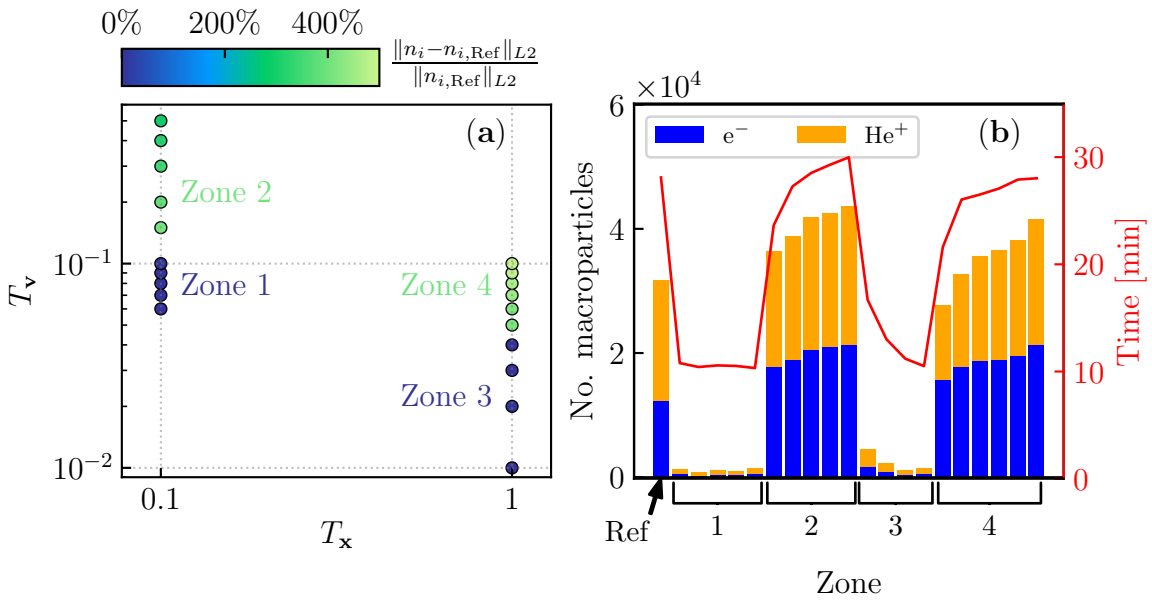

Figure 3.6: Parametric study of $(T_\mathbf{x}, T_\mathbf{v})$ using the 1D discharge benchmark from [Turner et al., 2013] over the last 10 µs of the simulation. (a): measured discrepancy of final ion density profile with respect to the reference solution as a function of $T_\mathbf{x}$ and $T_\mathbf{v}$. (b): averaged final number of ions and electrons in steady state and elapsed time for each simulation.

3.3.3 Parametric study on the $z - \theta$ benchmark

Going back to the axial-azimuthal configuration, a parametric study has been conducted on the tolerances $T_\mathbf{x}$ and $T_\mathbf{v}$ and on the target number of particles N_t per triangular cell. Without the merging splitting algorithm, Case 2, presented in Section 3.2, takes more than four days ($\sim$ 102 h) to reach 20 µs on 360 CPUs. Therefore, we must limit our study to a few sets $(T_\mathbf{x}, T_\mathbf{v}, N_t)$ to keep the computational time reasonable. Table 3.4 presents the tested sets $(T_\mathbf{x}, T_\mathbf{v}, N_t)$. The cases are sorted in the ascending order according to how the merging-splitting algorithm is able to actually merge and split the macroparticles under the constraints $T_\mathbf{x}, T_\mathbf{v}, N_t$. For instance, in Case A, the merging splitting is less active than in Case B and so on.
From Case A to Case E, tolerances on $T_\mathbf{x}, T_\mathbf{v}$ are gradually loosened to assess their effects on the simulation. As it will be demonstrated below, the target number N_t turns out to be important as well. Case F represents a simulation where the merging-splitting algorithm is quite aggressive. Indeed, since it uses the same $N_{ppc,ini} = 300$ as Case 3, the ionization source term from Section 3.1.2 injects four times more macroparticles than Case 1. It should be compared to Case C as they have identical $N_t, T_\mathbf{x}$ and $T_\mathbf{v}$ but Case F has more macroparticles to merge and split. All simulations are run up to 20 µs and the same diagnostics of Section 3.2 are generated.

3.3.4 Results and discussion

Effects on the statistics

In Figure 3.7, the statistical effects of the merging-splitting algorithm, on both the electrons and ions, are presented.

In Figure 3.7 (a), the final number of macroparticles per triangular cell $N_{ppc,fin}$ as a function

Name case	N_t	$T_{\mathbf{x}}$	$T_{\mathbf{v}}$
Reference	-	0	0
Case A	50	5×10^{-2}	5×10^{-3}
Case B	75	1×10^{-1}	1×10^{-2}
Case C	75	1×10^{-1}	5×10^{-2}
Case D	50	1×10^{-1}	5×10^{-2}
Case E	50	1×10^{-1}	1×10^{-1}
Case F ($N_{ppc,ini} = 300$)	75	1×10^{-1}	5×10^{-2}

Table 3.4: Tested sets $(N_t, T_{\mathbf{x}}, T_{\mathbf{v}})$ of the merging splitting algorithm. For simplicity, $f_t = 10$ for all cases. The reference case is Case 2 from Table 3.1. Cases A to E starts with the same initial conditions as Case 2 while Case F uses the same number of macroparticles as Case 3.

of x indicates that the number of electron macroparticles has been greatly reduced overall. The decrease of $N_{ppc,fin}$ is the lowest for Case A and the highest for Cases D and E which have very similar profiles. Cases B to F display a $N_{ppc,fin}$ that belongs to the interval $[-N_t/2; 2N_t]$ for all axial positions, except at the plume where the density must tend to zero. This means the algorithm, under the constraints $T_{\mathbf{x}}$ and $T_{\mathbf{v}}$, could actually merge the excess of electrons to reach the target, which is the desired behavior. Conversely, Case A did not meet the $[-N_t/2; 2N_t]$ target interval for all axial positions, as $N_{ppc,fin}$ has a maximum value of virtually 200. This suggests the constraints $T_{\mathbf{x}} = 5 \times 10^{-2}$ and $T_{\mathbf{v}} = 5 \times 10^{-3}$ were too strict and the algorithm was unable to identify clusters of similar particles. Finally, Case F displays a higher $N_{ppc,fin}$ than the reference case in the near plume in the $\sim 0.7L_x - 0.9L_x$ range. Yet, this does not mean that particles were split in this area because one needs to recall Case F started with four times more particles than the reference case, which is Case 2 from Table 3.1.

In fact, Figure 3.7 (c) shows that, for Case F, electron macroparticles have a mean statistical weight q_f always above the weight of Case 3, represented by a black dashed line. As a reminder,q_f is set at the beginning of the simulation by $q_f = (n_0 V_c) N_{ppc,ini}^{-1}$, (see Equation (2.4)), but will change over time when the merging-splitting algorithm is activated. Like Case 3, the reference case in blue exhibits a constant statistical weight q_f. Cases A to E have all a statistical weight q_f above the reference in the whole domain except near the anode at $x = 0$, which indicates particles are probably split there.

In the right column, the effect of the algorithm on ions is quite different. In Figure 3.7 (b), we can see the decrease of $N_{ppc,fin}$ is still visible but not as spectacular as in Figure 3.7 (a). For instance, Case A has a profile extremely close to the reference case, which means only a few particles have been merged. Overall, only Case E, which has the most loosened tolerances $T_{\mathbf{x}}$ and $T_{\mathbf{v}}$, can reach the target interval $[-N_t/2; 2N_t]$. Case F is spectacular because it can have four times more ions than electrons in the ionization region while $N_{ppc,fin}$ are similar for both e^- and Xe^+ downstream. Thus, it again means the algorithm could not find similar Xe^+ particles given the $T_{\mathbf{x}}$ and $T_{\mathbf{v}}$ constraints.

Since the plasma is quasi-neutral, the statistical weight q_f is logically lower in Figure 3.7 (d) for ions than it is for electrons in Figure 3.7 (c). For Case A, the profile is only slightly higher than the reference case except in the ionization zone, where it is superimposed.

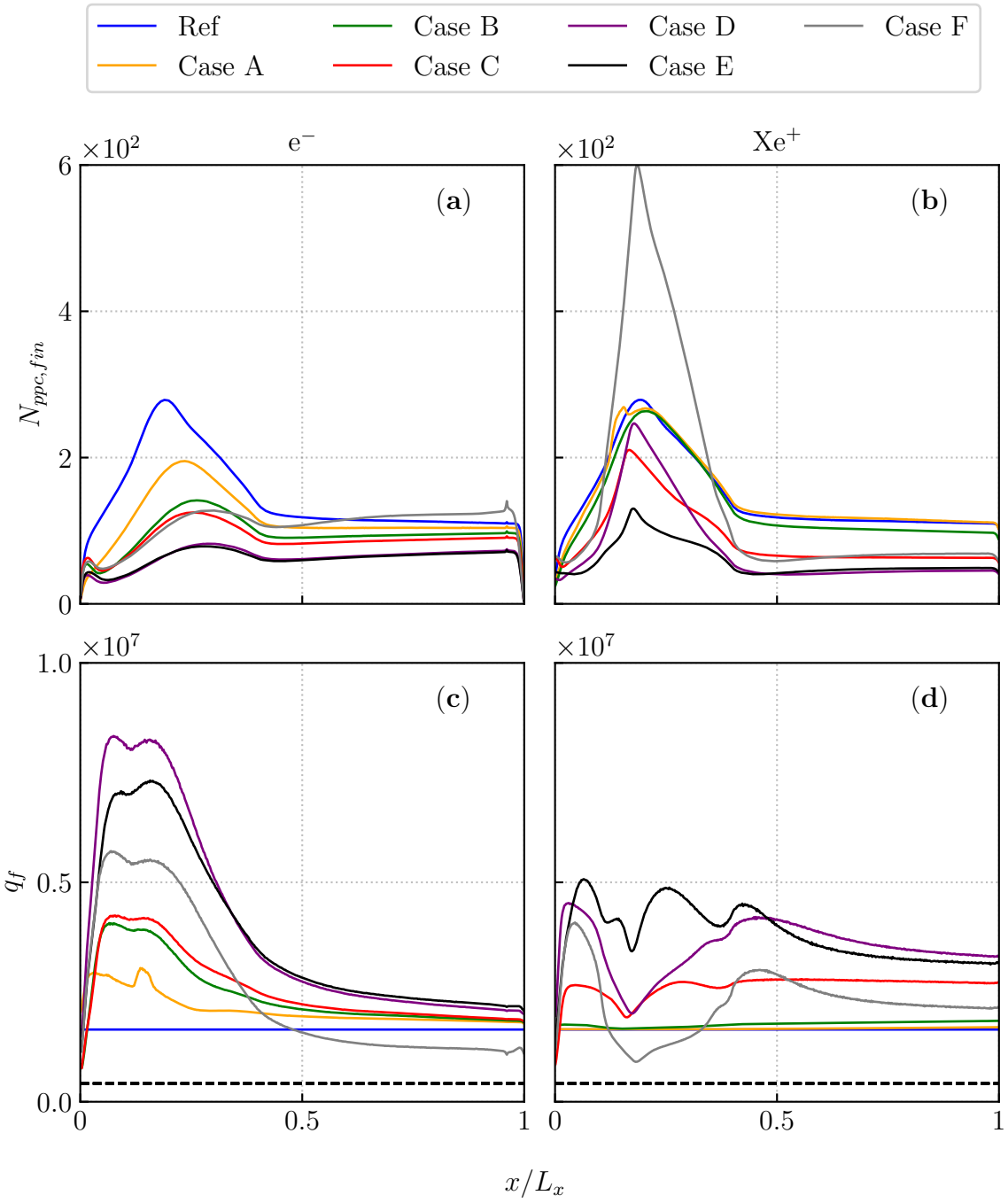

Figure 3.7: Statistical effects of the merging-splitting algorithm for e^- (left column) and Xe^+ (right column). (a-b): mean number of macroparticles per triangular cell $N_{ppc,fin}$ along the axial direction in the range 16-20 µs. (c-d): mean statistical weight q_f along the axial direction in the range 16-20 µs. In (c-d), the dashed black line represents the statistical weight of Case 3 from Table 3.1 that must be compared to Case F.

Overall, the algorithm has reduced the number of macroparticles through merging but also split some particles near the anode, where the density drops. Besides, in the present setup, electrons were more likely to be merged than ions. This latter observation is quite surprising since the electron velocity distribution function (EVDF) is likely to be more spread out than

that of ions. So it should be more difficult to identify similar electrons under the constraints $T_{\mathbf{x}}, T_{\mathbf{v}}, N_t$ than ions. As of today, we do not have an explanation for this result.

Effects on the physics

The effects on the physics can be explored by studying the axial profiles of ion density n_i, axial electric field E_x and total electron temperature T_e. Figure 3.8 (a) shows the ion density profiles are quite close for all cases except Case F which displays a significantly higher peak in the ionization region. The reference case is virtually superimposed to Case A. In Figure 3.8 (b), the conclusions are similar, Case F shows the most approximate profile and cases with strict $T_{\mathbf{x}}$ and $T_{\mathbf{v}}$ constraints fit well the benchmark result. The situation is more insightful when looking at the total electron temperature T_e in Figure 3.8 (c). Again, Case F is quite far from the expected result: its peak is similar but shifted downstream. For Cases A to D the profiles are in good agreement in the ionization zone but higher near the anode and downstream of the acceleration zone (zone II in Figure 3.2). Case A, which experiences the fewer merging and splitting processes, has the lowest temperature discrepancy while Case F with a more aggressive strategy displays a temperature increase of $\sim 50\%$. Therefore, it seems the merging splitting algorithm tends to introduce some numerical heating. The numerical heating can be controlled with reasonable values of $T_{\mathbf{x}} = 10^{-1}$ and $T_{\mathbf{v}} \sim 1 - 5 \times 10^{-2}$ which correspond to Case B-C even with a quite low target number $N_t = 50$ (Case D).

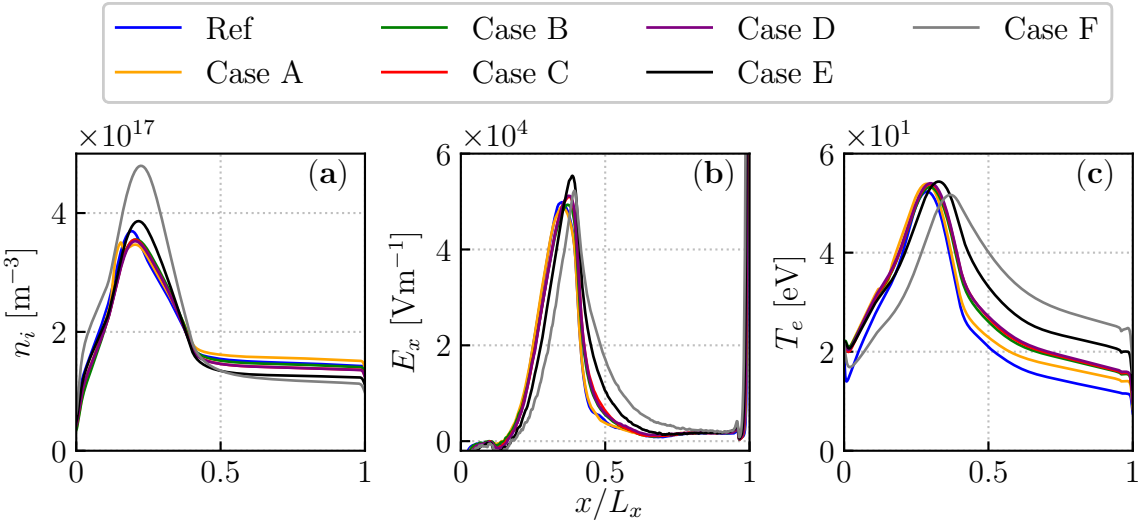

Figure 3.8: Comparison of main plasma parameters averaged over the 16-20 µs range obtained with different parameters of the merging-splitting algorithm: (a) ion density n_i, (b) axial electric field E_x and (c) total electron temperature T_e.

In addition to the main plasma parameters, it is crucial to ensure that the final instabilities are well recovered. To do so, we can look at the main normalized pulsation ω/ω_{pi} and azimuthal wavenumber $k_y\lambda_D$. Thus, in Figure 3.9, we report their values along the axial direction from a FFT analysis based on the last four microseconds of the simulation as in Figure 3.3.

In Figure 3.9 (a), the azimuthal wavenumber is supposed to transient from high values (zone I) to low values (zone II). When tolerances $T_{\mathbf{x}}$ and $T_{\mathbf{v}}$ are too relaxed as in Case E, this transition does not exist and $k_y\lambda_D$ actually increases. Although Case D showed a satisfactory agreement when comparing the main plasma parameters, it poorly captures the expected final instability.

For this particular case, it seems that the lack of particles is detrimental since it uses the same tolerances $T_{\mathbf{x}}$ and $T_{\mathbf{v}}$ as Case C but its target number N_t was set to 50 instead of 75. Case C is the first case using the merging splitting algorithm that actually predicts the correct transition from zone I to zone II. Values of $k_y\lambda_D$ are also closer to the reference case. Yet, results remain below in zone (I). The latter can be greatly improved by adjusting the tolerance on speed $T_{\mathbf{v}}$, which results in Case B, which fits well in both zones I and II. Surprisingly, Case A exhibits a lower accuracy in spite of performing the less merging and splitting of particles. However, as it was observed in Figure 3.7, its number of electrons (a) was still reduced, especially in the ionization zone. Thus, Case A is probably too far from statistical convergence to accurately describe the modified acoustic instability. Finally, Case F, which was already off regarding axial profiles of main plasma parameters, completely fails to describe the same instabilities as the reference case. The difference in results is striking considering that fact that it uses the same N_t, $T_{\mathbf{x}}$ and $T_{\mathbf{v}}$ as Case B. However, since Case F has more particles to merge and split than Case B, it seems the merging-splitting algorithm leads to an accumulation of error in the description of the velocity distribution function. Such deviation was already noticed by Luu et al. [2016], but it is supposed to remain limited as long as the $T_{\mathbf{x}}$ and $T_{\mathbf{v}}$ tolerances are reasonable. In the present case, a pragmatic solution would probably consist in limiting the application frequency f_t of the algorithm. Checking every 10 iterations if N_{ppc} lies in the $[-N_t/2; 2N_t]$ interval may be unnecessary and susceptible to cause errors.

The analysis conducted on the azimuthal wavenumber is similar for the normalized pulsation ω/ω_{pi} in Figure 3.9 (b). Cases D-E-F are off whereas Case A-B-C display a reasonably good agreement with the benchmark case. Yet, while Case B was closely related to the reference case in Figure 3.9 (a), the sharp decrease of ω/ω_{pi} at the transition from zone I to zone II is not very clear. Probably a better statistical convergence would improve accuracy here.

Effects on transients

So far the discussion has focused on the steady state. However, some significant differences with the benchmark case arise during the transient of the simulation. For this study, we compare the reference case with Case B, which describes relatively well the expected physics according to the previous subsections.

In Figure 3.10, the total exiting current, normalized by the azimuthal length L_y of the domain is shown for both cases. Both reach the steady state value of $J_m = 400\,\mathrm{A}\cdot\mathrm{m}^{-2}$, that is imposed by the ionization source term $S(x)$ from Section 3.1.2. For the reference case, there is initially an accumulation of charged particles in the ionization zone, but they are eventually convected away. Thus, a sharp peak of exiting current is measured at around 3 µs. Then, the current abruptly decreases before it slowly increases again. The current oscillates around $J_m = 400\,\mathrm{A}\cdot\mathrm{m}^{-2}$ until an equilibrium is reached between sources (ionization) and losses (exit). The dynamics is more disturbed when the merging-splitting algorithm is activated. The initial burst of particles flux occurs at a later time around 8 µs and is much higher.

In fact, the merging-splitting algorithm forces an artificial accumulation of charged particles. Thus, prior to the first current peak, the axial profile of electron density at $t = 5$ µs of Figure 3.10 (c) shows that electrons are piling up in the ionization zone. Most electrons originate from merging processes between other electrons created by ionization and injected at the cathode line. Only a small fraction of electrons have been split near the anode. This accumulation suggests that merging-splitting processes delay the convection of charged particles by the Lorentz force. As a result, when convection does occur, the measured exiting current is higher than in the reference case as noticed in Figure 3.10 (a). When no merging-splitting algorithm is used, the

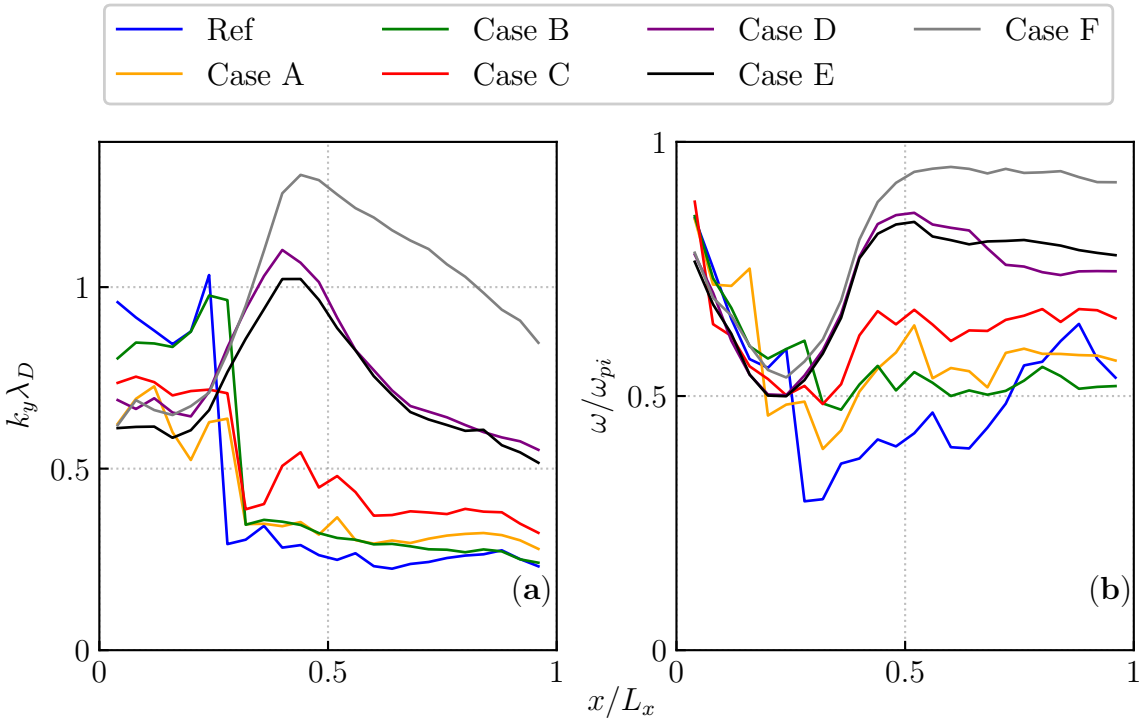

Figure 3.9: Comparison of spectral analysis over the 16-20 µs range obtained with different parameters of the merging-splitting algorithm: (a) normalized azimuthal wavenumber number $k_y\lambda_D$ and (b) normalized frequency ω/ω_{pi}

axial density profile at $t = 5\,\mu s$ shown in Figure 3.10 (b) has a lower maximum. In fact, a similar accumulation of particles takes place but earlier, starting around 1 µs and in smaller proportions. Note that the present decomposition of density profile according to the electron origins (ionization and cathode injection) is similar at steady state. Thus, Figure 3.10 (b) shows how cathode electrons travel upstream and get mixed with electrons generated by ionization near the anode.

Overall, it appears that transients are severely affected when the merging-splitting algorithm is activated, including in cases that retrieve reasonably well the steady state. A possible explanation lies in the fact that the algorithm can modify the velocity distribution function. In Figure 3.10 (d-e) are presented the axial velocity distributions of electrons along the axial direction after 50,000 iterations. The core of the distributions is visually the same but Figure 3.10 (e) indicates merging-splitting processes have artificially spread the distribution towards higher v_x values. Thus, Case B is initialized as if the electron temperature, measuring the spread of the distribution, was higher. At steady state, both distributions eventually look similar but numerical heating was nevertheless introduced, which was noticed in the axial temperature profiles in Figure 3.8 (c).

As an intermediate conclusion, Case B, which reached a similar steady state as the reference case, was nevertheless quite different during the transient because the merging-splitting algorithm introduced numerical errors, that can be seen in the velocity distribution function. In this parametric study, the algorithm controls the number of particles every $f_t = 10$ iterations, during the whole simulation. Thus, in the first 50,000 iterations, the algorithm was applied 5,000 times, which represents as many opportunities to introduce numerical errors. Besides, using so intensively the algorithm from the beginning of the simulation is probably excessive.

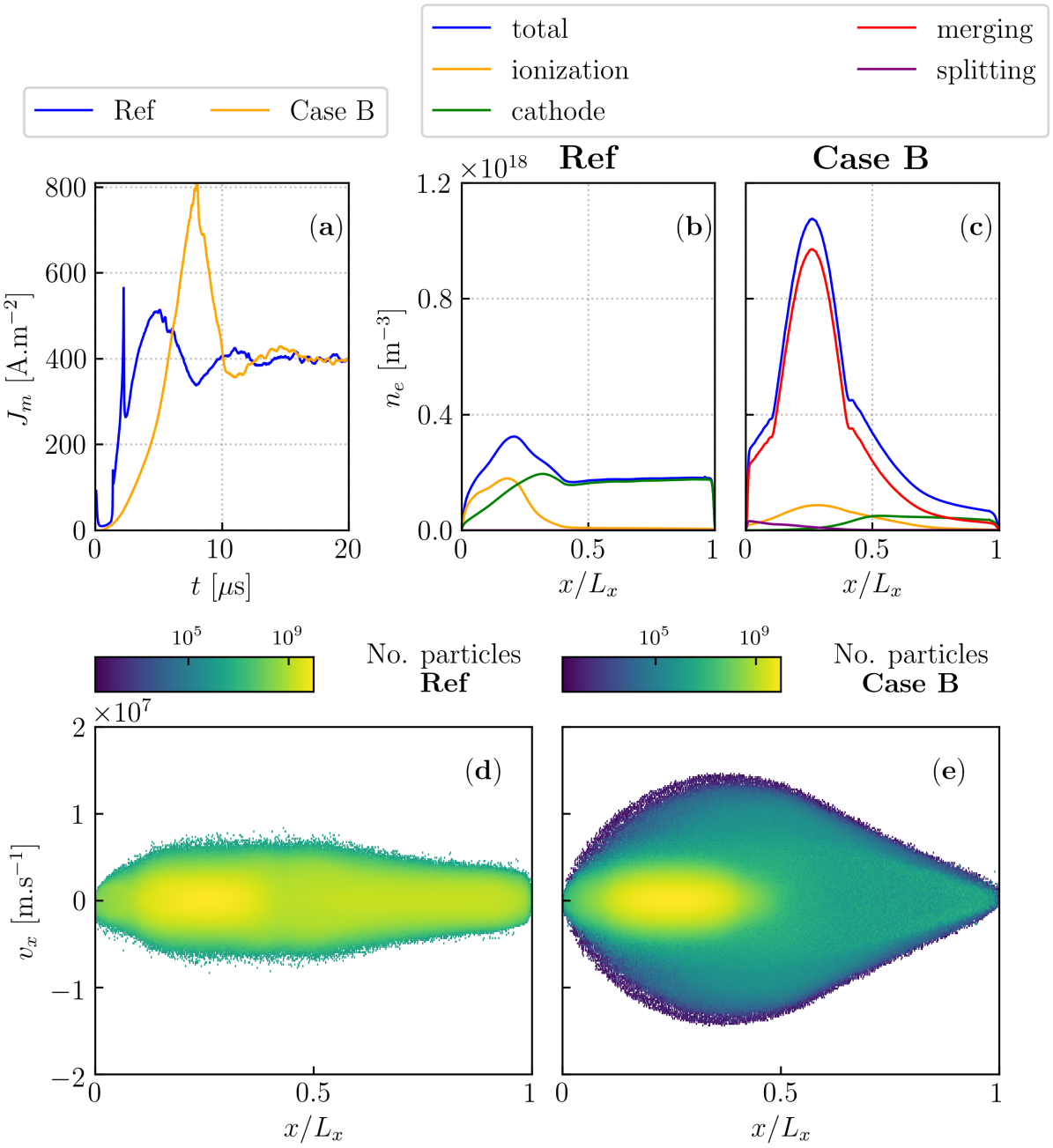

Figure 3.10: Comparison of transients between the reference case and case B. (a): temporal evolution of exiting current density J_m. (b-c): axial profile of electron density n_i for the reference case and case B respectively at $t = 5\,\mu s$. The composition of the total density in blue is detailed according to whether electrons stem from ionization, cathode, merging or splitting. (d-f): axial velocity distribution of electrons along the axial direction at $t = 0.25\,\mu s$ for the reference case and case B, respectively.

Indeed, the algorithm is primarily intended to control a sudden increase of numerical particles. In the reference case, the number of numerical particles starts increasing around 1 µs. So, using the algorithm in first moments of the simulation is probably useless or it can even introduce error in the distribution function as in Figure 3.10 (e). As a result, we should not only tune the usage frequency f_t, but also activate the algorithm only when it is necessary.

3.3.5 Toward a better use of the merging-splitting algorithm

Building upon the parametric study, an attempt was made to correct the discrepancies observed during the transient. To do so, a final set of parameters has been tested on the axial-azimuthal setup. For this case we use $T_{\mathbf{x}} = 10^{-1}$ and $T_{\mathbf{v}} = 10^{-2}$ as for the Case B, which seems good values for the physics of HTs.

In order to mitigate numerical errors, the usage frequency f_t is increased so that the algorithm will be applied only a few times during one average time range N_a. For this example we set $f_t = 1000$ iterations. Besides, the algorithm is activated from $t = 1\,\mu s$, which corresponds to the moment when the reference case experiences a strong increase of particles density in the ionization zone. By doing so we ensure the same initial conditions are used as in the reference case.

During the parametric study, it also appeared that the statistical convergence could be an issue. In order to keep a number of particles high enough while still performing merging processes we decided to use the same initial number of particles as in Case 1 from Table 3.1. Therefore, the simulation starts with twice the number of particles as the reference case, which is Case 2, and the ionization source term injects twice as many particles. With such a choice we place ourselves in a concrete application of the merging-splitting algorithm: keeping the minimal number of numerical particles with the correct physics. In order to choose the target number N_t accordingly, we can use Figure 3.7 (a-b). For the reference case, that is statistically converged, $N_{ppc,fin}$ varies between ~ 100 and 270 in most of the domain. Therefore $N_t = 150$ seems to be a good choice since the algorithm will attempt to split or merge particles if N_{ppc} falls in the $[-N_t/2; 2N_t]$ interval. The algorithm will still actively reduce the number of particles since $N_{ppc,fin}$ lies within ~ 200 and 540 for Case 2.

In Figure 3.11 we present a comparison between the reference case and the improved merging-splitting case.

In Figure 3.11 (a), it can be seen that in spite of using the merging-splitting algorithm, both transients are extremely similar throughout the simulation. This indicates the artificial density increase in the ionization zone observed in Case B has been eliminated.

In Figure 3.11 (b), we assess how well the instability is captured with the improved MS case. Downstream, in zone (II), both cases exhibit an excellent agreement, that is better than with Case B. Upstream, in zone (I) the fit is not as good but remains satisfactory. The transition between zone (I) and zone (II) is well recovered.

The main plasma parameters such as density and temperature are also very similar but we present only one macroscopic quantity in Figure 3.11 (c-d): the azimuthal electric field E_y. Both 2D maps look very similar overall. As it was already hinted by Figure 3.11 (b), the instability in zone (I) does not look as neat with the merging-splitting algorithm and it even seems more grainy. This observation might suggest that small structures like in zone (I) are more difficult to resolve with the algorithm, in spite of being less intrusive.

Overall, the steady state and transients are well retrieved by the merging-splitting algorithm. Small discrepancies remain in the zone (I) but one should also note that the number of numerical particles has been reduced by 30% with respect to Case 1. Furthermore, the elapsed time to run the simulation up to $20\,\mu s$ has been cut by $\sim 20\%$. For this particular case, the gain remains modest but it could be more important if collisions were taken into account.

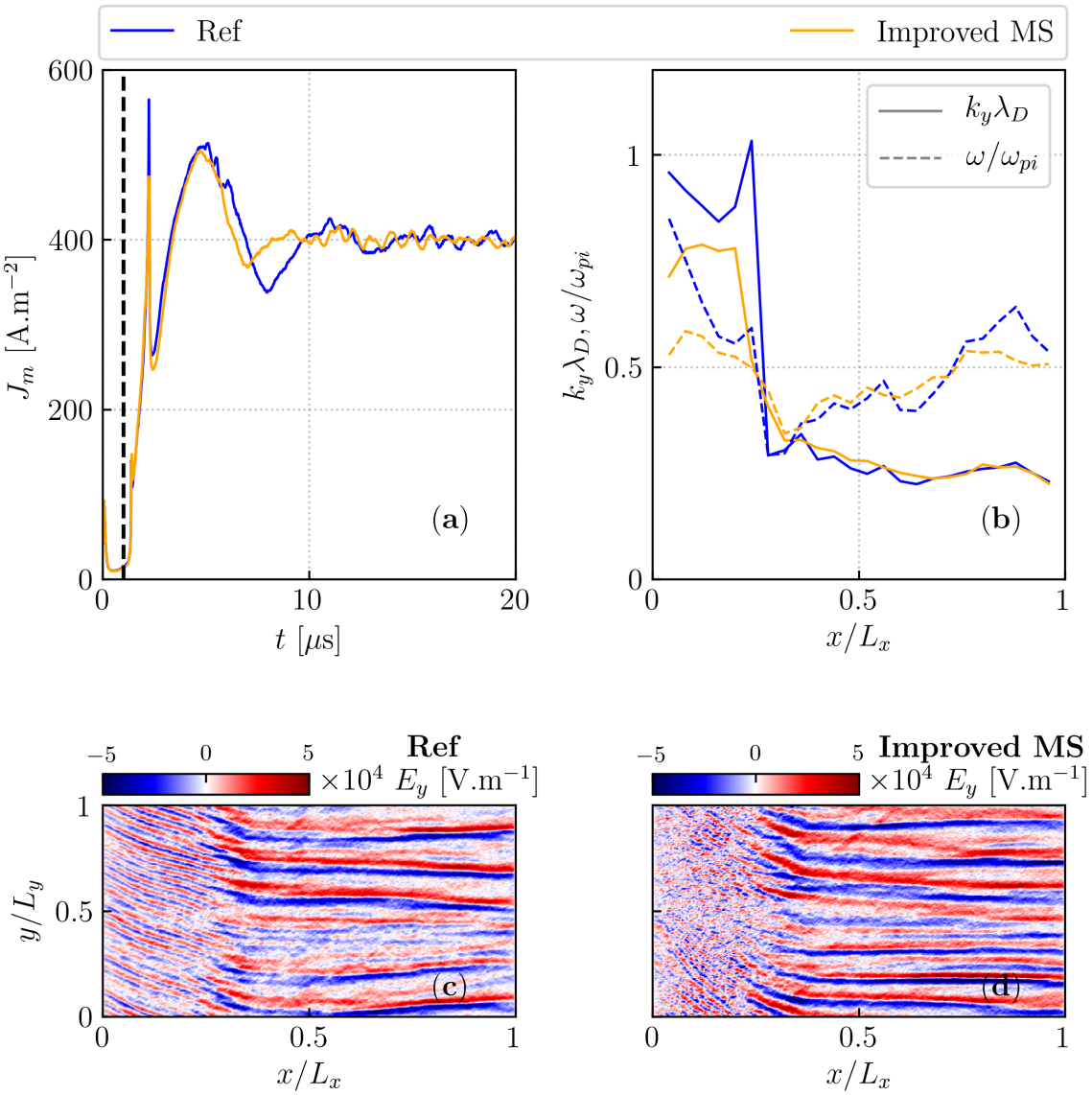

Figure 3.11: Comparison of the reference case and the improved splitting-merging case, denoted by MS. (a): transients of exiting current density J_m. The dashed black line indicates when the merging-splitting algorithm is activated. (b): normalized axial profiles of main azimuthal wavenumber k_y and man pulsation ω. (c-d): final azimuthal electric field E_y for the reference case and improved MS case, respectively.

3.4 Conclusion

In this chapter, we have presented the implementation of a 2D axial-azimuthal model in AVIP. The axial-azimuthal plane is ideal to study the electron transport across the magnetic barrier. Indeed, it was found that classical theory was unable to explain the actual axial electron transport which turned out to be much higher [Meezan et al., 2001]. Among possible explanations, one stands out and proposes that an azimuthal instability, the ECDI, could enhance the electron transport [Lafleur and Chabert, 2017; Charoy, 2020].

The implemented 2D axial-azimuthal model makes several simplifications such as ignoring collisions or imposing an ionization source term but it is sufficient to retrieve the ECDI as

predicted by the theory Lafleur et al. [2016a,b]. Within the framework of an international benchmark, AVIP could successfully retrieve the same averaged plasma quantities and the same azimuthal instability as seven other independent PIC codes [Charoy et al., 2019].

Another advantage of the current 2D axial-azimuthal model is that it provides a configuration for which new numerical methods can be developed and tested. Thus, the particle control algorithm through merging and splitting, presented in Section 2.6.1 can use this 2D setup as a suitable test case in order to estimate the appropriate values for its four input parameters $T_{\mathbf{x}}$, $T_{\mathbf{v}}$, N_t and f_t. These four parameters are case dependent but one can expect they remain similar for simulations capturing the representative physics of HTs. Because running the 2D axial-azimuthal simulation is nevertheless costly and needs at least several days to complete, the tolerances $T_{\mathbf{x}}$, $T_{\mathbf{v}}$ were first explored with the simpler 1D benchmark for plasma discharges from Turner et al. [2013]. This preliminary study indicated $T_{\mathbf{x}}$, $T_{\mathbf{v}}$ of the order of 10^{-1} and 10^{-2} respectively were good candidates. It also hinted that the algorithm was quite sensitive to the speed tolerance in particular. From this quick overview, a reduced number of sets of $T_{\mathbf{x}}$, $T_{\mathbf{v}}$ and N_t was tested in the 2D axial-azimuthal setup to confront the algorithm capability to capture the multidimensional and complex physics of HTs. When studying the statistics, it appeared the algorithm was able to reduce the number of particles in all cases but not always able to reach the target interval $[-N_t/2; 2N_t]$. Interestingly ions and electrons did not react the same way to the algorithm which suggests using different tolerances for charged particles could be considered. The analysis of the main plasma parameters (n_i, E_x, T_e) and the ECDI features (ω/ω_{pi}, $k_y\lambda_D$) confirmed that $T_{\mathbf{x}}$, $T_{\mathbf{v}}$ of the order of 10^{-1} and 10^{-2} were good picks for the simulation but also revealed the choice of the target parameter N_t was important. However, the transients were found to be significantly different because the velocity distribution function was severely modified. Such an effect could eventually be mitigated by adjusting the algorithm frequency f_t and by activating the algorithm only when the number of particles increases.

Overall it seems using $T_{\mathbf{x}} = 10^{-1}$, $T_{\mathbf{v}} = 10^{-2}$, $f_t = 1000$ leads to quite accurate results while reducing the number of particles. The N_t parameter should be set such that the statistical convergence is ensured. For 2D simulations, this number is probably around 200 per square cell [Charoy et al., 2019; Villafana et al., 2021]. A statistical convergence study will be presented in Chapter 5 for a 3D case. The parametric study has revealed the merging splitting algorithm should be used with great care. Therefore we recommend to activate it only when the Lagrangian kernel dramatically slows down the calculation. One inherent difficulty with the algorithm is that the current position and speed tolerances cannot be easily conceptualized and related to a degree of accuracy. For instance, it would be much more convenient to have a parameter representing the loss of accuracy accepted by the user with respect to the unmodified velocity distribution function. A final remark concerns the effect of the splitting processes. In the current setup, they did take place but at lower levels in comparison to merging processes. Indeed, no plasma expansion occurs here and therefore a better insight of their impact would be seen in a 2D radial-axial or in a 3D setup including the plume.

Chapter 4

Validation in a 2D $r - \theta$ setup

In the previous Chapter, a rigorous verification was given to a 2D axial azimuthal setup and useful insights on the ECDI and the plasma dynamics could be obtained. However, plasma wall interactions were therefore discarded whereas they can have an important impact on the physics and trigger the Modified-Two-Stream-Instability (MTSI) that can be coupled with the ECDI Janhunen et al. [2018b]; Héron and Adam [2013]. Therefore, as a continuation of the LANDMARK project, we propose a representative simulation test-case of $\mathbf{E} \times \mathbf{B}$ discharges accounting for plasma wall interactions with the presence of both the Electron Cyclotron Drift Instability (ECDI) and the Modified-Two-Stream-Instability (MTSI). Seven independently developed Particle-In-Cell (PIC) codes have simulated this benchmark case, with the same specified conditions. The characteristics of the different codes and computing times are given. Results show that both instabilities were captured in a similar fashion and good agreement between the different PIC codes is reported as main plasma parameters were closely related within a 5% interval. The number of macroparticles per cell was also varied and statistical convergence was reached. Detailed outputs are given in the supplementary data, to be used by other similar groups in the perspective of code verification.

This Chapter is a slight adaptation of published work [Villafana et al., 2021] and starts by a literature review on this topic in Section 4.1. In Section 4.2, the numerical setup is defined. In Section 4.3, AVIP PIC will detail what happens during the simulation and confirm the presence of both the MTSI and ECDI thanks to theoretical results stemming from linear theory of instabilities. In Section 4.4, the seven independent PIC codes participating in this benchmark are presented along with a cross comparison of all groups. A particular attention is also given to the statistical convergence and shows similar results as in the previous Chapter.

Contents

4.1 Literature review on plasma wall interactions and the MTSI . . . 117

4.2 Methodology and numerical setup 119

4.2.1 Numerical setup 119

4.2.2 Virtual axial model 121

4.2.3 Ionization 122

4.3 Results for the reference case with the code by CERFACS 122

4.3.1 Simulation timeline . . . 123
4.3.2 Spectral characteristics of the instabilities . . . 125
4.4 Benchmark results . . . 127
4.4.1 Code presentations . . . 127
4.4.2 Code comparisons . . . 129
4.4.3 Comparison of main plasma parameters . . . 131
4.4.4 ECDI-MTSI coupling . . . 131
4.4.5 Statistical convergence . . . 134
4.5 Conclusion and prospective . . . 135

4.1 Literature review on plasma wall interactions and the MTSI

Many devices, such as HTs [Goebel and Katz, 2008; Smirnov et al., 2006; Boniface et al., 2006] and magnetron discharges [Tsikata and Minea, 2015; Boeuf and Chaudhury, 2013] operate in the regime of partially magnetized $\mathbf{E} \times \mathbf{B}$ plasmas. Though it is generally understood that plasma fluctuations are responsible for the enhanced electron transport, typically larger than what would be expected from the classical collisional theory [Meezan et al., 2001], the exact nature of the instabilities resulting in anomalous electron current is not fully understood. A recent overview of different mechanisms of the instabilities and their interactions can be found in [Kaganovich et al., 2020].

One such mechanism is the Electron Cyclotron Drift Instability (ECDI) or Electron Drift Instability (EDI) driven by the $\mathbf{E} \times \mathbf{B}$ electron drift, as mentioned in Section 1.3.2. Over the past decade, this instability has attracted an intense interest as an important source of the anomalous transport in Hall thruster [Adam et al., 2004b; Héron and Adam, 2013; Lafleur et al., 2016a,b; Boeuf and Garrigues, 2018]. As a reminder, the instability occurs for the wave propagating in the $\mathbf{E} \times \mathbf{B}$ direction, perpendicular to the magnetic field. When the wave can also propagate along the magnetic field lines, it may trigger another kind of instability: the Modified Two-Streams Instability (MTSI). Finite value of the electric field perturbation along the magnetic field results in significant electron heating in this direction [Krall and Liewer, 1971; Hastings and Niewood, 1989]. Overall, it may result in comparable electron and ion heating [McBride et al., 1972], but in different directions. The unmagnetized ions are primarily heated up in the $\mathbf{E} \times \mathbf{B}$ direction, whereas electron heating occurs along $\mathbf{B}$. Such anisotropic heating may have important consequences for $\mathbf{E} \times \mathbf{B}$ discharges. For instance, in the case of magnetically shielded HETs, ion heating might increase the erosion near magnetic poles because of local magnetic field lines parallel to the walls [Mikellides and Ortega, 2020]. In a non-magnetically shielded HET, the magnetic field lines are essentially radial at the channel exit and so the electron heating along $\mathbf{B}$ tends to enhance the flux toward the walls [Sengupta and Smolyakov, 2020]. As a consequence, secondary electron emission (SEE) might increase [Taccogna et al., 2019]. Although SEE has a modest impact on electron transport [Garrigues et al., 2006], it might lead to other sheath instabilities [Sydorenko et al., 2008; Tavant et al., 2018].

The nonlinear coupling of ECDI and MTSI in the presence of plasma-wall interaction poses significant challenges to correctly evaluating the transport properties. The analytical treatment

of the kinetic equations provides useful insights but remains difficult to conduct [Lafleur et al., 2016b; Krall and Liewer, 1971]. Thus, it is common to study them numerically with PIC simulations. These instabilities are intrinsically multidimensional, so 2D or 3D simulations are required [Tsikata et al., 2010]. Unfortunately, most of the time, 3D simulations remain computationally too costly. For instance, only Taccogna and Minelli [2018] have captured both the ECDI and the MTSI in 3D PIC simulation using geometrical scaling factors. Recent progress on 3D PIC simulations are also reported in Chapter 5. As of today, most of the PIC simulations of $\mathbf{E}\times\mathbf{B}$ discharges are performed in 2D. In particular, radial azimuthal simulations are appropriate to study the effects of the plasma-wall interaction in HETs. Geometrical effects play a key role in this configuration since the curvature at the walls was found to greatly affect SEE yields, that can be coupled with the ECDI [Héron and Adam, 2013]. The setup can be further simplified by neglecting curvature effects while still providing relevant physics insights. By using a Cartesian grid, Croes et al. [2017] could verify that the ECDI was one important factor explaining electron anomalous transport. Besides, even with no curvature, Tavant et al. [2018] observed a coupling between the ECDI and SEE. Different regimes of sheath saturation were found possible depending on the choice of the wall material.

In 2D PIC simulations, in addition to the ECDI, the MTSI was identified by Janhunen et al. [2018b] and observed in Petronio et al. [2021]. Similarly, Hara [2019] have found the typical radial patterns resembling the MTSI. It was found in [Janhunen et al., 2018b] that the ECDI and MTSI had the expected two dimensional structure and that both instabilities seemed coupled demonstrating an inverse cascade towards the long wavelengths azimuthally and showing radial structures in the axial current. However, this study was limited to the first microseconds of simulation due to strong electron heating, partially amplified by the absence of the heating saturation mechanism in the simulations. Indeed, in order to capture the appropriate physics, a 2D3V radial-azimuthal simulation setup uses an off-plane axial electric field to maintain a $\mathbf{E}\times\mathbf{B}$ cross-drift current in the azimuthal direction. Therefore, with periodic boundary conditions in the azimuthal direction, the energy of particles keeps increasing in time due to the imposed axial electric field. This is not the case in a real HET with a finite length between the anode and cathode. One way to circumvent this difficulty and mimic the finite axial length of the discharge is to use a virtual axial length model in the axial/off-plane direction [Boeuf, 2017; Lafleur et al., 2016b]. In this model, the axial displacement of particles is tracked and particles are replaced with cold ones after having traveled the distance corresponding to the effective length of the discharge.

The re-injection of particles however has to be handled carefully. For example, Tavant [2019] showed that the use of a virtual axial model with random position re-injection effectively results in large numerical instabilities, which can dramatically impact the simulation results. This drawback has already been observed in 1D-azimuthal simulations [Lafleur et al., 2016a; Asadi et al., 2019; Smolyakov et al., 2020].

Therefore, PIC simulations in the radial-azimuthal plane remain intricate and require a careful analysis of the physics mechanisms of the instabilities as well as a careful treatment of numerical issues. We note here that, in spite of constant progress, the current time and spatial resolution of experimental measurements in $\mathbf{E}\times\mathbf{B}$ discharges in HET conditions do not allow a detailed validation of the different instabilities observed in simulations [Kaganovich et al., 2020].

At this stage, the verification of the physics and numerical implementations are important to provide confidence in the numerical results via code benchmarking, i.e. performing a code-to-code comparison. As a result, as part of the LANDMARK project, and similarly to what

was done in Section 3.2 and [Charoy et al., 2019], we propose a 2D PIC benchmark for the radial-azimuthal plane of a HET. Our goal is, with a relatively simple configuration, to include both the MTSI and the ECDI physics, compare the predictions of seven independent codes, and characterize the nonlinear features of fluctuations and structures arising in simulations. These simulations have been performed by seven independent research groups to provide a reference benchmark for the community.

4.2 Methodology and numerical setup

4.2.1 Numerical setup

For the radial-azimuthal PIC simulations presented in this work, we consider a square 2D Cartesian grid, with square cells, as shown in Figure 4.1. The azimuthal direction y is periodic and the curvature is neglected. In a real HET, a dielectric layer would cover the walls in the radial z direction, but for this benchmark, the simulation domain is instead bounded by two grounded walls with an imposed potential $\phi_0 = 0\,\mathrm{V}$. The time step Δt and cell size $\Delta y = \Delta z$ are chosen to comply to the PIC stability conditions [Birdsall, 1991] from Equations (2.5) and (2.6), that are reminded below,

$$\begin{cases} \Delta y < \frac{\lambda_D}{2}, \\ \Delta t < \frac{0.2}{\omega_{pe}}, \end{cases} \tag{4.1}$$

With $n_e = n_0 = 5 \times 10^{16}\,\mathrm{m}^{-3}$ and $T_e = T_{e,0} = 10\,\mathrm{eV}$, we find $\lambda_D = 100\,\mu\mathrm{m}$, $\omega_{pe} = 1.26 \times 10^{10}\,\mathrm{rad \cdot s}^{-1}$ and we set $\Delta y = 50\,\mu\mathrm{m}$ and $\Delta t = 1.5 \times 10^{-11}\,\mathrm{s}$.

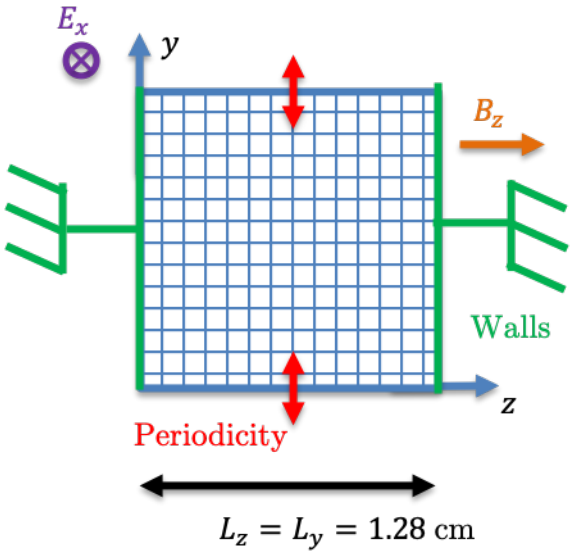

Figure 4.1: 2D radial-azimuthal (z, y) setup.

We consider only electrons and singly charged xenon ions, Xe^+, in a collisionless plasma. Collisions were not accounted for in this work because both the ECDI and MTSI can occur without them [Janhunen et al., 2018b]. Besides, the collisionless assumption makes the simulations running faster, which is advantageous for benchmarking. Initially, the particles are distributed uniformly in the domain with a density $n_0 = 5 \times 10^{16}\,\mathrm{m}^{-3}$ and a velocity sampled

from a Maxwellian distribution at temperature $T_{e,0}$ and $T_{i,0}$, for electrons and ions, respectively. The simulation is initialized with $N_{ppc,ini} = 100$ macroparticles per cells (for each species) which gives approximately $N_{ppc,fin} = 212$ macroparticles per cell at steady-state. We use a constant and uniform radial magnetic field B_z in the radial z direction in addition to an off-plane axial electric field E_x perpendicular to the simulation domain, which produces an $\mathbf{E} \times \mathbf{B}$ current along the azimuthal y direction. The particles reaching the walls are removed from the simulation. The electrons are magnetized, while the ions are not. The diagnostic data are averaged during the computation over $N_a = 1000$ time steps and the output files are generated every N_a. Numerical and physical parameters are summarized in Table 4.1.

Parameters	Symbol	Value	Unit
Simulation domain			
Cell size	$\Delta y = \Delta z$	50	µm
Azimuthal length	L_y	1.28	cm
Radial length	L_z	1.28	cm
Number of cells	N_{cell}	256×256	
Initial conditions			
Plasma density	n_0	5×10^{16}	m^{-3}
Ion temperature	$T_{i,0}$	0.5	eV
Electron temperature	$T_{e,0}$	10	eV
Number of particles/cell	$N_{ppc,ini}$	100	
Physical parameters			
Potential at walls	ϕ_0	0	V
Radial magnetic field	B_z	200	G
Axial electric field	E_x	10	$\mathrm{kV\,m}^{-1}$
Virtual axial length	L_x	1	cm
Computational parameters			
Time step	Δt	1.5×10^{-11}	s
Average time range	N_a	$1000\Delta t$	s
Final time	t_{max}	30	µs

Table 4.1: PIC simulations parameters.

4.2.2 Virtual axial model

Although we perform a 2D simulation of the radial-azimuthal (z, y) plane, in order to retrieve the behavior of an HET, a constant electric field E_x is set in the axial x direction. Note that the Poisson equation is solved only in the (y, z) plane at $x = 0$. As it is, the modeled system would not reach a steady state due to a constant input of energy, as observed in previous PIC studies [Janhunen et al., 2018b; Héron and Adam, 2013]. To reach a steady state, a virtual axial model inspired from 1D azimuthal [Lafleur et al., 2016a; Hara, 2019; Asadi et al., 2019] and 2D radial-azimuthal [Tavant et al., 2018; Croes et al., 2017; Taccogna et al., 2019] simulations is used and shown in Figure 4.2.

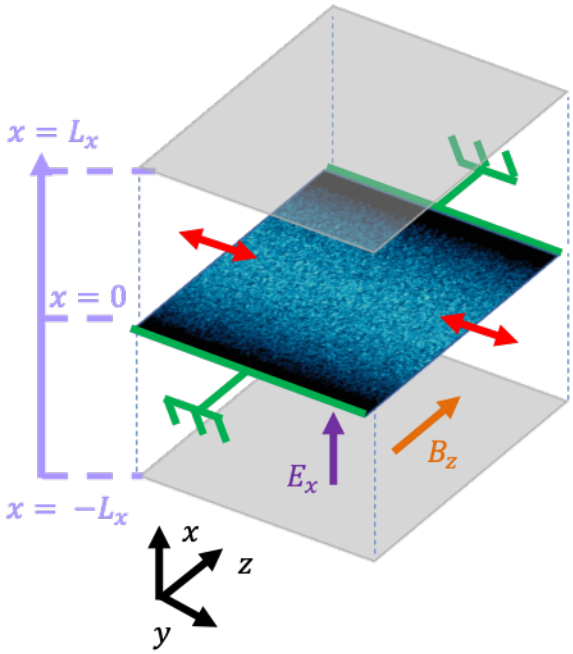

Figure 4.2: Virtual axial model used for the 2D radial-azimuthal simulation. The plasma dynamics take place in the $y - z$ plane.

All particles are initialized in the plane located at $x = 0$. The x location of each particle is updated and monitored whether it reaches the virtual axial boundaries situated at $x = \pm L_x$. The imposed axial electric field accelerates the ions towards the $+L_x$ boundary while the magnetized electrons drift in the azimuthal direction. Although electrons tends to be located in the $x < 0$ space, they gyrate around the magnetic field lines and some may be energetic enough to reach the $+L_x$ boundary.

Any particle crossing the $x > |L_x|$ boundaries is reinjected in the plane at $x = 0$, with the same y and z. The injection velocity is sampled from a Maxwellian distribution at the initial temperatures, $T_{e,0}$ and $T_{i,0}$ for electrons and ions, respectively. In this work, L_x is set to 1 cm. We chose this value to obtain a typical steady state that can take place in a HET. Too small values of L_x refresh velocities too often, which prevents any relevant physical phenomena to develop as the system is constantly reset to its initial state. Too high values of L_x can end up in large electron temperatures ($> 50 - 100$ eV), which is consistent with 1D simulation results [Lafleur et al., 2016a]. As an example, going from $L_x = 1$ cm to $L_x = 2$ cm, increases both the total energy of ions and electrons of $\sim 15 - 20$ eV at steady state.

4.2.3 Ionization

Particle losses at the walls also need to be compensated to reach a steady state. In this work, we consider a collisionless case generating new particles with a constant source term mimicking ionization, as in previous investigations [Hara and Tsikata, 2020; Charoy et al., 2019; Boeuf and Garrigues, 2018]. Similarly to a real HET, the ionization profile is higher in the center of the channel than at the walls. We have assumed the ionization is uniform in the azimuthal direction and that its radial profile is given by

$$\begin{cases} S(z) = S_0 \cos\left(\pi \frac{z - z_M}{z_2 - z_1}\right) \text{ for } z_1 \leq z \leq z_2, \\ S(z) = 0 \text{ for } z > z_2 \text{ or } z < z_1, \end{cases} \tag{4.2}$$

with S_0 the maximum value of the source term and $z_2 - z_1$ the width of the ionization zone. The coordinates z_1 and z_2 are symmetric with respect to $z_M = L_z/2$. The width of the ionization zone is chosen to be 1.1 cm ($\sim 86\% L_z$). The maximum of the ionization profile is chosen to be symmetric with respect to the centerline and its width is chosen considering the typical sheaths' dimensions in HET [Chabert, 2014]. Using the simulation parameters described above, $z_1 = 0.09\,\text{cm}$ and $z_2 = 1.19\,\text{cm}$. At steady state, the total current exiting at the walls must be equal to the current injected into the system by the ionization term. We can calculate the injected current density J_m as

$$J_m = e \int_0^{L_z} S(z) dz = \frac{2}{\pi}(z_2 - z_1) e S_0. \tag{4.3}$$

From Equation 4.3, we enforce the exiting density current to be $100\,\text{A} \cdot \text{m}^{-2}$ by setting the maximum value of the source term: $S_0 = 8.9 \times 10^{22}\,\text{m}^{-3} \cdot \text{s}^{-1}$. For a practical numerical implementation, one should first compute the number $N_{\text{Xe}^+/\text{e}^-}$ of physical pairs of X_e^+/e^- to be injected in the domain at each iteration given by

$$N_{\text{X}_\text{e}^+/\text{e}^-} = L_y \Delta t \int_0^{L_z} S(z) dz. \tag{4.4}$$

The new particles are injected in the plane $x = 0$. The in-plane location (y_i, z_i) of each $N_{\text{Xe}^+/\text{e}^-}$ pair is randomly chosen according to the ionization profile given in Equation (4.2). Explicitly, we used two random numbers R_1 and R_2 between 0 and 1, as

$$\begin{cases} y_i = R_2 L_y, \\ z_i = \arcsin\left(2R_1 - 1\right) \frac{z_2 - z_1}{\pi} + z_M. \end{cases} \tag{4.5}$$

Finally, the velocity of each particle is sampled from a Maxwellian distribution at $T_{e,0}$ and $T_{i,0}$, for electrons and ions, respectively.

4.3 Results for the reference case with the code by CERFACS

In this section, we present in detail the dynamics of the discharge and of ECDI and MTSI instabilities using the code by CERFACS (detailed in section Section 4.4.1).

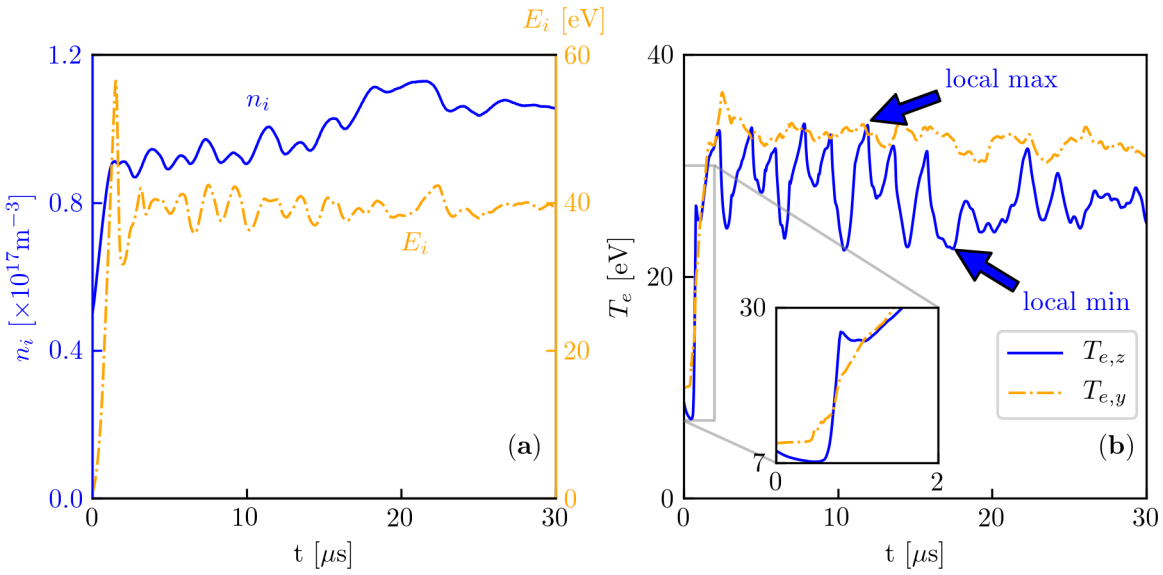

Figure 4.3: **CERFACS code**: Temporal profiles of ion density n_i and total ion energy E_i (a) and radial $T_{e,z}$ and azimuthal $T_{e,y}$ electron temperatures (b). In (a), the left y axis in blue corresponds to n_i and the right one in orange refers to E_i. Blue arrows in (b) indicate local extrema of $T_{e,z}$ at 11.7 µs (max) and 17.5 µs (min).

4.3.1 Simulation timeline

We show in Figure 4.3 the temporal profiles of ion density n_i, total ion energy E_i and electron radial and azimuthal temperatures ($T_{e,z}$ and $T_{e,y}$, respectively). At the beginning of the simulation, for $\sim$ 1 µs, the ion density increases linearly, because of the imposed ionization source term. Ions gain energy under the effect of the axial electric field for $\sim$ 1.5 µs. Then, most of the ions have reached the virtual boundary $L_x = 1$ cm, which brutally dissipates their mean energy. The electron azimuthal temperature $T_{e,y}$ remains at its initial value for 0.5 µs but then it increases by a factor of 3 between 0.5 µs and 1.7 µs. The radial electron temperature $T_{e,z}$ first decreases because the most energetic electrons leave the computational domain. Yet, it eventually sharply rises in 0.2 µs. After $t = 2$ µs, n_i, E_i, $T_{e,z}$ and $T_{e,y}$ reach an oscillatory plateau and only at $t = 17$ µs the oscillations get damped. This situation results in a radial electron temperature drop and in a small increase of ion density. In contrast, E_i and $T_{e,y}$ seem unaffected by the underlying physics and do not experience any clear drop or increase. Finally, after $t = 20$ µs, the oscillations seem to be mostly damped and a steady state is reached. These results show that the constant ionization source term successfully compensates particles losses at the walls and that the virtual axial model prevents an accumulation of energy in the system.

In order to understand more precisely the discharge behavior, we focus on specific times of interest. 2D snapshots of relevant parameters are displayed in Figure 4.4. First, at $t = 0.53$ µs, the azimuthal electric field exhibits a purely azimuthal instability with a wavelength of the order of 800-900 µm. Another instability, with both radial and azimuthal components has a lower growth rate and develops $\sim$ 0.2 µs later, as noticeable at $t = 0.75$ µs, and also revealed in the axial electron current. Janhunen et al. [2018b] identified these instabilities as the ECDI and the MTSI, respectively. The numerical evidence of two instability mode coexistence and their characteristics will be discussed in detail later. Interestingly, the radial electron current only contains the azimuthal component of the MTSI. The growth of the MTSI actually coincides

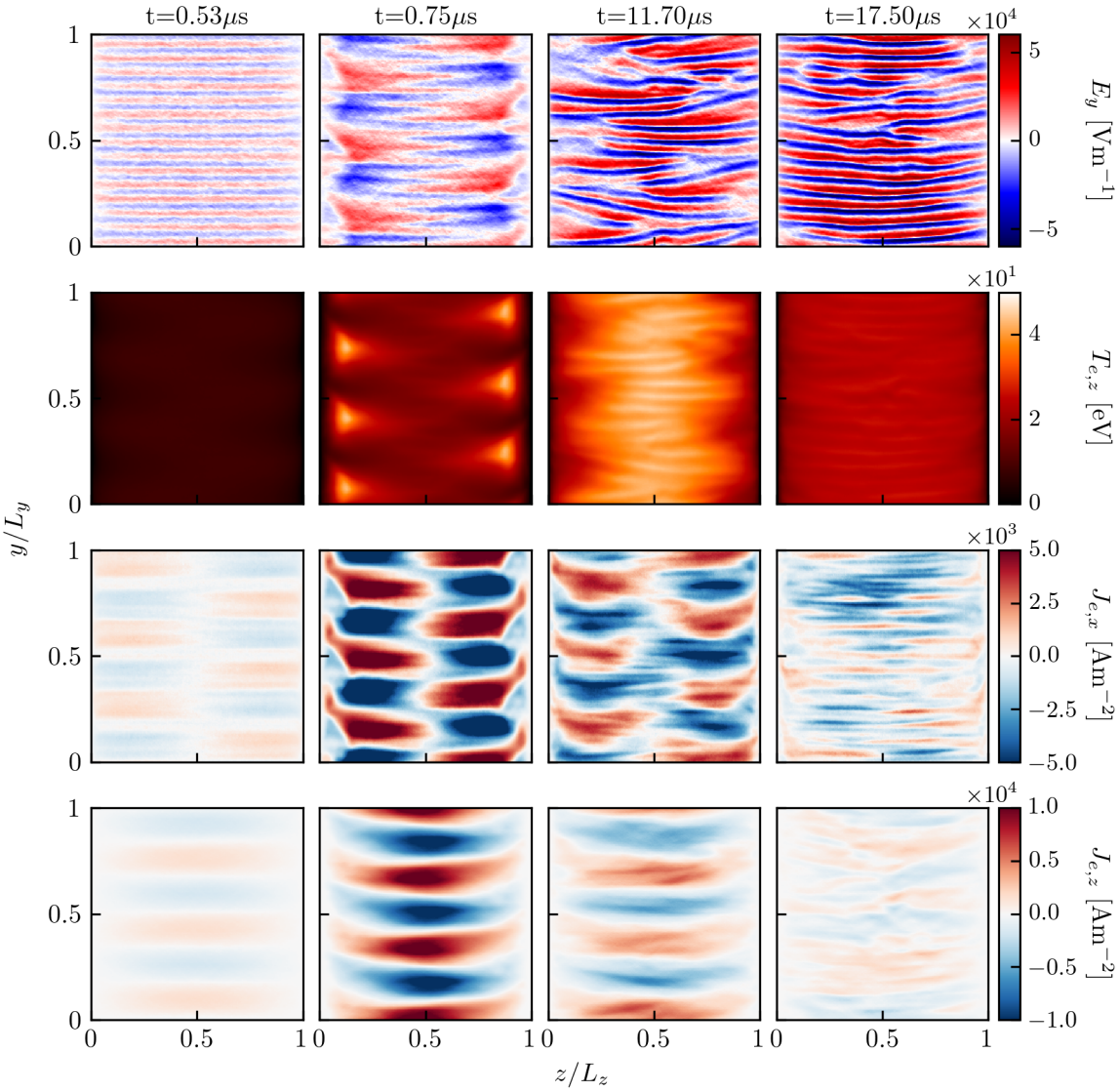

Figure 4.4: **CERFACS code**: 2D snapshots of azimuthal electric field E_y, radial electron temperature $T_{e,z}$, axial electron current $J_{e,x}$ and radial electron current $J_{e,z}$ at times $t = 0.53\,\mu s$, $t = 0.75\,\mu s$, $t = 11.70\,\mu s$ and $t = 17.50\,\mu s$. Local extrema of $T_{e,z}$ shown in Figure 4.3 correspond to times $t = 11.70\,\mu s$ and $t = 17.50\,\mu s$.

with the significant increase of the radial electron temperature $T_{e,z}$ observed in Figure 4.3. The 2D snapshots show that the electrons first heat up in the near-wall sheath at periodic locations in the azimuthal direction, which was also clearly observed in [Janhunen et al., 2018b]. In the present simulation, the azimuthal wavelength is around 4 mm while only a half-wavelength fits in the radial direction with a radial wavenumber $k_z = \pi/L_z$. The fast radial electron temperature increase enhances the loss of particles, which explains why the density stops growing linearly, as already noticed in temporal profiles in Figure 4.3. Moreover, these 2D snapshots can be related to the oscillations observed in the temporal profiles. Indeed, the system oscillates between two distinct states: the first one is seen at $t = 11.7\,\mu s$ when the MTSI is strong with well defined radial-azimuthal patterns. As a consequence, electrons heat up, which generates a local maximum of the radial electron temperature. Thus, particles leave the domain and the

density starts decreasing. The second state is seen at $t = 17.5\,\mu s$ with a local minimum of the temperature related to a mitigated MTSI. Thus particles tend to fill the domain, leading to a density increase.

4.3.2 Spectral characteristics of the instabilities

In this section, we provide more information on the spectral characteristics of the instabilities described in the previous section which clearly identify them as ECDI and MTSI. The ECDI is driven by the overlapping beam mode and cyclotron resonances [Lashmore-Davies and Martin, 1973; Lampe et al., 1971b] so the resonant condition in 2D is

$$k_y \approx m\frac{\Omega_{ce}}{v_0}, \text{ with } m = 1, 2, ... \tag{4.6}$$

where $v_0 = E_x/B_z$ is the electron drift velocity in the azimuthal direction and Ω_{ce} is the electron cyclotron frequency. Its discrete character as harmonics of the fundamental mode $k_0 = \Omega_{ce}/v_0$ has been observed in a number of simulations [Muschietti and Lembege, 2013; Janhunen et al., 2018b,a]. The MTSI is a long wavelength 2D instability typically with a characteristic wavenumber $k_y \ll k_0$ [Lashmore-Davies and Martin, 1973; Janhunen et al., 2018b]. We note also that its growth rate is smaller than that of the ECDI. Despite its lower growth rate, it becomes very pronounced in simulations at later stages [Janhunen et al., 2018b].

In the present work, we perform a spectral analysis using the Fast Fourier Transform (FFT) function from the Python package Numpy. In Figure 4.5, we present a spectral analysis of the results obtained in the previous section. In Figure 4.5 (a), the 2D FFT on the azimuthal electric field at $t = 0.4\,\mu s$ shows that the simulation starts with three discrete modes. Two of them have no radial component and only have an azimuthal wavenumber multiple of k_0. They correspond the first two ECDI resonances according to Equation (4.6). The last one has a wavenumber $k_y \sim 0.2k_0$ below the first ECDI resonance and a non-zero radial wavenumber. This mode was identified theoretically consistent with MTSI, as described by Janhunen et al. [2018b]. As noted in previous investigations [Barrett et al., 1972; Chen, 1965], plasma sheath effects make possible the existence of shorter wavenumbers below the geometrical constraint $k_z = 2\pi/L_z$. In the present work, the radial wavenumber of the MTSI $k_z \approx \pi/L_z$ ($k_z\lambda_D \sim 2.19 \times 10^{-2}$) corresponds to a half wavelength between the walls, which agrees with results obtained by Janhunen et al. [2018b].

In Figure 4.5 (b-c), we show temporal profiles for the MTSI and the first ECDI resonance. These profiles have been obtained by performing first a 1D FFT in the azimuthal direction at each radial location, then inferring a mean FFT profile in the azimuthal direction and then finally repeating this process for every output file, distinguishing each FFT coefficient.

From Figure 4.5 (b), we identify the linear stage for both instabilities, that is $\sim$ 0.3-0.73 µs for MTSI and 0.3-0.50 µs for the first resonance of ECDI. During this period, the growth is driven by the exponential factor $\exp\{(2\gamma t)\}$ and the growth rate γ can be obtained from a least square method. As noted by Janhunen et al. [2018b], the ECDI has a faster growth rate than the MTSI, except that here, the MTSI does not start growing after the ECDI saturation. In order to get further confidence in the numerical results, we can compare PIC measurements with theoretical results given by the linear dispersion relation $\omega(\mathbf{k})$, assuming cold ions [Cavalier et al., 2013],

$$1 + k^2\lambda_D^2 + \frac{\omega - \mathbf{k}\cdot\mathbf{V_d}}{\sqrt{2}k_z\rho\omega_{ce}}e^{-b}\sum_{m=-\infty}^{\infty} Z\left(\frac{\omega - \mathbf{k}\cdot\mathbf{V_d} - m\omega_{ce}}{\sqrt{2}k_z\rho\omega_{ce}}\right) I_m(b) - \frac{k^2\lambda_D^2\omega_{pi}^2}{(\omega - k_x v_p)^2} = 0, \tag{4.7}$$

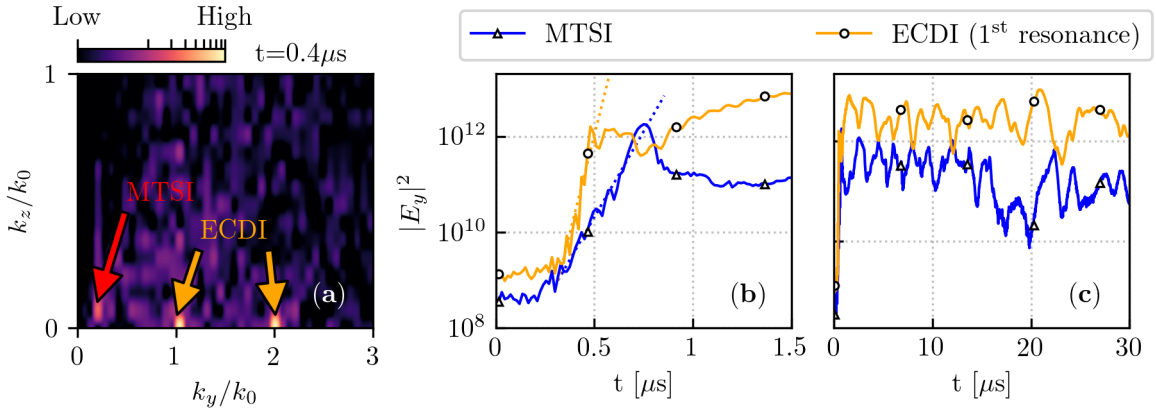

Figure 4.5: **CERFACS code**: Spectral analysis of the azimuthal electric field E_y. (a) 2D FFT at linear stage when both ECDI and MTSI start developing. (b) and (c) temporal evolution of the amplitude of the MTSI and ECDI modes in the E_y spectrum. The amplitude has been integrated over k_z components. In (b) the dotted lines mark the linear growth of the modes obtained from a least-square method.

where k_x, k_y, k_z are the components of the wavevector $\mathbf{k}$, $b = k_\perp^2 \rho_e^2$, $k_\perp^2 = k_x^2 + k_y^2$, $\rho_e^2 = v_{the}^2/\omega_{ce}^2$, $v_{the}^2 = k_B T_e/m_e$, $\lambda_D^2 = k_B \epsilon_0 T_e/n_0 q_e^2$, v_p is the ion beam velocity, $\mathbf{V}_d$ is the electron drift velocity relative to the ions, ω_{ce} is the electron cyclotron frequency, ω_{pi} is the ion plasma frequency, $Z(\xi)$ is the plasma dispersion function, and $I_m(x)$ is the modified Bessel function of the 1st kind. For this 2D case, $k_x = 0$ and the numerical solution of this relation was achieved through the algorithm developed by Cavalier et al. [2013] via a fixed point iteration. The theoretical solver was employed using simulation data from 0.4 µs, the time just before the linear growth stage of the instabilities, for which $n_e = 6.37 \times 10^{16}\,\mathrm{m}^{-1}$ and $T_e = 9.19\,\mathrm{eV}$. The theoretical growth rates are compared with PIC measurements in Figure 4.6.
From the theoretical dispersion relation, at $k_z\lambda_D = 2.19 \times 10^{-2}$, MTSI should feature a resonance at $k_y\lambda_D = 0.127$, and ECDI should feature a first resonance at $k_y\lambda_D = 0.714$. Overall, both azimuthal wavenumbers and maximum growth rates are in excellent agreement with the instabilities seen in the simulation during the linear stage of growth. This suggests that the initial diffusion toward the radial walls sets up a finite-k_z mode, and the MTSI seen in this study is initiated by this plasma-wall interaction.

At the end of its linear stage, Figure 4.5 (b) shows that the MTSI is briefly stronger than the ECDI around $t = 0.75$ µs, which is coherent with radial-azimuthal patterns appearing in the 2D snapshots at the same time on Figure 4.4. From Figure 4.5 (c), it is interesting to notice that the ECDI seems to get weaker when the MTSI strengthens, suggesting that both are coupled. Moreover, we count ten clear peaks in the MTSI FFT temporal profile that precede the same number of radial temperature peaks in Figure 4.3 (b). Thus, it seems the MTSI drives $T_{e,z}$, which is consistent with observations made on the 2D snapshots in the previous section. Between $t = 15 - 20$ µs, the MTSI is significantly damped, which coincides with the observed increase of density in Figure 4.3 (a). At steady state, between $t = 25 - 30$ µs, the MTSI stabilizes at a lower level than in the first 10 µs of the simulation. It is not clear why the level is lower and what caused the initial damping in the $15 - 20$ µs time range. Necessary investigations will be left for a future work.

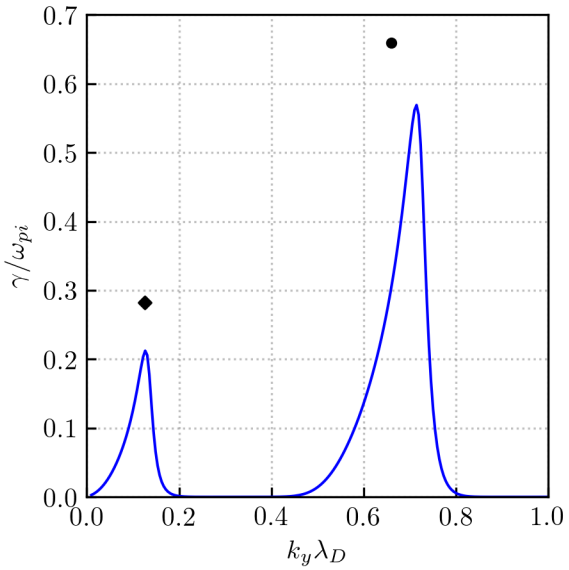

Figure 4.6: Theoretical growth rates, obtained from Stanford and USASK, using simulation values at the beginning of the linear stage when both ECDI and MTSI start developing for $k_z\lambda_D = 2.19 \times 10^{-2}$, set up by the plasma diffusion toward the walls. Symbols represent PIC measurements for MTSI (diamond) and first ECDI resonance (circle) from Figure 4.5.

4.4 Benchmark results

4.4.1 Code presentations

Seven independent research groups have participated to this benchmark. No code is open source and a detailed description of each of them is provided below.

CERFACS

The PIC variant of AVIP was used for this work. AVIP [Joncquieres et al., 2018; Joncquieres, 2019] is a 3D unstructured-grid plasma solver aimed to handle massively parallel computations. It was developed from AVBP, a well-known fluid solver for reactive gases in industrial geometries [Gicquel et al., 2011; Schonfeld and Rudgyard, 1999]. Written in Fortran 90, the code features parallelization with MPI and demonstrates excellent computational performances at high number of processors [Gourdain et al., 2009]. For the present simulations, the computational domain consists of square cells sliced into two isosceles right-angled triangles. Therefore the mesh has twice as many cells as the other groups. Displacement of particles is performed by the Haselbacher algorithm [Haselbacher et al., 2007] and no subcycling is used. Random numbers are generated with the built-in function of Fortran 90 with a hard-coded seed to make runs deterministic. Electrons and ions speeds are respectively updated by the standard Boris and leap-frog schemes. Domain decomposition relies on the external library PARMETIS [Karypis and Kumar, 2009] and it is updated if excessive load unbalance is detected among the processors. The in-plane potential is self-consistently calculated with the Poisson solver MAPHYS developed by INRIA [Agullo et al., 2017; Poirel, 2018] that will soon be available in the PETSc library.MAPHYS returns the potential with an accuracy of the second order and the electric field is computed with a second order accurate Green-Gauss formulation. Double floating point

precision is used in the code. AVIP-PIC was verified with the 1D discharge benchmark of Turner et al. [2013] and the 2D axial-azimuthal benchmark of Charoy et al. [2019].

LPP

The 2D3V particle-in-cell code used in the present work is *LPPic*. This Fortran90 code uses a structured Cartesian mesh and is parallelized using MPI domain decomposition. The initial distribution of particles is obtained using a random number generator seed provided by the internal clock of every CPU. All numerical variables are double precision floating points. The Poisson equation is solved using the PFMG solver of the open-source Falgout and Yang [2002] library. The potential is obtained with a second order accuracy, while the electric field is calculated from the plasma potential by a centered difference scheme with first order accuracy. The classical leap-frog and Boris schemes are used to move the particles. The code has been verified using the 1D He benchmark by Turner et al. [2013] and the 2D axial-azimuthal benchmark by Charoy et al. [2019].

USASK

The code is a 2D3V PIC based on the explicit leap-frog algorithm. The code uses the Boris scheme to solve particle motion equations. To reduce numerical cost, subcycling of electrons relative to ions is applied [Adam et al., 1982]. The random number generator is the Maximally Equidistributed implementation [Harase, 2009] of Well Equidistributed Long-period Linear generator WELL19937a [F. Panneton et al., 2006]. The 2D Poisson's equation in a rectangular domain periodic in one direction is solved using FFT transformation along the periodical direction, with the FFT procedure based on [Press et al., 2007]. The code is written in Fortran 90 and is parallelized with MPI. The particle processing algorithm of the code combines both domain and particle decomposition. The whole simulation domain is split into subdomains of the same size, the number of the subdomains is several times smaller than the total number of MPI processes. Particles belonging to the same subdomain may be shared between several processes. The balance of particle load between all MPI processes is achieved by changing the numbers of processes advancing particles in the subdomains. Double floating-point precision is used for all calculations in the code.

Stanford

The PIC code is written in C++ using MPI as the means of parallelization. Particle decomposition is used to split the number of macroparticles as evenly as possible between the different processors. Domain decomposition is used by the Poisson solver, Falgout and Yang [2002], with a symmetric SMG method as the preconditioner and a GMRES solver. A structured, rectangular grid is used. Double precision is used for all numerical variables. Random numbers are generated using the C Standard General Utilities Library by initializing different seed values for each individual processor. This benchmarking effort motivated the implementation of code acceleration techniques to speed up data management. This code has been benchmarked with other codes through the 2D axial-azimuthal benchmark by Charoy et al. [2019] and tested for other instability cases [Hara and Tsikata, 2020; DesJardin et al., 2019]

ISTP

The 2D PIC code [Taccogna et al., 2019] developed at ISTP is a combination of previous 1D-radial [Taccogna et al., 2008; Domínguez-Vázquez et al., 2018; Domínguez-Vázquez et al., 2019] and 1D-azimuthal [Asadi et al., 2019] PIC codes. The code is written in Fortran90 and it uses a structured, uniform, rectangular grid. The version used for the present benchmark is serial and performances reported in Table 4.2 refer to double precision option. The long period ($> 2 \times 10^{18}$) random number generator RAN2 of Numerical Recipes [Press et al., 2007] is implemented. Linear functions are used to interpolate particles onto the grid and the Poisson equation is solved by the cyclic reduction algorithm implemented in the routine PWSCRT of the open-source FISHPACK90 library [Adams et al., 2016]. The leap-frog with Buneman-Boris scheme is used as solver of particle equation of motion.

RUB

The PIC code used in the present benchmark differs from our group's implicit energy-conserving code utilized in the axial-azimuthal benchmark [Charoy et al., 2019]. It was now based on the standard explicit leapfrog time integration scheme. By employing the same approach as for the other codes but a different parallelization means, the intention was to demonstrate the latter's benefits. Except for the field solver, the code was parallelized on a graphics processing unit using the CUDA extension of the C programming language and a two-dimensional analog of the fine-sorting algorithm described in [Mertmann et al., 2011]. The field solver was implemented on a CPU using a combination of the FFT algorithm in the azimuthal direction and a tridiagonal solver in the radial direction for each of the azimuthal harmonics. The latter was based on the Thomas algorithm. Only one thread on CPU was utilized for the field solver. Such an implementation was balanced as the CPU and the GPU parts demonstrated comparable execution time for the typical parameters. The long-period xorshift128 algorithm proposed in [Marsaglia, 2003] has been used as a random number generator, with each thread starting initially with a randomly chosen seed.

LAPLACE

The 2D3V particle-in-cell code used in the present work is written in Fortran90 and uses a structured Cartesian mesh. To exploit the modern architecture of processors, an hybrid technique that combines distributed memory (MPI libraries) between cores and shared memory with Open Multi-Processing (OpenMP) between threads is considered [Garrigues et al., 2016; Boeuf and Garrigues, 2018]. A particle decomposition is employed, the initial particles being equally distributed between MPI cores and OpenMP threads. To reduce computational time during array accessibility due to random positions of particles with respect to the meshes of the simulation domain, a sorting algorithm has been implemented [Bowers, 2001]. The Poisson's equation is solved with the parallel sparse direct linear solver (PARDISO) subroutine included in the Intel®Math kernel Library (Intel®MKL) [Schenk and Gartner, 2004]. The classical leap-frog and Boris schemes are used to move the particles. The code has been verified using the 2D axial-azimuthal benchmark by Charoy et al. [2019].

4.4.2 Code comparisons

The seven groups have simulated the test-case presented in Section 4.3. In Table 4.2, this reference case is referred as Case A. Four groups have also simulated two supplementary cases

	CERFACS	**LPP**	**USASK**	**Stanford**	**ISTP**	**RUB**	**LAPLACE**
				Code implementation			
Language	Fortran	Fortran	Fortran	C++	Fortran	CUDA C + C	Fortran
Parellization	MPI	MPI	MPI	MPI	No	CUDA	MPI/OpenMP
Decomposition	Domain	Domain	Domain	Particle	No	Particle	Particle
Grid type	Unstructured	Structured	Structured	Structured	Structured	Structured	Structured
CPU/GPU type	Intel Skylake	Intel Haswell	Intel Skylake	Intel Sandy Bridge	Intel Ivy-Bridge	NVIDIA Volta (GPU) + Intel Skylake (CPU)	Intel Skylake
	2x18 cores/node	2x12 cores/node	2x20 cores/node	32 cores/node	2x12 cores/node	5120 cores (GPU) + 10 cores (CPU)	2 x 18 cores/node
	@ 2.3GHz - 96 GB	@ 2.6GHz - 64 GB	@ 2.4GHz - 202 GB	@ 2.6GHz - 32 GB	@ 2.4GHz - 256 GB	@ 1.5GHz - 32 GB (GPU) + @ 2.2GHz - 96 GB (CPU)	@ 2.30GHz - 64 GB
				Code module			
Pusher	Explicit	Explicit	Explicit	Explicit	Explicit	Explicit	Explicit
Poisson solver	MAPHYS	HYPRE	FFT	HYPRE	Fishpack	FFT+Thomas	PARDISO
Order of accuracy							
Potential	2	2	2	2	2	2	2
Electric field	2	1	2	2	1	1	1
Floating-point precision	Double	Double	Double	Double	Double	Single* Double**	Single* Double**
				Simulation time for 30 µs (elapsed time)			
Case A $N_{ppc,fin} \approx 212$	35 h (288 CPU)	64 h (144 CPU)	51 h (256 CPU)	168 h (64 CPU)	306 h (1 CPU)	11 h (1 GPU + 1 CPU)	12 h (180 CPU)
Case B $N_{ppc,fin} \approx 424$	50 h (540-900 CPU)	205 h (72 CPU)	98 h (256 CPU)	NA	NA	14 h (1 GPU + 1 CPU)	17 h (180 CPU)
Case C $N_{ppc,fin} \approx 848$	77 h (540-900 CPU)	152 h (216 CPU)	122 h (256 CPU)	NA	NA	29 h (1 GPU + 1 CPU)	27 h (180 CPU)

Table 4.2: Code characteristics. Explicit pusher refers to the standard Leap-frog/Boris algorithm. $\star$ and $\star\star$ symbols respectively refer to the particles (speed, position and weight) and to the fields (potential and electric field).

with a higher initial number of particles per cell ($N_{ppc,ini}$ = 200 or 400, which correspond respectively to Case B and Case C) to study the statistical convergence which will be analyzed in details in Section 4.4.5. The main code characteristics are also given in Table 4.2, along with the corresponding simulation times.

The average computing times show that results for all codes were rather obtained quickly, which is greatly beneficial for benchmarking. Moreover, the comparison of elapsed times on the cases A, B and C highlights the importance of parallel scalability for each particular code. For this particular benchmark, using a particle decomposition along with GPU seems especially effective. The presented runtimes cannot be directly compared between codes as each team used different machines and compilers; besides, GPU and purely CPU based codes remain difficult to compare in terms of computing performances. Yet, the present diversity of the codes provides a reference point for other codes similar to one used in the benchmark.

4.4.3 Comparison of main plasma parameters

First, we study the reference case (case A) simulated by all the groups. We see in Figure 4.7 (a-c) that all temporal profiles of density and radial electron temperature are in very good agreement during the first 3 µs. The linear increase of density displays the same slope while the sharp rise of radial electron temperature occurs around the same instant and experiences a similar growth. Therefore, all groups seem to describe the same discharge dynamics at early times, including the MTSI onset and growth.

After the first 3 µs, we see in Figure 4.7 (b-d) that the electron density and temperature exhibit a complex oscillatory behavior and discrepancies between the results of the different codes are observed. One of the major factors explaining these discrepancies is the use of different Random Number Generators (RNG) at initialization. Indeed, in a supplementary test (not presented here) each group tried to use the same initial locations for macroparticles to mitigate the effect of RNG. The obtained transients for both temperature and density were then extremely close and discrepancies were within statistical uncertainties. For $t > 20$ µs, Figure 4.7 (b-d) shows that both temperature and density reach an oscillatory quasi-steady-state.

In order to compare more precisely the results, the ion density and electron temperature are averaged both azimuthally and in time. These radial profiles are shown in Figure 4.8. The time interval for averaging is set to be 25-30 µs to average over several small oscillations. Both ion density and total electron temperature profiles exhibit an excellent agreement between all codes. The most significant differences appear in the centerline but they remain in a $\pm 2.5\%$ interval around the mean profile. Thus, in spite of the oscillations observed on Figure 4.7 (b-d), we show here that similar plasma parameters are obtained for all the codes using different RNG.

4.4.4 ECDI-MTSI coupling

We have seen in Section 4.3.2 that the observed oscillations are related to a coupling between ECDI and MTSI. The presence of both instabilities for all the codes is confirmed in Figure 4.9, with 1D FFT performed in the azimuthal direction. The azimuthal component of the MTSI is retrieved with a wavenumber $k_y \approx 0.07 k_0$, while we observe the first two ECDI resonances at $k_y \approx k_0$ and $k_y \approx 2k_0$.

Although both the ECDI and the MTSI appear distinctly, Figure 4.9 (a) points out that the MTSI is more important at the beginning of the simulation (between 5-10 µs) and then becomes weaker with time, which echoes with the previous observation on temporal profiles

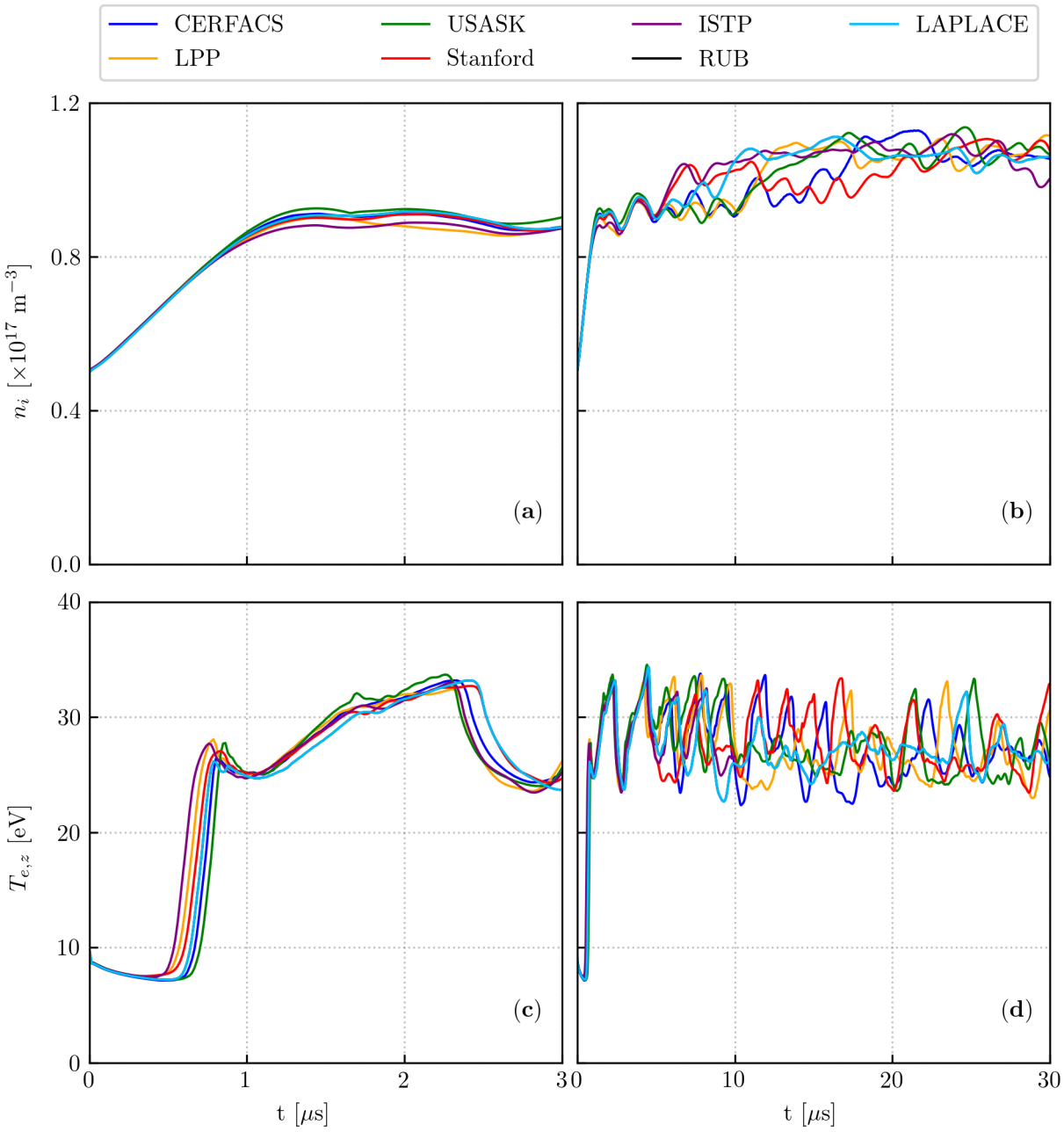

Figure 4.7: **Case A:** Temporal profiles of plasma density (a) up to 3 µs and (b) for the whole simulation time. (c) and (d) Temporal profiles of radial electron temperature on the same time ranges.

in Section 4.4.3: at some point, the radial electron temperature is decreasing for all codes, which leads to a density increase. Besides, we can notice some intermediate peaks between the MTSI wavenumber and the first ECDI resonance, especially at the beginning of the simulation. Their nature was not clearly identified and is left for further work. Finally, after the first ECDI resonance, the k-spectra decrease exponentially. The second resonance is still observable with a much lower amplitude and is surrounded by what seems to be numerical noise. At high frequencies, LPP, ISTP, LAPLACE and USASK seem to have lower noise levels that might be related to the use of different Poisson solvers and subsequent implementations.

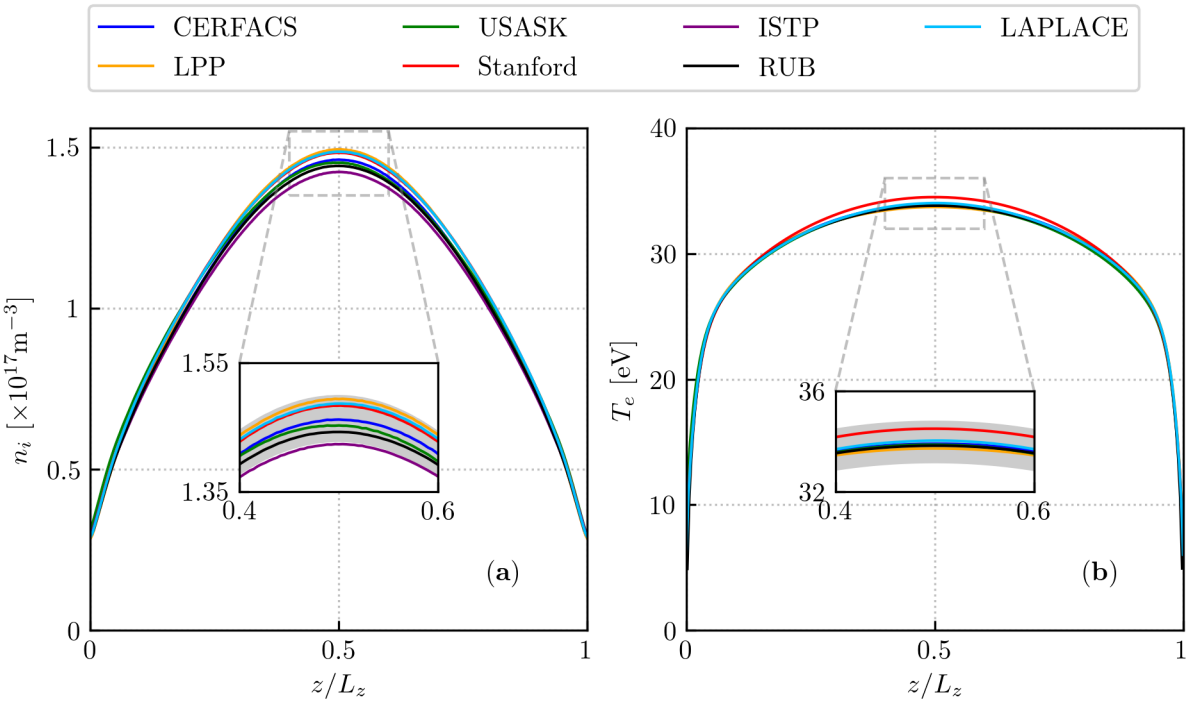

Figure 4.8: Mean radial profiles of ion density (a) and total electron temperature (b), averaged over 25-30 µs. A zoom on the centerline highlights the discrepancies between the codes. On (b) several profiles are superimposed. The shaded gray area indicates the range ±2.5% around the averaged radial profiles of all the groups.

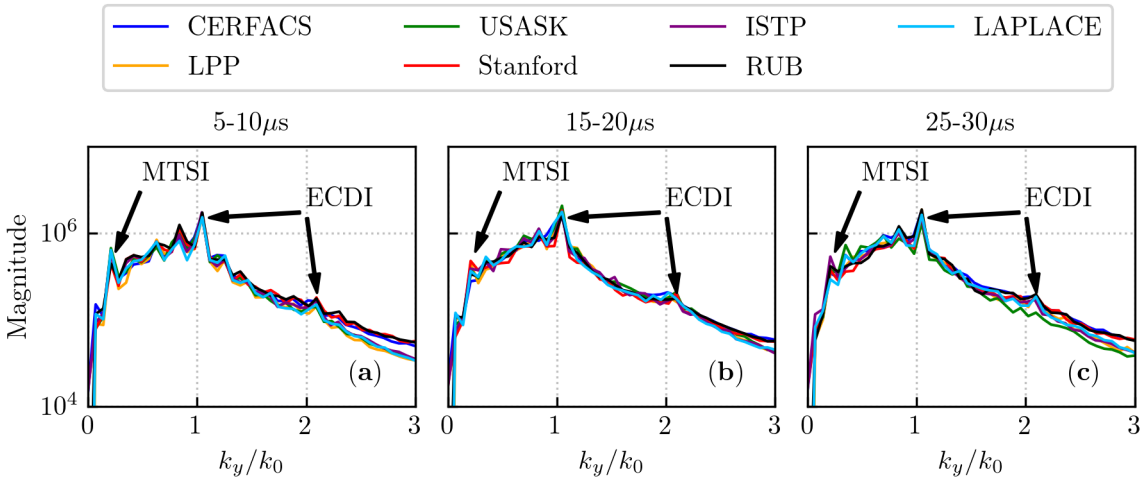

Figure 4.9: 1D azimuthal FFT of the azimuthal electric field E_y, averaged over all radial positions and over three temporal intervals: (a) 5-10 µs, (b) 15-20 µs, (c) 25-30 µs. MTSI and ECDI resonances are indicated by arrows.

Overall, we have found that the 1D FFT profiles are also very similar in the different codes, throughout the whole simulation.

4.4.5 Statistical convergence

In PIC simulations, the use of macroparticles can generate numerical noise. Okuda and Birdsall [1970] have shown that this noise can be viewed as numerical collisions with a frequency given by

$$\nu_{num} = \frac{\pi \omega_{p,e}}{16 N_{De}}, \tag{4.8}$$

with N_{De} the number of macroparticles in a Debye sphere. These numerical collisions can have a significant impact on the discharge behavior, which may lead to misinterpretation of the simulation results. At steady state, the Debye length is around 125 µm in most of the domain. For the reference Case A, the mean number of numerical particles per squared cell at steady state being 212, we can roughly estimate the ratio $\nu_{num}/\omega_{p,e} \approx 4.72 \times 10^{-5}$. According to Turner [2006], this ratio must be below 10^{-4} to ensure negligible numerical collisions, which is the case here for all groups.

However, to further confirm that numerical collisions are truly negligible and that statistical convergence is reached, tests with different numbers of particles per cell have been performed by five groups. The initial number of macroparticles $N_{ppc,ini}$ per cell was varied from 6, 12, 25, 50, 100, 200, 400 up to 800 particles. Then, the mean density at steady state was computed by taking the averaged density between 25 and 30 µs and shown in Figure 4.10 (a) depending on the final number of particles per cell.

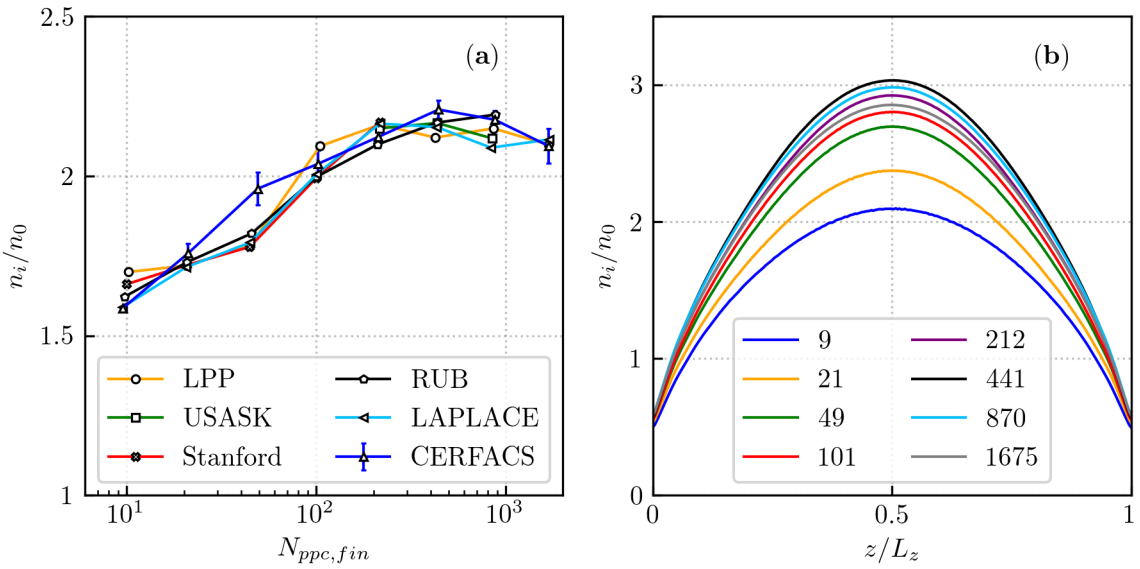

Figure 4.10: Assessment of statistical convergence between 25-30 µs: (a) mean value of ion density for five groups and (b) averaged radial profiles of density for CERFACS's code for various final number of macroparticles per square cells. In (a) error bars for CERFACS indicate the standard deviation around the mean value. The baseline case has around 212 particles per squared cell at steady state. In (b) radial profiles converge from light/green colors towards dark/blue colors.

We see that when a too low number of macroparticles per cell is used, the density can increase by more than 10% if $N_{ppc,fin}$ is multiplied by two, which means that the statistical convergence has not been reached. From 100-200 macroparticles per cell, the mean ion density becomes much less sensitive to $N_{ppc,fin}$ and a plateau at approximately $n_i \approx 2.17 n_0$ is reached.

The curves fluctuate around this value because of the natural variability around the mean ion density. In Figure 4.10 (b), radial profiles of the ion density is displayed for the CERFACS's code and we can see that convergence also appears for a number of macroparticles around $N_{ppc,fin}$ = 100-200. We note that the reference case presented in the previous sections is well converged with more than 200 macroparticles per cell. The criteria of 100-200 particles per cell to reach statistical convergence agrees with previous conclusions from Charoy et al. [2019].

4.5 Conclusion and prospective

In this paper, a 2D radial-azimuthal benchmark for $\mathbf{E} \times \mathbf{B}$ discharges was presented. For this benchmark, collisionless 2D3V-PIC models were used with a virtual axial re-injection model and a fixed ionization source term. The virtual axial model limits the energy growth by removing the high energy tail of the energy distribution functions. Besides, particle losses at the walls are compensated by imposing an ionization source term, similarly to Refs. [Charoy et al., 2019; Boeuf and Garrigues, 2018]. These two features provide a framework for benchmarking by allowing the discharge to reach a steady-state. Despite its apparent simplicity, this test-case was chosen as it captures two important instabilities: the ECDI and the MTSI. Both exhibit characteristics that are in agreement with the linear theory and, moreover, they are found to be coupled, which was also noticed by Janhunen et al. [2018b].

Seven independent PIC codes have simulated the same test-case. In spite of their differences, all the codes retrieved the ECDI and the MTSI at wavenumbers predicted by the theory. They also converged within a 5% interval on relevant plasma parameters. Transients are important in this configuration because they directly give an assessment of the ECDI and the MTSI growth and coupling. From temporal profiles and 1D FFTs, all the codes captured a similar development and interaction between both instabilities. Because of the use of different RNG, the transients can be shifted but the main steps of the simulation were eventually retrieved. Finally, the statistical convergence of the results was assessed. It appeared that at least 100-200 macroparticles per cell are needed. A similar conclusion was found in [Charoy et al., 2019] and this criteria could be used for future 2D PIC simulations.

The main goal of this work was to provide confidence on radial-azimuthal simulations, in which the results can be difficult to analyze due to the coupling between ECDI and MTSI or the use of artificial models to deal with the axial direction. Thanks to the benchmark presented in this paper, every radial-azimuthal code can be verified, which paves the way to further investigations accounting for wall and sheath effects. Moreover, even if we made some simplifying assumptions, such as neglecting the presence of neutrals or not accounting for self-consistent ionization, this case can also be used for insightful parametric studies. For instance, by varying the ionization source term, we can define the plasma density at steady-state, a parameter which plays a role in the instability dispersion relations. Hence, the role of this parameter on the ECDI or MTSI onset could be more easily studied.

Chapter 5

3D PIC simulation

Up to now, numerical simulations have been focused on 2D configurations. In Chapter 3, an axial-azimuthal setup was considered and brought to light the existence of the ECDI. As mentioned in Section 1.3.2, this azimuthal instability probably plays an important role in the axial electron transport and it is, therefore, a crucial feature to capture. In a radial-azimuthal configuration, Chapter 4 showed that the ECDI could be coupled with plasma-wall interactions and giving rise to another kind of instability: the MTSI. Although these simulations provided useful insights on the plasma dynamics, they are artificially constrained by their 2D nature.

Indeed, as demonstrated by experimental observations [Tsikata et al., 2010], instabilities are inherently three dimensional and so are HT's plasma physics. Therefore, in this Chapter we propose a simple 3D setup based on the geometry and features used in Chapter 3 and Chapter 4. Two main objectives are considered. First, we will investigate how the plasma behaves in the 3D geometry. In this effort, our 2D experience is highly valuable and will guide our analysis. A second lesson that we learned during this study is about numerical challenges related to the running of such 3D PIC simulation. Indeed, running AVIP PIC on a top supercomputer on a large configuration makes it imperative to precisely know computational performances and implies to deal with different hardware architectures than the one present at CERFACS. Thus, guidelines on future 3D runs will be also laid out in this regard.

Contents

5.1 Context . . . 137
5.1.1 Literature review . . . 137
5.1.2 Contribution of our new 3D PIC simulation . . . 138
5.2 Numerical setup . . . 139
5.2.1 Computational domain and grid . . . 139
5.2.2 Charged particles . . . 140
5.2.3 Electromagnetic fields . . . 142
5.3 Transient state . . . 146
5.3.1 1D temporal profiles . . . 146
5.3.2 2D maps . . . 147

5.4 Steady state 151
5.4.1 Main plasma variables 151
5.4.2 Spectral analysis 156
5.5 Comparison with 2D simulation 166
5.5.1 Context and numerical setup 166
5.5.2 Main plasma variables 169
5.5.3 Spectral analysis 173
5.6 Preliminary study on a cylindrical geometry 176
5.7 Scalability analysis and convergence study 180
5.7.1 Scalability analysis 180
5.7.2 Statistical convergence 183
5.8 Conclusion 185

5.1 Context

5.1.1 Literature review

As mentioned in Section 1.4.2, 3D PIC simulations are extremely rare.

In the 90's, the University of Tokyo developed a 3D PIC model of a Stationary Plasma Thruster, the SPT50, for which they had a prototype [Hirakawa and Arakawa, 1995, 1996]. They focused their work on the channel and the near plume region. This study was quite comprehensive as the main features affecting the plasma in a HT were modeled: collisions of neutral with charged particles, dielectric layer, self consistent electric field, electrodes, realistic magnetic field topology, curvature effects. Early on, they noticed azimuthal instabilities, which resemble to the ECDI, but no formal identification was made at that time. In order to carry out their work, they had to artificially lower the actual ion to electron mass ratio m_i/m_e and increase the vacuum permittivity ϵ_0. Reducing m_i/m_e (with a factor ~ 40 in this case), implies either faster ions, which reduces the convection time, or slower electrons, which allows to increase the time step Δt constrained by Equation (2.5). In both cases, the steady state is reached more quickly and the computational time is dramatically mitigated. Increasing the vacuum permittivity ϵ_0 results in relaxing the constraint on space step Δx by increasing the Debye length. Thus, a larger simulation domain can be considered. Although this is a pragmatic solution given limited computation resources, it inevitably alters the plasma dynamics. For instance, the dispersion relation of plasma instabilities involves the mass of charged particles and Debye length in a nonlinear way, so modifying any of these parameters will irremediably change their corresponding growth rate or phase velocity.

More recently, Minelli and Taccogna [2017]; Taccogna and Minelli [2018] attempted to address these issues and proposed a methodology to build a 3D PIC model for a miniaturized version of a SPT100 [Boeuf, 2017]. Their strategy consists in reducing the three space dimensions by a factor f, set to 10 in their work. In an effort to properly "scale down" the problem, some physical parameters must be adjusted. For instance, magnetic poles being f times closer, the magnetic field amplitude is multiplied by f while its topology remains unchanged. Eventually, the neutral density must be also multiplied by f to keep important dimensionless parameters such as the Knudsen number (ratio of the electron mean free path to domain size) or Hall

parameter (ratio of gyrofrequency to collision frequency) constant. The setup was focused on the channel region of the thruster to reduce further computational costs. Results showed that rescaled values of main parameters fairly agreed with data that Taccogna and Minelli could gather in the literature. They also assessed the impact of plasma wall interactions, secondary electron emission (SEE) in particular, and of the ECDI on the anomalous transport. Coherently with other work [Tavant et al., 2018], their results suggest that the SEE role remained modest in comparison to the ECDI, but that both phenomena were interacting with each other. Overall, Taccogna and Minelli paved the way for insightful and more accessible 3D PIC simulations, but they also recognize limitations to their approach. First of all, scaling down the geometry by a factor f unavoidably increases the area to volume ratio, which may enhance the effects of the walls on the plasma dynamics. Moreover, other important physical parameters such as the ion convection time or the cyclotron frequency Ω_{ce} are respectively multiplied by a factor f^{-1} and f^{1}. Increasing Ω_{ce} leads to an overestimation of the growth rate of the ECDI [Cavalier et al., 2013] while reducing the convection time is likely to modify the saturation mechanism of the instability. Finally, because the study focused on the sole channel region, the cathode cannot be accounted for. Therefore, an injection mechanism is implemented to mimic the dynamics of electrons entering into the channel and the velocity distribution function is assumed to be a half Maxwellian following [Hagelaar, 2008]. Besides, the potential value at the channel exit must be reasonably guessed from experimental measurements [Smith and Cappelli, 2009]

5.1.2 Contribution of our new 3D PIC simulation

Taking into account the different challenges encountered by these two attempts of 3D PIC simulations, we propose our own 3D setup that will serve as a starting point for more realistic simulations. A detailed description of the model is given in Section 5.2 but we can lay out its main characteristics.

First, Hirakawa and Arakawa [1995, 1996] and in contrast to Minelli and Taccogna [2017]; Taccogna and Minelli [2018], we consider both the channel region and the near plume region. Indeed, the electron velocity components entering the channel do not necessarily follow a half-Maxwellian distribution as the magnetic field is quite strong at the exit which is likely to lead to anisotropy. Besides, the modeling of the cathode and its subsequent injection mechanism is known to be crucial [Charoy, 2020; Cho et al., 2016, 2015]. Moreover, modeling the near plume region prepares for future 3D runs as we do not need to guess the potential profile at the exit and we can simply set the cathode potential $\phi = 0\,\mathrm{V}$. In contrast to Hirakawa and Arakawa, we choose to not rely on modified ion-to-electron mass ratio m_i/m_e and vacuum permittivity in order to preserve the actual growth and development of plasma instabilities such as the ECDI. Besides, another difference with Taccogna and Minelli's work is that we consider a larger simulation domain as the axial and radial directions are ~ 10 times longer while the azimuthal direction is around the same size. By doing so, the area to volume ratio is, perhaps, more preserved with our new setup. Finally, another important difference with both previous attempts is that, here, we use an unstructured grid to carry out our 3D simulation. To our knowledge, such effort is unparalleled in the HT community. Unstructured meshing eliminates the burden of re-implementing key modules, such as the Poisson solver or the particle pusher, if a cylindrical geometry is considered. In fact, any geometry can be discretized with no supplementary effort.

Of course, as this work is the continuation of the 2D cases from Chapter 3 and Chapter 4, we acknowledge some limitations of the model, i.e., no neutral particles (collisionless plasma), no

dielectric layer, no sophisticated magnetic field topology and no curvature effects are present. However, all these features are already available in AVIP PIC and we do intend to add them in a near future. The present 3D PIC simulation does not aim to reproduce experimental data but the objective is first to demonstrate the feasibility of performing 3D configurations using an unstructured grid. Second, this work is also an opportunity to explore in detail the contribution of 3D effects on the plasma physics.

5.2 Numerical setup

This section describes the numerical setup used for this work. The main simulation parameters are summarized in Table 5.1.

5.2.1 Computational domain and grid

The computational domain is based on the geometry used in Chapter 3 and Chapter 4. Therefore, similar dimensions are considered. The domain has a "T shape" that is extruded in the azimuthal direction. A view in the radial-axial direction is given in Figure 5.1 (a). Therefore, no curvature is accounted for in this configuration. The axial length L_x is set to 2.5 cm like in Chapter 3 while the azimuthal length L_y is slightly shorter at 1 cm. In the channel, the radial gap L_z is 1 cm and in the plume region the total height is $2L_z$.

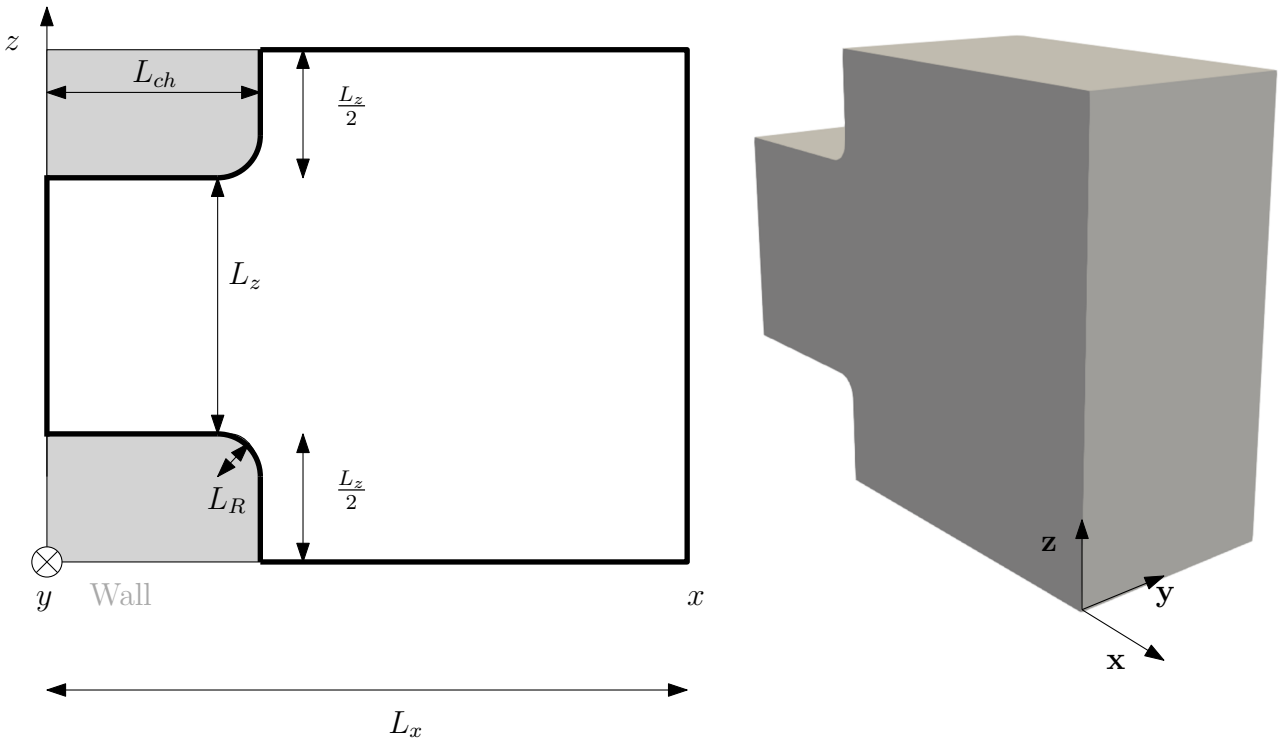

(a) (b)

Figure 5.1: (a): 3D computational domain from the radial-axial view. The azimuthal direction has a length L_y and is periodic. (b): whole 3D domain

The channel has a length $L_{ch} = 0.85$ cm. At its exit, rounded edges avoid an unrealistically high

electric field that would exit at sharp tips. There, the local curvature has a radius $L_R = 0.1\,\text{cm}$. The final 3D domain is shown in Figure 5.1 (b).

Because of these rounded edges, a regular and homogeneous mesh such as those described in Chapter 3 and Chapter 4 cannot be used here. A fully unstructured mesh made of tetrahedral cells is therefore necessary and was generated with the *Centaur* software. The software parameters are tuned so that cells have a typical size Δl that complies with the accuracy condition given by Equation (2.6). Although Equation (2.6) was initially derived for structured grids, we assume that they still apply for unstructured and irregular grids as well. A grid convergence study could help verify this assumption but this will be left for future work. For this work, the cell size is defined as

$$\Delta l = V_c^{\frac{1}{3}}, \tag{5.1}$$

where V_c is the cell volume. It was chosen to discard any mesh refinement as it may lead to spurious results for PIC simulations [Colella and Norgaard, 2010]. Indeed, a severe change of cell size in a refined zone can create a discontinuity during the charge interpolation process described in Section 2.3.2. As a consequence, *self-forces*, artificially created, arise and are a source of numerical errors. It may be possible to reduce these errors by adopting a more progressive mesh refinement than the one chosen by Colella and Norgaard but no study is available, as of today, in this regard.

In Figure 5.2 (a), a cut of the unstructured grid is shown with a zoom to the center of the domain. Qualitatively, the cells are similar in size and shape throughout the computational domain. This observation can be confirmed by plotting the cell size distribution as a function of the radial coordinate as shown in Figure 5.2 (b). It can be observed that the cell size Δl is below $100\,\mu\text{m}$ with a mean value around $67\,\mu\text{m}$, which is similar to the cell size used in Chapter 3 and Chapter 4. The number of cells suddenly drops outside the channel, which is expected as this part of the domain is smaller.
Overall, the mesh contains 2.36 million nodes and 13.5 million tetrahedral cells.

5.2.2 Charged particles

Initialization and pusher

In order to facilitate comparisons with previous 2D simulations, the plasma is made of singly charged ions X_e^+ and electrons e^-. The simulation starts with a uniform plasma density n_0 at thermal equilibrium with an electron and ion temperature $T_{e,0} = 10\,\text{eV}$ and $T_{i,0} = 0.5\,\text{eV}$. $N_{ppc,ini} = 120$ macroparticles are initialized in each cell for each type of particle. The initial density n_0 is set to $1 \times 10^{17}\,\text{m}^{-3}$, twice the value used in Chapter 3 and Chapter 4 to reduce the transient time and consequently the computational cost. The same initial conditions were used in the 2D-3D comparison in Section 5.5. As the cells have slightly different shapes and volumes, the statistical weight q_f is automatically adjusted in each cell to ensure a density n_0.

As usual, only electrons are sensitive to the magnetic field and rely on the Boris algorithm for particle displacement whereas ions are only affected by the electric field and use the Leap-Frog scheme. For this work, the ion position and speed are updated every $f_{sub} = 5\Delta t$, where Δt is the fixed time step. Following the stability condition from Equation (2.5), we set $\Delta t = 5 \times 10^{-12}\,\text{s}$.

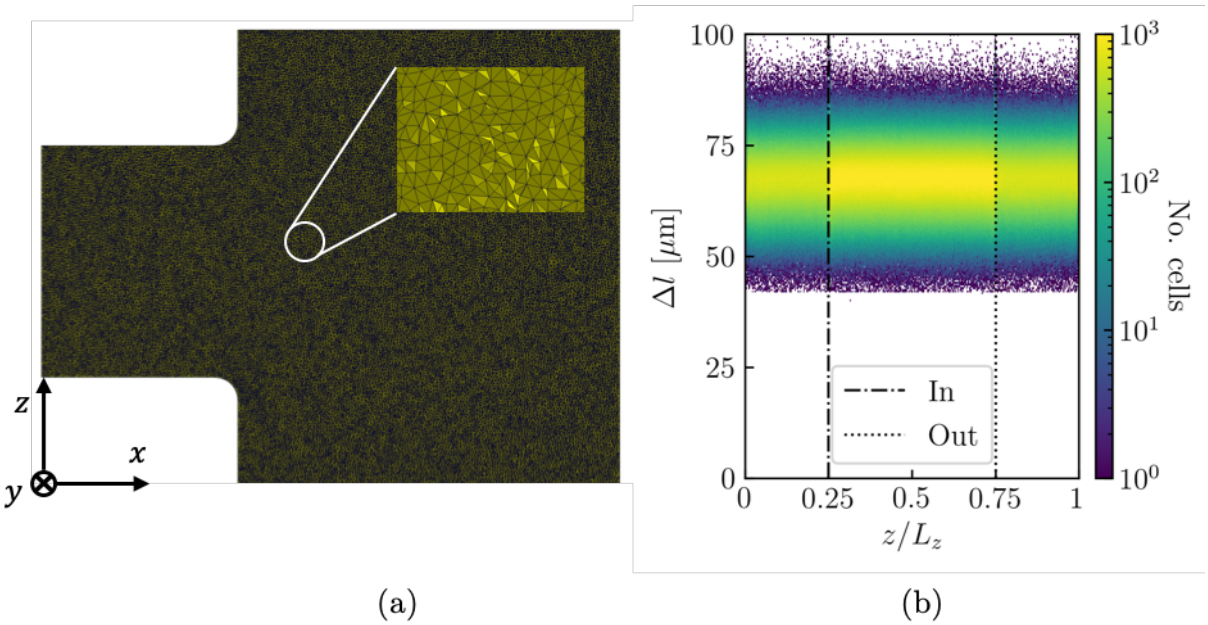

(a) (b)

Figure 5.2: (a): Mesh cut from the radial-axial view. Cells are in yellow and their edges are in black. A local zoom in provides details of the unstructured grid. (b): Radial distribution of the cell size. The dashed-dotted and dotted lines respectively represent the inner and outer channel radial location.

Ionization

Since no neutrals are present, the plasma is collisionless. Ionization is indirectly accounted for by using a similar source term as in the previous 2D configurations. The 2D radial-axial ionization profile is given by:

$$\begin{cases} \text{if } (x,z) \in [x_1,x_2]\times[z_1,z_2] & S(x,z) = S_0 \cos\left(\frac{x-x_m}{x_2-x_1}\right)\cos\left(\frac{z-z_m}{z_2-z_1}\right) \\ \text{else} & S(x,z) = 0, \end{cases} \tag{5.2}$$

where S_0 is the strength of the source term. (x_1, x_2) and (z_1, z_2) are respectively the axial are radial limits of the ionization zone. Their values are taken from the 2D configurations: $x_2 - x_1 = 0.75\,\text{cm}$ like in Chapter 3 while $z_2 - z_1 = 86\%L_z = 0.86\,\text{cm}$ as in Chapter 4. Finally, $x_m = (x_2 + x_1)/2$ and $z_m = (z_2 + z_1)/2$ are respectively the mean axial and radial values. An overview of the ionization layer is provided in Figure 5.3. The total extracted current can be computed with:

$$\begin{aligned} I_{tot} &= \int_{x_1}^{x_2}\int_{z_1}^{z_2}\int_0^{L_y} S(x,z)\,\mathrm{d}x\,\mathrm{d}y\,\mathrm{d}z \\ \iff I_{tot} &= e\frac{4}{\pi^2}S_0(x_2-x_1)(z_2-z_1)L_y, \end{aligned} \tag{5.3}$$

hence, the corresponding total current density through the surface channel L_yL_z can be calculated as:

$$J_m = \frac{I_{tot}}{L_yL_z} = e\frac{4}{\pi^2}S_0(x_2-x_1)\frac{(z_2-z_1)}{L_z}. \tag{5.4}$$

For this work, the current density J_m is set to $400\,\mathrm{A\,m^2}$, coherently with what was done in Chapter 3. Although typical values for HTs are around $1000\,\mathrm{A\,m^{-2}}$ [Boeuf, 2017], we set $J_m = 400\,\mathrm{A\,m^{-2}}$, as we did in Chapter 3, and it will be enough to capture oscillatory phenomena and the expected working conditions of a HT (see Section 5.4). As usual, pairs of $\mathrm{X}_e^+/\mathrm{e}^-$ are injected in the ionization zone delimited by the (x_1, x_2) and (z_1, z_2) coordinates following the profile $S(x, z)$. From a practical implementation point of view, the (x_P, y_P, z_P) coordinates of each pair are given by random numbers (R_1, R_2, R_3):

$$\begin{cases} x_P = \arcsin\left(2R_1 - 1\right)\frac{x_2 - x_1}{\pi} + x_m \\ y_P = R_2 L_y \\ z_P = \arcsin\left(2R_3 - 1\right)\frac{z_2 - z_1}{\pi} + z_m. \end{cases} \tag{5.5}$$

Furthermore, the velocity components are sampled from a Maxwellian distribution and Equation (2.12) is used with an injection temperature $T_{e,0}$ and $T_{i,0}$ for the electrons and ions, respectively. Finally, the particle weight of injected particles must be chosen by the user. To do so, we use the mean particle weight defined as:

$$\bar{q}_f = \frac{n_0 \Delta l^3}{N_{ppc,ini}}, \tag{5.6}$$

with n_0 the initial plasma density, $N_{ppc,ini}$, the initial number of particles per cell and Δ_l, the mean cell size from Section 5.2.1. This gives $\bar{q}_f \approx 256$.

Using this ionization model inevitably modifies the actual HT physics but makes it easier to compare with the previous 2D simulations, thus allowing code verification. The analysis of the physics is also easier as we have already had experience with such a source term. Besides, we do not have to deal with challenges related to ignition. Indeed, ignition is achieved by injecting electrons that are energetic enough to spark the emergence of first ions and new electrons by ionizing neutral particles. In previous tests we had performed, we learned such starting process was not trivial to achieve and will be the focus of future work.

Boundary conditions

All particles leaving the domain are removed from the simulation except at the periodic boundary conditions at $y = 0$ and $y = L_y$. In particular, this means no dielectric layers are accounted for in this work, for now, to keep consistency with Chapter 4. At the top, bottom and right boundaries (see Figure 5.3), the quasi-neutral (QN) cathode model described in Section 2.5.2 is used following recommendations from [Charoy, 2020; Szabo, 2001; Cho et al., 2016]. The injection electron temperature is set to $T_{e,0}$

5.2.3 Electromagnetic fields

Electric field

The Poisson equation is self consistently solved with the external linear solver MAPHYS. The coarse grid correction described in Section 2.6.1 was used and performances were evaluated in Section 5.7. Boundary conditions are Dirichlet and the imposed constant ϕ values are presented in Figure 5.3. In particular, in addition to the right side of the domain, the cathode also includes the top and bottom boundaries where the potential is zero. Neumann conditions were tested at the top and bottom boundaries as they seemed more realistic but they led to the creation

of an important potential bulk (several thousands of Volts) in the plume that was nonphysical. Furthermore, the choice of not accounting for a dielectric layer at the walls implies that we need to ensure continuity of the potential manually. The downstream section of wall, in yellow on Figure 5.3, is in contact with the cathode, and thus is set to $\phi_{W,2} = 0\,\mathrm{V}$. Between the anode and the wall, the potential must be continuous to avoid electric arcs. This is achieved by assuming that the potential decreases linearly from $\phi_a = 200\,\mathrm{V}$ to $0\,\mathrm{V}$ over a distance L_W. In this region, the potential is expressed as

$$\phi_{W,1} = -\frac{\phi_a}{L_W}x + \phi_a, \tag{5.7}$$

where L_W is set to $0.375\,\mathrm{cm}$. Other values for L_W and shapes for $\phi_{W,1}$ are possible but is acceptable as a first guess to reproduce HT operating conditions as shown by Joncquieres et al. [2020].

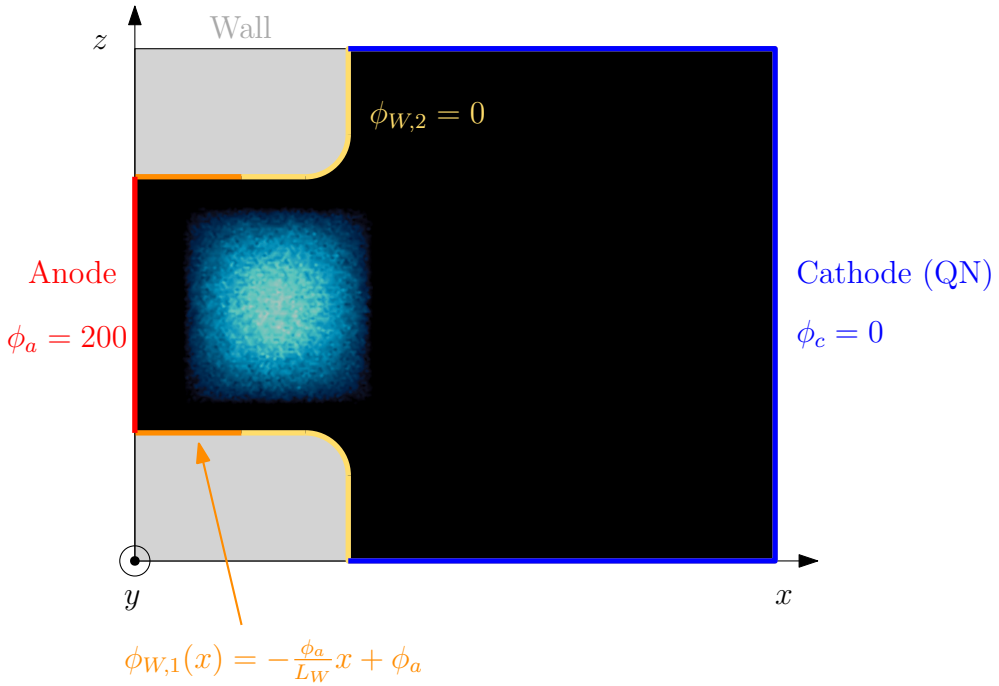

Figure 5.3: Boundary conditions and ionization layer for the 3D PIC simulation (radial-axial view). The ionization source term profile is given by Equation (5.2) is represented with a blue gradient. The anode is in red and set at the potential $\phi_a = 200\,\mathrm{V}$. The cathode is in blue and uses a quasi-neutral (QN) model. Its potential is $\phi_x = 0\,\mathrm{V}$. The walls are absorbent and the potential is split into two parts. In the upstream channel, in orange, the potential $\phi_{W,1}$ is an affine function that decreases from the anode potential ϕ_a down to $0\,\mathrm{V}$. The other part of the walls, in yellow, has a zero potential $\phi_{W,2}$.

Magnetic field

The choice of the magnetic field is less trivial than in the 2D cases as in reality, magnetic poles around the channel generate a 3D magnetic field topology. In order to calculate such magnetic field, the $\boldsymbol{\nabla} \cdot \mathbf{B} = 0$ equation has to be solved with appropriate boundary conditions. However, even for apparently basic configurations such as permanent ring cusp magnets [Ravaud et al., 2008], analytical formulas are incredibly complicated. One solution is to use experimental

measurements as in Taccogna and Minelli [2018] but in this case the numerical setup must be as close as possible to the real thruster. Besides, experimental data can be difficult to obtain as they can be classified by manufacturers such as Safran. If no data are available, one can turn to other open source solutions. On the Internet, the Finite Element Method Magnetics (FEMM) software proposed by Meecker, D. [2000] can generate a 2D magnetic field topology for a variety of configurations. The latter requires the knowledge of the electronic circuit of magnetic coils, which goes beyond the scope of this thesis. This solution is however possible for HT's simulations as it was performed by Garrigues et al. [2003]. Finally, another interesting open source approach consists of a recently developed Python package capable of calculating the magnetic field of simple permanent magnets [Ortner and Bandeira, 2020]. The total magnetic field stemming from several magnets is obtained by the superposition principle.

As of today, all these solutions seemed however premature as it is important to understand and verify the behavior of the 3D plasma dynamics in a simplified configuration first. Therefore, it was chosen to remain as close as possible to the previous 2D cases and the present magnetic field will keep the profile from Section 3.1.2. Therefore, we assume a purely radial magnetic field, varying in the axial direction with a Gaussian shape:

$$\mathbf{B}(x) = \left[a_k \exp\left(-\frac{(x - x_{B_{\max}})^2}{2\sigma_k^2} \right) + b_k \right] \mathbf{u}_z, \tag{5.8}$$

where $k = 1$ for $x \leq x_{B_{max}}$ and $k = 2$ for $x > x_{B_{max}}$. We set $\sigma_1 = \sigma_2 = 0.625\,\text{cm}$. The four coefficients a_k and b_k are chosen such that $B(x = 0) = 6\,\text{mT}$, $B(x = L_x) = 1\,\text{mT}$, $B(x = x_{B_{max}}) = 10\,\text{mT}$ and by satisfying the continuity at $x = x_{B_{max}}$. The profile is show in Figure 5.4.

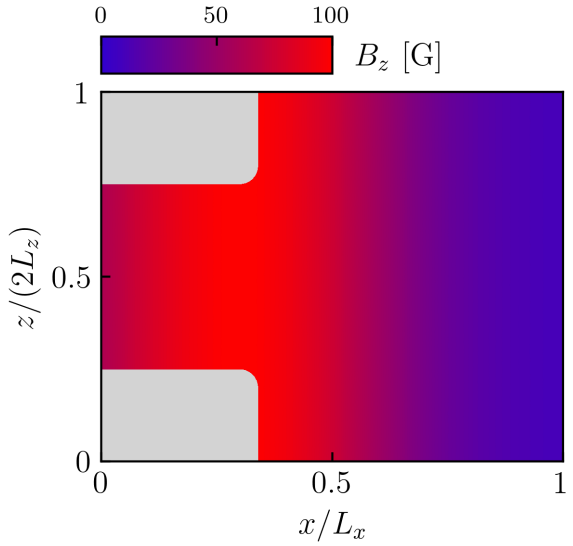

Figure 5.4: Magnetic field profile in 2D radial-axial view. The profile is uniform in the azimuthal y direction and the magnetic field is only radial

Parameters	Symbol	Value	Unit
Computational domain and grid			
Cell size	Δl	67	µm
Domain size	$L_x \times L_y \times L_z$	$2.5 \times 1 \times 1$	cm^3
Number of tetrahedral cells	N_{cell}	13.50×10^6	
Number of nodes	N_{nodes}	2.36×10^6	
Channel length	L_{ch}	0.85	cm
Rounded edge radius	L_R	0.1	cm
Initial conditions			
Plasma density	n_0	1×10^{17}	m^{-3}
Ion temperature	$T_{i,0}$	0.5	eV
Electron temperature	$T_{e,0}$	10	eV
Number of particles/cell	$N_{ppc,ini}$	120	
Ionization parameters			
Axial limits	(x_1, x_2)	(0.25,1.00)	cm
Radial limits	(z_1, z_2)	(0.57,1.43)	cm
Particle weight	$\bar{q}_f$	256	
Electromagnetic fields			
Anode potential	ϕ_a	200	V
Cathode potential	ϕ_c	0	V
Length of linear wall potential	L_W	0.375	cm
Wall potential	$\phi_{W,2}$	0	V
Maximum magnetic field	B_{max}	100	G
Position of maximum magnetic field	x_{Bmax}	0.75	cm
Magnetic field at anode	B_a	60	G
Magnetic field at cathode	B_c	10	G
Computational parameters			
Time step	Δt	5	ps
Average time range	N_a	$5000\Delta t$	s
Subcycling frequency	f_{sub}	5	iterations

Table 5.1: 3D PIC simulation parameters.

5.3 Transient state

5.3.1 1D temporal profiles

The first thing that can be observed is the temporal evolution of the simulation. 1D temporal profiles of the main variables of interest are thus presented in Figure 5.5. Overall, the simulation reaches a steady state in around 10 µs. During this period, we first verify that the implemented quasi-neutral cathode model injects the correct electron current I_{cd} into the domain. As a reminder the expected I_{cd} was derived in Equation (2.61). The numerical proof is given Figure 5.5 (b) for which one can see that I_{cd} is equal to $I_d + I_{be} - I_{bi} + I_{we} - I_{wi}$ during the whole simulation. On the other figures, three main periods can be discerned.

In the first moments, called phase I, of the simulation, the global density increases linearly thanks to the ionization source term because the losses remain limited. This situation goes on until ions traveling from the ionization zone reach the cathode boundary. At around 1.2 µs, the density is maximum as shown in Figure 5.5 (a). At this point, the total number of electron and ion macroparticles is around 4.26 billion. In the mean time, the electrons heat up, moderately at first, and then sharply from 0.2 up to 0.9 s (see Figure 5.5 (c)). In contrast to Chapter 4, the heating seems to occur at approximately the same rate and at the same time for the three directions. This behavior is probably related to different oscillatory phenomena that will be detailed in Section 5.4.2. On the other hand, ions present a strong anisotropy in Figure 5.5 (d). While the radial and azimuthal temperatures $T_{i,z}$ and $T_{i,y}$ barely rise, the axial ion temperature $T_{i,x}$ dramatically increases and is multiplied by more than 20. This sharp increase is due to the initial acceleration of ions toward the plume. At around 1.2 µs, $T_{i,x}$ slightly drops because the fastest ions have exited the domain.

During the second stage of the transient, phase II, from 1.2 to $\sim$ 5 µs, axial losses largely overtake the creation of particles. At first, up to 2.1 µs, losses remain moderate as shown in Figure 5.5 (a). This results in a drop in the three components of the electron temperature. Interestingly, while $T_{i,z}$ and $T_{i,y}$ decrease as well in Figure 5.5 (d), the axial temperature $T_{i,x}$ continues to rise. This apparent paradox will be further explained in Section 5.3.2. Around 2.1 µs, losses accelerate and a peak of injected current I_{cd} at the cathode is noted in Figure 5.5 (b). Electron temperatures decrease again as well as $T_{i,x}$.

Finally, in phase III, from 5 µs, most of the wall losses start to be balanced out and the simulation stabilizes. This process takes some time and the ion axial temperature continues to decrease until the steady state is reached from 8 µs.

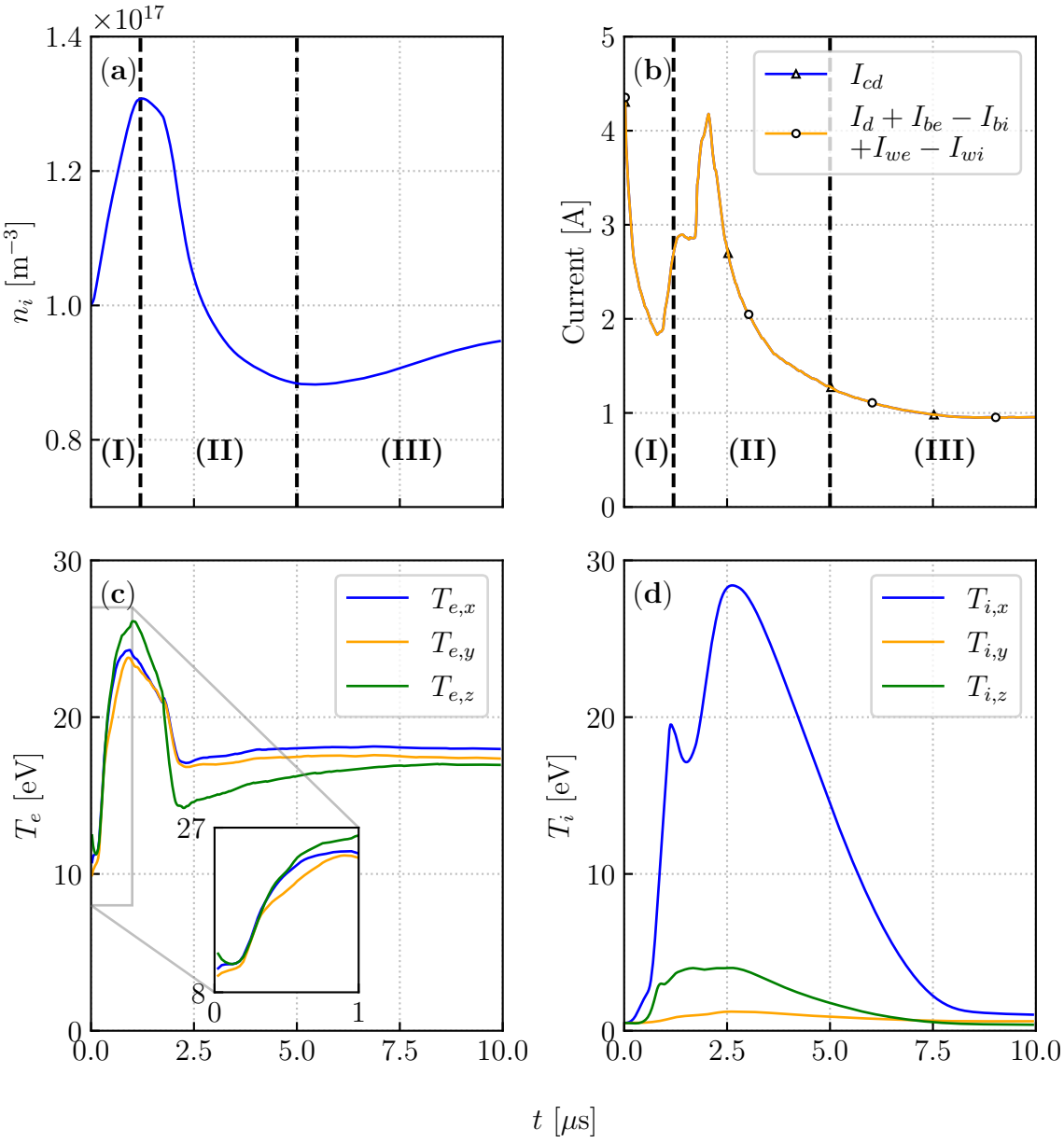

Figure 5.5: Temporal evolution of space-averaged quantities in the whole domain. (a): ion density n_i. (b): actual cathode electron current I_{cd} and expected cathode electron current $I_d + I_{be} + I_{bi} + I_{we} + I_{wi}$. (c): electron temperature components $T_{e,x}, T_{e,y}$ and $T_{e,z}$. (d): ion temperature components $T_{i,x}, T_{i,y}$ and $T_{i,z}$. The three different phases (I,II,II) are delimited in (a) and (b) with black dashed lines.

5.3.2 2D maps

More details on the transient state can be provided by looking at the main planes of interest of the simulation, starting with the axial-radial view $x - y$. Figure 5.6 presents the centered $x - y$ plane for four variables of interest at selected times.

During phase I, the plasma density is increasing near the ionization zone. At around 0.50 µs, under the effect of the axial electric field, a portion of the ionization zone detaches and accelerates in the axial direction. In the area of separation, the axial electric field is slightly negative,

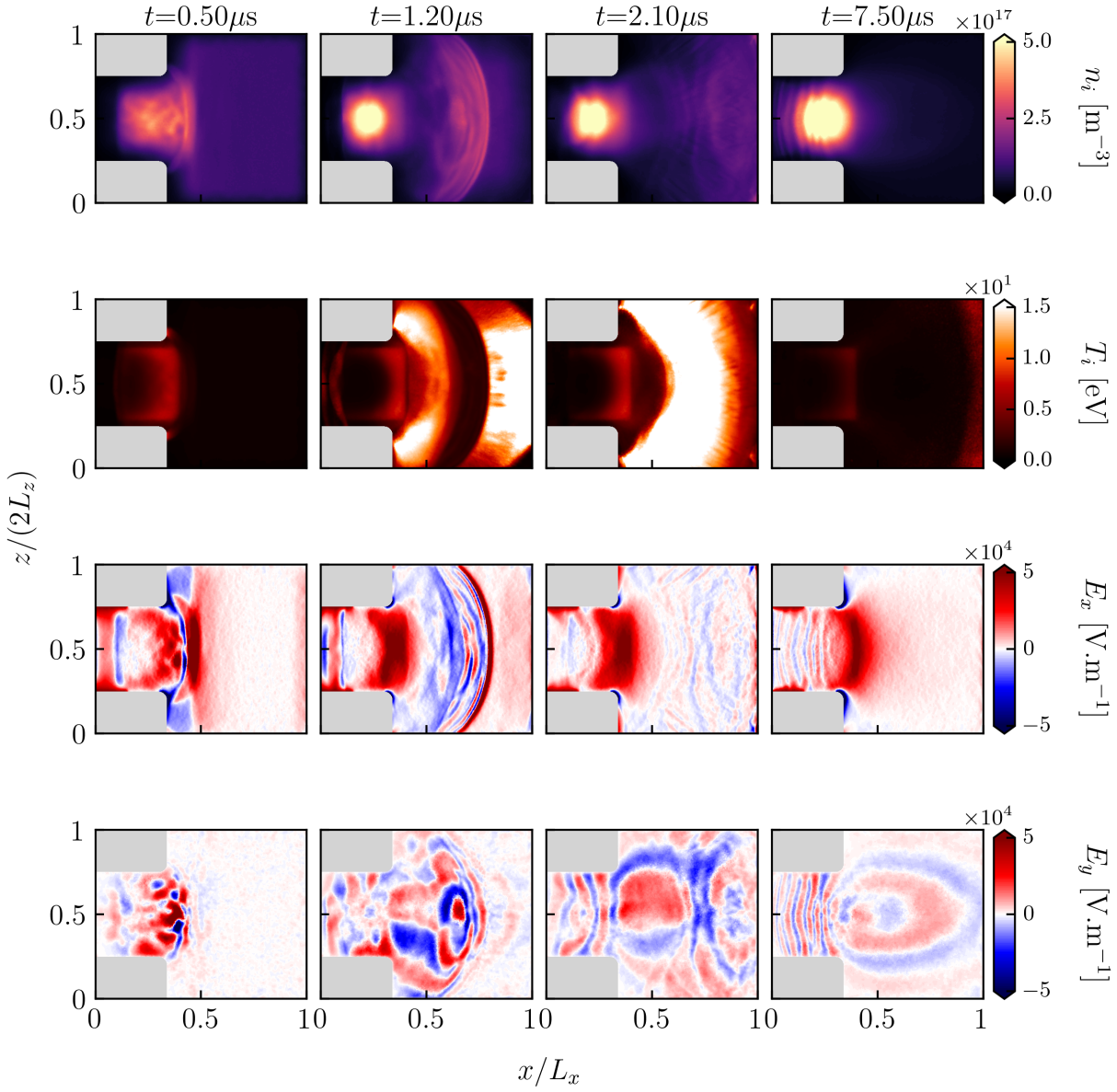

Figure 5.6: Timeline of variables of interest in the centered axial-radial $x-z$ plane at $y = L_y/2$. From the first to the fourth row are successively presented the ion density n_i, the ion temperature T_i, the axial electric field E_x and the azimuthal electric field E_y. Each column corresponds to a specific time: $t = 0.50, 1.20, 2.10$ and $7.50\,\mu s$.

hence highlighting a clear delimitation. In the meantime, the ions start heating up on the right side of the cubic ionization zone while no specific features can be observed in the azimuthal electric field E_y.

At the start of phase II, at $1.20\,\mu s$, the transient wave continues to travel downstream and most of the ions have not yet reached the cathode, which is consistent with the maximum plasma density observed in Figure 5.5 (a). Interestingly, the bulk of the wave remains at a moderate ion temperature whereas the heading and trailing edges are much hotter. It seems that this is mostly due to an inertial effect as the fastest ions get ahead, thus tending to distort and extend the local velocity distribution function (VDF). Similarly, the initially slowest ions, that eventually fall behind in time, also increase the dispersion of local VDFs. As soon as the

fastest ions start to leave the domain, the ion temperature coherently drops (Figure 5.5 (d)). At $t = 2.10\,\mu s$, T_i is nevertheless maximum as lagging ions continue to locally increase the temperature before they begin to be convected away.

In phase III, at $t = 7.50\,\mu s$ for instance, most of the transient plasma wave has exited the domain and the ion temperature continues to decrease. The axial electric field stabilizes as well with a maximum localized at the channel exit. In spite of smoothed edges, the local curvature is sufficient to rise the local electric field. The azimuthal electric field E_y exhibits an interesting oscillatory behavior propagating in the axial direction. In the channel, E_y varies mainly axially with a wavelength of the order of 1 mm. In the plume, the oscillations seem to propagate in both the radial and axial directions, as a spherical wave, with a wavelength increasing up to $\sim 7\,mm$. As will be discussed in Section 5.4.2, this wave is likely to be related to the already encountered ECDI.

The understanding of the instability affecting E_y can be further explored by studying the axial-azimuthal $x - y$ plane located at $z = L_z$. This is done in Figure 5.7 for which a similar timeline is presented for the axial electron current $J_{e,x}$, the radial electron current $J_{e,z}$ and the azimuthal electric field E_y.

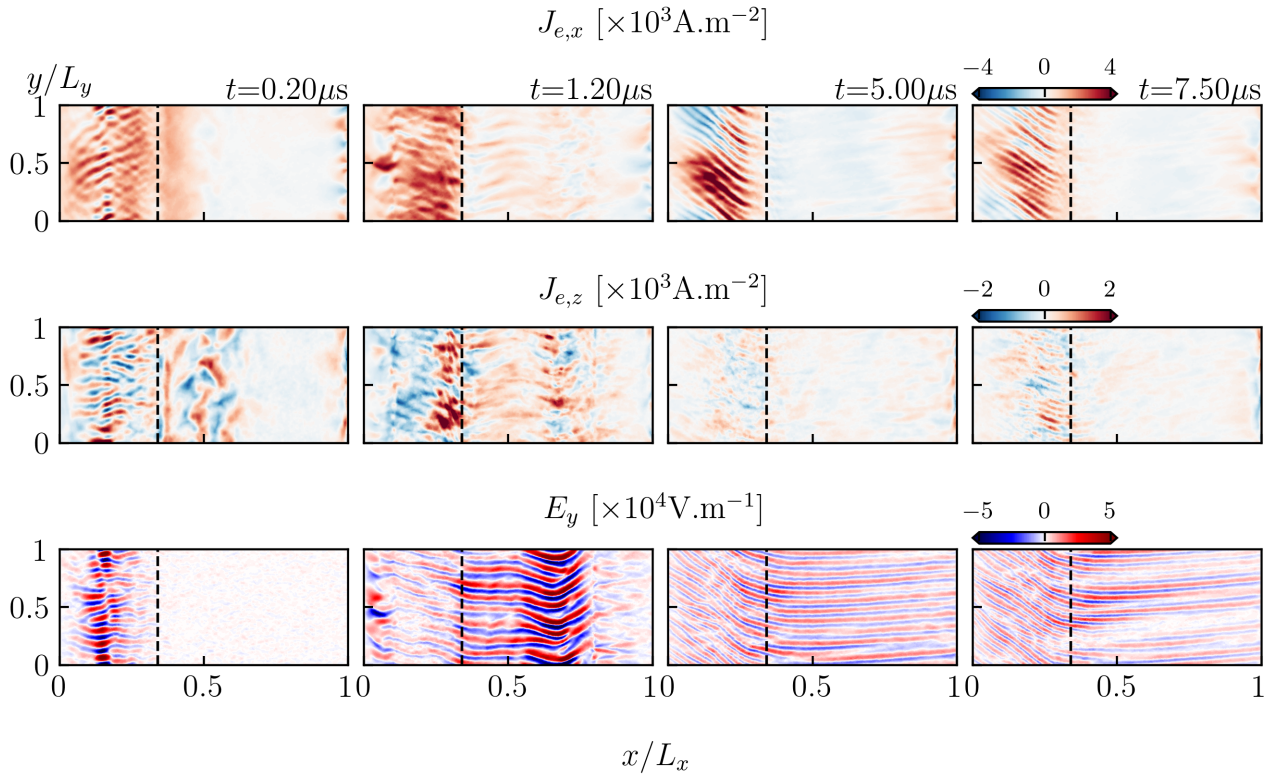

Figure 5.7: Timeline of variables of interest in the centered axial-azimuthal $x - y$ plane at $z = L_z$. From the first to the last row are successively presented the axial electron current $J_{e,x}$, the radial electron current $J_{e,z}$ and the azimuthal electric field E_y. Each column corresponds to a specific time: $t = 0.20, 1.20, 5.00$ and $7.50\,\mu s$. The dashed black line represents the channel exit at $x = 0.34L_x = 0.85\,cm$.

During the linear-like phase, at $t = 0.20\,\mu s$ for instance, we can see on the 2D map of the azimuthal electric field E_y the ECDI starting to develop upstream. Then, the ECDI is convected

away towards the plume by the transient ion wave. Finally, from around 5 µs, the ECDI seems to be established in almost the entire domain. In the channel, the wave vectors seem to have both axial and radial components while it is mostly axial in the plume. This was also observed in a pure 2D axial-azimuthal configuration (see Figure 3.2). For the 3D configuration we measure an azimuthal wavelength $\lambda_{y,ch} \approx 628\,\mu m$ in the channel while its is around $\lambda_{y,pl} \approx 913\,\mu m$ in the plume. The radial electron current $J_{e,z}$ is also very interesting. Similarly to E_y, $J_{e,z}$ presents short-wavelength azimuthal oscillations at the beginning of the simulation. During the travel of the transient ion wave, no organized structures seem to appear ($t = 1.20\,\mu s$). However from 5 µs another subtle pattern arises in the azimuthal direction at $x \sim 3 - 4\,mm$ ($0.12 - 0.16 L_x$). At 7.5 µs, this wave emerges more clearly in the axial electron current $J_{e,x}$ with a wavelength of the order of 1 mm. The wave is located in the same area as for $J_{e,z}$.

In order to deepen the analysis one can examine the radial-azimuthal $z - y$ plane in this area. This is done in Figure 5.8 for which the same quantities are presented in the channel plane located at $x = 0.12 L_x = 3\,mm$.

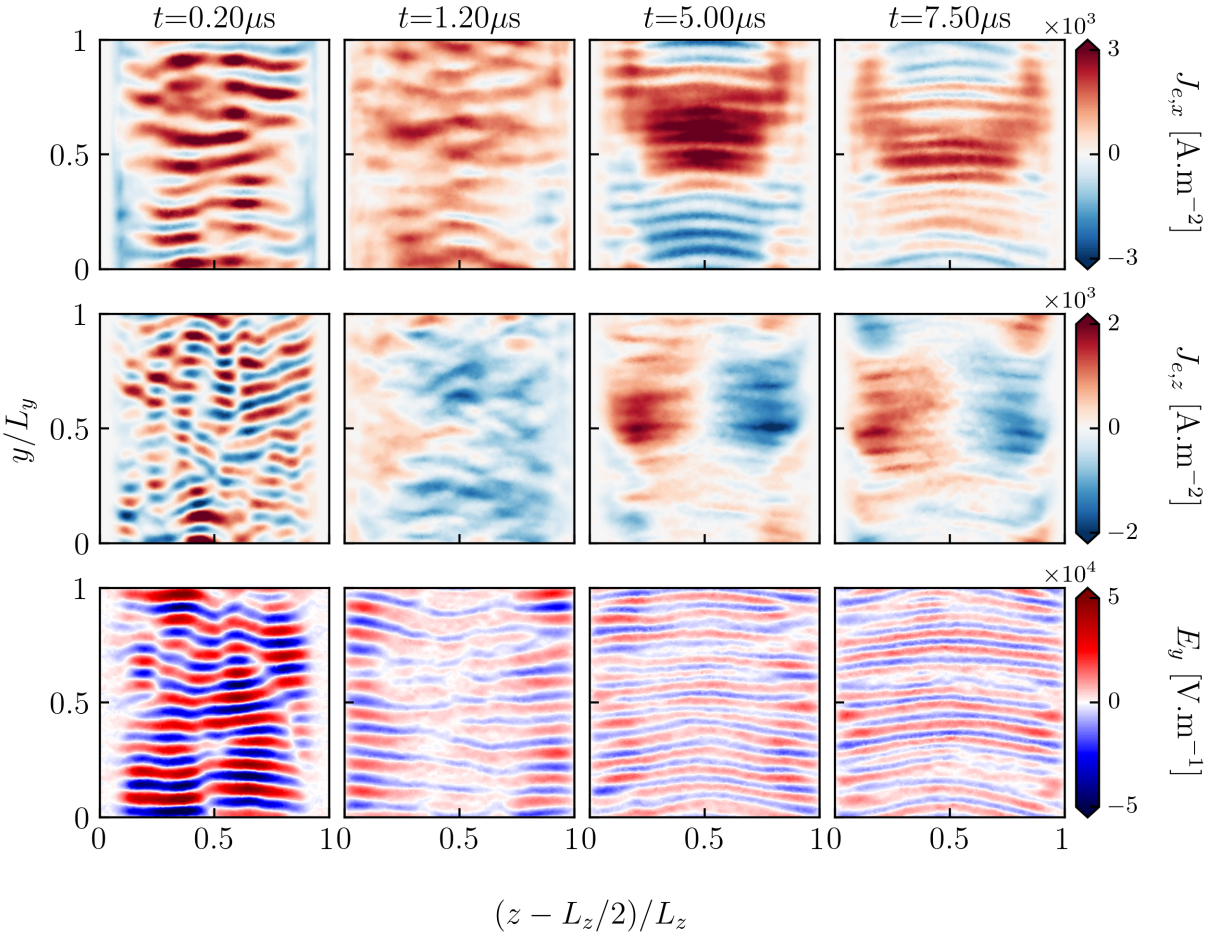

Figure 5.8: Timeline of variables of interest in the radial-azimuthal $z-y$ plane at $x = 0.12 L_x = 3\,mm$. From the first to the last row are successively presented the axial electron current $J_{e,x}$, the radial electron current $J_{e,z}$ and the azimuthal electric field E_y. Each column corresponds to a specific time: $t = 0.20, 1.20, 5.00$ and $7.50\,\mu s$.

As in Figure 5.7, a pure azimuthal wave, due to the ECDI, develops in the first moments of the simulation ($t = 0.20\,\mu s$). From $t = 1.20\,\mu s$, the short-wavelength ($\lambda_{\text{ECDI}} \sim L_y/10$) is still

clearly visible for the azimuthal electric field E_y but a radial pattern seems to emerge in the electron radial current $J_{e,z}$. This radial wavelength is around L_z. This larger oscillation also has an azimuthal component that distinctly appears at $t = 7.50\,\mu s$. The corresponding azimuthal wavelength is approximately L_y. Moreover, the pure azimuthal wave in the E_y 2D map sees its wavelength roughly divided by two when approaching the steady state. Overall, this large radial-azimuthal wave resembles the MTSI encountered in Chapter 4. This point will be further detailed in Section 5.4.2.

5.4 Steady state

5.4.1 Main plasma variables

The steady state is reached in about 10 µs. We can verify the proper functioning of the thruster by analyzing Figure 5.9.

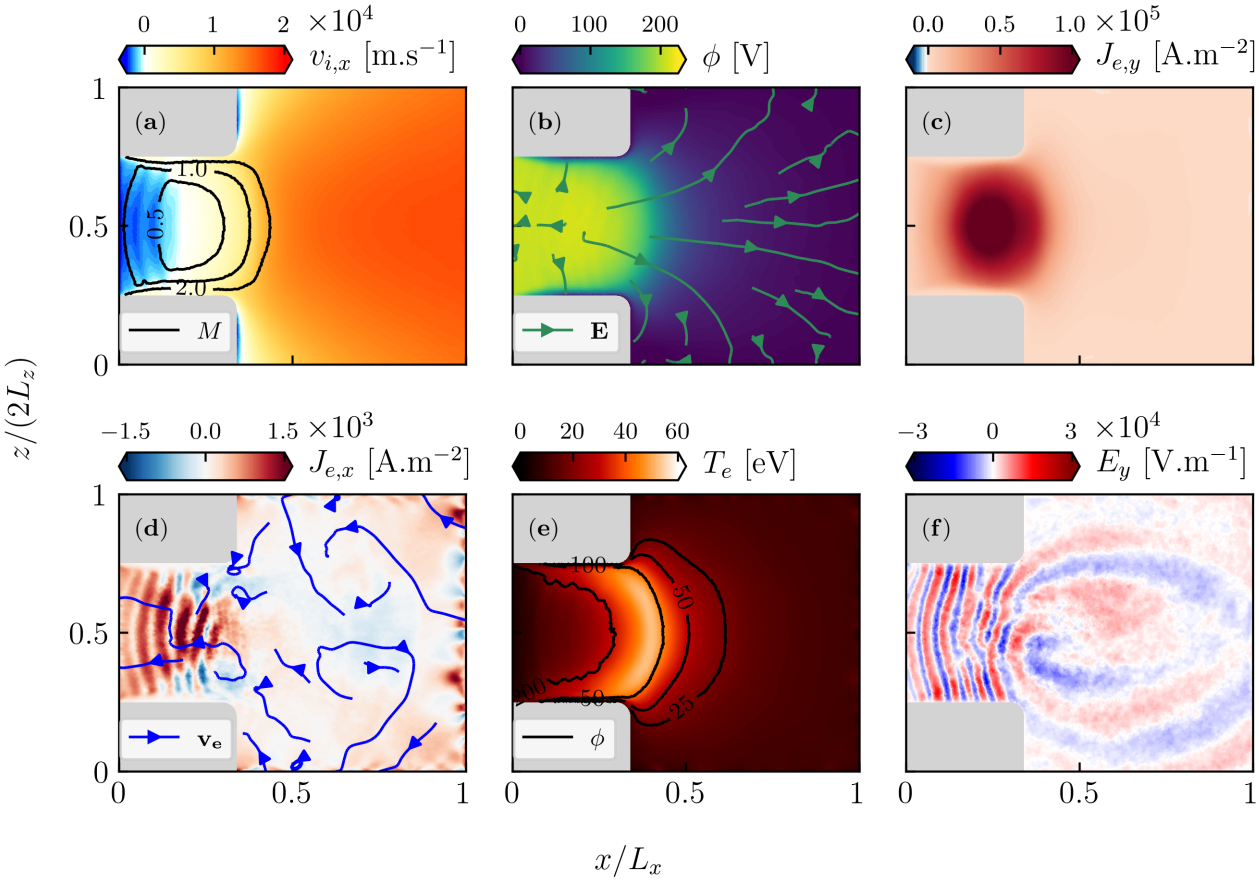

Figure 5.9: Radial-azimuthal view at steady state. (a): axial ion speed $v_{i,x}$ with iso-contour of Mach number M. (b): potential ϕ with streamlines of electric field $\mathbf{E}$ in the plane. (c): electron azimuthal current density $J_{e,y}$. (d): axial electron current density $J_{e,x}$ with streamlines of electron velocity $\mathbf{v}_e$ in the plane. (e): total electron temperature T_e with iso-contour of potential ϕ. (f): azimuthal electric field E_y.

In Figure 5.9 (a), we can see that the ions are greatly accelerated at the channel exit as the plasma flow becomes supersonic. We adopt here a classical definition of the Mach number M,

$$M = \frac{\|\mathbf{u}_i\|}{c_s}, \tag{5.9}$$

where $\|\mathbf{u}_i\|$ denotes the magnitude of the ion hydrodynamic velocity and c_s, the ion speed of sound defined as

$$c_s = \sqrt{\frac{k_B T_e}{m_i}}, \tag{5.10}$$

for which k_B, T_e and m_i are respectively the Boltzmann constant, the electron temperature and the ion mass. Additionally, we also note that $M \geq 1$ at the inner and outer walls of the channel and also at the vicinity of the anode at left, which marks the beginning of their respective sheath. For instance, we roughly measure a width of 1 mm at the inner/outer wall.

The acceleration is caused by an important potential drop seen in Figure 5.9 (b). The subsequent electric field lines are mostly directed toward the plume and have both a radial and axial components, suggesting that the divergence beam is important. This is coherent with the choice of using Dirichlet boundary conditions for Poisson's equation at the top and bottom boundaries in the plume. An important radial gradient of potential is also present in the downstream section of the channel, also highlighted by the iso-ϕ lines in Figure 5.9 (e), which means that a strong radial electric field takes place there. In the upstream section of the channel, we can see the effect of choosing a linearly decreasing potential from 200 (anode) to 0 V (channel exit) as a Dirichlet boundary condition. Besides, in the channel, a strong electron drift current is observed in the azimuthal direction under the effect of the **E** and **B** fields (Figure 5.9 (c)).

The global electron transport is shown in Figure 5.9 (d) with the help of the axial electron current $J_{e,x} = -en_e u_{e,x}$. With this definition, $J_{e,x} > 0$ means that $u_{e,x} < 0$. From the streamlines, we can see that electrons effectively enter into the channel despite the presence of recirculation zones near the walls. In the channel, the presence of these recirculation zones might be related to the radial azimuthal wave seen in Figure 5.8. In the plume, another recirculation zone is also visible. The situation is unclear here: the streamlines seem to follow the curvature of the azimuthal instability carried by E_y (see Figure 5.6 (f)). At this point, we cannot provide a satisfying explanation for these recirculation areas.

Another insight from Figure 5.9 (d) concerns the cathode. First, we notice some streamlines from the right boundary going to the top and bottom plume boundaries, which means that electrons are lost and will be re-injected by the cathode. This behavior is even more evident if we look closely at the right plume boundary where we note the current being alternatively positive and negative. Actually, a significant portion of newly injected cathode electrons leaves the domain after a few iterations, which is not a desirable trait as it artificially disturbs the local charge distribution. Cho et al. [2016] also noted a similar problem with their cathode model. Perhaps it would help to shift the injection surface slightly into the domain to help electrons stay inside the domain as it was done in [Charoy, 2020]. But as explained in Section 2.5.2, this is difficult to do in the context of unstructured grids. Another option would be to replace the random injection of electrons by a targeted injection consisting in injecting electrons where the charge difference between ions and electrons is the highest as in [Szabo, 2001].

Going back to the physical insights, Figure 5.9 (e) shows the space distribution of the electron temperature T_e. With a maximum of approximately 50 eV, it has a bell shape that is probably prescribed by the iso-potential lines topology. Where the iso-lines are the closest, the electric field is the highest and Joule heating $\mathbf{J} \cdot \mathbf{E}$ is the most intense. The plume is largely

cold with a weak electric field.

To get a more quantitative insight of the physics we can look at 1D profiles in different sections of the domain. This is done in Figure 5.10.

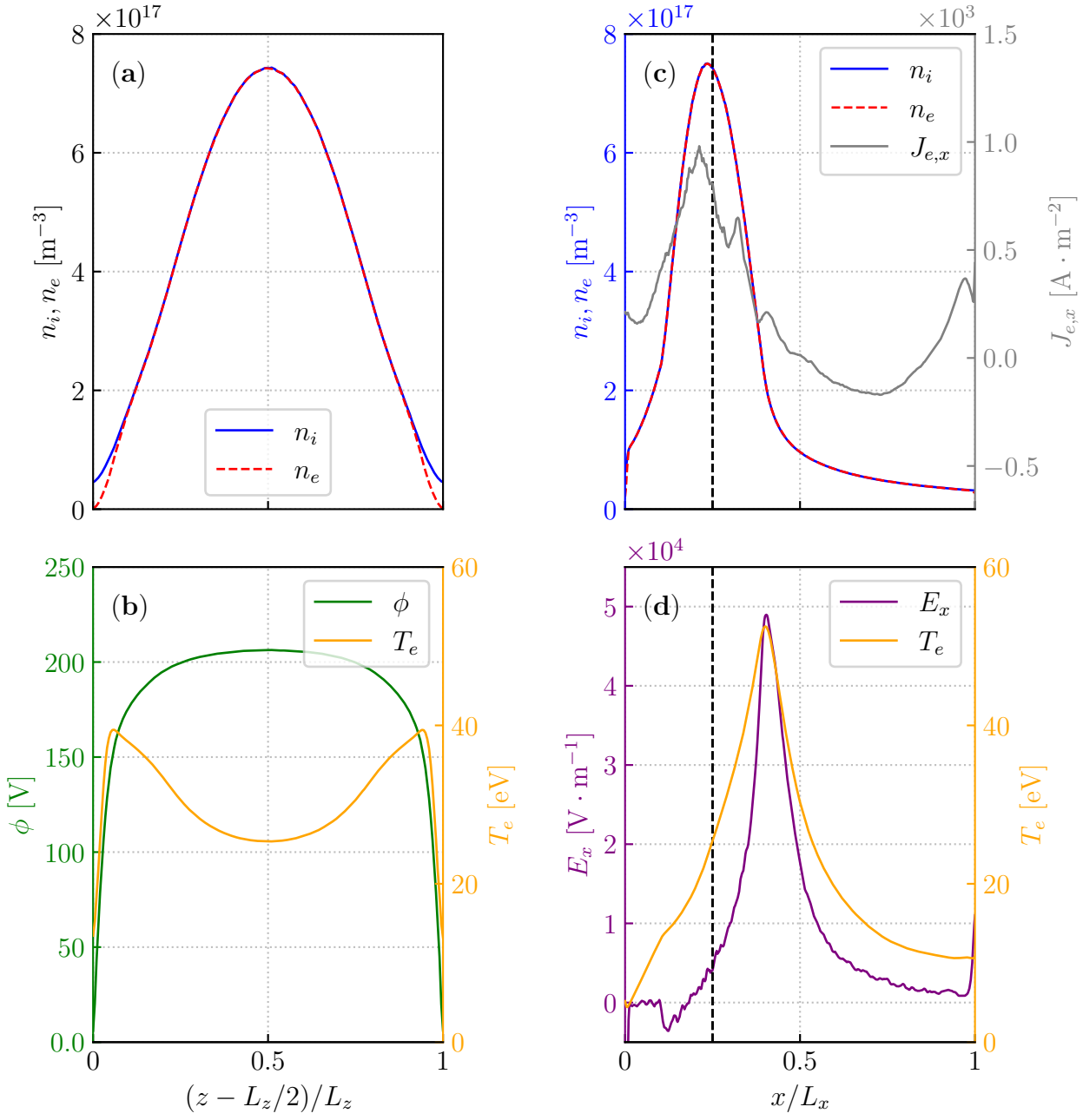

Figure 5.10: **Inside the channel at centerline**. (a) and (b): azimuthally averaged 1D radial profiles at $x = 0.25L_x = 0.625\,\text{cm}$ of plasma density n_i, n_e in (a) and potential ϕ and electron temperature T_e in (b). (c) and (d): azimuthally averaged 1D axial profiles at $z = L_z = 1\,\text{cm}$ (centerline) of plasma density n_i, n_e and electron axial current density $J_{e,x}$ in (c) and axial electric field E_x and electron temperature T_e in (d). The black dashed line in (c) and (d) corresponds to the axial cut position of (a) and (b), i.e, $x = 0.25L_x$.

In Figure 5.10 (a) and (b) we present the averaged radial profiles of the plasma density, the

potential and electron total temperature at $x = 0.25Lx = 0.625\,\text{cm}$, where the ionization source term is maximum. At this position, the plasma density has a usual bell shape from the wall up to the centerline of the domain at $z = L_z$ where $n_i = n_e \approx 7 \times 10^{17}\,\text{m}^{-3}$. Near the inner wall ($z = L_z/2$) and outer wall ($z = 3/2L_z$), the sheath starts whenever $n_i \neq n_e$ with a width of $\sim 0.1L_z = 1\,\text{mm}$, which is consistent with the iso-Mach lines from Figure 5.9 (a). Thus, in Figure 5.9 (b), the potential sharply decreases toward the Dirichlet condition $\phi = 0\,\text{V}$, while at the center we note a maximum value of $\phi = 210\,\text{V}$. The radial profile of the temperature is very interesting. From the wall, the temperature rises from 0 to 40 eV at $z = 0.63L_z$, and then decreases until it reaches a minimum at the centerline of 27 eV. This profile was already anticipated in Figure 5.9 (e) and is probably the result of a bent iso-potential line in the radial axial plane.

In Figure 5.10 (c) and (d), the azimuthally averaged profiles at the centerline are shown. From Figure 5.10 (c), we observe the plasma is mainly located in the channel with a maximum value of $\approx 7 \times 10^{17}\,\text{m}^{-3}$, as in the previous radial profile. The electrons massively enter into the channel with a maximum value of $J_{e,x} \approx 9.8 \times 10^3\,\text{A m}^{-2} > 0$. In contrast, the recirculation zone in the plume seen in Figure 5.9 (d) appears from $x = 0.4L_x = 1\,\text{cm}$ and ends at approximately $x = 0.88L_x = 2.2\,\text{cm}$. In Figure 5.10 (d) the acceleration of the ions can be observed at about $x = 0.4L_x = 1\,\text{cm}$ with a maximum electric field $E_x \sim 48 \times 10^4\,\text{V m}^{-1}$. At the same location the temperature of electrons is also maximum with $T_e = 55\,\text{eV}$.

The plasma structure looks different if we consider other axial and radial cut locations in the domain. As an example, we can investigate what happens in the plume at $x = 0.45L_x = 1.12\,\text{cm} > L_{ch}$ in Figure 5.11 (a) and (b). Downstream of the channel exit, the iso-potential lines are less bent and more parallel to the radial direction. As a result, the electron temperature radial profile T_e retrieves a bell shape. Additionally, the sheath has collapsed. This can be seen in the plasma density and potential profiles (Figure 5.11 (a) and (b), respectively) where $n_i = n_e$ is always maintained and the potential falls to zero before the radial positions $z = 0$ and $z = 2L_z$. This behavior is expected since the positions $z = 0$ and $z = 2L_z$ do not correspond to physical walls but to the delimitations of the plume. This result also indicates that the quasi-neutral cathode model, presented in Section 2.5.2, effectively plays its role and prevents the formation of artificial sheath.

In Figure 5.11 (c) and (d) we consider the azimuthally averaged axial profile at $z = 1.3L_z = 1.3\,\text{cm}$, above the centerline $z = L_z$ and near the outer wall of the thruster. In Figure 5.11 (c), the density profile is, as expected, lower than at the centerline but the shape is similar. At this radial location, the axial profile of $J_{e,x}$ is negative from $x = 0.2L_x = 0.5\,\text{cm}$ to $x = 0.36L_x = 0.9\,\text{cm}$. This corresponds to the recirculation zone in the channel already observed in Figure 5.9 (d). Finally the electron temperature and axial electric profiles in Figure 5.11 (d) are very similar to those in the centerline.

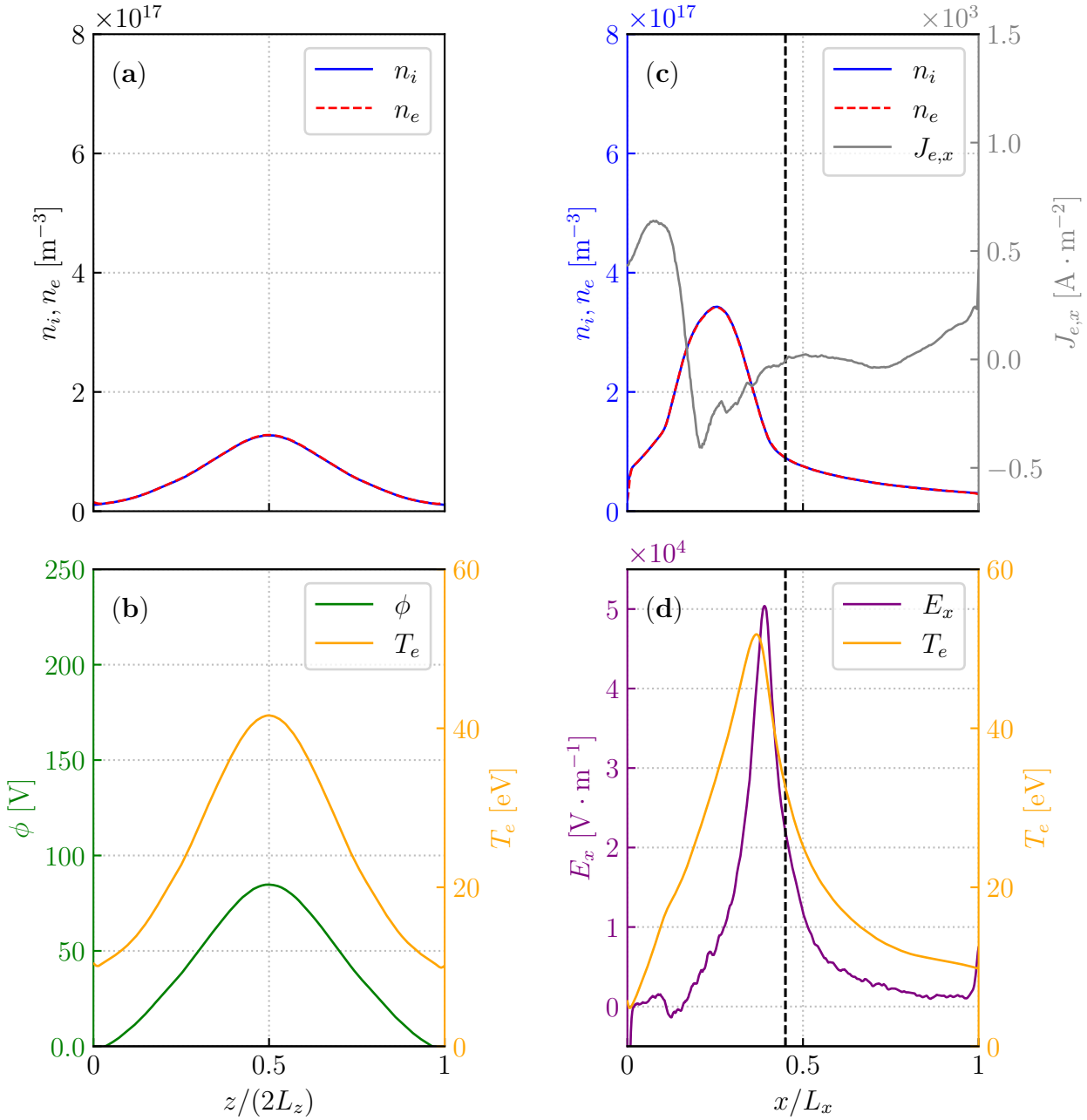

Figure 5.11: **Outside the channel and near the outer wall**. (a) and (b): azimuthally averaged 1D radial profiles at $x = 0.45L_x = 1.12\,\text{cm}$ of plasma density n_i, n_e in (a) and potential ϕ and electron temperature T_e in (b). (c) and (d): azimuthally averaged 1D axial profiles at $z = 1.3L_z = 1.3\,\text{cm}$ (near the channel outer wall) of plasma density n_i, n_e and electron axial current density $J_{e,x}$ in (c) and axial electric field E_x and electron temperature T_e in (d). The black dashed line in (c) and (d) corresponds to the axial cut position of (a) and (b), i.e, $x = 0.45L_x$.

5.4.2 Spectral analysis

Overview with a Dynamic Mode Decomposition approach

In Section 5.4.1, the discussion focused on the radial and axial directions of the HT but the azimuthal direction is crucial as well and is best explored through spectral analysis. During the transient phase, detailed in Section 5.3, several instabilities arise with different wavelengths in different directions. In order to highlight the modes present in the system, we use the Python library `Anatres` [Antares Development Team, 2020] and we perform a Dynamic Mode Decomposition (DMD) from Schmid [2010]. In Figure 5.12, we show the spectrum of the radial electron current density $J_{e,z}$, the axial electron current density $J_{e,x}$ and the azimuthal electric field E_y, as these three quantities present the most interesting oscillatory features according to Figure 5.8.

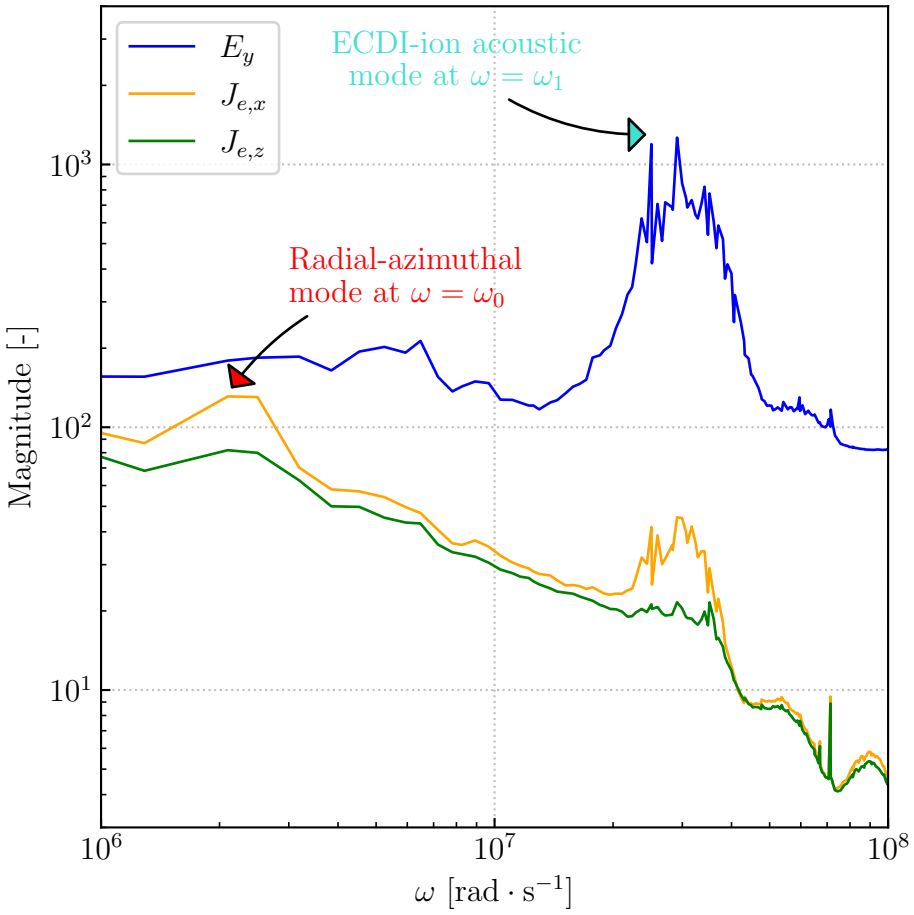

Figure 5.12: DMD spectrum obtained over the last microsecond for the azimuthal electric field E_y, the electron axial current density $J_{e,x}$ and the electron radial current density $J_{e,z}$. Two resonances at ω_0 and ω_1 can be observed.

For the azimuthal electric field E_y, we recognize a main peak at $\omega_1 \approx 3.3 \times 10^7\,\mathrm{rad\,s^{-1}}$, which corresponds to the main short-wavelength azimuthal instability of Figure 5.8. This dominant mode can be interpreted as the presence of the ECDI-ion acoustic instability. We shall provide more theoretical argument for this in the next paragraph.We can begin to be convinced of this by looking at the reconstructed mode of the azimuthal electric field E_y corresponding to $\omega = \omega_0$ in Figure 5.13.

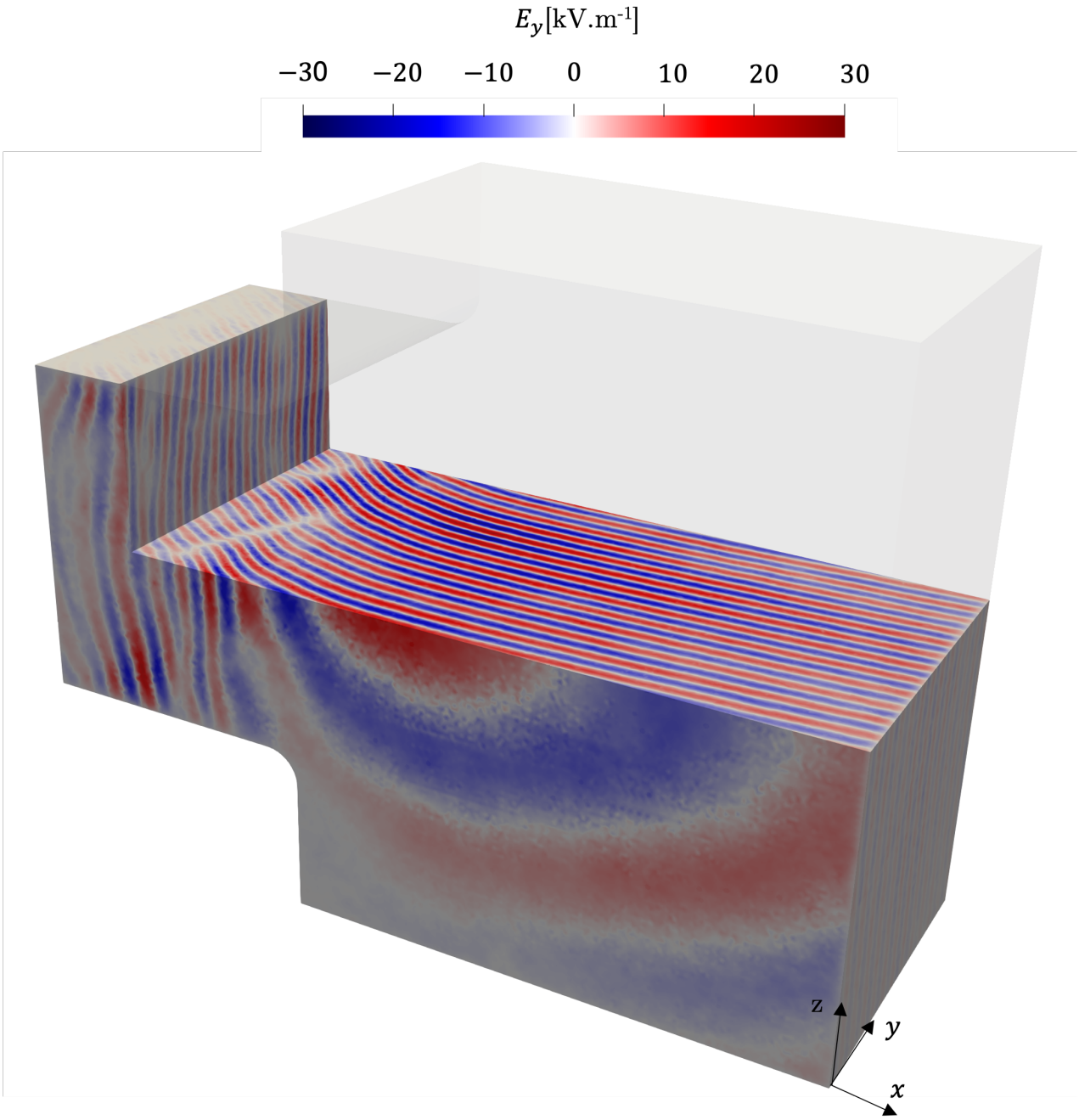

Figure 5.13: 3D clip view of the reconstructed mode $\omega = \omega_0$ of the azimuthal electric field E_y. Shaded grey areas correspond to the part of the domain that is not plotted here, i.e. satisfying both conditions $x > 0.12L_x = 3\,\text{mm}$ and $z > L_z = 1\,\text{cm}$.

In this 3D view we observe an azimuthal instability in the axial-azimuthal plane and in the radial-azimuthal plane, which is very similar to Figure 5.7 and Figure 5.8. Furthermore, we can see that this main mode is also responsible for the E_y pattern, resembling spherical-like waves, observed in the axial-radial plane in the plume region (see Figure 5.9 (f)). These first results show how useful the DMD is to identify and decouple multiple modes in this simulation.

This main mode is also present in the electron current densities $J_{e,x}$ and $J_{e,z}$, but with a much lower amplitude as seen in Figure 5.12. Another resonance, we call $\omega_0 \sim 2 \times 10^6\,\text{rad}\,\text{s}^{-1}$,

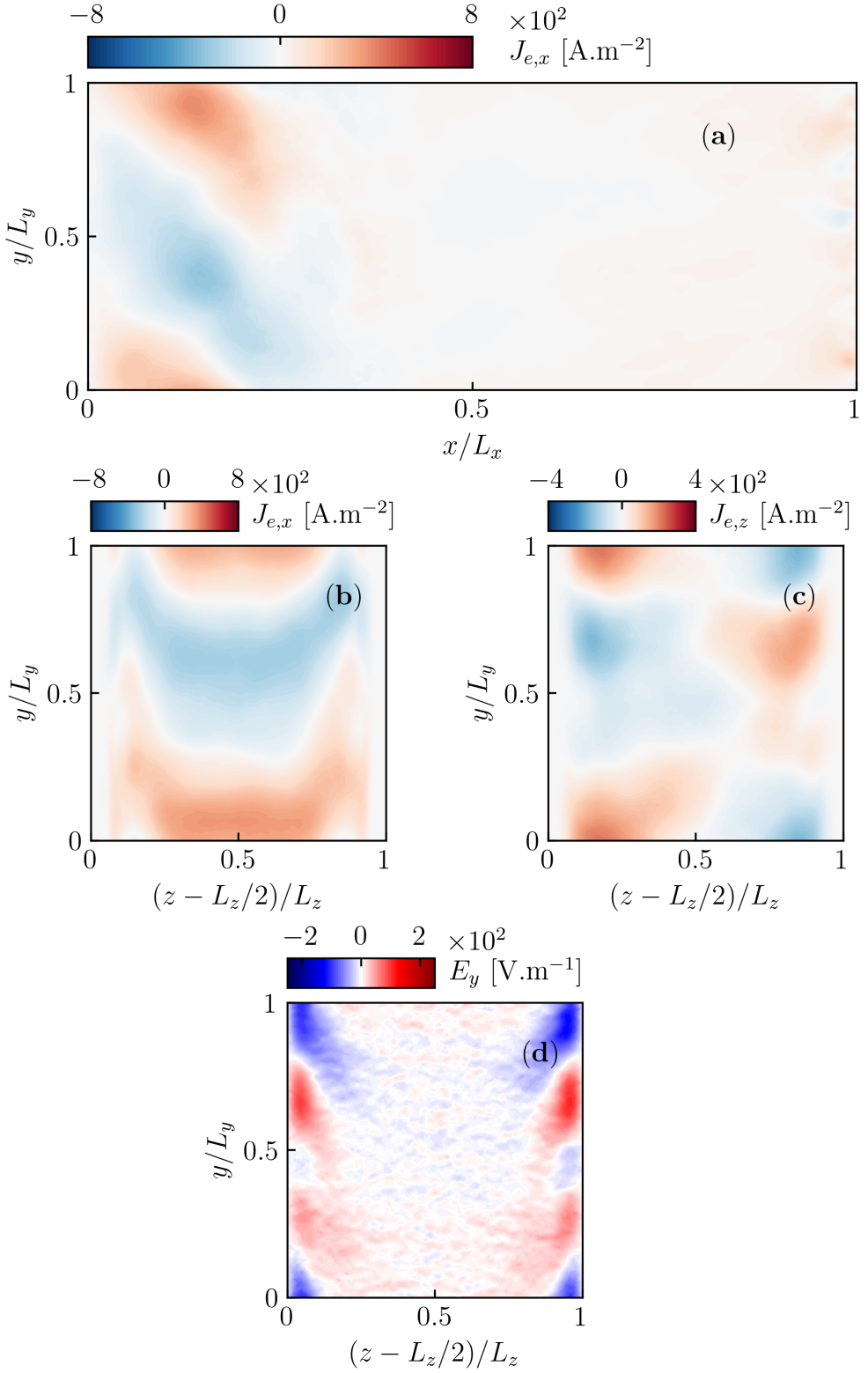

Figure 5.14: 2D views of the reconstructed mode $\omega_0 = 2 \times 10^6\,\mathrm{rad\,s^{-1}}$. (a): axial electron current density $J_{e,x}$ in the axial-azimuthal plane at $z = L_z$ (centerline). (b): axial electron current density $J_{e,x}$ in the radial-azimuthal plane at $x = 0.12L_x$ (inner channel). (c): radial electron current density $J_{e,z}$ in the radial-azimuthal plane at $x = 0.12L_x$. (d): azimuthal electric E_y in the radial-azimuthal plane at $x = 0.12L_x$.

shows up at low frequency, and is clearly visible for both the electron current densities $J_{e,x}$ and $J_{e,z}$. If we look at the corresponding reconstructed mode for $J_{e,x}$, $J_{e,z}$ and E_y, we obtain a radial-azimuthal pattern as shown in Figure 5.14. For $J_{e,x}$, the main features are visible in the axial-azimuthal and radial-azimuthal planes, depicted in Figure 5.14 (a) and (b) respectively. We observe that the instability is mainly azimuthal, with a wavenumber $k_y = 2\pi/L_y$, although a small radial component is also present in the radial-azimuthal plane. In Figure 5.14 (c), we show $J_{e,z}$ in the radial-azimuthal plane as well: a clear radial pattern is present with a wavenumber $k_z = \pi/L_z$. Again, the features observed on the raw data in Figure 5.8 are retrieved and a clear radial-azimuthal instability is captured. The azimuthal electric field, shown in Figure 5.14 (d), has a similar azimuthal wavenumber $k_y = 2\pi/L_y$ but note that the magnitude is around 15 times lower than the main mode presented in Figure 5.13. Although azimuthal radial instability is therefore present, it is very weak in comparison to what was observed in the pure 2D radial-azimuthal configuration presented in Chapter 4. Besides, as a reminder, the patterns were reversed in Chapter 4, meaning that $J_{e,z}$ showed a pure long wavelength azimuthal component whereas $J_{e,x}$ displayed a radial-azimuthal instability. At this point, there is no clear explanation for this inversion of patterns between 2D and 3D configurations.

Comparison with theoretical results: ECDI-ion acoustic wave

In order to consolidate our analysis we shall compare our numerical experiments with theoretical results.

First, we focus on the dominant mode labeled "ECDI-ion acoustic" in Figure 5.12. Thanks to the transient analysis and Figure 5.7 (last row, first column) in particular we know that this azimuthal mode grows inside the channel first. Therefore, we first apply a spectral analysis in the radial-azimuthal plane at the axial location $x = 0.12L_x$ for the azimuthal electric field E_y. In Figure 5.15 we present the temporal evolution of azimuthal wavenumbers. This is done by

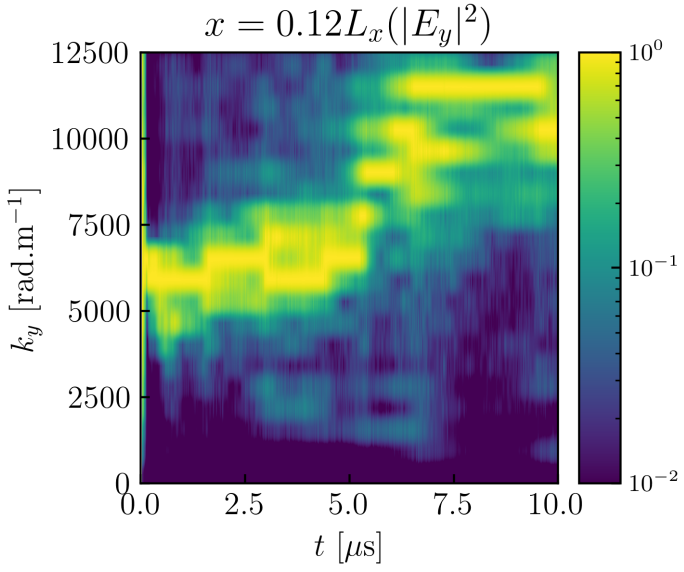

Figure 5.15: Temporal evolution of azimuthal wavenumbers k_y in the radial azimuthal plane located at $x = 0.12L_x$. Spectrum components have been normalized to the maximum value for each time.

performing a 1D FFT at each radial location at each time. We can can see that at the beginning

of the simulation a single mode appears dominant with a wavenumber $k_y \approx 6283\,\mathrm{rad\,m^{-1}}$. This situation goes on until around 5 µs, from which k_y increases meaning the azimuthal wavelength is reduced, which was exactly observed in Figure 5.7 and Figure 5.8.

Nonlinear effects play an important role in the evolution of plasma instabilities [Lampe et al., 1971a, 1972; Lafleur et al., 2016b] and dramatically complicate their analysis. Therefore we can start by focusing our efforts on the beginning of the simulation, when the linear theory of instabilities still applies. For this work, we can use the 3D dispersion relation (DR) derived by Ducrocq et al. [2006], that is recalled in Equation (5.11) and was already presented in Section 1.3.2:

$$\begin{aligned} 1+k^2\lambda_D^2 + \mathrm{g}\left(\frac{\omega - k_y V_d}{\Omega_{ce}}, \left(k_x^2 + k_y^2\right) r_L^2, k_z^2\rho^2\right) \\ - \frac{k^2\lambda_D^2\omega_{pi}^2}{\left(\omega - k_x v_p\right)^2} = 0, \end{aligned} \tag{5.11}$$

where λ_D is the Debye length, $\omega_p i$ the ion plasma frequency, Ω_{ce} the cyclotron frequency, $V_d = E_x/B_y$ the electron drift velocity, r_L the Larmor radius of electrons, v_p the velocity of the ion beam and k_x, k_y and k_z the axial, azimuthal and radial components of the wavenumber $\mathbf{k}$. $\mathrm{g}(\Omega, X, Y)$ is the Gordeev function [Gordeev G. V., 1952] that can be expressed in two ways:

$$\begin{aligned} \mathrm{g}(\Omega, X, Y) &= i\Omega \int_0^{+\infty} e^{-X[1-\cos(\varphi)] - \frac{1}{2}Y\varphi^2 + i\Omega\varphi}\mathrm{d}\varphi, \\ &= \frac{\Omega}{\sqrt{2Y}}\mathrm{e}^{-X} \sum_{m=-\infty}^{+\infty} \mathrm{Z}\left(\frac{\Omega - m}{\sqrt{2Y}}\right) \mathrm{I}_m(X), \end{aligned} \tag{5.12}$$

where I_m is the modified Bessel function of the first kind and Z the plasma dispersion function.

In contrast to earlier 2D PIC studies [Petronio et al., 2021; Janhunen et al., 2018a; Lafleur et al., 2016b; Boeuf and Garrigues, 2018; Hara and Tsikata, 2020], the DR does not need to be approximated and can fully take leverage of the present 3D PIC simulation. There is no analytical solution of Equation (5.11), but it can be numerically solved using a fixed point scheme described by Cavalier et al. [2013]. We implemented the DR solver using Python, well suited for this task [Oliphant, 2007], and the built-in Fadeeva function from `Scipy`. The `Plasmpy` package [Community et al., 2021] can directly provide the plasma function Z as well. For given plasma parameters and wavenumbers k_x, k_y and k_z, the scheme converges to a complex number $\Omega = \omega + i\gamma$ where ω and γ are the theoretical angular frequency and growth rate of the plasma wave. Input parameters are normalized with the ion plasma frequency ω_{pi}, the Debye length λ_D and the ion sound speed $c_s = (k_B T_e/m_i)^{-1/2}$ depending on whether they express a temporal frequency, spatial length or speed. Therefore, we start by rescaling the temporal evolution of the spectrum presented in Figure 5.15 and we obtain Figure 5.16 (a). First, we note that the previously observed increase of azimuthal wavenumber k_y is not reflected in the dimensionless quantity $k_y\lambda_D$, suggesting $k_y\lambda_D$ remains fairly constant over time except at the beginning of the simulation where $k_y\lambda_D \approx 0.5$. λ_D is calculated at each time as an average in the selected 2D plane at $x = 0.12L_x$ without the sheaths that were measured to be around 1 mm (see Section 5.4.1). In the first moments of the simulation, we can observe how the single mode $k_y \approx 6283\,\mathrm{rad\,m^{-1}}$ develops as shown in Figure 5.16 (b) in the dark green solid line. We can see that this component frequency quickly undergoes an exponential growth, that indicates we are in the linear stage of the plasma instability, i.e. $\partial_t E_y^2 \approx 2\gamma E_y^2$, where γ is the growth rate of the instability carried out by the azimuthal electric field. Note that this short period of time corresponds to the strong electron temperature increase observed in Figure 5.5 (c). With

least-square interpolation, we measure the exponential factor 2γ and we can compare it with the expected growth rate for this radial-azimuthal plane. The input parameters used by the DR solver at the beginning of the exponential growth are reported in Table 5.2.

Parameters	Symbol	Value	Unit
Plasma parameters			
Ion density	n_i	1.05×10^{17}	m^{-3}
Electron temperature	T_e	12.5	eV
Ion beam velocity	v_p	0	$\mathrm{m\,s}^{-1}$
Axial electric field	E_x	25.6×10^3	$\mathrm{V\,m}^{-1}$
Radial magnetic field	B_z	82.2	G
Wavenumbers			
Axial wavenumber	k_x	0	$\mathrm{rad\,m}^{-1}$
Azimuthal wavenumber	k_y	$0 - 5/\lambda_D$	$\mathrm{rad\,m}^{-1}$
Radial wavenumber	k_z	$\pi/L_z = 3.14 \times 10^2$	$\mathrm{rad\,m}^{-1}$

Table 5.2: Input parameters for the DR solver measured in the radial-azimuthal plane at $x = 0.12L_x$ at 0.5 µs without sheaths.

In Table 5.2, plasma parameters are averaged in the $x = 0.12L_x$ radial-azimuthal plane without the sheath. The azimuthal wavenumber spans the range $0 - 5/\lambda_D$, where λ_D is computed from the aforementioned plasma parameters. k_x is set to 0, meaning we assume the instability do not propagate in the axial direction, in the linear stage at least. Looking back at Figure 5.7 (last row, first column), it seems the instability is indeed purely azimuthal, which supports our choice. Furthermore, the effect of k_x turns out to be neutral on the growth rate γ because k_x is only involved in the $k_x v_p$ term in Equation (5.11). The same holds true for v_p. As shown by Cavalier et al. [2013], the final complex angular frequency ω can be written as $\omega = k_x v_p + \kappa$ where κ is some complex number with a non-negative imaginary part whereas $k_x v_p \in \mathbb{R}$ is a pure real number. Therefore assuming $k_x = 0$ or even $v_p = 0$ does not matter if we are only interested in the growth rate of the instability. Finally, the radial wavenumber k_z is set to π/L_z, similarly to what was done in Chapter 4, because plasma sheath effects make possible the existence of shorter wavenumbers below the geometrical constraint $k_z = 2\pi/L_z$ [Barrett et al., 1972; Chen, 1965]. For this particular case, the corresponding theoretical curve, shown in Figure 5.16 (c), was found to be relatively insensitive to setting either $k_z = \pi/Ł_z$ or $k_z = 2\pi Ł_z$ anyway. On this plot, we also report the numerical growth rate γ, labeled as "exp", previously computed in Figure 5.16 (b) and we can see there is an excellent agreement with the linear theory, with a maximum growth rate achieved for $k_y \lambda_D = 0.5$. We also note that the DR curve is not smooth but presents oscillations around a mean value. This effect was predicted by Cavalier et al. [2013]'s parametric study as the DR can transition from a discrete set of resonances, the growth rate being close to zero between each cyclotron resonances, to a continuous function that can be treated as an ion acoustic DR. The corresponding continuous ion acoustic DR for the growth rate, derived by [Lafleur et al., 2016b], is also shown on Figure 5.16 (c) and its

analytical expression, for the given conditions, is reminded in Equation (5.13).

$$\gamma = \sqrt{\frac{\pi m_e}{8 m_i}} \frac{k_y V_d}{(1 + (k_y \lambda_D)^2)^{3/2}} \tag{5.13}$$

We note that the ion acoustic DR (orange curve) is separate from the actual DR (blue curve), which indicates the transition to an ion acoustic mode is not achieved yet. However, since the actual DR exhibits a single resonance with small remaining oscillations, it suggests that we are already halfway between a pure discrete nature of the DR and a fully continuous ion acoustic DR. Besides, looking back at Figure 5.16 (a), we note that the main azimuthal wavenumber quickly increases from $k_y \lambda_D = 0.5$ to higher values. This result seems in agreement with a complete transition toward the ion acoustic DR as the maximum growth rate for Equation (5.13) is obtained for $k_{y,\max} \lambda_D = \sqrt{2}^{-1}$. This value is highlighted in Figure 5.16 (a) (red line) and we can see that it corresponds reasonably well to the maximum values extracted from the simulation after the linear stage.

The previous analysis can be extended to other radial azimuthal planes in the channel to verify how well the numerical results agree with linear theory. To do so, we select the most dominant mode in the first instants of the simulation for each considered axial position and we compute the corresponding growth rate with a least-square interpolation in Figure 5.16 (b). In the meantime, we also compute the theoretical DR using local plasma parameters and we extract the maximum growth rate. In all cases, the maximum growth rate was achieved approximately at the same dimensionless $k_y \lambda_D$ wavenumber. The final axial profile of the growth rate is shown in Figure 5.16 (d). Overall, we can see that numerical measurements are in excellent agreement with the linear theory, confirming that the dominant azimuthal mode is the ECDI. Yet, we also observe that the first growth rate obtained by the PIC simulation at $x = 0.04 L_x$ is about two times lower than expected. This might be due to a too low temporal resolution, which makes the linear regression difficult to conduct as we only have a handful of points to work with this axial position. Besides, the position $x = 0.04 L_x$ corresponds to $x = 1\,\text{mm}$, i.e. very close to the anode sheath, which is likely to create plasma conditions violating the assumptions used to derive the DR from linear theory. The other axial positions show that the dimensional γ growth rate decreases with x, which suggests the ECDI truly starts growing in the upstream section of the channel and is not an artifact of the axial profile of the Debye length λ_D. This result is consistent with what was observed in the 2D maps of azimuthal electric field E_y during the transient phase (Figure 5.7). However, since a convective wave appears during the transient (see Section 5.3) and the final azimuthal electric field also shows an axial periodic pattern, the initial ECDI wave probably acquires an axial wavenumber k_x at some point. In order to fully understand how and why this happens non-linear theory of plasma wave is necessary.

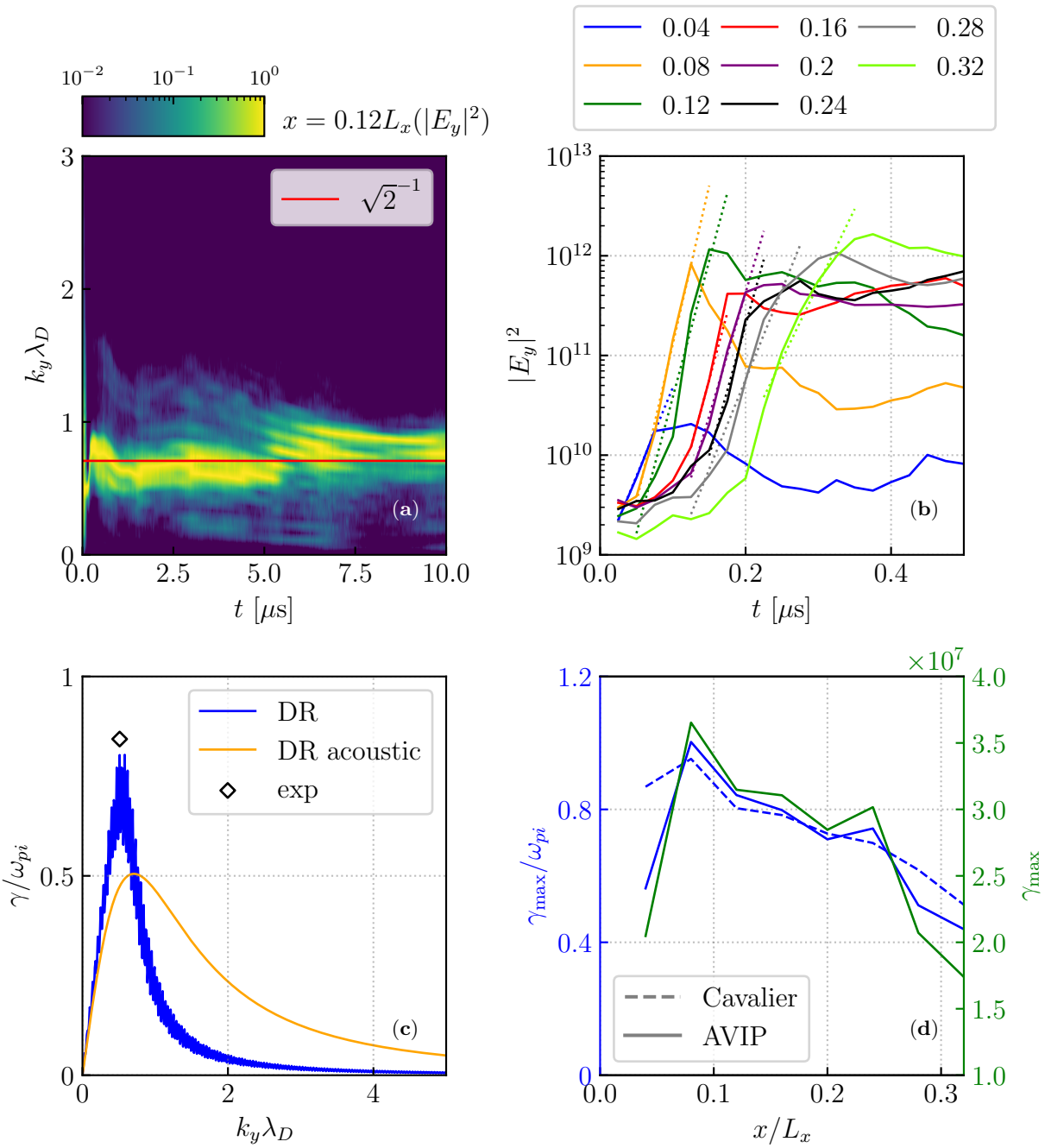

Figure 5.16: Growth and temporal evolution of the ECDI-ion acoustic instability. (a): temporal evolution of the dimensionless azimuthal wavenumber $k_y\lambda_D$ in the radial-azimuthal plane at $x = 0.12L_x$. The solid red line corresponds to the $k_y\lambda_D$ for which maximum growth rate is achieved for the ion acoustic wave [Lafleur et al., 2016b]. (b): temporal evolution of the dominant azimuthal wavenumber $k_y = 6283\,\mathrm{rad\,m^{-1}}$ at different axial locations expressed as a fraction of the axial length L_x. The exit channel is located at $x = 0.34L_x$. The dotted lines indicate the linear regression obtained with a least square method during the exponential growth of the instability. (c): comparison of the dimensionless growth rate γ/ω_{pi} (labeled as "exp") measured in the $x = 0.12L_x$ plane with linear theory (blue DR from Cavalier et al. [2013]) and asymptotic ion acoustic DR from Lafleur et al. [2016b] (orange solid line). (d) Axial profile of measured growth rates in its dimensionless and dimensional form γ/ω_{pi} (left y axis) and γ (right y axis). Results are compared with predicted dimensionless values stemming from linear theory by [Cavalier et al., 2013] (dashed line).

Discussion on the radial azimuthal mode

So far we focused our investigation on the dominant mode that is likely to be the ECDI as shown by the linear theory of instabilities. Besides, Figure 5.16 (c) suggests that a single Bernstein mode is actually excited in the channel. Overall, this result is consistent with the DMD spectrum presented in Figure 5.12 as a single mode dominates the whole domain. Indeed, the radial azimuthal mode, shown in Figure 5.14 (d) remains quite modest for the azimuthal electric field E_y given the amplitude is around $200\,\mathrm{V\,m^{-1}}$ vs $30\,\mathrm{kV\,m^{-1}}$ for the main ECDI mode (see Figure 5.13). At this point of our investigations, it is unclear why the radial azimuthal pattern is more visible in the current density fields $J_{e,x}$ and $J_{e,z}$. As a reminder, in the previous purely 2D radial-azimuthal case, two modes were excited: the MTSI and the ECDI (see Figure 4.6). Although it seems premature to confidently claim that the observed radial-azimuthal mode is the MTSI, Figure 5.17 suggests that the resemblance with the MTSI is nevertheless important. In this figure we select the radial azimuthal mode from the 3D simulation and also the identified MTSI from Chapter 4 in the dimensionless $(k_y\lambda_D, k_z\lambda_D)$ plane. In 2D, the set of couples $(k_y\lambda_D, k_z\lambda_D)$ leading to a maximum growth rate $\gamma_{\max}$ for the MTSI can be approximated by a simple parabola equation derived by Petronio et al. [2021] whose dimensionless form reads:

$$k_z\lambda_D = \frac{m_e E_x}{eB_z^2\lambda_D}(k_y\lambda_D)^2. \tag{5.14}$$

For both the 2D and 3D simulations, the corresponding parabolas were computed based on local plasma conditions. For the 2D simulation, the couple $(k_y\lambda_D, k_z\lambda_D)$ is coherently found to be close to the maximal growth rate of the MTSI. For the 3D simulation, the radial-azimuthal mode is also very close to the 2D maximum growth rate, which invites us to consider that the MTSI is also present in this configuration. Obviously, since the parabola equation was derived for a 2D configuration, no formal proof can be inferred at this point. However, this finding encourages us to explore other initial plasma conditions to assess whether or not it is possible to trigger a clear MTSI in 3D.

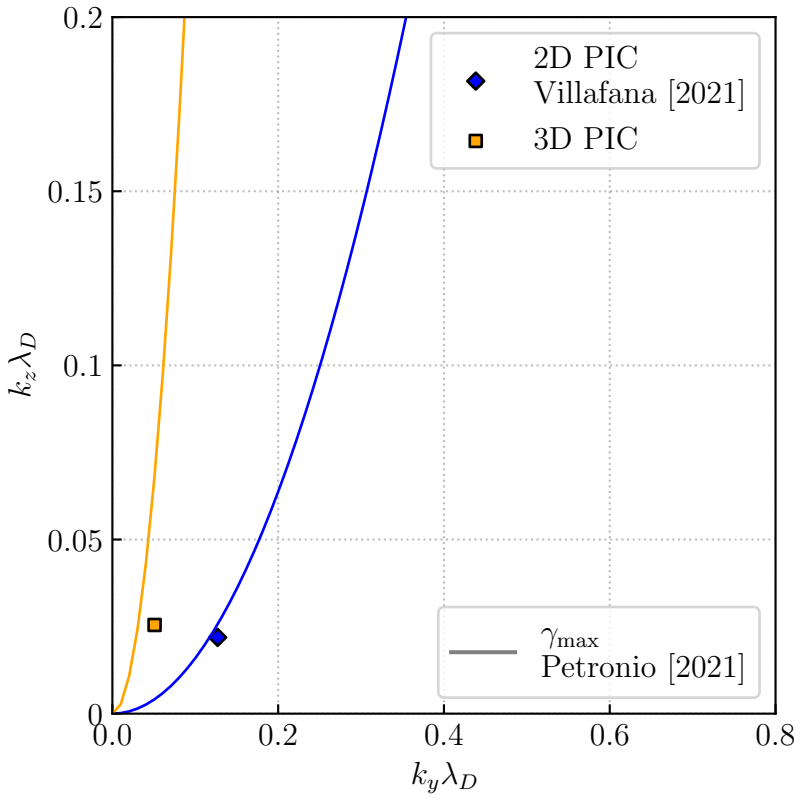

Figure 5.17: Comparison of 2D and 3D PIC results with the theoretical maximum growth rate for the MTSI in 2D [Petronio et al., 2021]. The 2D result is taken from Chapter 4 that was published in [Villafana et al., 2021]. The 3D result is obtained from the radial azimutal mode, i.e. $k_y = 2\pi/L_y$ and $k_z = \pi/L_z$, at $x = 0.12L_x$.

5.5 Comparison with 2D simulation

5.5.1 Context and numerical setup

As mentioned in Section 1.4.2, most PIC simulations are performed in 1D-2D academic configurations mainly because of the tremendous numerical cost of 3D runs. This constraint can affect the 3D nature of the HT physics. Therefore, in this Section, we propose to explore and assess the differences that might arise between the present 3D simulation and an analogous pure 2D-3V setup.

For this effort we decided to consider a 2D axial-azimuthal domain and to use the same parameters as in the 3D simulation. We could also have considered a 2D radial-azimuthal domain as in Chapter 4, but two concerns emerged. First, the axial electric field is imposed and so it is uniform in the domain whereas it clearly varies in time and space in the 3D simulation. In fact the axial electric field will self adjust to the existing plasma conditions. Second, a steady state can only be obtained by assuming an axial virtual model, that gets rid of the most energetic particles. The chosen axial length and the way of re-injecting particles will inevitably affect the evolution of instabilities and the overall plasma dynamics. Such an effect was already reported by Tavant [2019]; Lafleur et al. [2016a]; Asadi et al. [2019]; Smolyakov et al. [2020]. As a result, it seemed complicated to design a 2D simulation as close as possible to its 3D counterpart.

Going back to the axial azimuthal configuration, we consider a rectangular domain that is similar to the centered 2D plane obtained with a cut at $z = L_z$ in the 3D case. The simulation domain is shown in Figure 5.18. Most parameters defining the original 3D domain in Table 5.1 can be immediately used for the 2D simulations and are reported in Table 5.3. In particular the axial and azimuthal lengths, L_x and L_y respectively, are the same. The boundary conditions in the axial and azimuthal directions are also identical: periodicity at $y = 0$ with $y = L_y$ and "exit" conditions for particles at $x = 0$ and $x = L_x$. The potential is set to 200 V at the anode and 0 V at the cathode, where the quasi-neutral (QN) model is used. The magnetic field strictly follows Equation (5.8) as in the 3D case. The 2D mesh also has a similar cell size with $\Delta x = \Delta y = 50\,\mu\text{m}$, whereas it was $\Delta l = 67\,\mu\text{m}$ in the 3D case. Computational parameters and initialization conditions are the same. Finally, the 2D ionization source term profile $S_{2\text{D}}$ is the same as in Chapter 3, given by

$$\begin{cases} \text{if } x \in [x_1, x_2] & S_{2\text{D}}(x) = S_0 \cos\left(\frac{x - x_m}{x_2 - x_1}\right) \\ \text{else} & S_{2\text{D}}(x) = 0. \end{cases} \tag{5.15}$$

Note that this profile exactly corresponds to the 3D profile $S_{3\text{D}}$ in the centered axial-azimuthal plane. Mathematically this results in writing: $S_{2\text{D}}(x) = S_{3\text{D}}(x, z = z_M)$. One consequence of this choice is that the current densities $J_{m,2\text{D}}$ and $J_{m,3\text{D}}$ cannot be equal for both simulations and from Equation (5.4) we can infer:

$$\left.\begin{aligned} J_{m,2\text{D}} &= \tfrac{I_{tot}}{L_y} = e\tfrac{2}{\pi} S_0 (x_2 - x_1) \\ J_{m,3\text{D}} &= \tfrac{I_{tot}}{L_y L_z} = e\tfrac{4}{\pi^2} S_0 (x_2 - x_1) \tfrac{(z_2 - z_1)}{L_z} \end{aligned}\right\} \Rightarrow \frac{J_{m,2\text{D}}}{J_{m,3\text{D}}} = \frac{\pi}{2} \frac{L_z}{z_2 - z_1} > 1. \tag{5.16}$$

Therefore, this geometrical effect results in actually setting $J_{m,2\text{D}} \approx 730.5\,\text{A m}^{-2}$ vs $J_{m,3\text{D}} \approx 400\,\text{A m}^{-2}$. In order to check that we have chosen the closest ionization profile for our 2D case, we also performed a simulation with $J_{m,2\text{D}} \approx 400\,\text{A m}^{-2}$. It appeared that the final density level was much lower than in the 3D case and therefore this case was discarded.

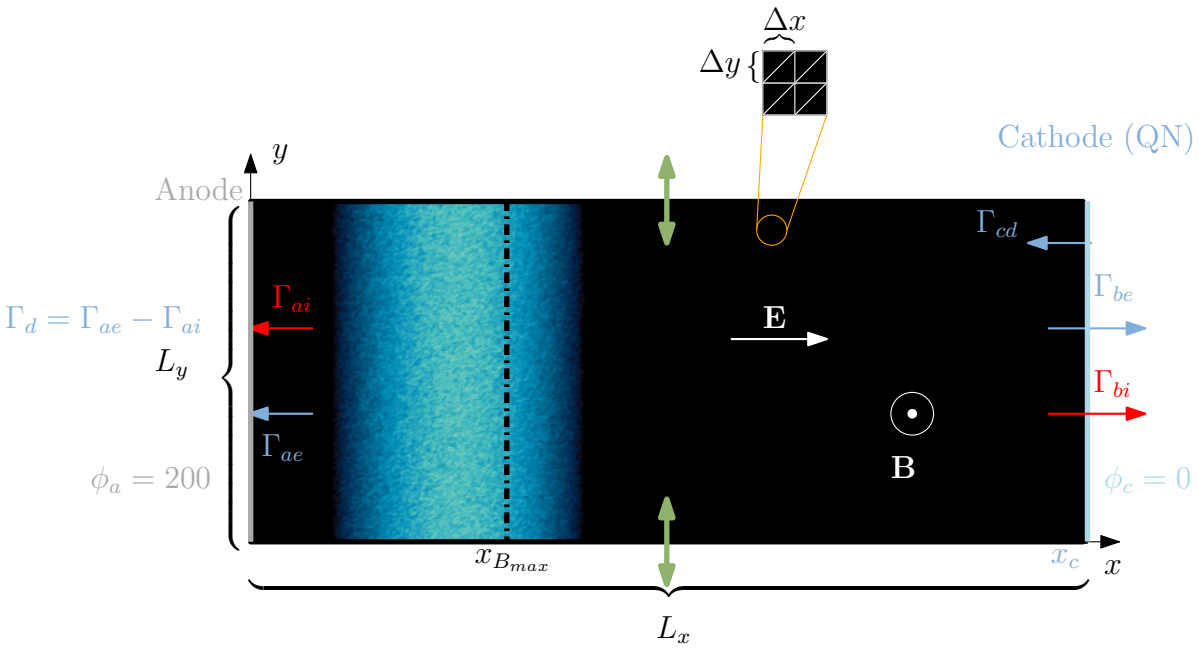

Figure 5.18: 2D axial azimuthal simulation domain compared to 3D results measured at $z = L_z$.

Parameters	Symbol	Value	Unit
Simulation domain			
Cell size	$\Delta x = \Delta y$	50	µm
Domain size	$L_x \times L_y$	2.5×1	cm^3
Number of triangular cells	N_{cell}	$500 \times 200 \times 2$	
Number of nodes	N_{nodes}	100.701	
Initial conditions			
Plasma density	n_0	1×10^{17}	m^{-3}
Ion temperature	$T_{i,0}$	0.5	eV
Electron temperature	$T_{e,0}$	10	eV
Number of particles/cell	$N_{ppc,ini}$	75	
Ionization module			
Axial limits	(x_1, x_2)	(0.25,1.00)	cm
Electromagnetic fields			
Anode potential	ϕ_a	200	V
Cathode potential	ϕ_c	0	V
Maximum magnetic field	B_{max}	100	G
Position of maximum magnetic field	x_{Bmax}	0.75	cm
Magnetic field at anode	B_a	60	G
Magnetic field at cathode	B_c	10	G
Computational parameters			
Time step	Δt	5	ps
Average time range	N_a	$5000\Delta t$	s
Subcylcing frequency	f_{sub}	5	iterations

Table 5.3: Simulations parameters for the 2D axial-azimuthal simulation domain that is compared to 3D results measured at $z = L_z$. As a reminder, the 3D case parameters are defined in Table 5.1

5.5.2 Main plasma variables

As usual, we can start looking at the temporal evolutions of profiles of interest.

In Figure 5.19 (a), the mean ion density profile n_i is shown for both configurations. In the first instants, the density linearly increases with the same slope, which indicates our choice for the ionization source term create similar plasma conditions for both the 2D and 3D simulations. Nevertheless, from around 1 µs, n_i continues to rise for the 2D case whereas it starts to saturate in the 3D simulation. This difference may be due to the presence of the walls in 3D, which probably limits the maximal possible density. In 2D, losses are mitigated. In the 2D case, the density reaches a maximum value $n_i = 4 \times 10^{17}\,\mathrm{m}^{-3}$ at 2.5 µs. It then drops until 5 µs before slowly increasing again to stabilize at around $3 \times 10^{17}\,\mathrm{m}^{-3}$ at 15 µs. These strong variations are due to the initial plasma wave leaving the domain at the cathode. Therefore, this phenomenon is similar to what was described in the 3D case in Figure 5.6. However, n_i does not vary with the same magnitude compared to the 3D simulation. In this regard, wall losses probably avoid the strong initial overshoot, which helps the simulation to reach a steady state more quickly. As a result, the 3D case only need 10 µs to stabilize vs 15 µs in 2D.

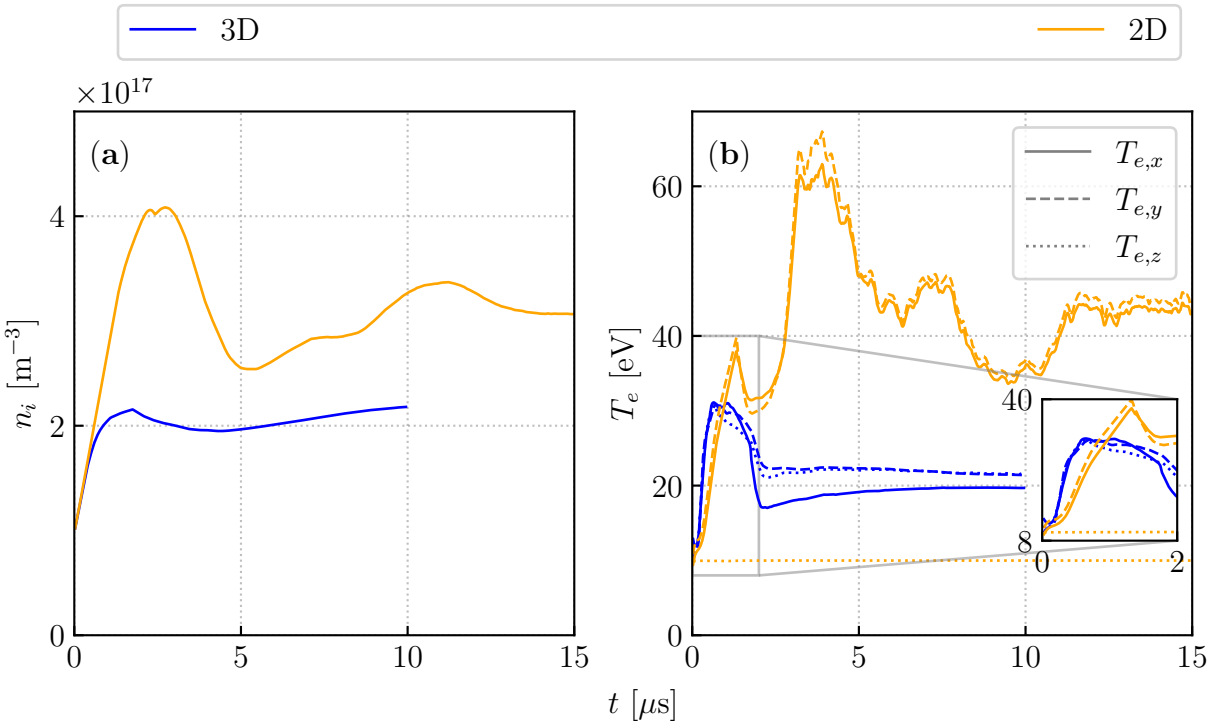

Figure 5.19: Comparison of temporal evolutions of (a) mean ion density n_i and electron temperature components $T_{e,x}$ (axial), $T_{e,y}$ (azimuthal) and $T_{e,z}$ (radial) for the pure 2D simulation (orange lines) and the corresponding axial azimuthal domain at $z = L_z$ from the 3D simulation (blue lines).

In Figure 5.19 (b), we compare the electron temperature components in 2D and 3D. In both cases, the axial and azimuthal temperature $T_{e,x}$ and $T_{e,y}$ increase in the first moments of the simulation. However, we note that the slope is stiffer in 3D than in 2D, but the heating is also less durable. In approximately 0.5 µs the temperature reaches a maximum of 30 eV in 3D. In contrast, the 2D case shows a long lasting heating and the temperature continues to rise up to 1.5 µs with a maximum of 40 eV. At this point, it is not clear why the slope of temperature

increase is higher in 2D but the short duration of the heating could again be related to the presence of walls. Another noteworthy difference lies in the radial electron temperature profile $T_{e,z}$. It is constant in the 2D case as it is parallel to the imposed magnetic field, whereas it varies in a similar manner as the azimuthal electron temperature profile $T_{e,y}$ in 3D. After the first microseconds, the temperature slightly decreases in 3D before stabilizing at its final value around 20 eV. In 2D, the situation is quite different. Indeed, $T_{e,x}$ and $T_{e,y}$ sharply increase again at 2.5 µs and reach a maximum of $\sim$ 65 eV. Then, both $T_{e,x}$ and $T_{e,y}$ drop at around 35 eV before stabilizing at 45 eV.

In conclusion, the plasma is overall hotter and denser in 2D than in 3D. We shall now investigate what are the subsequent implications for the steady state shown in Figure 5.20.

Figure 5.20 (a) and (b) provide more details about the distribution of the plasma density in the domain. The 3D case presents higher levels of n_i in the channel but the 2D case shows a denser plasma in the plume. In the channel, a similar short-wavelength azimuthal wave, characteristic of the ECDI propagates in the $\mathbf{E} \times \mathbf{B}$ direction. In the plume however, the 2D case shows a long-wavelength azimuthal instability as it was observed in Figure 3.2. In 3D no such structure can be seen at this point. The dynamics of electrons are also very different in both cases. In 2D, electrons are shifted toward the $+y$ direction during their travel from the cathode to the anode. Their trajectory is also perturbed when they cross the longer wavelengths in the plume. In 3D, the situation differs greatly. First, some electrons from the cathode go back toward the cathode, which is again a side effect of the quasi-neutral (QN) model noticed earlier and that seems to be amplified in 3D. Furthermore, the electrons preferentially move in the $-y$ direction in the plume, which is surprising. Although this means that the $v_{e,y}$ component is important, it does not prevent electrons to actually enter the 3D channel. In fact, if we remember Figure 5.9 (d), the electrons do enter the channel from the top and bottom exit.

In Figure 5.20 (c) and (d), the ECDI waves propagating in the $\mathbf{E} \times \mathbf{B}$ direction are clearly visible but with some differences. In the channel, both the 3D and 2D have similar wavelengths but the 3D case show a slightly greater k_x contribution, resulting in a more inclined pattern. In the plume, the wave is perpendicular to the y direction for both cases, but we note a stark difference as well. In 3D, the wavelength in 3D looks very similar as in the channel, whereas, in 2D the wavelength is twice the wavelength in the channel. Overall, we also note that the magnitude of oscillations is three times bigger in 2D than in 3D. The difference in magnitude could be related to local plasma conditions (n_i, T_e) that reach greater levels in 2D as seen in Figure 5.19.

In Figure 5.20 (e) and (f) we continue our investigation with the electron axial current density $J_{e,x}$. Again the 2D maps are quite different. In 3D, $J_{e,x}$ presents the ECDI wavelength in the channel along with the large azimuthal wavelength whose size is $\sim$ Ł$_y$ as detailed in Section 5.4.2. In the plume, no pattern can be detected. Side effects are visible near the cathode on the right where part of the electrons enter and leave the domain several times. In 2D, the cathode effect is not visible and no ECDI pattern can be seen in the channel. However, the long azimuthal wavelengths of the plume are well described once again. In 3D, it seems that the transition from short-wavelengths (channel) to long ones (plume) happens whenever the Mach number $M_e > 0.5$. We can also note that $J_{e,x}$ is in average ten times lower in 3D than in 2D.

Finally, in Figure 5.20 (g) and (h), we highlight another difference between 2D and 3D simulations. In 2D, in Figure 5.20 (h), the 2D maps seems mostly uniform. In contrast, the 3D case in Figure 5.20 (g) highlights the presence of the long azimuthal wavelength of size $\sim L_y$,

which suggests wall effects are visible even in the centerline of the channel.

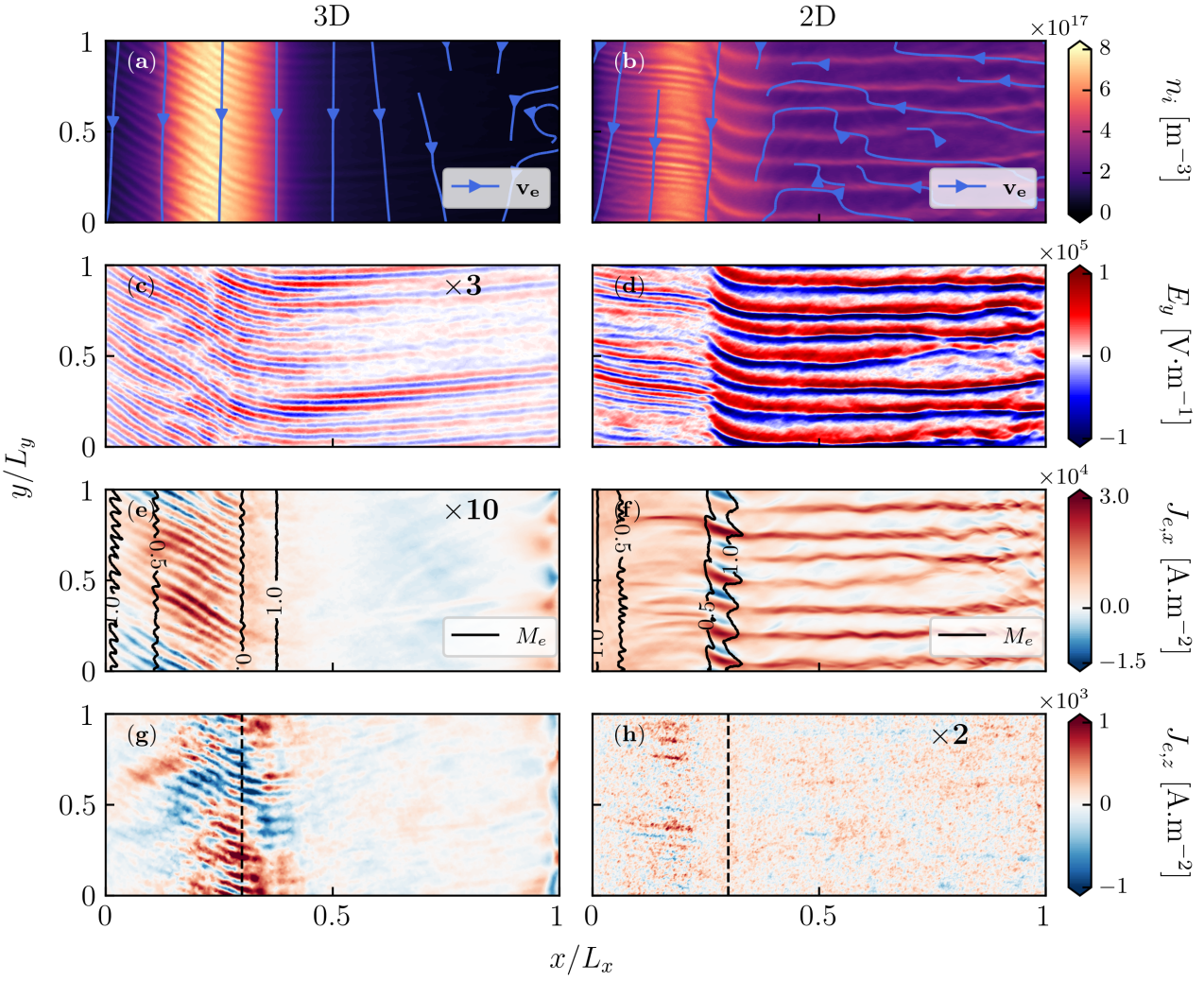

Figure 5.20: Comparison of steady states between the 3D (left column) and 2D (right column) simulations. (a-b): ion density n_i with electron streamlines $\mathbf{v}_e = v_{e,x}\mathbf{x} + v_{e,y}\mathbf{y}$. (c-d): azimuthal electric field E_y. In (c), E_y values have been multiplied by 3 to fit on the same scale as (d). (e-f): electron axial current $J_{e,x}$ with iso-Mach lines. In (e), $J_{e,x}$ values have been multiplied by 10 to fit on the same scale as (f). (g-h): electron radial current $J_{e,z}$. Dashed line indicates maximum of magnetic field. In (g), $J_{e,z}$ values have been multiplied by 2 to fit on the same scale as (h).

In order to get more quantitative information on the steady state, we can compare different axial profiles at steady state as shown in Figure 5.21. Figure 5.21 (a) confirms the observation made in Figure 5.20 (a) and (b) concerning the ion density n_i. In 3D, n_i reaches a higher maximum value of 7.5 m^{-3} vs 5.8 m^{-3} in 2D. Because of the plasma expansion, the density dramatically drops in the plume in 3D while it stabilizes at $\approx$ 2.5 m^{-3} in 2D. Overall the averaged density in the whole domain is higher in 2D. In Figure 5.21 (b), we can see that the plasma is hotter in 2D with a maximum of 73 eV vs 53 eV in 3D. We also note that the maximum happens at $x = 0.25L_x$ in 2D whereas it occurs at $x \approx 0.38L_x$, which is outside the channel exit located at $x = 0.34L_x$. Another interesting feature to look at is the axial profile of

the mobility. As a reminder from Equation (1.21), the mobility μ_{PIC} can be calculated as the ratio of the axial electron speed $u_{e,x}$ to the axial electric field E_x:

$$\mu_{\text{PIC}} = \left| \frac{u_{e,x}}{E_x} \right|. \tag{5.17}$$

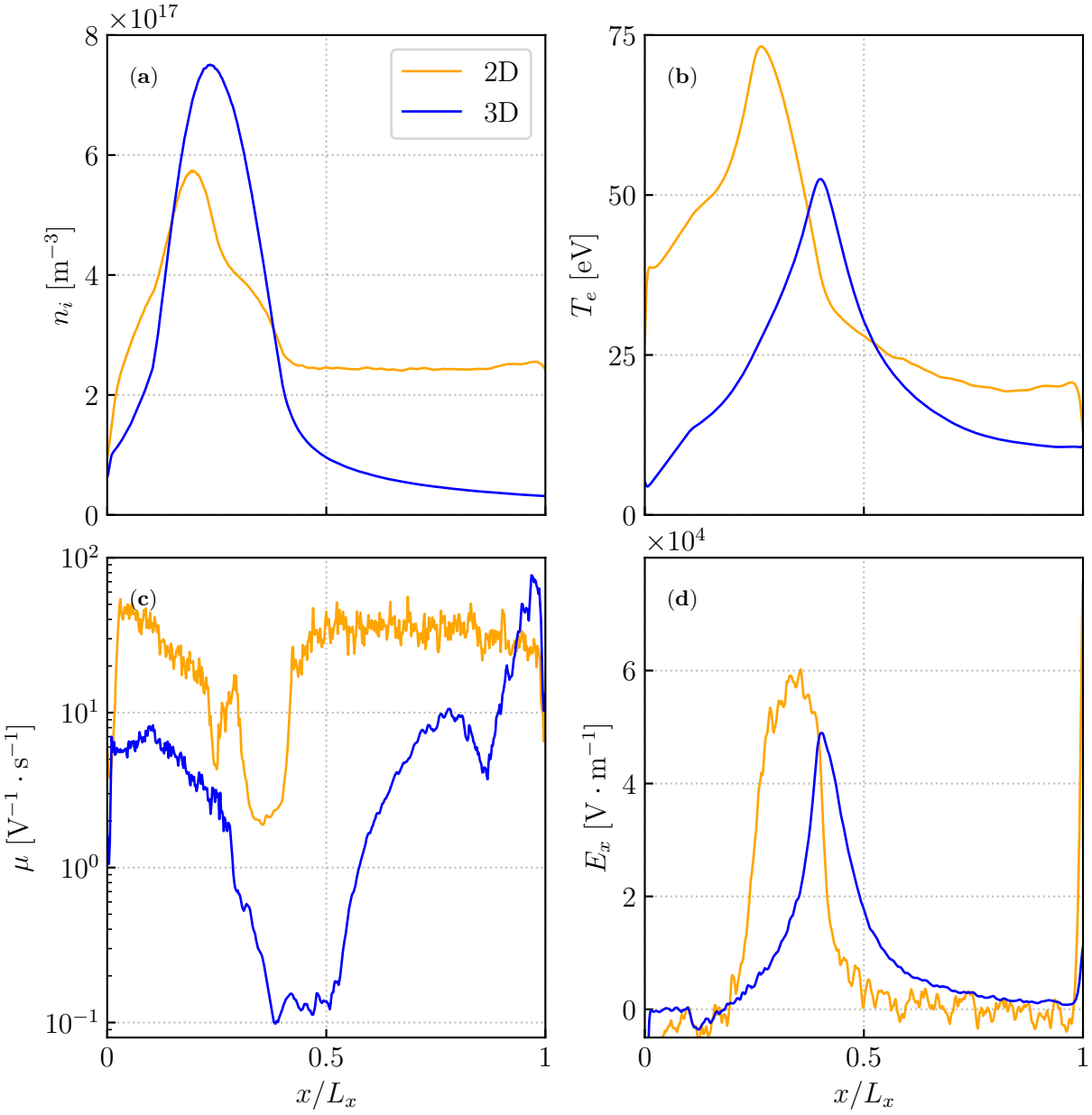

Figure 5.21: Comparison of averaged axial profiles at the steady state between the 2D (orange) and 3D case (blue). (a): ion density n_i. (b): total electron temperature T_e. (c): measured mobility μ_{PIC}. (d): axial electric field E_x.

For the results presented in Figure 5.21 (c), we can see that in both 2D and 3D the mobility drops around the channel exit by several orders of magnitude, which is expected. However, while in 2D μ_{PIC} is divided by 10, it is decreased by a factor of 20 in 3D. Overall, the mobility is much lower in 3D than in 2D which results from a lower axial electron velocity in 3D. Indeed,

Figure 5.21 (d) shows similar levels of axial electric field E_x, but with a shift of maximum values similar to that of Figure 5.21 (b). As detailed in Section 1.3.2, this observation is coherent with the predicted mobility in a collisionless plasma for which μ is proportional to coherent azimuthal fluctuations of the azimuthal electric field E_y with the electron density n_e. Yet, as seen in Figure 5.20, azimuthal fluctuations have overall a much lower magnitude in 3D than in 2D, which is coherent with a lower mobility. Therefore, a further understanding of the instabilities taking place in the domain is required. This will be the subject of the next section.

5.5.3 Spectral analysis

We can start our investigation by looking at the linear stage, when the ECDI grows exponentially. This is done in Figure 5.22. We can see that while the ECDI develops near the anode in 3D, the azimuthal instability appears in the near plume region first at $x \sim 0.5L_x$ in 2D at a later time (0.4 µs vs 0.2 µs). Azimuthal fluctuations also grow near the anode but with a slight delay.

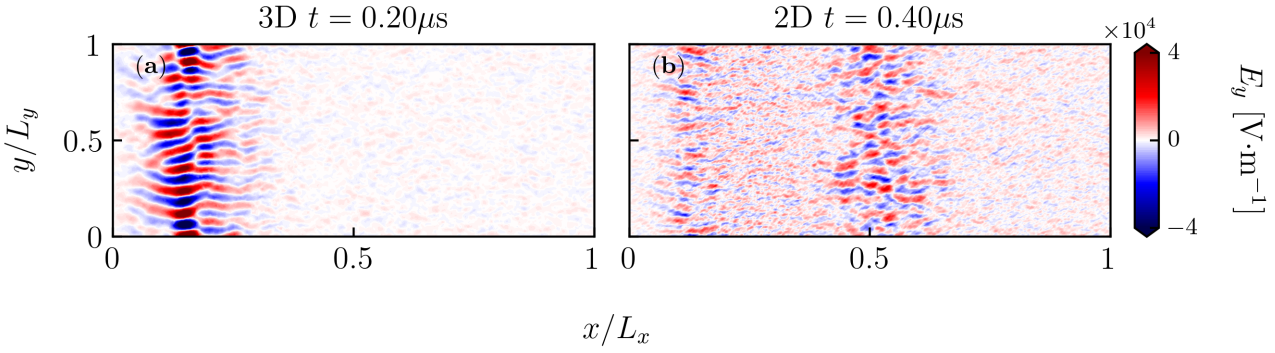

Figure 5.22: Comparison of azimuthal electric field E_y in the first moments of the simulation in 3D (left) and 2D (right). The same scale is used for both the 2D and 3D configurations.

In order to understand why the ECDI first appears in the near plume region in 2D we would need to use the linear theory of instabilities as it was done in Section 5.4.2. Unfortunately, Equation (5.11) cannot be used because the Gordeev function detailed in Equation (5.12) does not converge for $k_z = 0$, which is the condition imposed in 2D. A more specific theory would have to be developed in this case.

However, we can still analyze the azimuthal instabilities at steady state. Indeed, as explained by Lafleur et al. [2016a,b], the initial ECDI in 2D and 3D can transition toward an ion acoustic-like instability. In this case the dispersion relation (DR) $\omega_R(\mathbf{k})$ is given by Equation (3.5) at two axial positions: in the channel at $x = 0.12L_x$ and in the plume at $x = 0.6L_x$. In the channel (Figure 5.23 (a) and (b)), we can see that the main modes in both the 2D and 3D simulations are well predicted by the modified ion acoustic DR. In 2D, the results seem to be more continuous as the dominant modes closely follow the theoretical DR whereas in 3D a single mode appears to prevail. We can also note that in both simulations, the transition to the ion acoustic wave led to a different main mode: $(k_{y,\max}\lambda_D = 0.4, \omega_{\max}/\omega_{pi} = 0.4)$ for the 3D case vs $(k_{y,\max}\lambda_D = 1.02, \omega_{\max}/\omega_{pi} = 0.71)$ in 2D.

In the plume (Figure 5.23 (c) and (d)), both the 3D and 2D differ. In 3D (Figure 5.23 (c)), the azimuthal wave now has a higher $(k_{y,\max}\lambda_D = 0.8, \omega_{\max}/\omega_{pi} = 0.63)$ than in the channel. In contrast, in 2D we observe the inverse phenomenon: both the angular frequency and the

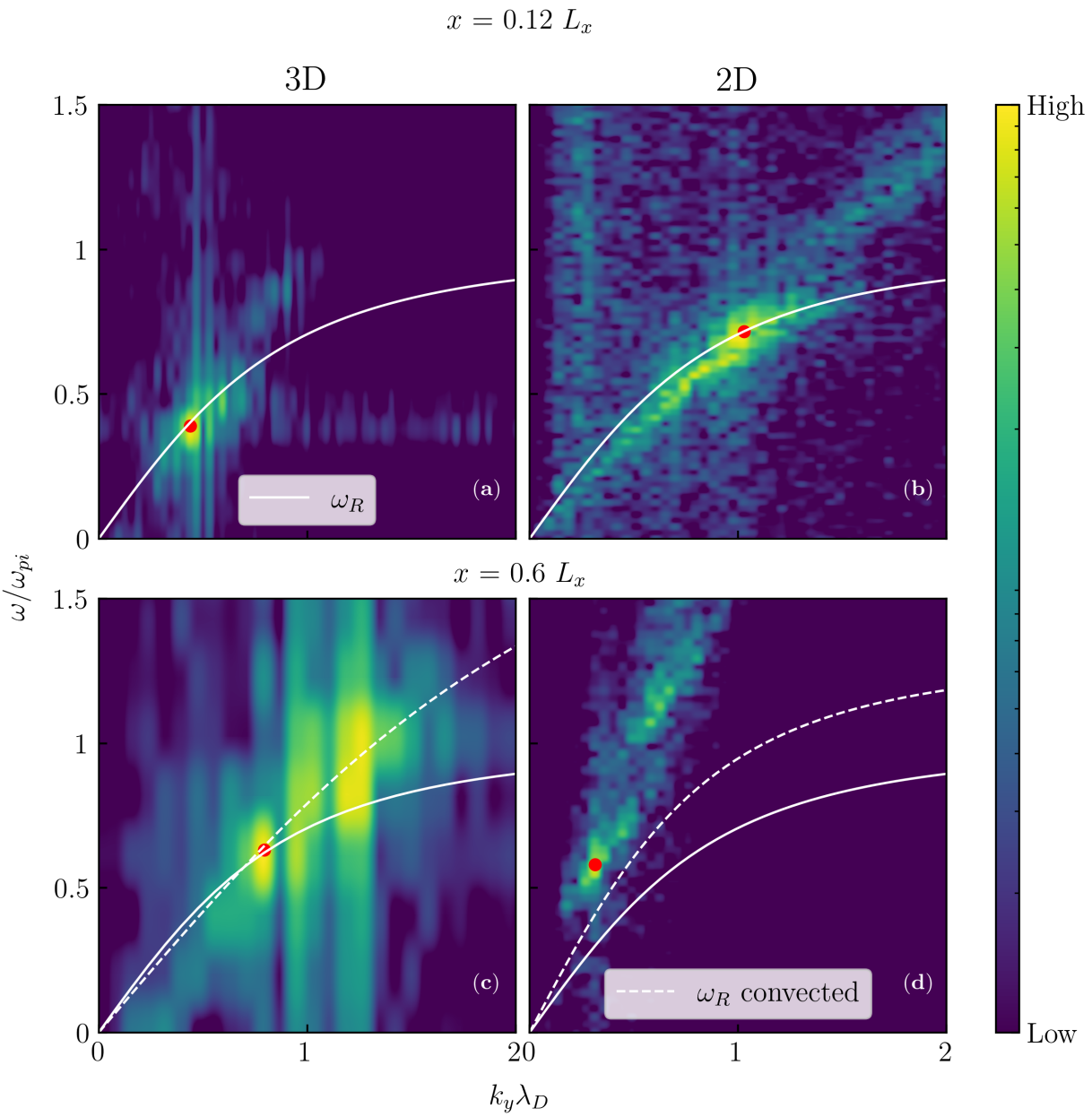

Figure 5.23: Numerical dispersion relation in 3D (left column) and 2D (right column) at two different axial locations at steady state: in the channel at $x = 0.12L_x$ (first row) and in the plume at $x = 0.6L_x$. The modified ion acoustic dispersion relation $\omega_R(\mathbf{k})$ is indicated by the white solid line. In (c-d), the white dashed line corresponds to $\omega_R(\mathbf{k})$ from the channel at $x = 0.12L_x$ normalized with local plasma conditions at $x = 0.6L_x$. In all plots, red dots correspond to the dominant resonance.

azimuthal wavenumber have decreased with respect to the channel: ($k_{y,\max}\lambda_D = 0.3, \omega_{\max}/\omega_{pi} = 0.57$). Besides, in the 2D case, the main mode is not well predicted by the theoretical DR $\omega_R(\mathbf{k})$. The discrepancy might be resolved by assuming that in 2D, the ion acoustic wave first grows in the channel before being convected away in the plume where it does not grow anymore. In such a case, the initial DR from the channel at $x = 0.12Lx$ would remain approximately unchanged in the plume. Using local plasma conditions λ_D, ω_{pi} at $x = 0.6L_x$ to normalize

the DR, we obtain the white dashed line in Figure 5.23 (d). We can see that this convected DR would match 2D numerical results better. This observation is consistent with previous 2D axial-azimuthal investigations [Charoy, 2020, Chapter 6] and [Tavant, 2019, Chapter 7]. In 3D, a similar situation seems to happen as well, but is not as clear as in 2D because the "local" DR is not too different from the "convected" DR.

The transition from the channel to the plume is clearly visible in both 2D and 3D cases in Figure 5.24. In the channel, the 2D simulation present a higher $(k_y\lambda_D, \omega/\omega_{pi})$ than the 3D case, before the situation is reversed in the plume from approximately $x = 0.34L_x$, which corresponds to the channel exit (see Figure 5.24 (a)). In 3D, both $k_y\lambda_D$ and ω/ω_{pi} show greater values in the plume partly due to the respective increase and decrease of λ_D and ω_{pi}, as shown in Figure 5.24 (b). In 2D, the reverse occurs.

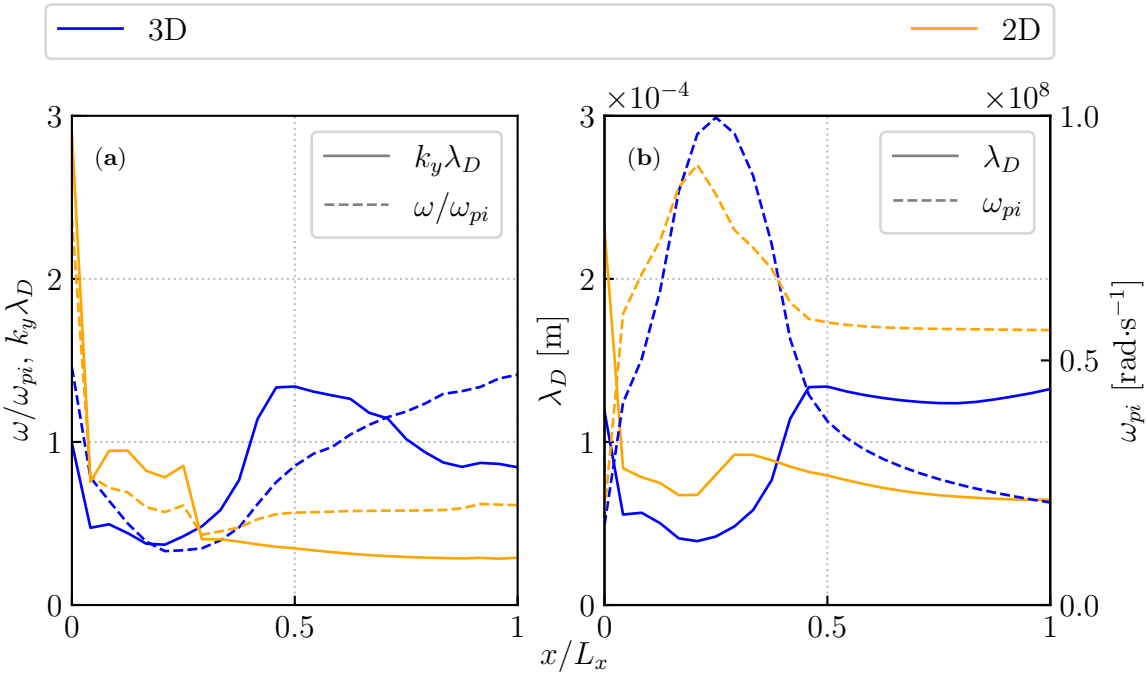

Figure 5.24: Axial evolution of (a) main dimensionless azimuthal wavenumber $k_y\lambda_D$ (solid line) and angular frequency ω/ω_{pi} (dashed line) and (b) Debye length λ_D (solid line) and ion plasma frequency ω_{pi} (dashed line) in 2D and 3D.

A final difference can be noted regarding the ion trapping phenomenon. According to the theory of beam-cyclotron instabilities [Lampe et al., 1972, 1971a; Dewar, 1973] and recent work [Lafleur et al., 2016b], ion trapping is expected to play a role in the saturation of the azimuthal instability and thus limit its initial exponential development. In 1D [Lafleur et al., 2016a] and 2D [Boeuf and Garrigues, 2018] simulations, ion trapping therefore appears systematically during the saturation of the instability. In Figure 5.25 we represent the ion phase space along the azimuthal y direction to assess ion trapping in 2D and 3D. In Figure 5.25 (a) (3D case), we can see typical loops of ion trapping of a rather small amplitude, the average minimum speed being $\sim -4 \times 10^4\,\mathrm{m\,s^{-1}}$. The number of loops is imposed by the azimuthal wavelength of the electric field E_y. In 2D, ion trapping is also present but the loops have much higher amplitude with an average minimum speed of $\sim -12 \times 10^4\,\mathrm{m\,s^{-1}}$. The discrepancy in magnitude can be related to the difference of amplitude oscillations observed in Figure 5.20 (c-d) where the azimuthal

electric field E_y in 2D was approximately three times greater than in 3D.

Overall, it appears that a pure 2D case presents similarities with a more physics comprehensive 3D simulation. An azimuthal instability quickly appears in the first moments of the simulation and ends up being a modified ion acoustic instability in the channel. In the plume, the ion acoustic instability does not grow but is likely to be the result of an azimuthal wave in the channel that was convected away. The saturation mechanism is in both cases probably due to the ion trapping but the latter is more important in 2D. Because no radial direction is present in the pure 2D case, plasma wall interactions do not exist. The long wavelengths observed in the 3D channel, associated with the radial patterns, are therefore absent. Finally, the lower wall losses and the plasma expansion in the plume are likely to greatly modify the local plasma conditions such as the Debye length and the plasma frequency, which inevitably affects the evolution of instabilities in the system.

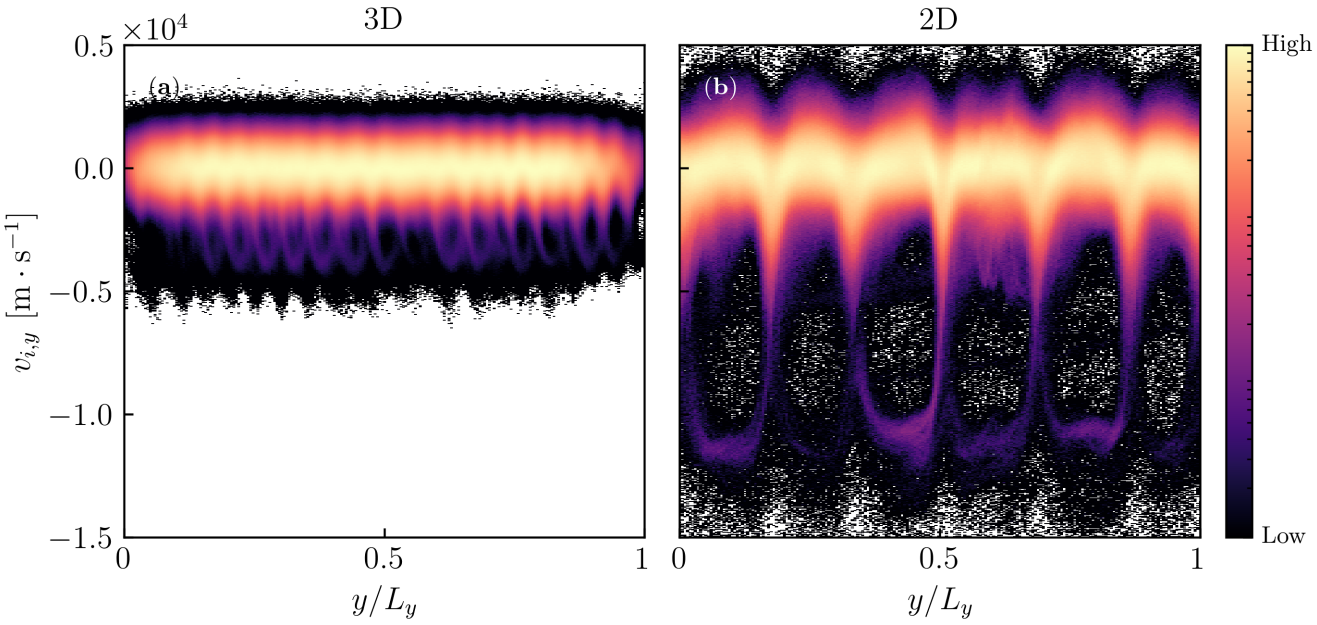

Figure 5.25: $y - v_{i,y}$ phase space of the ions in the near exit region for (a) the 3D simulation and (b) the 2D simulation. Every colored dot represents a particle (warm-yellow colors indicate maximum concentration whereas the black color represents the opposite).

5.6 Preliminary study on a cylindrical geometry

Up to now, we have only considered a cartesian geometry, i.e. the initial "T shape" from Figure 5.1 was simply extruded in the azimuthal direction and no asymmetry is assumed. However, in a real-world HT, the geometry is curved, which results in key differences. Among them, the outer wall has a greater surface area than the inner one. Thus, we could expect greater plasma-wall interactions such as heat losses or SEE, if any. Moreover, some new electron current density gradients might arise as well in regions of high electric and magnetic fields. Indeed, for a similar drift velocity $\mathbf{E} \times \mathbf{B}/B^2$, electrons near the outer wall have to travel a further distance than at the inner wall. Finally, the curvature imposes to change the external magnetic

field to comply with the null divergence condition. We can convince ourselves by recalling the divergence formulation in cartesian and cylindrical coordinates in Equation (5.18).

$$\boldsymbol{\nabla} \cdot \mathbf{B} = \begin{cases} \frac{\partial B_x}{\partial x} + \frac{\partial B_y}{\partial y} + \frac{\partial B_z}{\partial z} \text{ (cartesian)} \\ \frac{1}{r}\frac{\partial}{\partial r}(rB_r) + \frac{1}{r}\frac{\partial B_\theta}{\partial \theta} + \frac{\partial B_x}{\partial x} \text{ (cylindrical)} \end{cases} \tag{5.18}$$

In a cartesian geometry we can easily set the radial magnetic field component B_z to a Gaussian shape varying axially. Yet, in a cylindrical geometry this cannot be done because of the factor r in $\frac{\partial}{\partial r}(rB_r)$. In fact, the problem can be solved by adjusting an axial component B_x that is not zero anymore. In this more realistic $\mathbf{B}$ topology, the angle of intersection of the magnetic field with the walls may significantly modify the sheath structure [Moritz et al., 2019; Chodura, 1982; Ahedo, 1997]. Around the magnetic poles, where magnetic field lines narrow, electrons can also be reflected back as if a magnetic mirror, well described by [Chen, 1974, Chapter 3], was in present. Such a phenomenon was already observed for Hall thruster [Keidar and Boyd, 2005].

For these different reasons, we decided to perform some preliminary work on a cylindrical geometry and we considered the simulation domain shown in Figure 5.26. The strategy used to discretize the domain and the main geometrical parameters are the same as those described in Section 5.2.1. Instead of being extruded, the initial "T shape" in Figure 5.1 is rotated by an angle $\theta_0 = 5\,\text{rad}$ and the domain starts at a radius $R_{\min} = L_z$. The maximal radius is given by $R_{\max} = R_{\min} + 2L_z = 3L_z$. This radius $R_{\min}$ and the angle θ_0 were chosen such that the axial azimuthal plane at the centerline, located at the radius $\bar{r} = R_{\min} + L_z = 2L_z$, has an axial length similar to the previous 2D case, i.e., $L_\theta = \theta_0 \bar{r} = L_z = L_y$. Besides, the total number of nodes and cells in the mesh remains the same as previously. As a result, it is possible to simulate a sector of HT with the same performances as in the extruded geometry.

As explained above, the magnetic field must be modified to ensure the null divergence condition. Unfortunately, finding adequate $\mathbf{B}_x$ $\mathbf{B}_z$ is actually challenging (see Section 5.2.3) and we would require more time to do it. Nevertheless, a first approximation consists in assuming a purely radial magnetic field, whose magnitude varies in both the radial and axial directions (it is uniform in the azimuthal direction), i.e. $\mathbf{B} = B_r(r, x)\mathbf{u}_r$. We can also assume that the axial profile has a Gaussian shape $B(x)$ as in the 3D Cartesian setup (see Equation (5.8)). Thus, we get $B_r(r, x) = f(r)B(z)$, where $f(r)$ is a function to specify and $B(z)$ the Gaussian profile from Equation (3.1). Using the expression of the divergence in cylindrical coordinates, we get:

$$\begin{aligned} &\frac{\partial}{\partial r}(rB_r(r, x)) = 0 \\ \iff &\frac{d}{dr}(rf(r)) = 0. \end{aligned} \tag{5.19}$$

Therefore, the null divergence requirement can be obtained by the trivial solution $f(r) = r_0/r$, where r_0 is a constant. Therefore, the final magnetic field for the cylindrical geometry is given by:

$$\mathbf{B} = \frac{r_0}{r} B(x)\mathbf{u}_r, \tag{5.20}$$

for which the constant r_0 is conveniently chosen such that the centerline axial-azimuthal plane, at $\bar{r}$, has the same magnetic field as in the previous 3D case. Thus, we set $r_0 = \bar{r}$. In the radial axial plane, the chosen magnetic field gives the topology shown in Figure 5.27. Although the

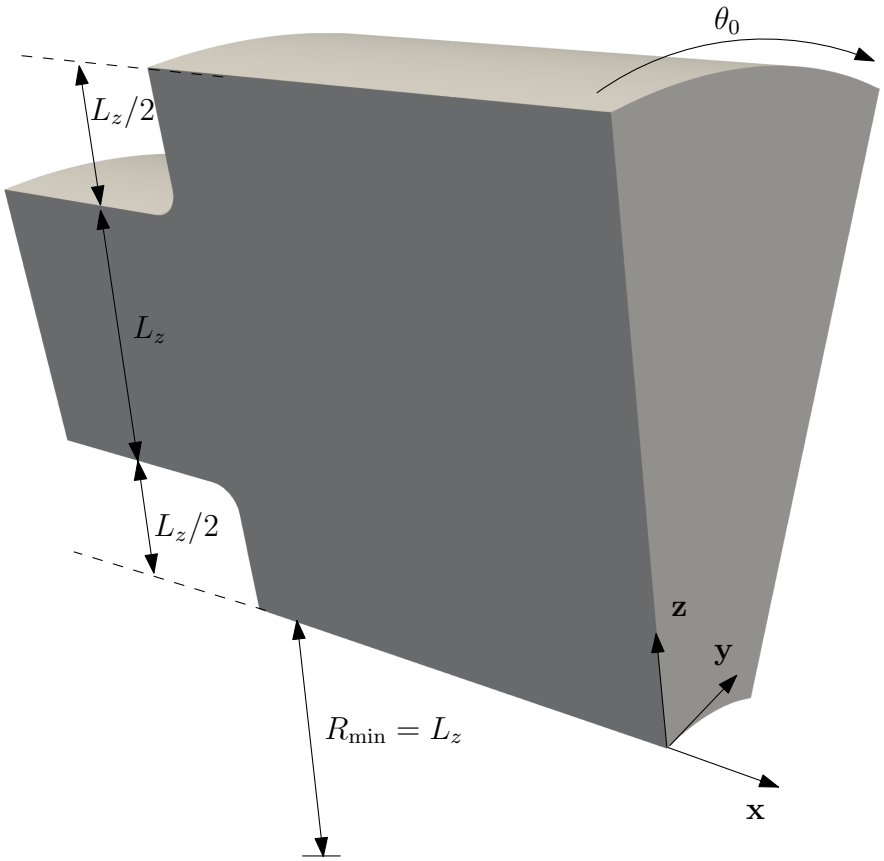

Figure 5.26: 3D view of cylindrical domain investigated.

magnetic field is appropriate for a cylindrical geometry, it is far from what is found in a real HT as it should be symmetric with respect to the centerline $r = \bar{r}$ [Morozov and Savelyev, 2000]. As of today, a few 3D simulations using this cylindrical geometry were performed using the same initial conditions as in Table 5.1 with the exception of the initial number of particles $N_{ppc,ini}$, which was set to 30 to speed up the calculations. Thus, the results are not fully converged statistically (see Section 5.7.2) but give an overview of what to expect. As shown in Figure 5.28 (a-b), the electron temperature topology remains unchanged, i.e., with a "bell shape", suggesting the potential field lines are also similar in both cases. The plasma structure is therefore globally the same, and ions from the ionization zone are in both cases extracted and accelerated into the plume. Among differences, the ECDI, visible in the 2D map of the azimuthal electric field in Figure 5.28 (c-d), seems to be distorted by the magnetic field gradient in the radial direction. The symmetric structure in the cartesian case is lost and the radial waves in the plume no longer propagate downwards. Nevertheless, a long azimuthal wavelength is still retrieved (see Figure 5.28 (e-f), suggesting this might be a robust feature in 3D. Finally, changing the magnetic field substantially modified the electron dynamics as the recirculation zones were lost in the cylindrical setup (see Figure 5.28 (a-b)). Besides, electrons acquire an important radial speed and seem less inclined to enter into the channel.

Although these results are interesting and could be the starting point of future theoretical studies on the curvature and gradient effects of the magnetic field, it would be wise to consider a more realistic **B** topology. This could be done via experimental measurements or by numerically

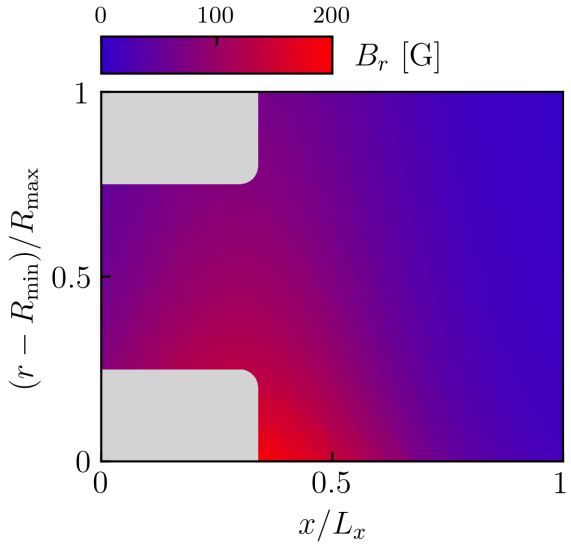

Figure 5.27: Magnetic field profile in 2D radial-axial view for the 3D cylindrical geometry. The profile is uniform in the azimuthal θ direction and the magnetic field is only radial.

solving the $\nabla \cdot \mathbf{B} = 0$ equation and we encourage future research work in this direction.

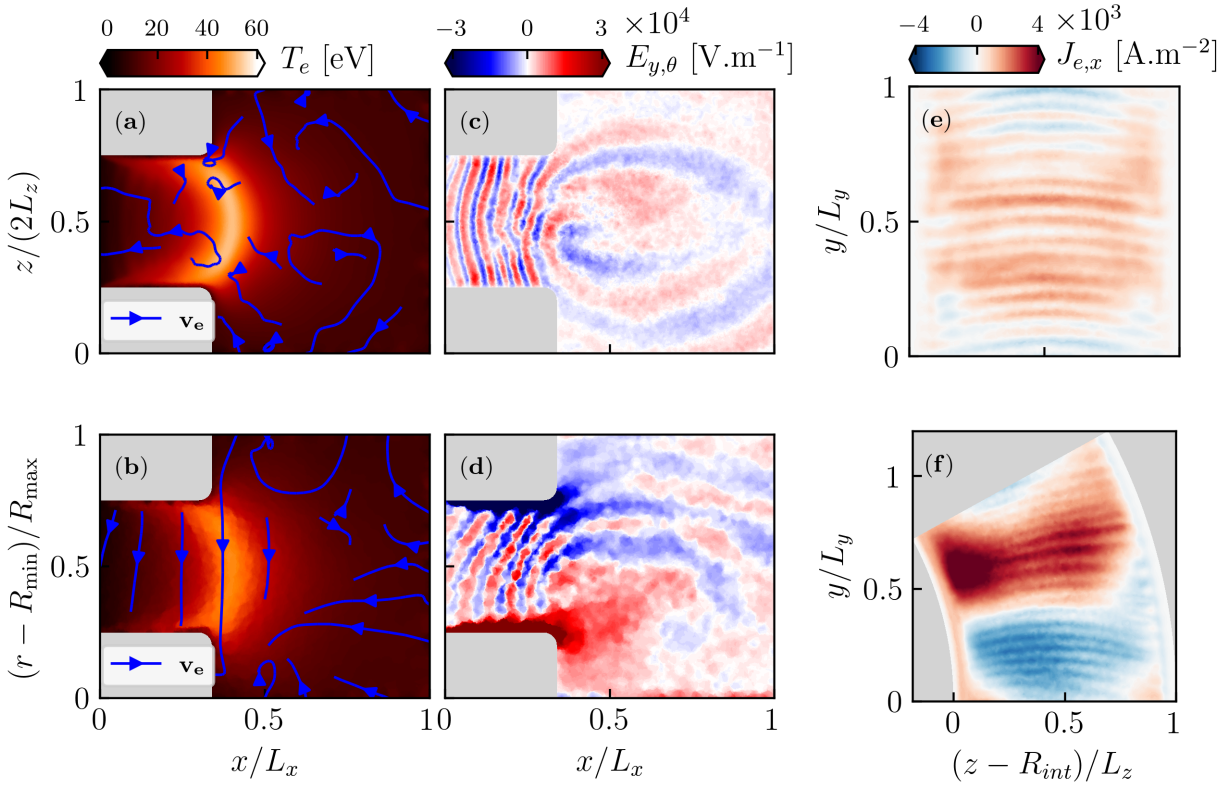

Figure 5.28: Comparison of first 3D results of the previous cartesian geometry (top row) with the cylindrical geometry (bottom row). (a-b): total electron temperature T_e in the radial axial plane. (c-d): azimuthal electric field $E_{y,\theta}$ in the centered radial axial plane. (e-f): axial electron current density $J_{e,x}$ in the radial azimuthal plane at $x = 0.12L_x = 3\,\text{mm}$.

5.7 Scalability analysis and convergence study

5.7.1 Scalability analysis

The different 3D simulations that were performed for this Chapter required a good assessment of the computing performances of AVIP. Although preliminary results were presented in Section 2.6.2, it is crucial to repeat a scalability study for each new simulation. This work was performed on the Irene cluster located at the French Alternative Energies and Atomic Energy Commission (CEA in French), near Paris. On Irene, two kinds of nodes were used for the runs and their main characteristics are reported in Table 5.4.

Characteristics	Skylake	Rome AMD
CPU architecture	2x24-cores Intel Skylake @2.7 GHz (AVX512)	2x64 AMD Rome @2.6 GHz (AVX2)
Cores/Node	48	128
Nodes	1656	2292
RAM/Core	3.75 GB	2 GB
RAM/Node	180 GB	256 GB

Table 5.4: Nodes used on Irene cluster at CEA for 3D PIC simulations. This work used the HPC resources of IDRIS/TGCC/CINES under the allocation A0102A06074 made by GENCI.

Running on these two nodes was made possible by the versatility of AVIP, intrinsically designed to be operational on as many architectures as possible. However, Rome AMD nodes were mostly used as they turned out to be more efficient. This result was not too surprising as a single Rome AMD node contains more cores than a Skylake one, which reduces inter-node communications for a prescribed number of cores. Even though, the scalability study did not measure I/O performances, the latter were optimized following advice from Wauteleta and Kestenera [2011].

The scalability analysis presented here was performed on the Cartesian geometry. To do so, we have run three times the first 50 iterations for each number of processors to discard any outliers. We also considered three values for $N_{ppc,ini}$, the initial number of particles per cell, to assess the statistical convergence. In Figure 5.29 (a) we assess the performances for the least converged case, i.e. $N_{ppc,ini} = 30$. For this case, the MAPHYS grid coarse correction detailed in Section 2.6.1 was turned off. Because the number of particles is fairly low, solving the Poisson equation is by far the most expensive module, AVIP easily spending more than 80% of the CPU time in it. Lagrangian modules such as particle interpolation and their respective transport scale very well, which was expected. Surprisingly, the modules handling the injection of particles generated by ionization or at the cathode showed poor scalability. Further analysis revealed that ionization was primarily responsible for that deteriorated performance. Indeed, at every iteration, all processors will check if the pairs X_x^+/e^- to be injected are located in their respective CPU domain. This lookup process is not expected to be faster when using more processors and can even become less effective when the CPU domain gets smaller. Note that the lookup algorithm was improved for this work and is probably the best solution we could find at this point.The cathode injection has also a limited scalability because the total number of new

electrons is computed using a collective communication. Interestingly, the sorting algorithm showed a poor scalability as well in contrast to what was observed in Figure 2.26. Additional tests have shown that the way in which the injection is carried out, especially for ionization, was responsible for this deterioration of performances. As of today, no explanation on that matter could be found. However, in a self-consistent simulation, injection issues related to our imposed ionization source term are likely to disappear because the ionization module will be replaced by the Monte Carlo Module, which has been designed to be highly scalable. Overall, we see that the optimum point for this run is obtained for 3840 processors. Assuming those performances remain constant during the whole computation, Figure 5.29 (d) indicates that the total CPU cost for this optimal simulation will be around 800.000 h. For this cost, the simulation (10 µs of physical time) could be theoretically completed in about a week according to Figure 5.29 (e). This assumes the simulation never stops, which of course is not true as run times are for instance limited to 24 uninterrupted hours.

We can now focus on the other simulations with $N_{ppc,ini} = 60$ and $N_{ppc,ini} = 120$. For these runs, we tested the grid correction option of MAPHYS in an attempt to reduce the computational cost. As a reminder (see Section 2.6.1), the CG correction aims to speed up the convergence of the Poisson solver at the CPU boundaries by reducing the size of the linear system to solve.

Indeed, the cost of Lagrangian and injection modules is proportional to the number of particles as shown on Figure 5.29 (a-b-c). As a result, colored dashed lines on Figure 5.29 (d) show that without the coarse grid correction the total cost is estimated at 1.2 and 2 million CPU hours for the $N_{ppc,ini} = 60$ and $N_{ppc,ini} = 120$ cases respectively. A cost-saving alternative consists in using fewer CPUs for a moderate return time. This can be achieved thanks to the coarse grid correction. As shown on Figure 5.29 (b-c), this option has two consequences on the Poisson solver scalability profile. First, the optimum point for MAPHYS is shifted to a lower regime of CPUs (around 2000) and the time spent per iteration in the module is increased by approximately 30%. This increase can be surprising at first because the grid correction is designed to optimize the Poisson solver. However, we draw the reader's attention to the fact that the CG correction's effects depend on each geometry [Poirel, 2018]. We can still take advantage of this CG correction here by noticing the Poisson solver profile is mostly flat from approximately 1000 to 3000 CPUs in Figure 5.29 (b-c). Indeed, this meaning we can reduce the number of CPUs for similar performances. Thus, as shown in Figure 5.29 (d), a similar CPU cost can be overall obtained in the 1000-2000 CPUs range.For the $N_{ppc,ini} = 60$ case, the minimum CPU cost, of 800.000 h, is obtained with 1280 processors. On Figure 5.29 (e) we read that this value leads to an acceptable return time of 20 days so we retain 1280 processors. For the $N_{ppc,ini} = 120$ case, we notice on Figure 5.29 (e) that the return time is already high so we prefer using more processors and we finally picked 1920 of them to target a return time of 28 days. The CPU cost is then 1.4 million hours.

We can finally compare what would have been the results if we did not have used the CG correction. In this scenario, for both $N_{ppc,ini} = 60$ and $N_{ppc,ini} = 120$ cases, using 3840 processors is the optimum point, i.e, the return time stops decreasing and is about 15 days and 20 days respectively. The corresponding CPU costs are then 1.2 million hours and 2 million hours respectively. Therefore, by turning the CG correction option ON, we can approximately save 30-35% of CPU cost by accepting the return time to increase by the same factor, which was deemed acceptable. Note that simply reducing the number of CPUs without the CG option would have lead to a poorer trade-off: the CPU cost would have been cut by ∼25% with a return time increasing of ∼75-100%.

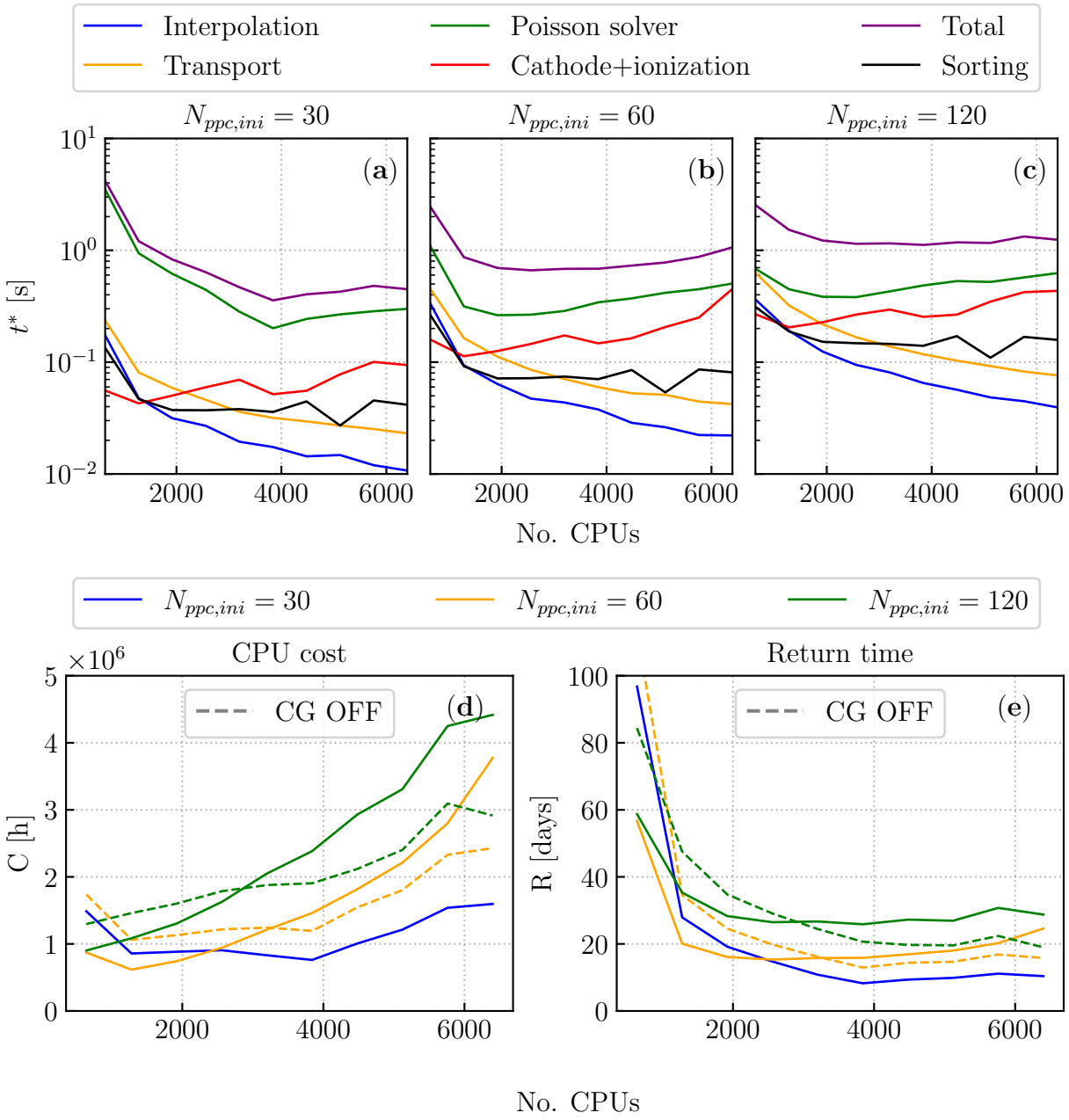

Figure 5.29: Strong scalability analysis for the first 50 iterations using an increasing number of initial particles per cell $N_{ppc,ini}$ (30, 60 and 120). (a-b-c): performances of AVIP PIC modules for the different $N_{ppc,ini}$ values (30, 60 and 120 respectively). (a): the computation with $N_{ppc,ini} = 30$ does not use a coarse grid correction for the Poisson solver MAPHYS as described in Section 2.6.1. (b-c): the computation with $N_{ppc,ini} = 60 - 120$ uses a coarse grid correction. (d): Total CPU cost. The dashed lines represent the CPU cost in the case the coarse grid (CG) correction is turned off. Note that, for now, the CG option was not tested for the $N_{ppc,ini} = 30$ case. (e): Estimated physical time to simulate 10 µs. The dashed lines represent the return time in the case the coarse grid (CG) correction is turned off.

As a result, the CG correction offers flexibility for the present simulations and we either choose a "fast" option, for which the return time is minimal, or we can consider an "economical"

option, for which we can wait a bit more to optimize CPU hours.

5.7.2 Statistical convergence

A final recommendation can be made on the number of numerical particles to use in future 3D simulations. Indeed, as mentioned in Section 1.4.2, PIC simulations need to have enough numerical particles in order to accurately describe the distribution functions in the Boltzmann equation. Therefore it is crucial to perform a convergence study on the number of particles. To do so, we performed several simulations of the 3D cylindrical and cartesian geometries using different initial number of particles per tetrahedral cells: $N_{ppc,ini} = 5, 10, 20, 30$ for the cylindrical geometry and $N_{ppc,ini} = 30, 60, 120$ for the cartesian geometry. For lack of time, we, unfortunately, could test the same $N_{ppc,ini}$ for both geometries but wan can still assess the convergence of the respective simulations.

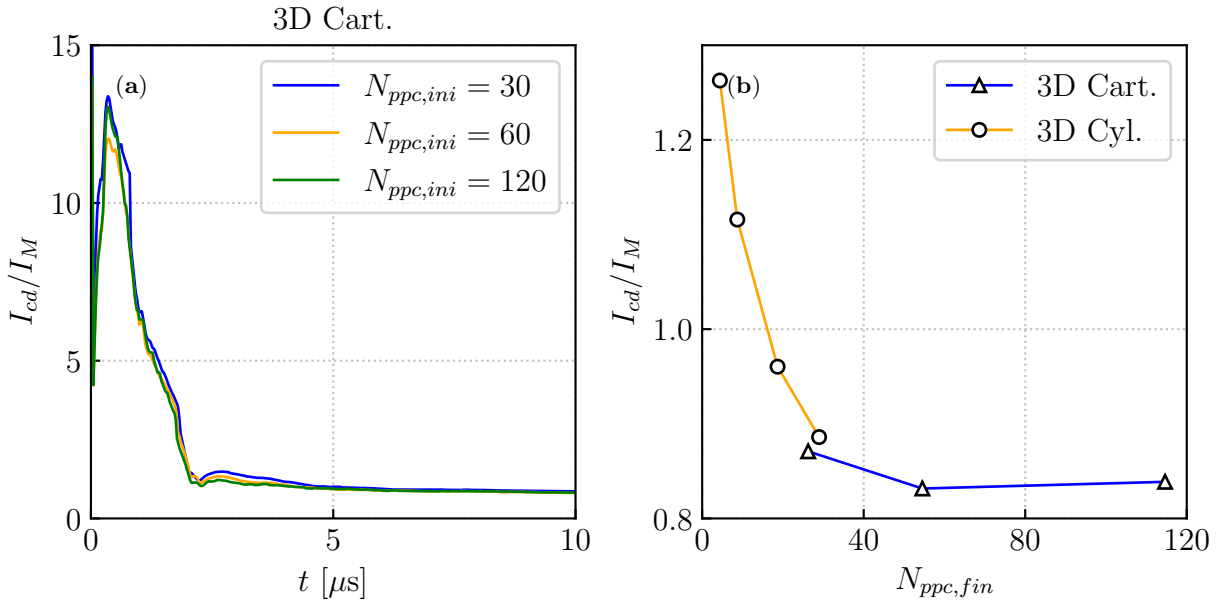

Figure 5.30: Statistical convergence of 3D PIC simulations using the current ratio I_{cd}/I_M. (a) Temporal evolution of current ratio I_{cd}/I_M with different $N_{ppc,ini}$ for the cartesian geometry. (b) Final current I_{cd}/I_M level at steady state vs the final number of particles per tetrahedral cell for both the cartesian and cylindrical geometries.

In Figure 5.30 (a), we present the temporal evolution of the current ratio I_{cd}/I_M in the 3D cartesian case for $N_{ppc,ini} = 30, 60$ and 120. As a reminder I_{cd} is the electron current injected at the cathode following our convention in Figure 2.20, while I_M is the imposed current due to ionization. After a transient phase during which many electrons are injected into the domain, all profiles stabilize at a steady state value of $I_{cd}/I_M = 0.83$. As mentioned in previous work [Boeuf and Garrigues, 2018], in a real HT this ratio should rather be around 30%, but this quantity can, however, be used to study the statistical convergence of the simulation. In this plot, no clear difference appears when using more particles. This observation is confirmed in Figure 5.30 (b), in which we present the steady state value of I_{cd}/I_M as a function of the final number of particle per cell $N_{ppc,fin}$: for the cartesian case (blue solid line), the least resolved case seems to be already converged. Note that $N_{ppc,fin} < N_{ppc,ini}$ because of wall and plume losses. Here additional tests would be necessary with fewer particles in order to properly establish the

lower limit of convergence. Nevertheless, we have some available data, with a fewer number of particles, for the cylindrical case detailed in Section 5.6. On Figure 5.30 (b), we can see that the ratio I_{cd}/I_M decreases with a higher $N_{ppc,fin}$ but has not reached the statistical convergence yet. It is not certain how much we can guess what would be the trend on the low $N_{ppc,fin}$ range for the cartesian case, but we can reasonably assume the statistical convergence would not be obtained either. Overall, for globally averaged data, such as the current ratio I_{cd}/I_M, it appears statistical convergence is virtually obtained with $N_{ppc,ini} = 30 - 60$. Nevertheless, we would like to draw the reader's attention to the fact that other quantities might actually need more particles per cell as they converge more slowly to an asymptotic value. For instance, we noticed that the spectrum of the azimuthal electric field E_y, that was calculated with the DMD in Figure 5.12 can significantly vary with the value of $N_{ppc,fin}$ as shown in Figure 5.31. In this figure, we can see that the main ECDI mode is recovered in all three cases, but some higher resonances are present with $N_{ppc,ini} = 30$ and 60. These resonances do not seem to have any physical meaning because their respective magnitude is reduced as we increase the number of particles per cell. In our most converged case, i.e., $N_{ppc,ini} = 120$, they have completely disappeared.

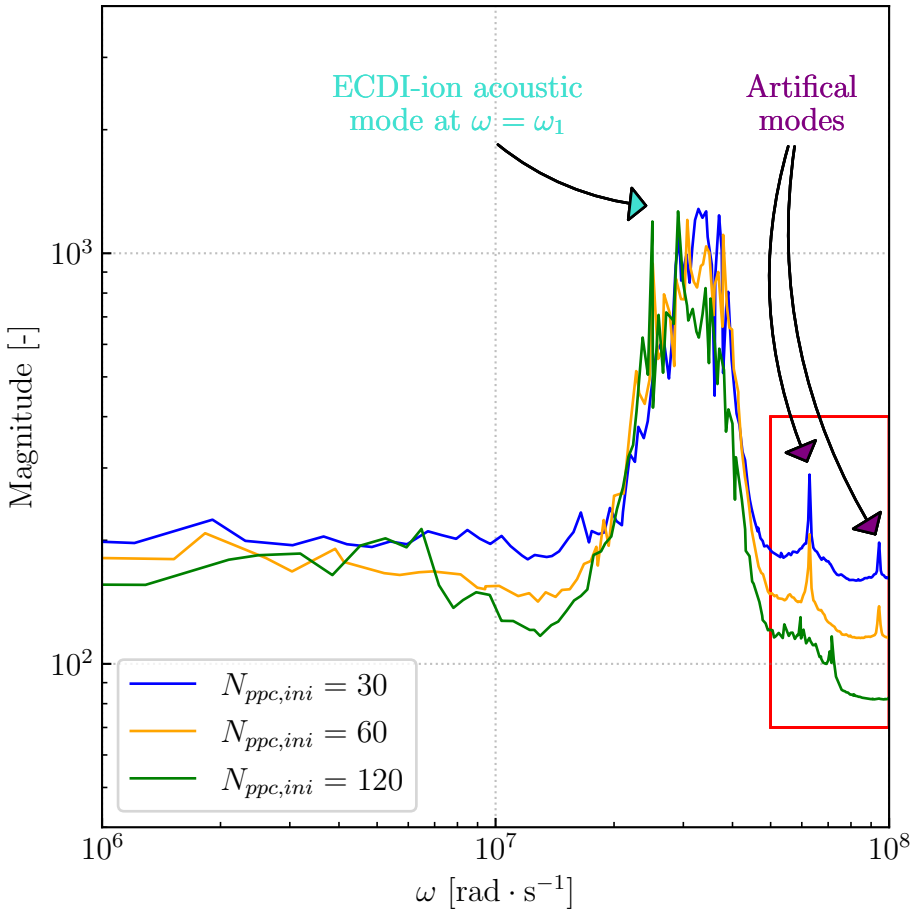

Figure 5.31: Spectrum of azimuthal electric field E_y obtained the DMD at steady state. The red rectangle highlights higher frequency resonances that disappear as we increase the number of particles per cell.

As a conclusion, it seems that for "low order" quantities, such as globally averaged data (the current ratio I_{cd}/I_M for instance), initializing the simulation with, at least, between 30 to

60 particles per tetrahedral cells is enough. However, for "higher order" quantities, related to a detailed spectral analysis, more particles are required. In this case, we recommend to use, at least, between 60-120 particles per tetrahedral cells whose size satisfies the accuracy criteria given by Equation (2.6).

5.8 Conclusion

In this chapter, we focused our attention on a 3D configuration, whose geometrical features are inspired from the previous 2D axial-azimuthal (Chapter 3) and radial-azimuthal (Chapter 4) simulations. The simulation domain includes a shortened channel and the near plume region. In order to highlight the solely 3D effects, a similar imposed ionization source term and magnetic field topology have been considered. No curvature effects were taken into account at first. The simulations use an unstructured grid of 2.36 millions tetrahedral cells that complies with classical stability and accuracy PIC criteria.

During the transient phase, numerical results show that multidimensional plasma instabilities appear. With the help of Python tools dedicated to spectral analysis, such as FFT and DMD, the main mode could be isolated. Thanks to theoretical calculations from linear theory [Cavalier et al., 2013], this main mode, carried by the azimuthal electric field, was identified to be the ECDI. The latter was already observed in the previous chapters and in numerous other academic PIC simulations in the literature. The ECDI starts appearing near the anode and develops in other axial locations in the channel as well, the growth rate being lower downstream. In the plume the plasma expansion seems to greatly affect the initial azimuthal wave which then develops in a radial and axial pattern. Another resonance, clearly visible in the axial and radial electron currents, was also detected. It showed a long azimuthal wavelength but also a radial component in the channel that is similar to the MTSI of Chapter 4. In the azimuthal electric field, this radial-azimuthal resonance is extremely low and therefore never visible with the raw data. Such results are not surprising since according to our theoretical calculations, the MTSI is not excited under the plasma conditions of the simulations. Yet, recent work on the MTSI performed by Petronio et al. [2021] suggests that this radial-azimuthal instability could be the signature of the MTSI. Testing other 3D plasma conditions would probably confirm this hypothesis.

At steady state, the plasma structure presents the usual characteristics of a working Hall thruster. Highest density levels are located in the channel and the plasma enters into a supersonic regime thanks to a drop of potential in the axial direction. The subsequent axial electric field combined with the magnetic field create a Hall current in the azimuthal direction. Iso-potential lines determine the electron temperature distribution, that presented a bell shape near the channel exit. The presence of recirculation zones in the channel and in the plume was also observed and is likely to be related to the presence of the instabilities in the system. The quasi-neutral cathode model was used in this work and injected the correct amount of electrons in the system while effectively ensuring a quasi-neutral plasma in the plume. Electrons from the cathode made their way to the channel but a non negligible portion of them ends up going back to the cathode. This point could be improved in the future. The cathode consisted of the bottom, top and right sides of the plume boundary. Indeed, since the simulated plume domain remain small and close to the channel exit, it was found that not imposing a constant potential value there failed to contain the plasma in the channel and led to the creation of a nonphysical potential bulk in the plume. With a larger plume area, thus with farther domain boundaries, other choices could be possible.

This work also made it possible to highlight the contribution of multidimensional effects in the physics of HT by comparing 2D and 3D simulations The comparison was made with the centered axial-azimuthal plane of the 3D case. It appears that the 2D simulation leads to a globally higher plasma density and temperature. In 2D the plasma is virtually hotter in the wall domain with a maximum temperature 50% higher than in 3D. The plasma density is higher in the channel region in 3D but much lower in the plume, suggesting that plasma expansion plays an important role in the physics, that is challenging to account for in a pure 2D setup. In both cases azimuthal instabilities take place in the system. In 2D, what seems to be the ECDI appears at two separate axial locations: near the anode, as in 3D, and in the plume region. As of today, it is not clear why azimuthal instabilities start growing at different positions as theoretical calculations cannot apply to a pure 2D case. Nevertheless, the system ends up with a modified ion acoustic instability that closely follows the analytic predictions from Lafleur et al. [2016b]. Two behaviors have been identified. In the channel, the 3D case excites a single mode while the numerical dispersion relation seems more continuous in 2D. In the plume region, results suggest that, in both cases, the instability is the result of an ion acoustic wave being convected away from the channel into the plume. The transition from the channel to the plume, that seems to occur at a Mach number $M_e = 0.5$, follows opposite trends in 2D and 3D: the azimuthal wavenumber and angular frequency increase in 3D while the reversed evolution happens in 2D. Besides, the ion acoustic instability saturates at a different level, with an azimuthal electric field three times larger in 2D than in 3D. This results in a larger ion trapping in the near exit region in comparison to the 3D case. The mobility μ_{PIC}, related to the ECDI and ion acoustic wave [Lafleur et al., 2016b], was also measured. It is in average several orders of magnitude lower in 3D compared to 2D. This result is not too surprising as μ_{PIC} is expected to be proportional to coherent fluctuations of the density and azimuthal electric field, that are weaker in 3D than in 2D. Finally, the mark of the radial-azimuthal instability, with a large wavelength of size $\sim L_y$ is clearly visible in the 3D simulation but totally absent in the 2D counterpart, showing another limitation of pure 2D simulations.

We also discussed the performances of AVIP PIC and the potential of performing future 3D runs. A strong scalability analysis allowed us to optimize the available resources on national supercomputers and to handle up to more than four billions particles with 13.6 millions cells and reach a steady state within $\sim$ 1-1.5 months. The CPU cost can be roughly estimated of the order of 1-2 millions CPU hours. We also found that the statistical convergence depended on what quantities we were interested into. For globally averaged data, such as a current ratio, between 30-60 particles per cell at initialization seemed enough. However, for higher order quantities, related to spectral data for instance, a higher resolution is needed and we should at least use between 60-120 particles per cell at initialization. With the current performances of AVIP, we can envision to use a sector of a Hall thruster. We performed some preliminary work on this regard and we defined a 5 rad sector for which the mesh size remained unchanged with respect to our initial cartesian case. During our study, we found it was necessary to adapt our current magnetic field topology to still ensure a null divergence. A simple analytic formulation with a symmetric magnetic field at the centerline, which is usually used in real HT [Morozov and Savelyev, 2000], is impossible to obtain for such an annular geometry. Nevertheless, with a simplified asymmetric magnetic field we could still perform our simulation. It resulted that the global plasma structure remained similar with the presence of both the ECDI and the radial-azimuthal pattern resembling to the MTSI. However, their respective 2D maps were distorted due to the magnetic field gradient in the radial direction. To go further, experimental data or fields previously calculated by dedicated a magnetic numerical solver are necessary.

Overall, this 3D PIC simulation is among the very few that exists in the literature, with the exception of Hirakawa and Arakawa [1995, 1996] and [Taccogna and Minelli, 2018; Minelli and Taccogna, 2017]. But in contrast to these previous works, no numerical artifacts such as increasing the vacuum permittivity or equaling the mass of ions and electrons were used. In addition we did take into account the plume region in our 3D simulation. Besides, this 3D PIC work is perhaps the first example of a Hall thruster simulation using an unstructured grid. We believe it offers a framework to understand more precisely the plasma physics and instabilities existing in a Hall thruster and ultimately paves the way for more predictive tools to help the industry and the low-temperature plasma community.

Chapter 6

Conclusion

6.1 Summary of this thesis

During this PhD, performed at CERFACS and sponsored by Safran, a major French aerospace company, we continued the development of an explicit Particle-In-Cell code, AVIP PIC, to improve the modeling of Hall thrusters. AVIP PIC is a massively parallel code built upon the AVBP solver, a world standard tool in the domain of combustion and reactive flows. One innovative aspect of AVIP PIC is its capability to handle unstructured grids, which provides the freedom to consider any kinds of geometry. This represents a considerable progress for the HT community because, to our knowledge, all existing codes still consider structured grids, thus most often restricting their range of applications to simplified academic configurations. However, the use of structured grids is not without advantages. First, the plasma physics in HTs is incredibly complex and simplified configurations still provide useful insights. Secondly, PIC simulations remain extremely costly and it is obviously easier to work with structured grids to get an efficient and fast code than dealing with unstructured meshes. In spite of the inherent difficulty to handle unstructured grids, AVIP PIC showed excellent performances compared to the major existing codes in the HT community in axial-azimuthal (Chapter 3) and radial-azimuthal configurations (Chapter 4).

This achievement was made possible by a careful design of AVIP PIC as presented in Chapter 2. At each iteration, the classical loop of an explicit PIC code is completed: integration of the equations of motions, modeling of collisions, interactions with the boundaries of the computational domain.The Poisson equation can be solved with either the standard PETSc library or by a cutting-edge external module, MAPHYS, that is specifically designed for unstructured meshes. MAPHYS offers the possibility to speed up the calculation in the case of large meshes (several millions of nodes) thanks to a "coarse grid" option. Particles management is optimized by using an advanced Array of Structures of Array (AoSoA) to find a compromise between cache/RAM memory limitations, data loading speed and readability of the code. During this PhD, an additional tool to lower the cost inherent to particles continued to be implemented. It consists of an active particle control algorithm that allows the user to adjust the number of particles in the simulation according to tolerances on their position and speed. The number of particles is reduced or increased through merging-splitting processes according to four parameters: the target number of particles par cell N_t, the tolerances on position and speed $T_{\mathbf{x}}$ and $T_{\mathbf{v}}$ that serve to identify clusters of similar particles, and the frequency of use of the algorithm f_t. A particular attention was also paid to the development of new boundary conditions.

In particular, dielectric boundary conditions can now be modeled along with the subsequent electric field jump, in the framework of unstructured grids. Secondary electron emissions were also implemented from standard models available in the literature. Moreover, two cathode models based on the current equality or on the quasi neutrality conditions are now available. Overall, the Lagrangian aspects of AVIP PIC, encompassing modules related to particles only (transport, collisions, interpolation), can be parallelized beyond 95%. This PhD also revealed that solving the Poisson equation was in fact the limiting factor for large simulations.

Because the implementation of AVIP PIC is highly sophisticated, it is crucial to validate it and to confront its results with other PIC codes from the community. That is first done in Chapter 3, where we used the AVIP PIC in an academic 2D axial-azimuthal benchmark jointly performed with six other international institutions [Charoy et al., 2019]. For this case, ionization was replaced by an imposed source term that was implemented in AVIP PIC as well. Although simplification assumptions were made, AVIP PIC, along with the other groups, were able to retrieve the overall functioning of a HT, i.e, ions are extracted and accelerated from the ionization zone into the plume and electrons from the cathode are trapped into a Hall current at the magnetic field barrier. Besides, we were able to retrieve fundamental azimuthal plasma instabilities. The latter are identified to be the ECDI that transitioned into a modified ion acoustic instability. The ECDI is an important feature of HTs because it is likely to actively participate in the axial anomalous transport of electrons, a hot topic in the community (see Section 1.3.2). In spite of the highly coupled displayed physics, all groups, with codes that greatly differ in terms of implementation (structured-unstructured grids, floating-point precision, parallelization strategy) and running conditions (different machines and compilers), could retrieve these instabilities and their characteristics. AVIP PIC being validated on this configuration, we were able to use this benchmark as a starting point to test the aforementioned active particle control algorithm. During our investigation it was found that the target number of particles N_t needed to satisfy the statistical convergence was around 200 particles per square cells. Concerning the tolerances $T_{\mathbf{x}}$ and $T_{\mathbf{v}}$, optimal values of the order of 10^{-1} and 10^{-2} respectively have been highlighted. These values even make it possible to retrieve thin structures regarding the azimuthal instabilities. It appeared that the choice regarding the tolerance on speed $T_{\mathbf{v}}$ was quite sensitive, small variations being able to lead to significantly different steady state results. Finally, the algorithm should be applied parsimoniously to make the method as less intrusive as possible ($f_t \sim 1000$ was found to be a good pick in our tests). Overall, we recommend to use the algorithm only when necessary, i.e. when Lagrangian cost becomes prohibitive, which can typically occur during transients or strong oscillatory phenomena such as breathing mode events.

In Chapter 4, we continued our careful verification of AVIP PIC with another benchmark, simulating the radial-azimuthal plane of a HT. This configuration was considered because plasma-wall interactions can greatly influence the plasma physics. In particular, in addition to the ECDI, previous work reported the presence of a radial-azimuthal instability, the so-called MTSI. Unfortunately, these investigations were limited to the transitory regime of the simulation and never reached a steady state. Besides, other studies in the literature did not observe the MTSI, which puzzled the community. Therefore, we led an international collaboration, made of six other groups, to clarify and bring agreement on the presence of the MTSI in HT simulations [Villafana et al., 2021]. To do so, we set up a simplified collisionless test case, equipped with an ionization source term similar to that in Chapter 3. We also implemented a virtual axial model

to mimic the presence of the off plane cathode in this direction. This new feature is important as it now offers the possibility to consider pure 2D cases in the radial-azimuthal direction and to reach a steady state. During this study, thanks to theoretical calculations from the linear theory of plasma instabilities, we confirmed the presence of the MTSI that appeared to be coupled with the ECDI. Our findings were backed up by our six partners that observed the same transients and instabilities. At steady state, the main profiles of interest closely fit within a 5% interval. Such a close agreement was quite outstanding considering the multiple sources of differences between the codes, in terms of parallelization strategy, interpolation scheme accuracy or hardware architectures for instance. As in Chapter 3, it is believed that the statistical convergence, found around 200 particles per square cells, was crucial to achieve this result.

Based on our experience on pure 2D configurations, in the axial azimuthal and radial azimuthal planes, we went forward to demonstrate the capability of AVIP to perform 3D simulations in Chapter 5. The objective was also to prepare future research on 3D configurations as the plasma physics is inherently multidimensional [Tsikata et al., 2010]. Besides the industry needs to go beyond 2D academic geometries and ramp up its modeling capability to speed up the development of new thrusters for a rapidly expanding market. There are only a few studies on 3D configurations, some focusing on the channel region only for a miniaturized HT [Taccogna and Minelli, 2018; Minelli and Taccogna, 2017] and others [Hirakawa and Arakawa, 1995, 1996] using permittivity and mass scaling ratios. Those choices made possible 3D simulations with limited computational resources but they also inevitably modified the plasma physics. For instance, the vacuum permittivity being present in every plasma dispersion relation, any change of its value artificially can affect the actual growth and development of waves or, perhaps, even trigger waves that would not have existed in reality. Therefore, we decided not to use any geometrical or physical scaling. The simulation domain is based on the geometrical dimensions of the two previous 2D cases developed in Chapter 3 and Chapter 4 in order to isolate as much as possible 3D effects only. During this study, we followed our systematic methodology and first assessed the computational performances of AVIP PIC in this case. We distinguished two regimes: one with a high number of processors that completes 10 µs in a fast timeline, and another more economical that cuts CPU cost by 50% by accepting a return time increased by around 30%. Again the Poisson solver was found to be the main limiting factor for larger simulations. In the end, we considered a Cartesian 3D geometry that models the near channel region and also the plume expansion domain. Numerical results showed that the overall functioning of HT was retrieved. Electrons from the cathode effectively entered into the channel and ions are accelerated before the plasma expanded into the plume. The acceleration region was located in the area of maximum magnetic field. Multidimensional instabilities, primarily carried by the azimuthal electric field, quickly appeared during the first instants of the simulations. A detailed spectral analysis, based on the linear theory of plasma instabilities [Lampe et al., 1972, 1971a; Dewar, 1973] and using a dispersion relation solver [Cavalier et al., 2013] showed that the dominant mode was the ECDI. The latter starts appearing in the channel before being convected out into the plume where the instability acquires a radial component as well. At this time it is believed that this is due to the plasma expansion in the plume. In addition to the ECDI, we detected a radial azimuthal mode that is well visible on the radial and axial electron currents but weak in the azimuthal electric field spectrum. We suspect the latter to be the signature of the MTSI observed in Chapter 4, which could be more important under other initial conditions.

We also compared 3D results with their 2D counterparts. It revealed that in 2D, the plasma

has a structure similar to that in 3D but with different orders of magnitude. Thus, in 2D, the plasma was overall hotter and much denser. We noted that the main discrepancy with the 3D case is due to the plume region, which does not undergo a similar plasma expansion in 2D. We also observed notable differences in the propagation of instabilities in the simulation domain. First, while the ECDI grows in the channel from the near anode region in 2D and 3D, it also simultaneously develops in 2D at the channel exit for unknown reasons as of today. In both cases, the ECDI has transitioned into a modified ion acoustic wave as described by [Lafleur et al., 2016b]. Because the plasma is in general hotter and denser in 2D, it seems that saturation, due to ion trapping in the azimuthal direction, is three times more significant in 2D than in 3D. As a result, because the electron mobility is expected, in this case, to be proportional to azimuthal fluctuations of density and azimuthal electric field [Lafleur et al., 2016b], it was overall found much lower in 3D than in 2D. This observation leads to believe that accounting for wall losses and the plume expansion, are important aspects of the simulation domain to consider when studying plasma instabilities.

6.2 Perspectives

6.2.1 Short-term goals

As of today, AVIP PIC possesses all the necessary tools to simulate, in a realistic manner, any 2D or 3D configurations of a Hall thruster. In particular, we can model the walls, the cathode and collisions between neutral and charged particles. Besides, by making the effort to solve the Poisson equation, the sheath can be naturally and accurately described. In addition to the work presented in this manuscript, we could easily investigate other phenomena.

First, we could certainly study the effects of dielectric walls and secondary electron emissions (SEE) on the physics. [Tavant, 2019, Chapter 4] led investigations on this matter but did not notice significant differences in comparison to metallic walls. However, in contrast to Chapter 4, MTSI was not present in Tavant's case and we could expect an important interaction between the MTSI and SEE [Janhunen et al., 2018b]. Indeed, the MTSI will tend to increase electron temperature at the walls, which could enhance SEE accordingly. Such work could be quite easily carried out in the near future with AVIP PIC.

Another fairly accessible analysis concerns a detailed study of the MTSI in 3D. As observed in Chapter 5, a similar radial-azimuthal mode was indeed detected but at a much weaker level than the main ECDI mode. Such a result is in agreement with the plasma linear theory but we could reasonably create the appropriate plasma conditions for it to appear and grow more vigorously. All parameters dictating the MTSI growth rate and its initial developments can be wisely and easily chosen with the exception of the axial electric field. We do not necessarily need to reach a steady state for all cases as the MTSI grows in the first instants of the simulation, which makes such a work realistic even with a moderate amount of CPU hours.

Finally, at the end of this PhD thesis, we have now at our disposal 2D and 3D PIC configurations that have been validated and verified. This database can already be used to guide our current development of AVIP fluid, based on a full fluid modeling, and of AVIP hybrid. For instance, the heat flux, currently set to 0 in our fluid formulation, could be improved with new laws we could deduce from our PIC numerical experiments. Thus, a systematic validation of AVIP fluid is now possible using the same configurations presented in this thesis. Our simplifications, such as a collisionless plasma and an imposed ionization source term are in this regard an advantage as they facilitate the comparison of fluid and PIC results.

6.2.2 Improvement of code performances and efficiency

During this PhD, a great care was given to the assessment and improvement of the code. Indeed, the main limitation of PIC simulations remains its computational cost and especially in 3D. We can propose potential solutions in this regard.

First, we could adjust the mesh spatial resolution in the plume and increase the average cell size. Indeed, the cell size is constrained by the Debye length that tends to increase in the plume due to the significant rarefaction of the plasma flow. It would be important to assess the impact of the potential *self-forces*, that can arise if the cell size changes too rapidly [Colella and Norgaard, 2010]. Such an effort could however be rewarded by either reducing the number of nodes and cells in the domain, or by expanding the plume further away from the channel exit. Mesh refinement and related techniques are a common procedure in CFD and we could certainly take leverage of the existing expertise at CERFACS.

Besides, as mentioned in Section 6.1, solving the Poisson equation as our current main limiting factor as the Poisson solver does not scale very well, which makes the CPU cost for long simulations, i.e., beyond a few tens of microseconds, unbearable. Moreover, since we need very high precision to capture thin structures that are crucial for plasma instabilities, it is difficult to go beyond a few tens of microseconds of physical time without relying on additional numerical artifacts. An interesting solution could be provided by a Deep Learning approach based on neural networks. Indeed, the Poisson equation is a well-known problem for which we could build a database suited for the Hall thruster physics. The database would be obtained by using classic linear solvers such as MAPHYS or PETSc and the neural network could train on it. CERFACS is already performing ongoing investigations on this matter [Cheng et al., 2021]. The advantage of such an approach is that it tremendously mitigates the computational cost to obtain the potential and electric field. However, as of today, it seems unlikely a deep learning approach could entirely replace usual linear solvers because of the required accuracy. For instance, thin structures arising in the linear stage growth of instabilities necessitate a very good knowledge of the local potential field and thus an extremely low error level in the Poisson equation.

But hybrid solutions can be imagined where we could regularly calculate the potential with a linear solver, for accuracy, and rely on our neural network otherwise.

As a final recommendation, our experience in 3D taught us that it is essential to keep the code up to date with new hardware architectures and library/compiler versions. Indeed, the careful optimization of AVIP PIC requires an excellent knowledge of the supercomputer to use to ensure and maintain the compatibility of the code with the machine. Sometimes, as it was the case for Chapter 5, it is even necessary to manually adjust collective communication options, which can be significantly time-consuming. Help from IT engineers and support from the supercomputer team might be necessary. Besides, new hardware architectures, based on GPU, that seem promising in terms of performance, should also be kept in mind for the long-term development of the code.

6.2.3 Toward more realistic cases

For more realistic cases, we could first consider adding the dielectric layer along with secondary electron emissions in our 3D geometry. Indeed, even if their contribution to the electron anomalous transport seems modest, plasma wall interactions, via SEE, may be coupled with the electron drift instability as suggested by Taccogna and Minelli [2018]. This possible coupling could play a greater role than previously thought, especially if the MTSI, which enhances SEE, could

effectively be reproduced in the 3D geometry.

Another step forward in our 2D and 3D cases could be to re-introduce neutral particles in the simulations. Indeed, for the sake of simplicity and with the exception of Turner et al. [2013] benchmark presented in Section 3.3.2, no neutral Xenon particles have been considered. Before going into 3D, we could start modeling neutral particles again in our 2D cases first. In order to sustain the discharge, we would need to make sure we understand how to properly ignite the thruster. Ignition would be achieved by electrons from the cathode ionizing neutral particles, the neutral density profile being obtained by constant injection of X_e at the anode. We could thus address one of the limits of our current 3D model. This will also be the opportunity to test the merging splitting algorithm in case the number of particles becomes too high during the transient.

For 3D cases, it also appeared in Chapter 5 that in order to simulate a sector of HT, we needed more realistic data from actual Hall thrusters. For instance, it is obvious that we should use a more realistic magnetic field that must be symmetric with respect to the center plane. To do so, inputs from our industrial partner, which has a great expertise with magnetic fields, could be absolutely valuable.

2D and 3D cases could also benefit from improvements regarding the modeling of the cathode. Indeed, so far the cathode is modeled as a straight line (2D case) or as a plane (3D case), that is usually placed at one extremity of the domain.However, in reality, the cathode has a more sophisticated shape, such as a cylinder, and does not necessarily occupy one side of the domain. In Hall thrusters, the cathode is located at the axis of rotation of the annular geometry or around the external radius of the thruster. Accounting for simple shapes representing the cathode in the domain with various locations could be another goal in the long term. Such additional modeling could also pave the way for future comparisons with new experimental data. Indeed, as mega constellations of small satellites are about to be deployed, micro HTs, such as the PPS-X00 [Vaudolon et al., 2019], are being developed to meet the market demand. One advantage of microthrusters is that PIC simulations become more easily to carry out because the domain is much smaller. Therefore, little or no compromises would be necessary, which would increase the reliability of the simulation. Even if measurements in the channel are more challenging to perform, the plume could still be probed by invasive and noninvasive techniques, which could allow for direct comparisons with the 3D PIC simulation. Besides, since the plasma rarefies in the plume a PIC model would be a particularly suitable solution for such a situation.

Finally, future simulations would be greatly accelerated and guided with a better understanding of plasma waves and related oscillatory behavior that can occur in a Hall thruster. During this PhD thesis, all simulations could be verified by arguments stemming from linear theory and that was very helpful. In general, the few theoretical studies that exist in the community, for instance [Ducrocq et al., 2006; Cavalier et al., 2013; Lafleur et al., 2016b], are extremely popular in the community. Unfortunately, the non linear evolution of plasma waves and their interactions remain obscure and more theoretical support is needed. A greater interaction between the plasma theory community and the Hall thruster community would definitely help to fill our knowledge gaps.

Appendix A

Unit test case for the dielectric implementation

In this appendix, we present a simple test case of our implementation in Section 2.3.4. We consider a square domain as shown in Figure A.1. In the central blue area, a charge difference $n_i - n_e$ is imposed and follows a cosine law:

$$(n_i - n_e)e = \rho_0 \cos\left(\frac{\pi}{3}\left(\frac{x}{h} + \frac{1}{2}\right)\right), \tag{A.1}$$

where h is the width of the two dielectric layers at the left and right sides of the domain. Our goal is to find the potential ϕ, and the electric fields E_x and E_y obtained with AVIP and to compare them with analytic formulations. At $x = 0$ and $x = L_x$, we respectively impose Dirichlet boundary conditions with $\phi_1 = 0\,\mathrm{V}$ and$\phi_2 = 0\,\mathrm{V}$. At $y = 0$ and $y = L_y$, we impose periodic boundary conditions.
This problem can be solved analytically and we find the following coefficients that will be used:

$$\begin{cases} \Delta = 3h\left(1 - \frac{1}{\epsilon_r} + \frac{L_x}{\epsilon_r}\right) \\ a_3 = \frac{1}{\Delta}(\frac{h}{\epsilon_r\epsilon_0}(15\rho_0\frac{h}{\pi} - (4\sigma(L_x - h) + \sigma(h))) - \phi_1 + \phi_2 - \frac{L_x}{\epsilon_r\epsilon_0}(-\sigma(L_x - h) + \rho_0 3\frac{h}{\pi})) \\ a_1 = (\frac{\sigma(h)}{\epsilon_0} + a_3 - 3h\frac{\rho_0}{\pi\epsilon_0})\frac{1}{\epsilon_r} \\ b_1 = \phi_1 \\ a_2 = (-\frac{\sigma(L_x - h)}{\epsilon_0} + a_3 + 3.0h\frac{\rho_0}{\pi\epsilon_0})\frac{1}{\epsilon_r} \\ b_2 = \phi_2 - L_x a_2 \\ b_3 = ha_1 + \phi_1 - ha_3, \end{cases} \tag{A.2}$$

where $\sigma(h)$ and $\sigma(L_x - h)$ are the local charge surface area at $x = h$ and $x = L_x - h$, respectively. These coefficients appear in the analytical expressions of the potential ϕ and of the electric fields E_x and E_y:

$$\begin{cases} \forall x < h,\ \phi(x) = a_1 x + b_1 \\ \forall x > L_x - h,\ \phi(x) = a_2 x + b_2 \\ \forall x \in [h; L_x - h],\ \phi(x) = \rho_0(3.0\frac{h}{\pi})^2 \frac{\cos\left(\frac{\pi}{3}(\frac{x}{h} + \frac{1}{2})\right)}{\epsilon_0} + a_3 x + b_3 \end{cases} \tag{A.3}$$

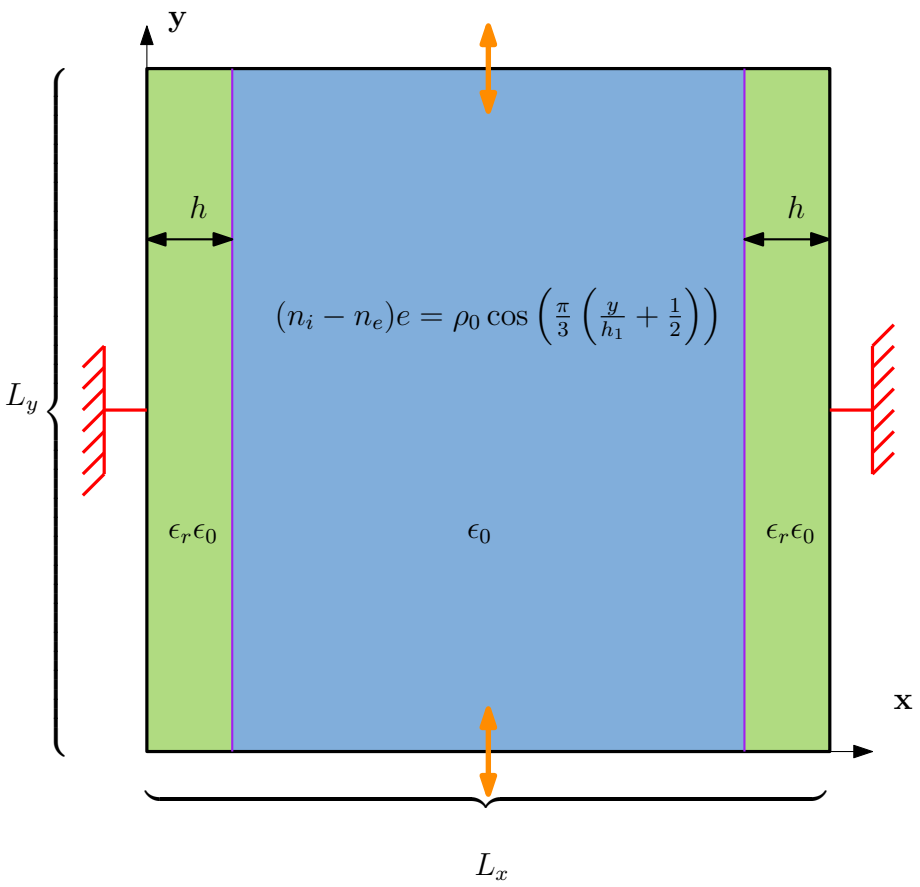

Figure A.1: Schematic of unit test case for the dielectric. The dielectric layers are highlighted in green and delimited by the plasma flow (blue) by the dielectric interface shown in purple.

$$\begin{cases} \forall x < h,\ E_x(x) = -a_1 \\ \forall x > L_x - h,\ E_x(x) = -a_2 \\ \forall x \in [h; L_x - h],\ E_x(x) = \rho_0 (3.0\frac{h}{\pi}) \frac{\sin\left(\frac{\pi}{3}(\frac{x}{h} + \frac{1}{2})\right)}{\epsilon_0} - a_3 \end{cases} \tag{A.4}$$

$$\forall x,\ E_y(x) = 0. \tag{A.5}$$

Therefore, we can compare the analytical solution with results from AVIP. The numerical parameters are summed up in Table A.1. Numerical results are presented and verified in Figure A.2. In the first row are shown the 2D maps of the potential and electric fields. In the second row, we present their corresponding profiles in the x direction along with the analytical expression derived in Equations (A.3) to (A.5). We can see there is an excellent agreement of the 1D profiles in all cases. In particular the potential remains continuous and the discontinuity of the orthogonal component of the electric field, i.e., E_x is well captured. The tangential component, i.e., E_y remains continuous and has a very small magnitude due to numerical noise.

		Symbol	Value
Simulation domain			
	y space step	dy	$2\,\mathrm{cm}$
	x space step	dx	$1\,\mathrm{cm}$
	Domain size	$L_x \times L_y$	$1 \times 1\,\mathrm{m}^2$
Poisson equation parameters			
	Wall potential (left)	ϕ_1	$0\,\mathrm{V}$
	Wall potential (right)	ϕ_2	$200\,\mathrm{V}$
	Relative dielectric permittivity	ϵ_r	5
	Dielectric layer width	ϵ_r	$20\,\mathrm{cm}$
Imposed charge distribution $e(n_i - n_e)$			
	Strength of source term	ρ_0	$-8.01 \times 10^{-8}\,\mathrm{C\,m}^3$
	Surface distribution at $x = h$	$\sigma(h)$	$0\,\mathrm{C\,m}^2$
	Surface distribution at $x = L_x - h$	$\sigma(L_x - h)$	$0\,\mathrm{C\,m}^2$

Table A.1: Parameters of unit test case

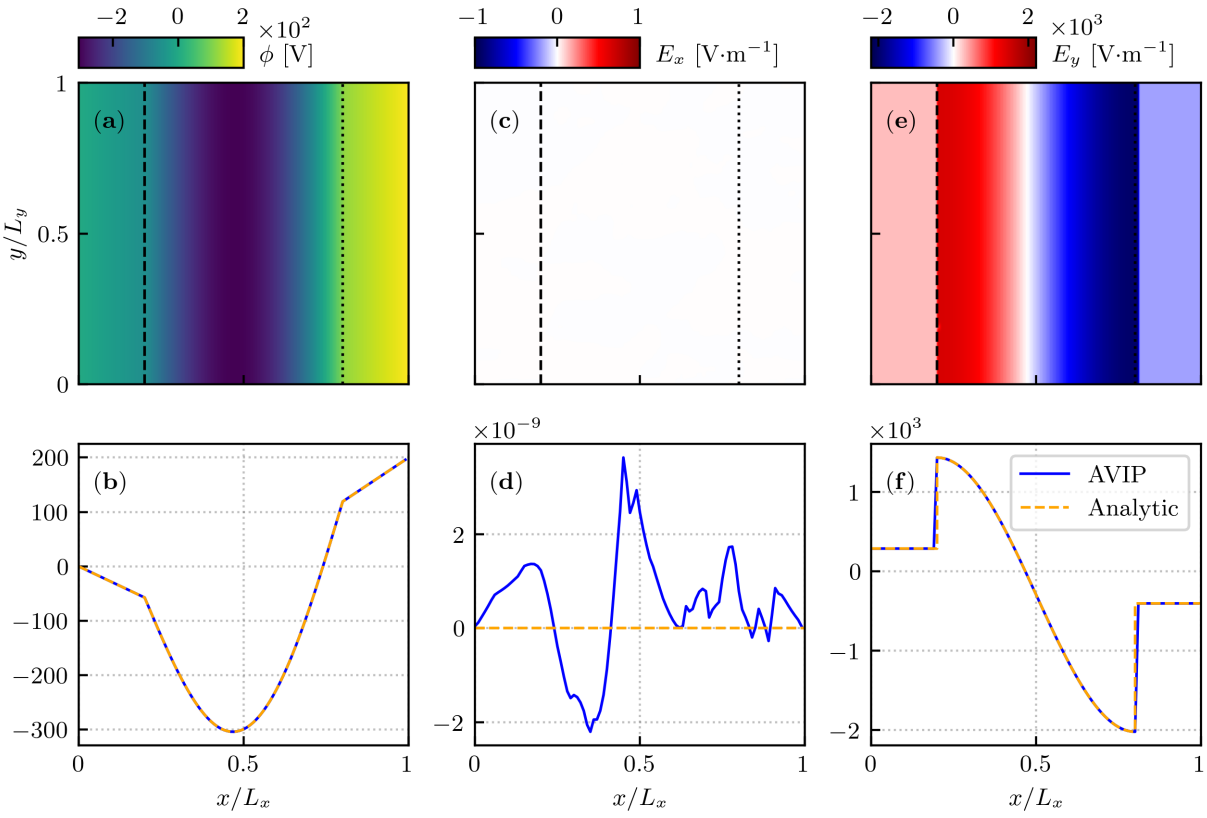

Figure A.2: Comparison of numerical results with analytical ones for the unit test case. (a): 2D map of potential ϕ. (b): 1D profile of ϕ in the x direction. (c): 2D map of electric field E_x. (d): 1D profile of E_x in the x direction. (e): 2D map of electric field E_y. (f): 1D profile of E_y in the x direction. Black dashed and dotted lines at the first row indicate the dielectric layer interface with the plasma flow.

Appendix B

Paper draft on axial-azimuthal benchmark

2D axial-azimuthal Particle-In-Cell benchmark for low-temperature partially magnetized plasmas

T. Charoy[1], J.P. Boeuf[2], A. Bourdon[1], J.A. Carlsson[3], P. Chabert[1], B. Cuenot[4], D. Eremin[5], L. Garrigues[2], K. Hara[6], I.D. Kaganovich[7], A.T. Powis[8], A. Smolyakov[9], D. Sydorenko[9,10], A. Tavant[1,11], O. Vermorel[4], W. Villafana[4,11]

[1] *Laboratoire de Physique des Plasmas, CNRS, Ecole polytechnique, Sorbonne Université, Université Paris-Sud, Observatoire de Paris, Université Paris-Saclay, PSL Research University, 91128 Palaiseau, France*

[2] *LAPLACE, Université de Toulouse, CNRS, F-31062 Toulouse, France*

[3] *RadiaSoft LLC, Boulder, CO 80301, USA*

[4] *CERFACS – 42, avenue Gaspard Coriolis, 31057 Toulouse, France*

[5] *Ruhr University Bochum, Universitaetsstrasse 150, 44801 Bochum, Germany*

[6] *Texas A&M University, College Station, TX 77843*

[7] *Princeton Plasma Physics Laboratory, Princeton, New Jersey 08540, USA*

[8] *Princeton University, Princeton, New Jersey 08544, USA*

[9] *Department of Physics and Engineering Physics, University of Saskatchewan, 116 Science Place, Saskatoon SK S7N 5E2, Canada*

[10] *University of Alberta, Edmonton, Alberta T6G 2E1, Canada*

[11] *Safran Aircraft Engines, 27208 Vernon, France*

E-mail: `thomas.charoy@lpp.polytechnique.fr`

June 2019

Abstract. The increasing need to demonstrate the correctness of computer simulations has highlighted the importance of benchmarks. We define in this paper a representative simulation case to study low-temperature partially-magnetized plasmas. Seven independently developed Particle-In-Cell codes have simulated this benchmark case, with the same specified conditions. The characteristics of the codes used, such as implementation details or computing times and resources, are given. First, we compare at steady-state the time-averaged axial profiles of three main discharge parameters (axial electric field, ion density and electron temperature). We show that the results obtained exhibit a very good agreement within 5% between all the codes. As $\boldsymbol{E}\times\boldsymbol{B}$ discharges are known to cause instabilities propagating in the direction of electron drift, an analysis of these instabilities is then performed and a similar behaviour is retrieved between all the codes. A particular attention has been paid to the numerical convergence by varying the number of macroparticles per cell and we show that the chosen benchmark case displays a good convergence. Detailed outputs are given in the supplementary data, to be used by other similar codes in the perspective of code verification.

Keywords: **ExB** discharges, Benchmark, Particle-In-Cell, Electron drift instability

Submitted to: *Plasma Sources Sci. Technol.*

1. Introduction

In different applications of low-temperature plasmas, such as Hall Thrusters for electric propulsion [1, 2] or magnetron discharges for plasma processing [3, 4], the gas pressure is relatively low (typically between 0.1 and 10 mTorr) and the plasma is confined by a magnetic field to enhance ionization. This external static magnetic field is imposed in the direction perpendicular to the electric field from the cathode to the anode, and hence a cross-field drift is induced in the $\boldsymbol{E}\times\boldsymbol{B}$ direction ($\boldsymbol{E}$ is the electric field and $\boldsymbol{B}$ the imposed magnetic field). For an efficient plasma confinement, the $\boldsymbol{E}\times\boldsymbol{B}$ direction is closed, corresponding to the azimuthal direction in a cylindrical geometry. The main difference with fusion plasmas is that the electrons are strongly magnetized, while the ions are not (the ion Larmor radius is much bigger than the plasma dimensions), which is the reason why these plasmas are often called "partially magnetized plasmas".

The presence of the magnetic field can trigger many fluctuations in ExB discharges thus increasing significantly the physics complexity, and, in particular, resulting in electron cross-field mobility several orders of magnitude higher than the expected classical collisional mobility. Combinations of gradients of plasma density, temperature and magnetic field, electron ExB drift, ionization and collisions can all be sources of fluctuations in various regions of the discharges [5, 6]. Recently, the kinetic instability due to strong electron drift, often called Electron Cyclotron Drift Instability (ECDI) [7] has attracted much attention as a possible source of the anomalous electron transport in Hall thrusters [8, 9, 10]. This instability does not require any gradients nor collisions and may be active in the region of large electric field. It has been further studied for conditions of Hall trusters [11, 12, 13] and magnetron discharges [14, 15]. This instability is kinetic in nature but the Boltzmann equation is so complex in these systems that no good analytical solution can be derived. Hence, Particle-In-Cell (PIC) simulations are required to better understand its origins and effects on the electron transport.

However, one of the challenges in these devices is that the collisionless instabilities and collisional phenomena (e.g. ionization) occur simultaneously [16]. Due to the relatively high plasma density (typically $n \approx 10^{18}$ m^{-3}), small cells (typically $\Delta x \approx 20$ μm) and time steps (typically $\Delta t \approx 1$ ps) are required to simulate device scale phenomena on the order of a few cm and 10 kHz. In addition, the multi-dimensional nature (axial convection, azimuthal $\boldsymbol{E}\times\boldsymbol{B}$ drift, radial wall effects) of the plasma flow makes PIC simulations of $\boldsymbol{E}\times\boldsymbol{B}$ discharges computationally expensive.

In the last decade, the growing performances of computer facilities have stimulated the development of simulation codes, that have become indispensable tools in plasma studies. However, as the numerical models have become more and more complex, the

validity of the results must be investigated. They could be affected by various numerical errors and uncertainties (such as numerical noise), algorithms and models used, or even by the configuration of input parameters. Therefore, there is an increasing need for verification and validation (V&V) of simulation codes. While validation implies comparison with real experiments, verification could be done in many ways such as unit and mezzanine tests for specific parts of a code [17], or benchmarking, i.e. code-to-code verification. The early work of Surendra [18], in which the results of twelve different codes (kinetic, hybrid and fluid) on a 1D low-pressure (30, 100 and 300 mTorr) radio-frequency discharge in helium were compared, is considered as a pioneer for the benchmarking of simulation codes in the low-temperature plasma community. Later, a similar 1D case in helium was benchmarked by Turner *et al.* [19] with five independently developed PIC codes, and they demonstrated that the results obtained for 4 pressures (30, 100, 300 and 1000 mTorr) were statistically indistinguishable. It paved the way to an increased benchmarking activity for different types of plasma discharges. In particular, in [20], two 1D PIC codes have been compared on a parallel plate glow discharge in helium at 3.5 Torr. In [21], six 2D fluid codes have been compared on the simulation of axisymmetric positive streamers in dry air at atmospheric pressure on three test cases of increasing complexity, and the authors stated that "the results agree reasonably well".

Even though a 1D helium benchmark is an efficient tool to verify the main algorithms of a PIC code (such as the Poisson solver and equations of motion) along with the Monte Carlo Collision (MCC) module, this case is only one dimensional with no magnetic field and hence, it would be beneficial for the low-temperature plasma community to benchmark simulation codes using a more complex model, such as $\boldsymbol{E}\times\boldsymbol{B}$ discharges. Moreover, it has been observed recently by Janhunen *et al.* [22, 23] that numerical noise may influence the results of PIC simulations by imitating the effect of collisions and hence, it is important to better understand the influence of the numerical parameters. The chosen simulation model should exhibit the relevant physics of an $\boldsymbol{E}\times\boldsymbol{B}$ discharge (high peak value of axial electric field, azimuthal instabilities, etc.) and in the meantime, it should be simple enough to be simulated in a reasonable computational time. In this paper, a 2D simulation model close to the one proposed by Boeuf and Garrigues [24] is adopted, with a longer azimuthal length and a higher number of macroparticles per cell to assess numerical convergence. The advantage of this test case is that a steady state is reached quickly, which facilitates comparison of the results. Moreover, the computational cost of PIC simulations has increased the need for quicker algorithms and made code parallelization compulsory. Hence, the seven independent codes considered here exhibit different features to decrease computational times and it makes this benchmarking activity even more relevant. An agreement on insightful parameters of the discharge will strengthen the confidence in our codes and legitimize them for further analysis of $\boldsymbol{E}\times\boldsymbol{B}$ discharges. This test case is not only intended to study the physics of a Hall thruster, but also could be used in a general way to benchmark all $\boldsymbol{E}\times\boldsymbol{B}$ discharge codes.

In this paper, we first describe in section 2 the simulation model chosen, along

with the detailed algorithms used. Then, the specificities of each independent PIC code are given in section 3 along with the computational times and resources. Section 4 is dedicated to the comparison of the results. Azimuthally and time averaged (at steady state) axial profiles of main discharge parameters (axial electric field, ion density and electron temperature) are first compared and then, we look at the characteristics of the azimuthal instabilities. The sensitivity of the benchmark and the numerical convergence according to the number of macroparticles per cell is then discussed in section 5, prior to conclude on the agreement obtained between all the codes.

2. Description of the model

To study the azimuthal $\boldsymbol{E}\times\boldsymbol{B}$ electron drift instability and the associated axial electron transport, a 2D axial-azimuthal Particle-In-Cell benchmark case is considered with conditions close to those of a typical $\boldsymbol{E}\times\boldsymbol{B}$ discharge. Some simplifying assumptions have been made to make the case reproducible in a reasonable computational time. Indeed, the intermolecular collisions and neutral transport are neglected while a given ionization source term is imposed [24] and hence, we are able to obtain a steady state result in a short time (i.e. 10 μs).

2.1. Simulation domain

As illustrated in figure 1, the computational domain corresponds to a 2D structured Cartesian mesh, which models the axial (x) and azimuthal (y) directions of an $\boldsymbol{E}\times\boldsymbol{B}$ discharge. Hence, the curvature of the (x,y) plane is neglected. The left-hand side boundary of the domain represents the anode plane, with a fixed potential of 200V, while the right-hand side corresponds to the cathode plane, where electrons are emitted. The distance between the anode and the cathode corresponds to the axial length of L_x=2.5 cm, with the position of radial magnetic field maximum at x=0.75 cm. To reduce computational times, a small region (L_y=1.28 cm) in the azimuthal direction is taken into account and periodic boundary conditions are imposed.

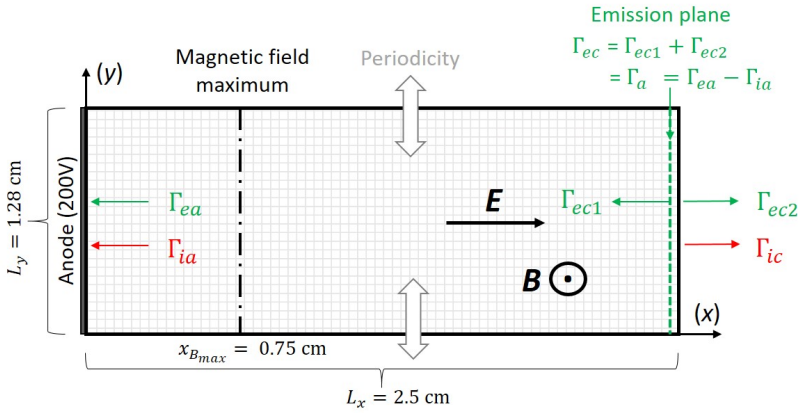

Figure 1: Simulation domain. x is the axial direction, y the (periodic) azimuthal direction. Black pointed dashed line ($x_{B_{max}}$=0.75 cm): position of maximum radial magnetic field. Green dashed line (x_e=2.4 cm): plane from which electrons are emitted uniformly along the azimuthal direction. The azimuthally averaged fluxes are represented. Γ_{ea} and Γ_{ia}: respectively electron and ion fluxes through the left boundary. Γ_{ec1}: electron flux from the cathode going into the discharge. Γ_{ec2} and Γ_{ic}: respectively electron and ion fluxes through the right boundary.

As most of the codes used are explicit, the cell size Δx and time step Δt needed to satisfy the PIC stability conditions :

$$\begin{cases} \Delta t \leq \dfrac{0.2}{\omega_p} \\ \Delta x \leq \lambda_d \end{cases} \tag{1}$$

with $w_p = \sqrt{\frac{n_e e^2}{m\epsilon_0}}$ and $\lambda_d = \sqrt{\frac{\epsilon_0 k_B T_e}{n_e e^2}}$ being respectively the angular plasma frequency and the electron Debye length, with n_e the electron density, e the electron charge, m the electron mass, T_e the electron temperature and ϵ_0 the vacuum permittivity. In our case, the current density is fixed at 400 A.m^{-2}, which gives a maximum plasma density of around 5 $\times 10^{17}$ m^{-3} and electron temperatures of about 50 eV. Hence, the minimum values for Δt and Δx will respectively be 6×10^{-12} s and 70 μm. For the benchmark case, a time step of $\Delta t = 5 \times 10^{-12}$ s and a grid spacing of Δx=50 μm with a grid of 500×256 cells are used. 4×10^6 time steps are simulated, i.e. 20 μs of the discharge, and the diagnostics are averaged every 5000 time steps.

Electrons and ions are initially loaded with a density of 5×10^{16} m^{-3} uniformly throughout the simulation domain, with velocities chosen from a Maxwellian distribution with a temperature T_e=10 eV and T_i=0.5 eV, respectively. To reduce numerical heating due to statistical noise, the number of macroparticles per cell at initialisation for the nominal case is fixed at $N_{ppc,ini} = 150$ (case 1), i.e. 150 electrons and 150 ions per cell. Then, approximately $N_{ppc,fin} \approx 550$ macroparticles per cell are obtained at stationary state. As mentioned before, this parameter could have an influence on the numerical

results and hence, an extensive study of code convergence has also been conducted by simulating two other cases with $N_{ppc,ini} = 75$ (case 2) and $N_{ppc,ini} = 300$ (case 3).

All the simulation parameters are summarized in Table 1.

Table 1: Input parameters.

Parameter	Symbol	Value	Unit
Computational parameters			
Time step	Δt	5×10^{-12}	s
Cell size	$\Delta x = \Delta y$	5×10^{-5}	m
Final time	T_{final}	20×10^{-6}	s
Cells in axial direction	N_x	500	
Cells in azimuthal direction	N_y	256	
Axial length	L_x	2.5	cm
Azimuthal length	L_y	1.28	cm
Initial state			
Macroparticles per cell	$N_{ppc,ini}$	75/**150**/300	
Plasma density	$n_{p,ini}$	5×10^{16}	m^{-3}
Physical parameters			
Discharge voltage	U_0	200	V
Electron initial temperature	$T_{e,ini}$	10	eV
Ion initial temperature	$T_{i,ini}$	0.5	eV

2.2. Imposed axial profiles

Radial magnetic field The axial profile of the radial magnetic field is imposed with a Gaussian shape, as shown in figure 2:

$$B(x) = a_k \; exp(-\frac{(x - x_{B_{max}})^2}{2\sigma_k^2}) + b_k \tag{2}$$

with $k = 1$ for $x < x_{B_{max}}$ and $k = 2$ for $x > x_{B_{max}}$. The values of the a_k and b_k coefficients can be easily calculated from the given parameters: B_0=B(x=0)=6 mT, $B_{L_x} = B(x = L_x)$=1 mT, B_{max}=10 mT, $x_{B_{max}} = 0.3L_x$=0.75 cm and $\sigma_1 = \sigma_2 = 0.25L_x$=0.625 cm. Their formula are given in Appendix A.

Ionization profile For this benchmark case, no collisions are considered. However, ionization events are taken into account as a source term for the plasma to sustain the discharge. To do so, electron-ion pairs are injected at each time step according to the profile of a given ionization rate $S(x)$, dependent on x only (uniform in azimuthal direction). $S(x)$ has a cosine shape, as shown on figure 2:

$$\begin{cases} S(x) = S_0 \; cos(\pi \dfrac{x - x_m}{x_2 - x_1}) \text{ for } x_1 \leq x \leq x_2 \\ S(x) = 0 \text{ for } x < x_1 \text{ or } x > x_2 \end{cases} \tag{3}$$

with $x_1 = 0.25$ cm, $x_2 = 1$ cm and $x_m = \frac{x_1 + x_2}{2} = 0.625$ cm.
The maximum ion current density J_M can be extracted from the steady-state continuity

equation, accounting for the ionization profile in equation 3 by:

$$J_M = e\int_0^{L_x} S(x)dx = \frac{2}{\pi}(x_2 - x_1)eS_0 \tag{4}$$

Hence, we impose $\frac{J}{M} = 400$ A.m^{-2} by fixing the maximum value of the ionization profile to $S_0 = 5.23 \times 10^{23}$ m^{-3}.s^{-1}.
The number of electron-ion pairs to inject at each time step Δt is given by $L_y \Delta t \int_0^{L_x} S(x)dx$ and the positions (x_i,y_i) are chosen randomly such as:

$$\begin{cases} x_i = x_m + sin^{-1}(2r_1 - 1)\dfrac{(x_2 - x_1)}{\pi} \\ y_i = r_2 L_y \end{cases} \tag{5}$$

with r_1 and r_2 two random numbers uniformly distributed over the interval [0,1]. For one pair, the electron and the ion are injected at the exact same position. Their velocities are chosen from a Maxwellian distribution with the same temperature as initialisation (T_e=10 eV and T_i=0.5 eV).

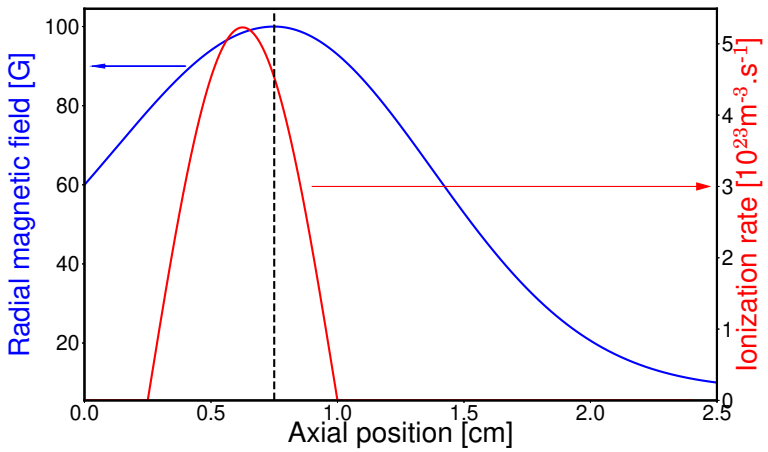

Figure 2: Axial profiles of the imposed radial magnetic field and ionization rate. Dashed line corresponds to the position of maximum magnetic field.

2.3. Boundary conditions

Electrons and ions which cross the left or right boundary plane of the domain are removed from the simulation. However, to ensure current continuity and neutralization of the extracted ion beam, electrons are injected from the cathode plane. The emission line is set on the downstream of the simulation domain, at 1 mm from the right domain boundary. The number of electrons injected at each time step is calculated using the current conservation through the discharge to obtain Γ_{ec}, the absolute value of azimuthally averaged emitted electron flux:

$$\Gamma_{ec} = \Gamma_a = \Gamma_{ea} - \Gamma_{ia} \tag{6}$$

with Γ_{ea} and Γ_{ia} being respectively the absolute values of azimuthally averaged electron and ion fluxes to the anode side, displayed on figure 1. Hence, by counting the number of electrons and ions that cross the anode boundary at each time step (respectively ΔN_{ea} and ΔN_{ia}), the corresponding number of electrons emitted from the emission plane can be calculated as:

$$\Delta N_{e,emi} = \Delta N_{ea} - \Delta N_{ia} \tag{7}$$

These electrons are injected uniformly in the azimuthal direction, with a Maxwellian velocity distribution with a temperature $T_{e,emi}$=10 eV.

However, this method for calculating the number of emitted electrons does not prevent an artificial cathode sheath to form. To suppress artificially this sheath, the emission plane is shifted by 1 mm from the right boundary plane (i.e. to the position x_e=2.4 cm) and its potential is adjusted at each time step by imposing a zero azimuthally averaged potential at this location. Hence, the azimuthally averaged potential drop between the anode and the emission plane is maintained constant and equal to the applied voltage (200V). To do so, we solve the Poisson equation for U:

$$\Delta U = -\frac{e}{\epsilon_0}(n_i - n_e) \tag{8}$$

with boundary conditions $U(0, y) = U_0$ and $U(L_x, y) = 0$. Then, we obtain the electric potential ϕ by subtracting the azimuthally averaged potential at the emission plane $\overline{U_e}$ from the solution $U(x, y)$ of Poisson equation:

$$\phi(x, y) = U(x, y) - \frac{x}{x_e}\overline{U_e} \tag{9}$$

with:

$$\overline{U_e} = \frac{1}{L_y}\int_0^{L_y} U(x_e, y)dy \tag{10}$$

The right boundary plane will have a varying negative potential but this drop in potential between the emission plane and the right boundary plane does not have any useful physical meaning and does not affect the main discharge physics.

3. Code specificities

Seven groups participated in this study, each group using its own independently developed simulation code. While the codes are all Particle-In-Cell (PIC) codes, they mainly differ in the way the equation of motion and the Poisson equation are solved. All the codes are using a bilinear interpolation scheme (Cloud-In-Cell) and ions are considered unmagnetized, due to their large Larmor radius compared to the domain dimensions. The exact physical charge-to-mass ratio for ions (here Xenon ions are considered) is used by all the codes. As described in the previous section, periodic boundary conditions are imposed in the azimuthal direction, whereas the plasma potential is fixed at 200V at the left boundary (anode) and 0V at the right boundary (cathode).

As the benchmark cases are quite computationally expensive, the code performances are obtained through parallelization. This could be done via MPI (Message Passing Interface), combined or not with OpenMP (Open Multi-Processing), or using GPU instead of CPU. Each processor can consider one portion of the computational grid (domain decomposition) or one portion of the particles in the domain (particle decomposition) in order to speed-up the computation. Another way of decreasing significantly the computational time is to move the ions every N_{sub} electron time steps, as they are way slower than the electrons and barely move during one time step [25].

A summary of the codes specificities is provided in table 2, along with the simulation times for the 3 benchmark cases.

*3.1. Group **LPP**: T. Charoy, A. Tavant, A. Bourdon, P. Chabert*

The 2D-3V PIC-MCC simulation code *LPPic* was used. The code features a structured Cartesian mesh fixed in time, the Poisson equation is solved using an iterative parallel multigrid solver (PFMG from the open source HYPRE library [26]) and the particles are advanced via a classic leapfrog scheme, along with a Boris scheme [27]. The code is parallelized via MPI through a domain decomposition. It has been verified with the 1D helium benchmark of Turner *et al* [19] (further details in [28, 29]) and extensively used to simulate the radial-azimuthal plane of a Hall Thruster [28, 30, 31]. For this benchmark, the code was adapted to the axial-azimuthal plane and accelerated via a load-balancing algorithm (adjusting periodically the size of each processor domain to have approximately the same number of particles inside each processor). Ions are moved every 11 electron time steps to decrease computational time [25]. It was checked that it has a negligible influence on the obtained results. The Random Number Generator (RNG) used is the *Fortran 2003* RNG, seeded by the internal clock of every CPU.

*3.2. Group **LAPLACE**: L. Garrigues, J.P. Boeuf*

Explicit electrostatic PIC-MCC models developed at Laplace resolve the space in two-dimensions [32, 33, 34, 35, 36, 37, 38] and three-dimensions [39, 40] (Cartesian coordinates with structured meshes) and three dimensions in velocity phase. Trajectories of charged particles are integrated according to a standard leap-frog scheme with a Boris algorithm [27]. Poisson's equation is solved using the direct PARDISO solver included in the MKL library of INTEL. A particle decomposition method is used and an hybrid approach coupling MPI and OpenMP techniques is used to accelerate parallelization. Typically, a MPI thread per socket is attached and a number of OpenMP threads is taken identical to the number of cores per socket. No subcycling technique is used (ions are moved every time step). The RANDU function is used to generate pseudo-random numbers between 0 and 1 [41].

*3.3. Group **CERFACS**: W. Villafana, B. Cuenot, O. Vermorel*

The PIC version of the AVIP code was used. AVIP is a massively parallel code able to model the plasma dynamics of Hall thrusters in complex 2D/3D geometries using unstructured grids. AVIP has been built upon the AVBP combustion code structure [42], which has been extensively validated and specifically designed for efficient calculations with a high number of processors [43]. Both PIC and fluid modelings are available [44, 45]. For the present PIC simulations, ions and electrons velocities are respectively updated with standard Leap-Frog and Boris schemes [27]. Poisson equation is solved thanks to the open-source solver MAPHYS currently developed by INRIA. It combines both direct and iterative methods for fast and accurate results [46, 47]. Domain decomposition is performed using the external library PARMETIS [48]. Domain partitioning is regularly updated to ensure a correct load balancing between processors. In order to speed up the simulation, subcycling is used for the ion motion and their position and speed are updated every 5 electron time steps. The standard RNG of Fortran 95 is used with the same seed for each run in order to ensure reproducibility of the results.

*3.4. Group **RUB**: D. Eremin*

The 2D-3V PIC code used in the present work is adopted from the implicit energy- and charge-conserving scheme suggested in [49]. The approach iteratively utilizes the Crank-Nicolson method to calculate the electrostatic field on the new time level, simultaneously with the particle orbit integration. Note that this approach employs the same shape function for the electric field and the current density (as opposed to the same shape function for the electric field and the charge density in the conventional explicit leapfrog scheme-based PIC variant implemented in all the other codes used in this benchmark), which makes the linear momentum conservation inexact. However, as the results demonstrate, this does not seem to hamper the model.

In order to reduce the computational cost, the Poisson equation rather than Ampere's formulation was adopted for the electrostatic field. In case of a charge-conserving scheme, both approaches are equivalent, but the Poisson equation requires calculating the charge density only at the end of a time step, instead of having to add contribution to the current density each time a particle crosses a grid cell if the divergence of Ampere's law is used. The charge density was calculated using the quadratic spline shape function, whereas the linear shape function was used for the electric field. Since the original work [49] did not contain treatment of boundaries at the electrode surfaces, the modifications necessary to include such effects were introduced. In order to account for the periodicity in the azimuthal direction, the field solver used the discrete Fourier transformation in this direction, after which the axial profile for each of the azimuthal field harmonics was obtained by solving the corresponding one-dimensional Poisson equation with the Thomas algorithm.

It should be emphasized that the implicit iterative scheme employed for the RUB

code is quite different from and is much more computationally expensive compared to the commonly used explicit algorithm. In contrast to the latter, the implicit scheme is predominantly aimed at self-consistent modelling of plasmas with high densities, where the need to resolve the Debye length to avoid the finite-grid instability makes the explicit approach prohibitively expensive. However, the energy-conserving implicit algorithm being relatively new, it is important to establish equivalence of its' results to the ones provided by the explicit scheme whenever possible. This dictated our choice of the algorithm for this particular benchmark. Because of the high computational cost of the scheme, everything except the field solver (which was implemented on CPU) was parallelized on GPU (NVIDIA V100 32GB) using CUDA C. Due to the limited amount of GPU memory, the case 3 was parallelized on two GPUs using an additional domain decomposition in the azimuthal direction to ensure even load balance. For the RNG, the xorshift128 method suggested in [50] has been used.

*3.5. Group **USask**: D. Sydorenko, A. Smolyakov*

The code is an explicit electrostatic particle-in-cell 2D-3V resolving 2 coordinates (x and y) and 3 velocity components for each particle. It was used in [23] and the earlier 1D version [51] was used in [22]. A leap-frog numerical scheme is used and the velocity is advanced using the Boris scheme [27]. The Poisson equation solver involves discrete Fourier transformation along the periodic direction to reduce dimensionality of the problem. The code is parallelized with MPI and domain decomposition is used. Subcycling of electrons relative to ions is used (ions moved every 11 electron time steps) to reduce numerical cost [25]. The RNG is the maximally equidistributed version of Mersenne Twister 19937 [52, 53].

*3.6. Group **TAMU**: K. Hara*

The explicit PIC code is written in C++ using Message Passing Interface (MPI). Particle decomposition is used to make the number of particles per processors to be approximately equal. Domain decomposition is used to calculate the potential via the Poisson equation using HYPRE [26], in which a multigrid method is used as a preconditioner to the GMRES solver. Double precision is used for all numerical variables and no electron subcycling is used, i.e., the ions and electrons are updated at the same time step. For the results shown, ion and electron densities as well as the potential are calculated on cell centers while similar results are obtained in calculations based on storing information on nodes. Random numbers are generated using the C Standard General Utilities Library by initializing different seed values in the individual processors.

*3.7. Group **PPPL**: A.T. Powis, J.A. Carlsson, I.D. Kaganovich*

This new electrostatic Particle-in-Cell code was developed at the Princeton Plasma Physics Laboratory and Princeton University. It was designed from the ground up for

scalability and performance on modern super-computing facilities. The code features parallelism via MPI, OpenMP, and algorithms are designed to take advantage of modern vector registers. Poisson's equation is solved over the grid using domain decomposition and via the HYPRE [26] package, which has demonstrated excellent scalability on up to 100,000 cores [54]. Particle's are distributed and shared as a list, rather than via domain decomposition. The software is capable of modeling a two-dimensional box, with arbitrary boundary conditions (conducting, periodic, mirror) and allows particle sources and losses through the walls. Particles are evolved explicitly with double precision in 2D-3V via the Boris algorithm [27]. Random numbers are generated using the double precision SIMD oriented Fast Mersenne Twister (dSFMT) package [55].

Table 2: Main codes specificities.

	LPP	**LAPLACE**	**CERFACS**	**RUB**	**USask**	**TAMU**	**PPPL**
Algorithms							
Pusher solver	Explicit	Explicit	Explicit	Implicit	Explicit	Explicit	Explicit
Poisson solver	Hypre	Pardiso	Maphys	FFT Thomas	FFT	Hypre	Hypre
Floating-point precision	Double	Single(pusher) Double (Poisson)	Double	Single(pusher) Double (Poisson)	Double	Double	Double
Code acceleration							
Architecture	CPU	CPU	CPU	GPU	CPU	CPU	CPU
Parallelization	MPI	MPI/OpenMP	MPI	CUDA	MPI	MPI	MPI/OpenMP
Decomposition	Domain	Particle	Domain	Both	Domain	Particle	Particle
Language	Fortran	Fortran	Fortran	C+Cuda C	Fortran	C++	C
Simulation times (days)							
Case 1 ($N_{ppc,ini} = 150$)	8 (360 CPU)	5 (108 CPU)	7 (360 CPU)	14 (1 GPU)	21 (32 CPU)	15 (300 CPU)	2.5 (224 CPU)
Case 2 ($N_{ppc,ini} = 75$)	5 (360 CPU)	3 (108 CPU)	4 (360 CPU)	9 (1 GPU)	11 (32 CPU)	11 (200 CPU)	2.5 (112 CPU)
Case 3 ($N_{ppc,ini} = 300$)	14 (360 CPU)	6 (180 CPU)	13 (360 CPU)	14 (2 GPU)	20 (64 CPU)	22 (400 CPU)	2.5 (448 CPU)

Before converging to the final benchmark results presented in the next section, many small implementation mistakes were found. To guide the next users of this benchmark, some general guidelines are given in Appendix A.

4. Results

Prior to performing any detailed benchmarking, it was important to make sure that all codes converge to a steady state. To do so, the time evolution of the electron axial current is compared. The electron current density injected at the emission plane J_{ec} is split in two parts : $J_{ec} = J_{ec1} + J_{ec2}$, where J_{ec1} corresponds to the electron

current density entering the channel and J_{ec2} is used to neutralize the extracted ion beam $J_{ec2} = J_{ic}$, fixed by the imposed ion current density. Hence, J_{ec1} could be used to characterize the anomalous cross-field transport in the discharge. For the comparison of results, J_{ec1} is normalized by the imposed total ion current $J_M = J_{ia} + J_{ic}$, which is set to 400 A.m^{-2} at steady state.

The time evolution of $\frac{J_{ec1}}{J_M}$ is shown in figure 3(a) for all simulation codes. It can be seen that all simulation codes reach a steady state after around 10 μs. However, it can be noticed that a small oscillation appears at steady state, with a frequency of the order of hundreds of kHz, as shown on figures 3(b) and 3(c) for code **LPP**. As this phenomena is retrieved for all the codes, we decided to average our results in time to smooth out these oscillations, which could be physical or numerical, focusing on benchmarking of time-averaged phenomena. The period has been chosen as a compromise between the need to capture enough oscillation periods at steady state and keeping a reasonable computational time, i.e. 4 μs between 16 and 20 μs.

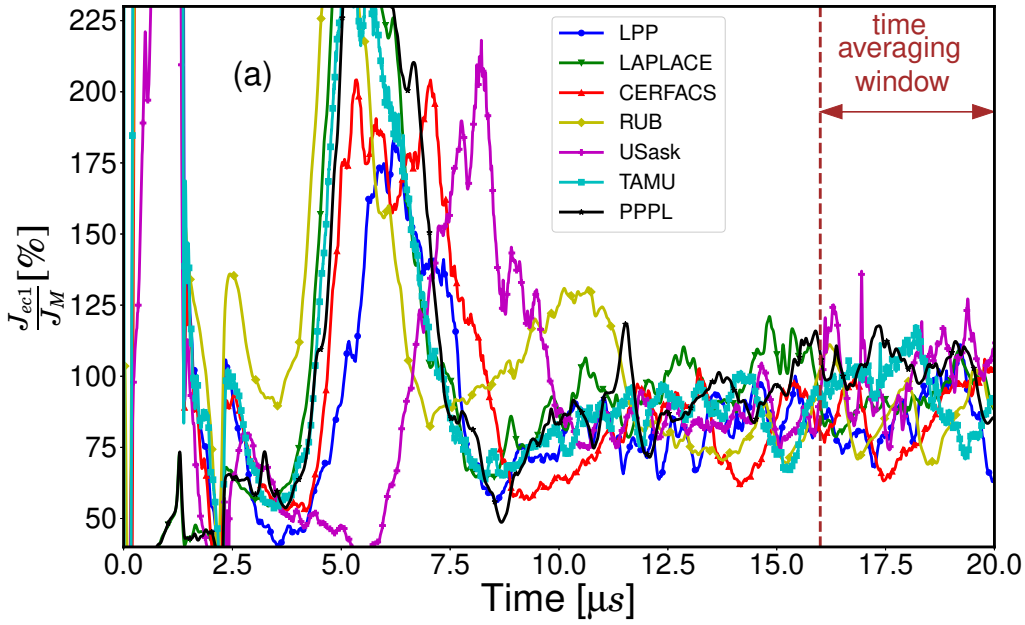

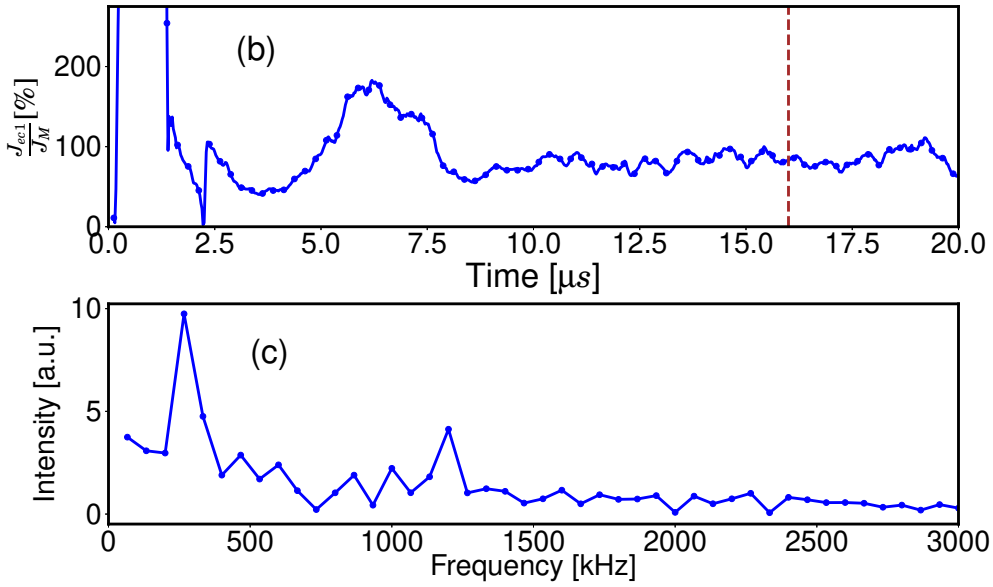

Figure 3: (a) : Time evolution of $\frac{J_{ec1}}{J_M}$ for Case 1 for all the codes. Brown dashed line: beginning of time averaging interval (until 20 μs). (b): Time evolution of $\frac{J_{ec1}}{J_M}$ for Case 1 with code **LPP**. (c): Corresponding Fast-Fourier-Transform taken from data between 12 and 20 μs.

Moreover, as mentioned before, some high-frequency instabilities propagate in the azimuthal $\boldsymbol{E}\times\boldsymbol{B}$ direction, as seen on figure 4 for the azimuthal electric field and the ion density, obtained with code **LPP** at $t = 20$ μs. To make the benchmarking of large-scale phenomena, it was decided to average in this direction. It can also be noticed that two distinct zones for the oscillations of the azimuthal electric field exist: a short wavelength zone between the anode and the location where the radial magnetic field is at maximum, called zone (I), and a long wavelength zone downstream, called zone (II). Such transition of the plasma waves is discussed more in detail in section 4.2.

One can notice on Table 2 that the computational times and resources needed to reach this steady state are quite high, with around 10 days in average for the nominal case (which corresponds to around 60000 CPU hours). Compared with the computational time of the 1D helium benchmark of Turner *et al* [19] that was around a couple of hours, parallelization of computational codes is needed to increase drastically the code performances. Moreover, it can be seen that the 7 codes simulate the cases with a broad range of computational times (between 2.5 and 21 days for the nominal case) and it shows that this benchmark is also a powerful tool to characterize the performance of a simulation code.

Below in section 4.1, the azimuthally and time averaged axial profiles of the main discharge parameters (axial electric field, ion density and electron temperature) are first analysed. Due to the interest towards understanding the effects of azimuthal plasma

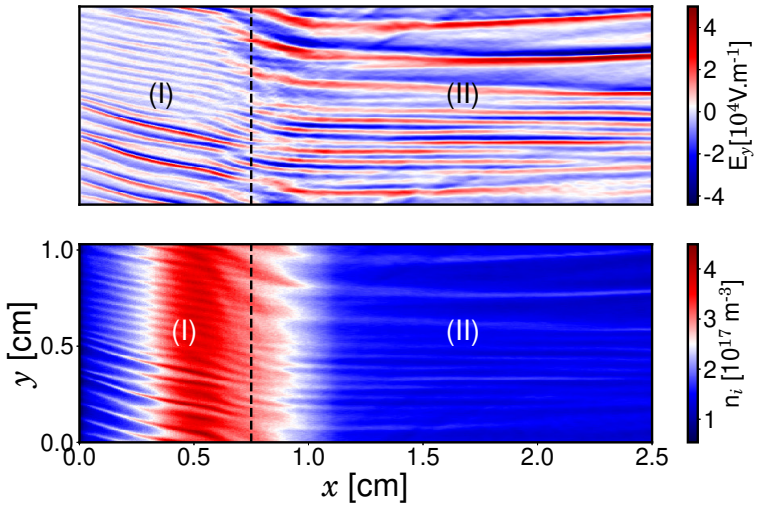

Figure 4: 2D axial-azimuthal maps of the azimuthal electric field (top) and ion density (bottom) obtained with code **LPP** at $t = 20$ μs. Dashed line corresponds to the position of maximum magnetic field that separates zone (I) and zone (II).

waves on the electron anomalous transport, the azimuthal instabilities are compared in section 4.2, investigating their dominant mode characteristics (wavelength and frequency). These comparisons are done for the 3 cases considered in this benchmark, that differ only by their number of macroparticles per cell, given in Table 3.

Table 3: Three benchmark cases. N_{ppc} is the number of macroparticles per cell. The nominal case is Case 1.

Case	**$N_{ppc,ini}$ at initialisation**	**$N_{ppc,fin}$ at steady state**
1	150	550
2	75	275
3	300	1100

4.1. Main plasma parameters

For benchmarking purposes, three parameters are chosen to be shown in this paper: the axial electric field, the ion density and the electron temperature. Since the low-frequency oscillations on the order of hundreds of kHz are not the focus of the benchmarking, the results are averaged in the azimuthal direction and in time (between 16 and 20 μs) to obtain a steady state result.

The axial profiles for the nominal case are shown on figure 5. We can see that the 7 codes display a good agreement for all the parameters. The differences are mainly on the peak value and the profile in zone (II) but the overall mean relative error is less than 5%. This difference is measured by using the mean value between all the curves and

calculating the mean relative error for every curve, that has a maximum below 5 %. It is also important to notice that all results from different codes capture the characteristics of an $\boldsymbol{E}\times\boldsymbol{B}$ discharge: a high axial electric field peaks near the maximum of radial magnetic field while the ion density is high on the anode side, just before the magnetic field peak. In particular, the results display an important feature of Hall thrusters, namely the overlapping between the ion density peak (ionization zone) and the axial electric field peak (acceleration zone). One can notice the sharp increase of the axial electric field near the right boundary that is due to the artificial sheath created outside of the region of interest (between the emission plane ($x_e = 2.4$ cm) and the right boundary). It has been shown that this region does not affect the main discharge results [24].

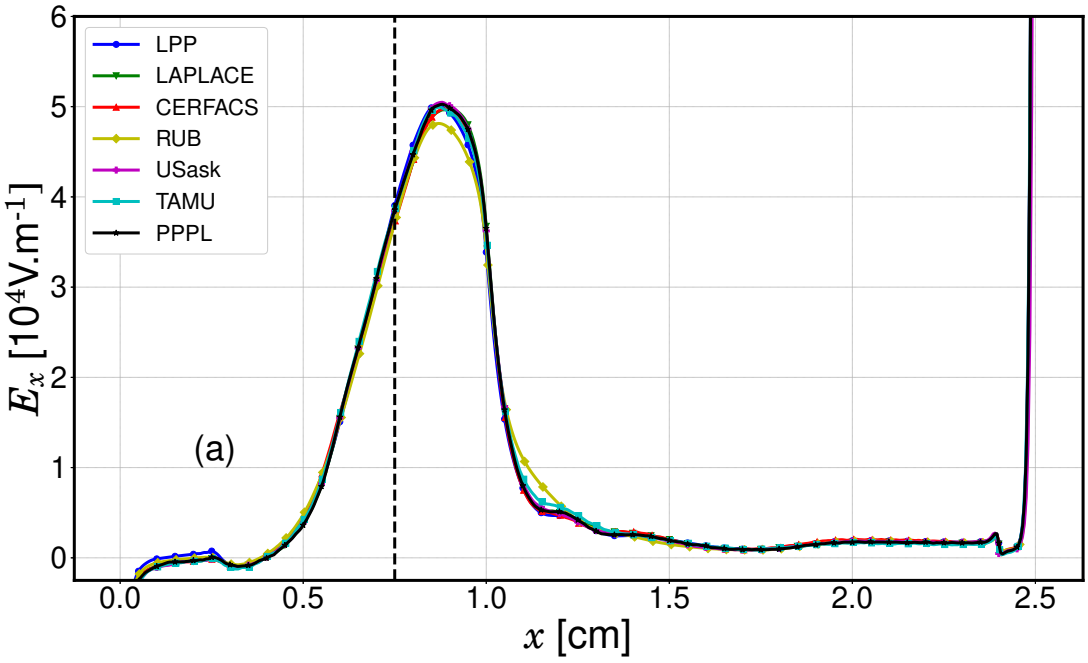

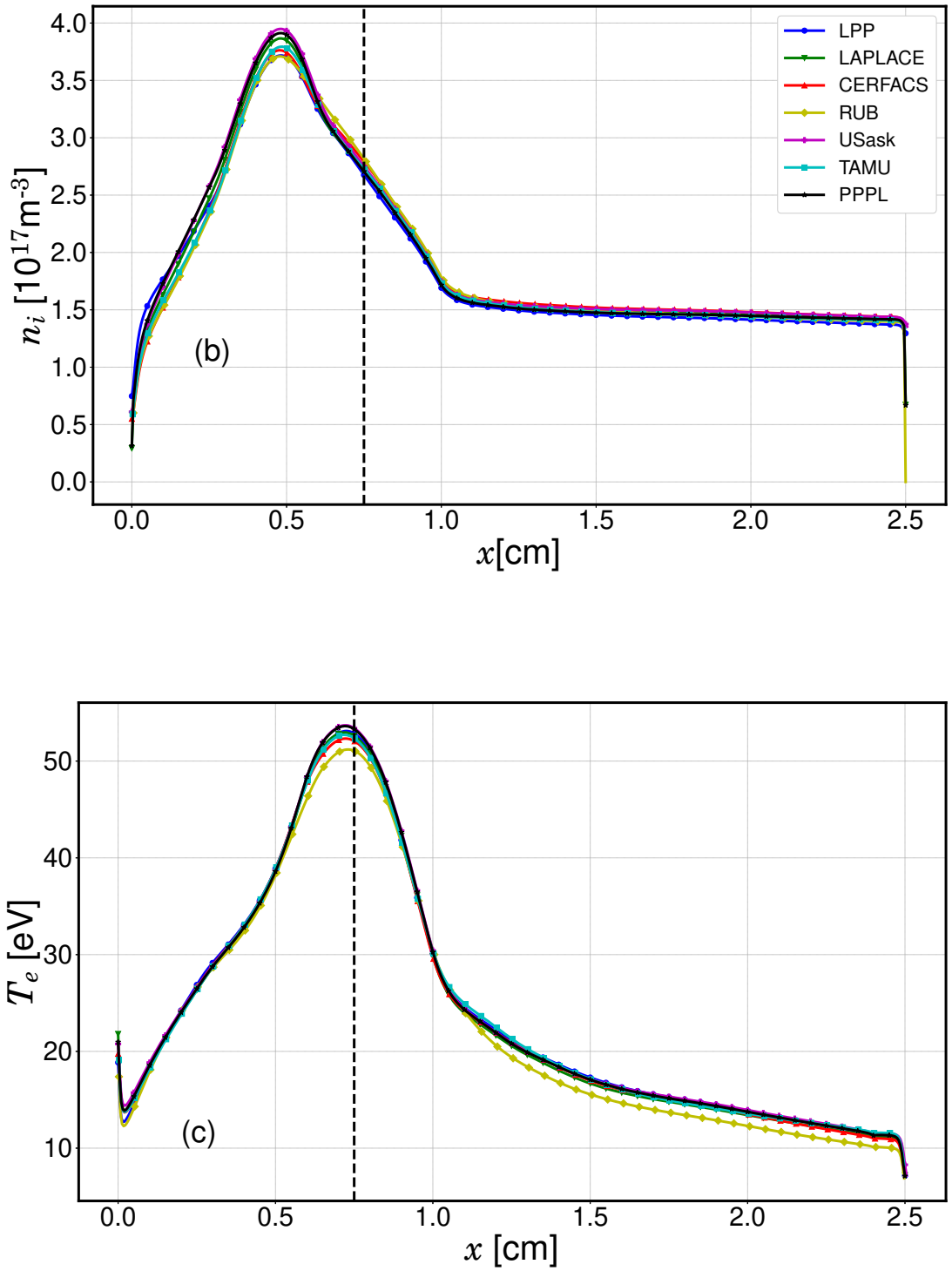

Figure 5: **Case 1** : Azimuthally and time (between 16 and 20 μs) averaged axial profiles of axial electric field (a), ion density (b) and electron temperature (c). Dashed line corresponds to the position of maximum magnetic field.

The same comparison is done for the two other cases and the results are displayed on

figures 6 and 7 respectively. They both exhibit a similar behaviour than the nominal case shown in figure 5, with an overall mean relative error between the codes less than 5%. The main reason for the slight discrepancies comes from the low-frequency oscillation behaviour, as can be seen from figure 3.

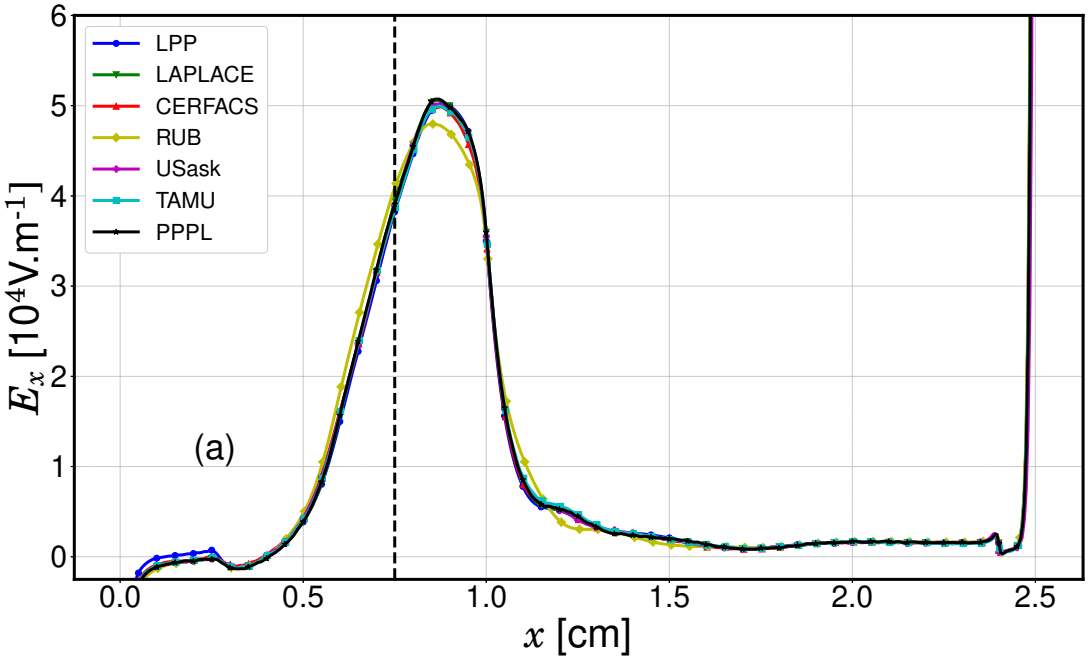

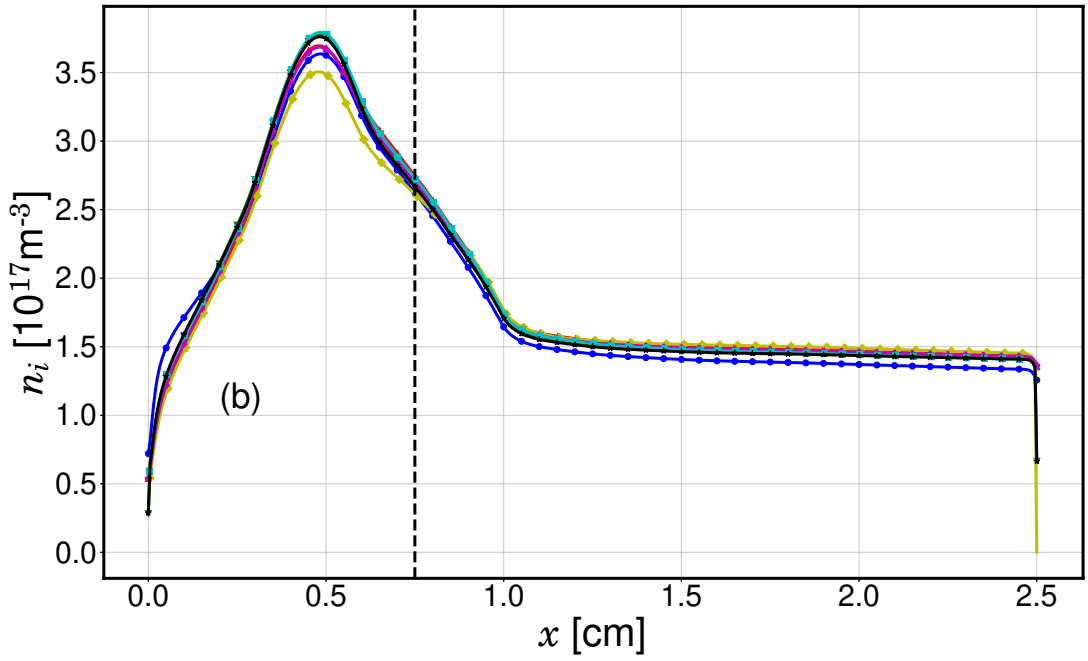

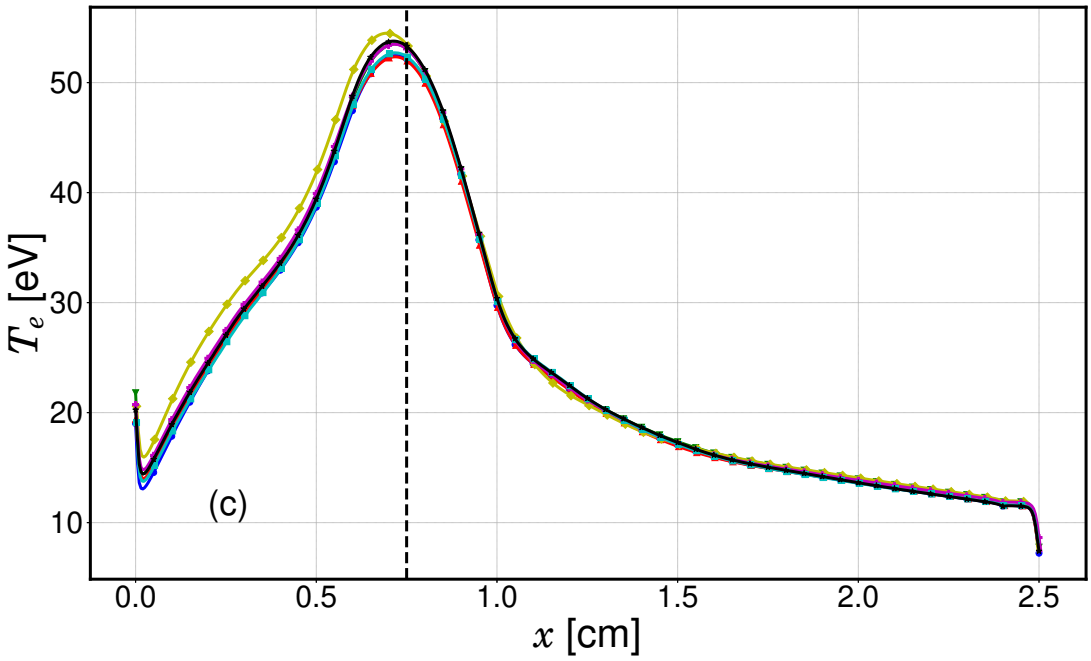

Figure 6: **Case 2** : Azimuthally and time (between 16 and 20 μs) averaged axial profiles of axial electric field (a), ion density (b) and electron temperature (c). Dashed line corresponds to the position of maximum magnetic field.

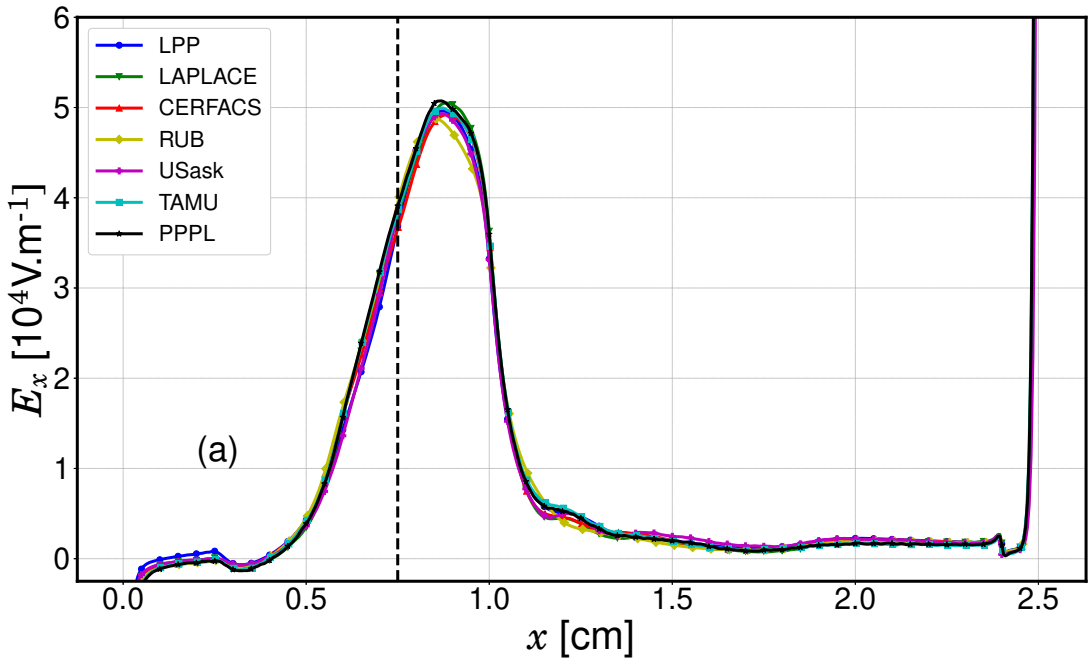

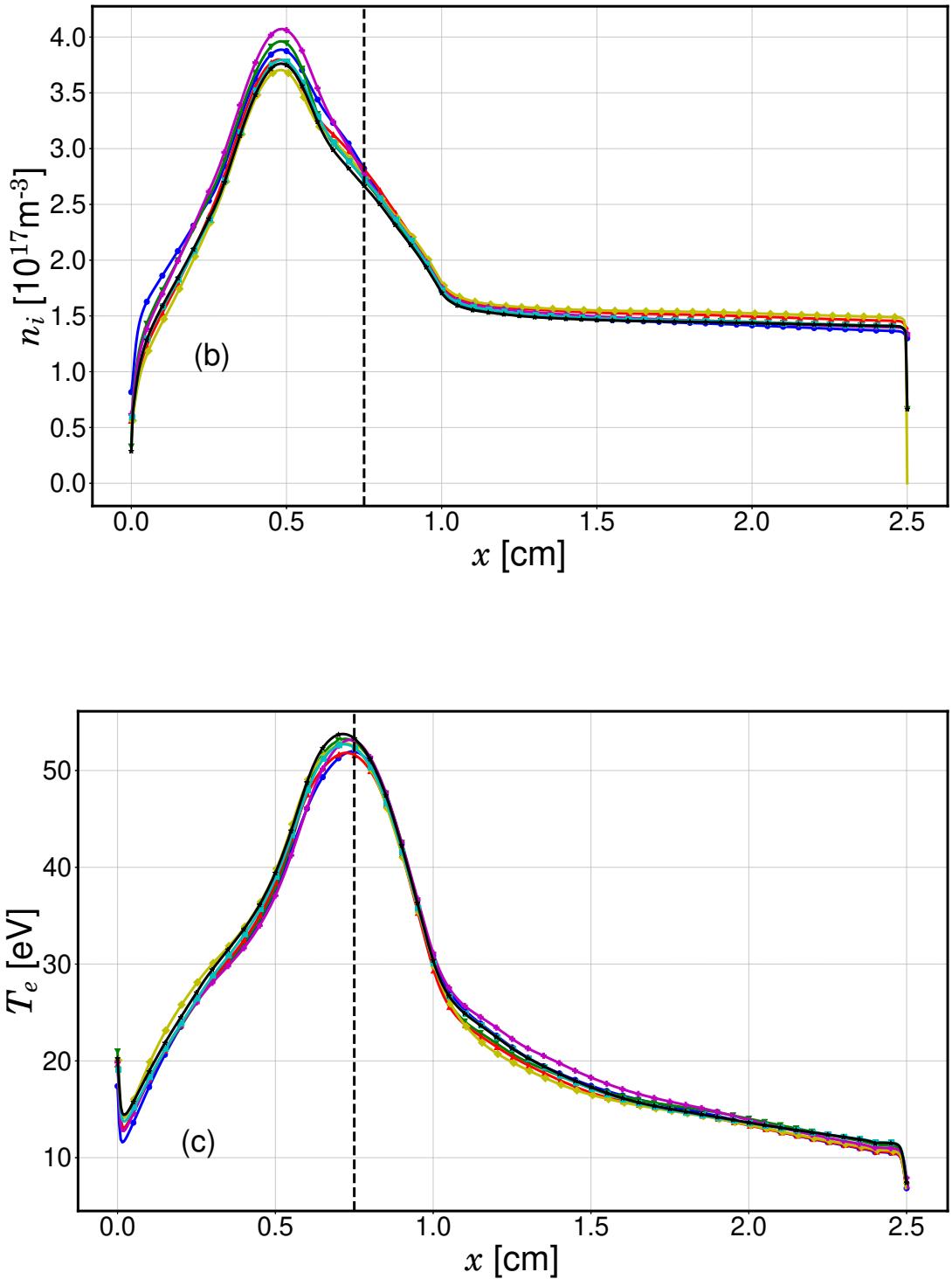

Figure 7: **Case 3** : Azimuthally and time (between 16 and 20 μs) averaged axial profiles of axial electric field (a), ion density (b) and electron temperature (c). Dashed line corresponds to the position of maximum magnetic field.

4.2. Azimuthal instabilities

In addition to the time-averaged plasma properties, the instabilities propagating in the azimuthal direction, shown on figure 4, also serve as a useful phenomenon for benchmarking of different simulation codes. Usually in 2D, when the direction parallel to the magnetic field is neglected, the ECDI exhibits a discrete behaviour around the cyclotron resonances $k_y V_E = m\omega_{ce}$, $n = 1, 2, ..$ [10]. When the wave propagation along the magnetic field is included, one can show from the linear theory that the ECDI can transition to an ion-acoustic instability [7, 9, 56, 57]. Nonlinear effects can also potentially result in transition to the ion-acoustic instability [58, 22]. The quasilinear theory of the anomalous transport based on the modified ion-acoustic instability in the conditions of Hall thruster has been proposed [56, 57]. The dispersion relation for the ion-acoustic instability in plasmas with moving ions has the form:

$$\omega_R \approx \boldsymbol{k}.\boldsymbol{v_i} \pm \frac{kc_s}{\sqrt{1 + k^2\lambda_d^2}} \tag{11}$$

A 2D Fast-Fourier-Transform (FFT) is applied to the azimuthal electric field at fixed axial positions (between 16 and 20 μs) to get the corresponding spectrum. The results for two different axial positions are displayed on figure 8 for code **LPP**. It is shown that in zone (I) (at $x = 0.3$ cm) a continuous dispersion relation is well fitted to the analytical expression of equation 11. This continuous behaviour was already observed in experiments [59] and in other 2D PIC codes that are self-consistent with the plasma generation [13]. However, closer to the cathode in zone (II) (at $x = 1.5$ cm), the dispersion relation exhibits a different behaviour, which seems more discrete.

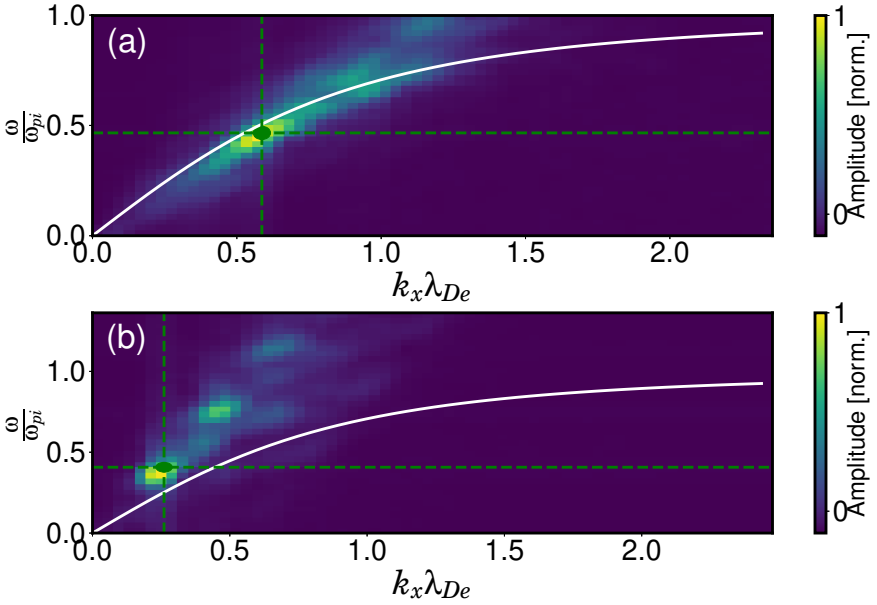

Figure 8: 2D FFT of the azimuthal electric field at x=0.3 cm (a) and x=1.5 cm (b), obtained with code **LPP**. Solid white line: ion acoustic dispersion relation. Green dashed lines: wavelength and frequency of the dominant mode.

As this paper is focused on the benchmarking of different simulation codes, detailed study of the dispersion relations of the plasma waves is out of scope. Instead, to be able to compare the results of the different codes, it was decided to extract the dominant mode at each axial position. Hence, the wave characteristics (wavelength and frequency) are compared as function of the axial position.

This axial dependence of the dominant mode characteristics for all the codes is shown on figure 9 for the nominal case. It can be seen that, in all simulation results, the wavelength and the frequency change abruptly at the position of maximum radial magnetic field. In zone (I) near the anode, the oscillations have a small wavelength ($\lambda \approx 0.5$ mm) and a high frequency ($f \approx 5$ MHz) while near the cathode in zone (II), the frequency drops to $f \approx 3$ MHz with almost a wavelength 4 times bigger ($\lambda \approx 2$ mm). The Debye length and ion plasma frequency are displayed on the bottom row for comparison. The same behaviour is retrieved for the two other cases, as seen on figures B1 and B2 that have been placed in appendix for clarity purpose. Considering the complexity of the phenomena involved, the agreement between the codes is satisfactory.

The maximum wavelength for the dominant mode is around 2 mm which is well-resolved by the length in the azimuthal direction of 1.28 cm. However, further development of long-wavelength structures may be limited either by this limited azimuthal length or by the axial convection of the modes (due to the ion flow) from the most unstable region. As this work is focused on a benchmark comparison with a simplified domain, this question will require further studies with a larger domain.

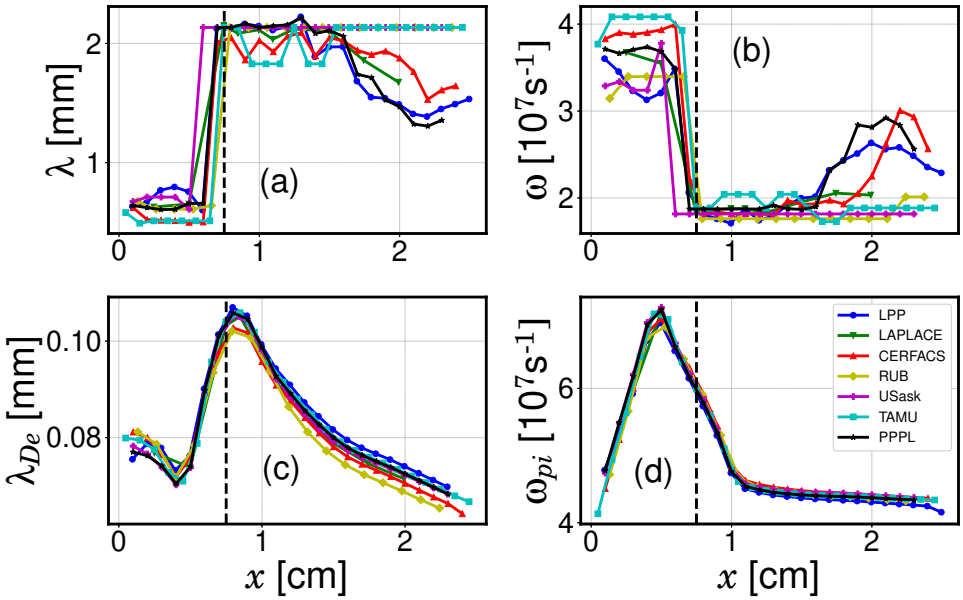

Figure 9: **Case 1**: Axial evolution of dominant mode characteristics for azimuthal electric field (azimuthal instabilities). (a) Wavelength. (b) Frequency. (c) Debye length. (d) Ion plasma frequency. Dashed line corresponds to the position of maximum magnetic field.

5. Discussion

5.1. Numerical convergence

In a PIC simulation, we consider finite-sized particles and hence, numerical collisions play a role. They can lead to fluctuations induced by thermal noise and this noise could have an impact on the study of the azimuthal instabilities and the related anomalous electron transport.

Okuda and Birdsall [60] defined a frequency for these numerical collisions in 2D simulations:

$$\nu_{num} \approx \frac{\pi \omega_{pe}}{16 N_D} \tag{12}$$

with N_D the number of macroparticles in a Debye sphere. For our nominal case (Case 1, $N_{ppc,ini}$=150), we will have around $N_{ppc,fin} \approx 550$ macroparticles per cell at steady state, in average. Looking at figure 9, we can see that the minimum Debye length is around 70 μm and hence, we have around 2π cells in a Debye sphere (worst case). It corresponds to a numerical collision frequency of $\nu_{num} \approx 5.6 \times 10^{-5} \omega_{pe}$. Turner [61] has shown that the numerical collisions can be neglected if $\frac{\nu_{num}}{\omega_{pe}} \leq 10^{-4}$ and hence our case complies with this criterion.

It is also important to assess the numerical convergence of this benchmark case more rigorously, by varying the number of macroparticles per cell. The mean value at steady state of the ratio $\frac{J_{ec1}}{J_M}$ of electron current entering the channel to the total ion

current was used as a convergence criterion. Indeed, as mentioned earlier, this ratio is related to the electron axial transport in the discharge. This transport can be enhanced by numerical collisions and hence, decreasing N_{ppc} will increase the transport and $\frac{J_{ec1}}{J_M}$ will be higher. We can retrieve this behaviour by looking at how the averaged profiles of ion density and axial electric field evolve when the number of macroparticles per cell is decreased. We observe on figure 10 for code **LPP** that if N_{ppc} is decreased, the axial electric field is increased and the ion density is decreased which is characteristic of a higher axial transport.

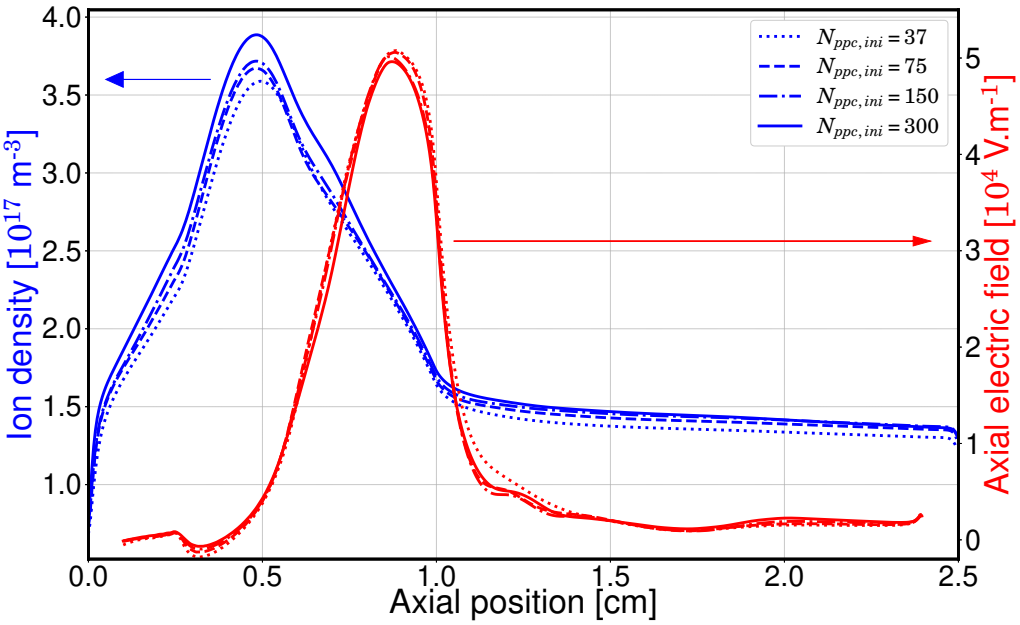

Figure 10: Azimuthally and time (between 16 and 20 μs) averaged axial profiles of axial electric field and ion density for different number of macroparticles per cell at initialisation $N_{ppc,ini}$. Results obtained with code **LPP**.

Figure 11 shows the mean value of $\frac{J_{ec1}}{J_M}$ at steady state for all seven codes, as function of the number of macroparticles per cell at steady state. We can see that we obtain a good convergence: when N_{ppc} is increased, $\frac{J_{ec1}}{J_M}$ is decreased and reaches a plateau. This plateau corresponds to the three benchmark cases that we have chosen (Case 1 with $N_{ppc,final}$=550, Case 2 with $N_{ppc,final}$=275 and Case 3 with $N_{ppc,final}$=1100). It is interesting to notice that the curve has a knee at around 250 macroparticles per cell which gives a numerical collision frequency close to the criterion of [61]. Furthermore, this benchmark case shows that the number of macroparticles per cell commonly used in 2D PIC simulations (i.e. $N_{ppc,final}$=100) is not enough to reach convergence. This need to increase the number of macroparticles per cell to prevent numerical collisions was also reported in [8] and more recently in [13], in which 800 macroparticles per cell were used on average at the end of the simulation.

One can also notice that the differences between the codes are this time bigger than 5%. The origin of this discrepancy still remains unclear and its analysis is let as future work.

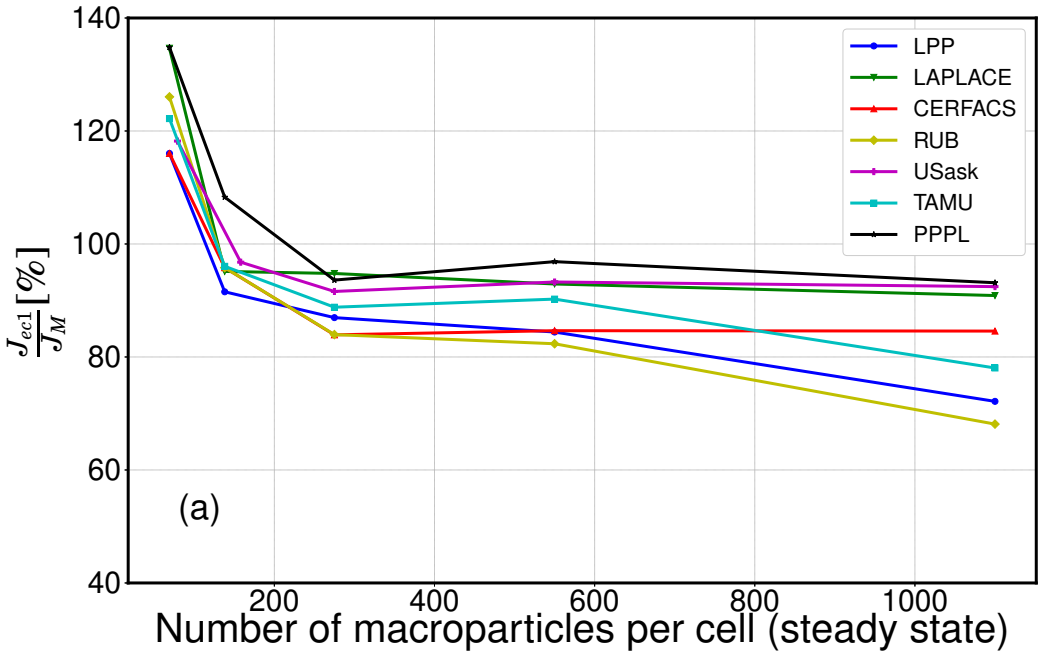

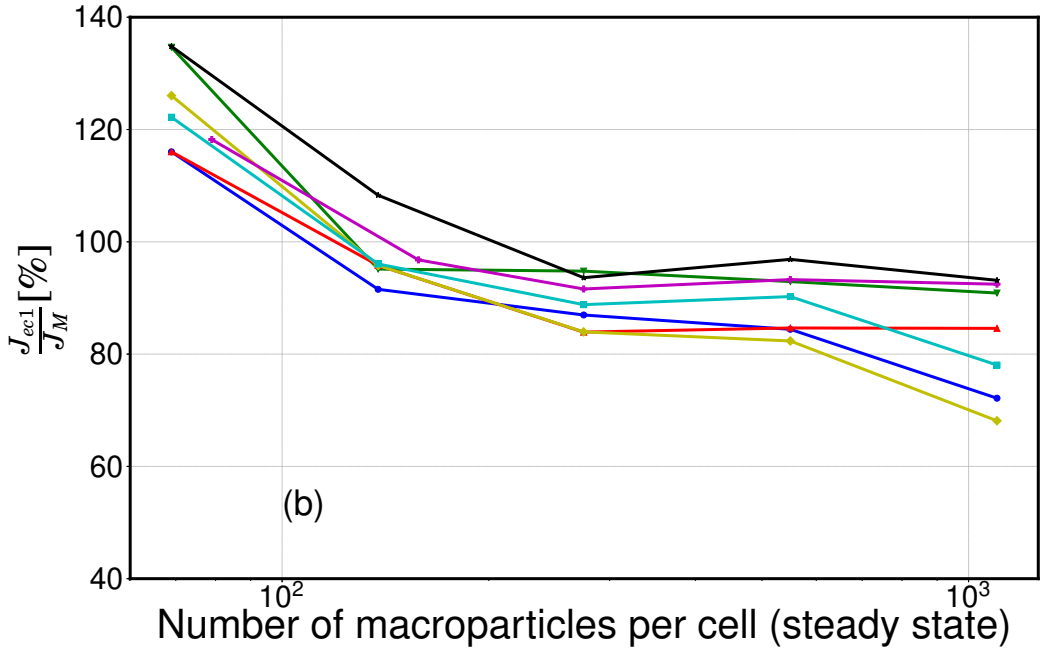

Figure 11: Mean value (between 12 and 20 μs) of $\frac{J_{ec1}}{J_M}$ depending on $N_{ppc,final}$ in normal scale (a) and semi-log scale (b). The three benchmark cases correspond to $N_{ppc,final} = 550$ (Case 1), $N_{ppc,final} = 275$ (Case 2) and $N_{ppc,final} = 1100$ (Case 3).

5.2. Case sensitivity

The agreement obtained between the seven codes in section 4 is good, but it is worth noting that the results obtained are not "statistically indistinguishable" (corresponding to less than 1% difference) as in the 1D helium benchmark [19]. As the present benchmarking test case is more challenging and more complex (two dimensions, magnetic field, emitting cathode, etc.) with the presence of turbulent phenomena, it is expected to obtain bigger differences.

To better characterize the sensitivity of this benchmark case, one code (code **LPP**) is used and the same simulation (same input parameters, corresponding to Case 2) is repeated 3 times. Figure 12(a) shows the different time evolutions of the $\frac{J_{ec1}}{J_M}$ ratio for these 3 simulations. It can be seen that while the beginning of the transient state (first 4 μs) is quite similar, some differences appear quickly and the oscillations at steady state become quite different. In fact, when time averaging is done between 11 and 15 μs, different axial profiles are retrieved for the ion density and axial electric field (the electron temperature is not shown here but displays a similar behaviour), as seen on figure 12(b). These differences are of the order of 5% and could be considered as the closest agreement we would get between the seven codes.

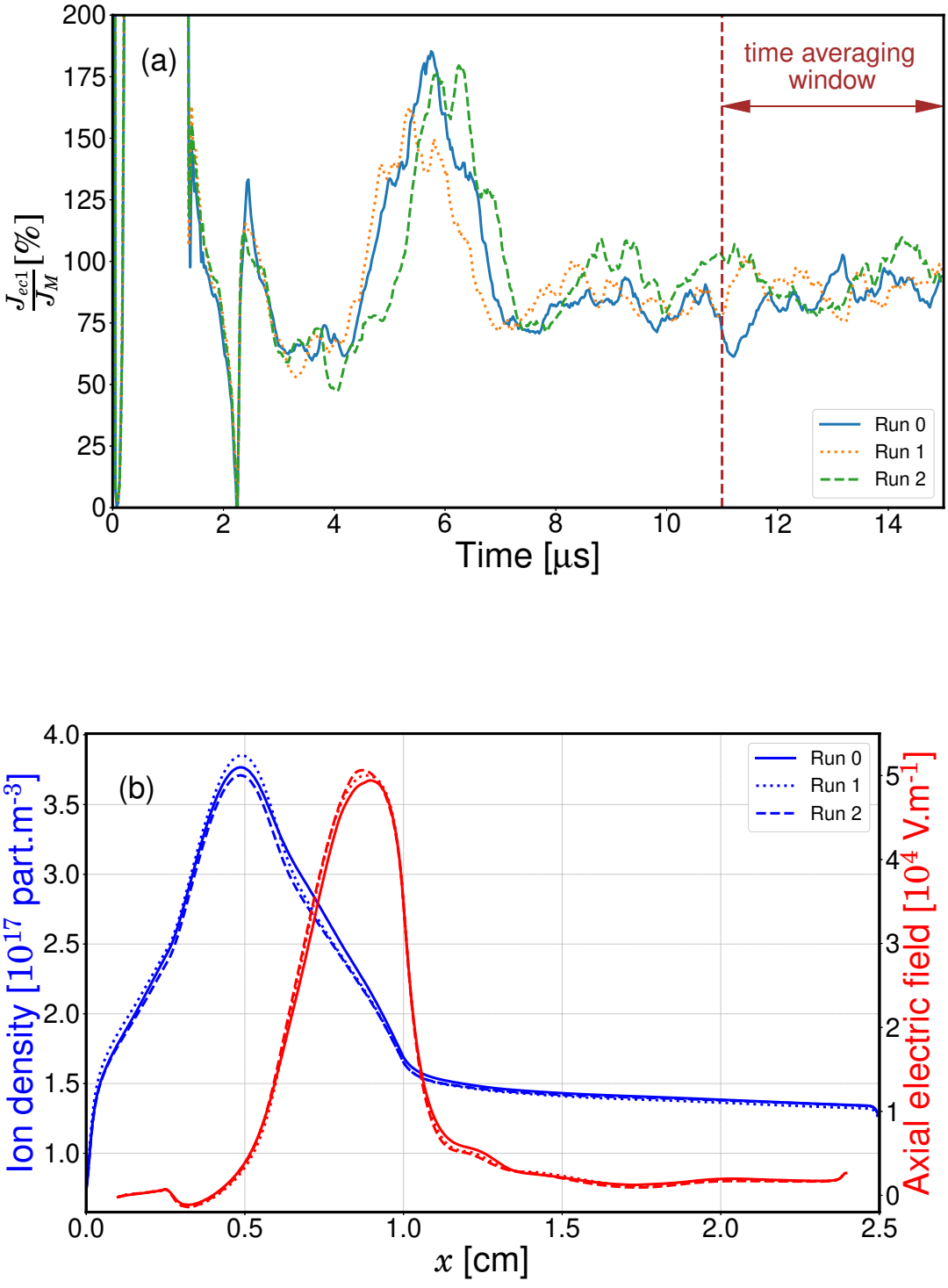

Figure 12: Comparison of 3 simulations with the same code (**LPP**) for the same input parameters (Case 2). (a): Time evolution $\frac{J_{ec1}}{J_M}$. (b): Azimuthally and time (between 11 and 15 μs as shown on (a)) averaged axial profiles of ion density (blue) and axial electric field (red).

There is a reason why identical results are not obtained with the same code. In fact,

as described in section 2, a Random Number Generator (RNG) is frequently used for routines that are crucial for the discharge behaviour (ionization and electron emission). Hence, as this RNG is seeded randomly depending on the processors used, differences are expected on the random numbers that will propagate due to the inherent chaotic behaviour of the discharge.

Indeed, it was confirmed that when the seed number of this RNG is fixed in the **LPP** code (and the same procedure as before is repeated), a perfect overlap is obtained for the time evolution of the current (and hence for the averaged parameters). The result is not shown here for clarity purpose but this study has shown clearly that the intrinsic turbulent nature of the discharge makes this case very sensitive and it made us more confident on the quality of the agreement obtained for this benchmark.

6. Conclusion

A 2D axial-azimuthal benchmark model for low-temperature partially magnetized plasmas has been presented here. Seven independently developed Particle-In-Cell (PIC) codes have been used to simulate this case and their results are compared.

Despite the relative complexity of this benchmark, a good agreement was obtained on the averaged axial profiles of the main discharge parameters (axial electric field, ion density and electron temperature). All codes show the presence of a very strong kinetic instability propagating in the $\boldsymbol{E}\times\boldsymbol{B}$ azimuthal direction that plays a significant role on the cross-field electron transport. The characteristics of the dominant mode of these instabilities have been compared and exhibit a good agreement between all the codes. The remaining differences of around 5% are explained by the inherent unstable nature of the discharge in this case, correlated with the fact that different Random Number Generators (RNG) were used between the codes. The issue of numerical noise due to a too-low number of macroparticles was also assessed. It appears that around 250 macroparticles per cell were needed to get convergence in this 2D benchmark, which is however much less than the 10000 macroparticles per cell used in the 1D case studied in [22].

The seven participants converged on the main purpose of this 2D benchmark that was to increase confidence in our codes by verifying that the results produced were consistent with other implementations. Moreover, as mentioned earlier, these codes are often used to simulate cases that are very computationally expensive. With this in mind, this work also gave insights on the computational efficiency of different solvers, with computational times that could vary from 2.5 to 21 days for the nominal case. It is important to highlight that for simulations of $\boldsymbol{E}\times\boldsymbol{B}$ discharges, the required computing resources are quite large (around 60000 CPU hours in average for the nominal case of this benchmark) and it makes the need for benchmarking even more important.

Even though the case chosen here enabled to test different aspects of a 2D axial-azimuthal electrostatic PIC code, some simplifying assumptions have still been made, particularly concerning the absence of collisions. The earlier work of Turner *et al.* [19]

could be used to verify the Monte Carlo Collision (MCC) module of PIC codes, or another benchmark case could be defined with a self-consistent treatment of ionization with the addition of neutrals and collisions. Hence, the work presented here should be considered as a step towards the benchmarking of PIC codes of low-temperature partially magnetized plasmas.

Acknowledgments

T.C., A.T., A.B. and P.C. acknowledge support from the Agence Nationale de la Recherche under the reference ANR-16-CHIN-0003-01 and Safran Aircraft Engines within the project POSEIDON. They also acknowledge access to the HPC resources of CINES (under the allocation A0040510092 made by GENCI) and of CERFACS at Toulouse. The work at Laplace was granted access to the HPC resources of CALMIP supercomputing center under the allocation 2013-P1125. CERFACS group was granted access to the HPC resources of GENCI HPC resources under the Grant A0032B10157. D.E. gratefully acknowledges support by DFG (German Research Foundation) within the framework of the Sonderforschungsbereich SFB-TR 87. The work at the University of Saskatchewan was supported by NSERC Canada, the Air Force Office of Scientific Research No. FA9550-18-1-0132 and No. FA9550-15-1-0226, and computational resources from Compute Canada/WestGrid. K.H. acknowledges the support by the US Department of Energy, Office of Science, Office of Fusion Energy Sciences under Award Number DESC0019045. The simulations were performed on the ada cluster within the High Performance Computing Facility at Texas A&M University. Development of the PPPL code was supported by the Princeton University Program in Plasma Science and Technology. Simulations using the PPPL code utilized resources of the Perseus cluster at the TIGRESS high performance computer center at Princeton University, which is jointly supported by the Princeton Institute for Computational Science and Engineering and the Princeton University Office of Information Technology's High Performance Research Computing Center.

Appendix A. Supplementary implementation details

Radial magnetic field

The parameters for the radial magnetic field have the following formulas:

$$\begin{cases} a_1 = \dfrac{B_m - B_0}{1 - exp(-\frac{1}{2}(\frac{x_{B_{max}}}{\sigma_1})^2)} \\ a_2 = \dfrac{B_m - B_{L_x}}{1 - exp(-\frac{1}{2}(\frac{L_x - x_{B_{max}}}{\sigma_2})^2)} \\ b_1 = (B_0 - \dfrac{B_m.exp(-\frac{1}{2}(\frac{x_{B_{max}}}{\sigma_1})^2))}{1 - exp(-\frac{1}{2}(\frac{x_{B_{max}}}{\sigma_1})^2)} \\ b_2 = (B_{L_x} - \dfrac{B_m.exp(-\frac{1}{2}(\frac{L_x - x_{B_{max}}}{\sigma_2})^2))}{1 - exp(-\frac{1}{2}(\frac{L_x - x_{B_{max}}}{\sigma_2})^2)} \end{cases} \tag{A.1}$$

Benchmark guidelines

We listed here some general advices to perform this benchmark:

- **Temperature of emitted electrons**: it needs to be full 3D-Maxwellian electrons with a temperature of 10 eV. It was found that the discharge behaviour was very sensitive to the temperature of these electrons.
- **Velocity and temperature diagnostics**: if the leapfrog scheme is used to solve the equations of motion, the velocity needs to be adjusted by half a time step before using it for the diagnostics. It can lead to important differences on the electron velocities and temperatures.
- **Total axial current**: at steady state, as a current equality is imposed in the system, the total axial current (ion+electron) should be constant axially. One can also check that the divergence of the total current is null, with the divergence of the ion current being the imposed ionization source term.

Appendix B. Supplementary comparison figures

For the azimuthal instabilities (section 4.2), we also obtained a good agreement for the cases 2 and 3, as seen on figures B1 and B2 respectively.

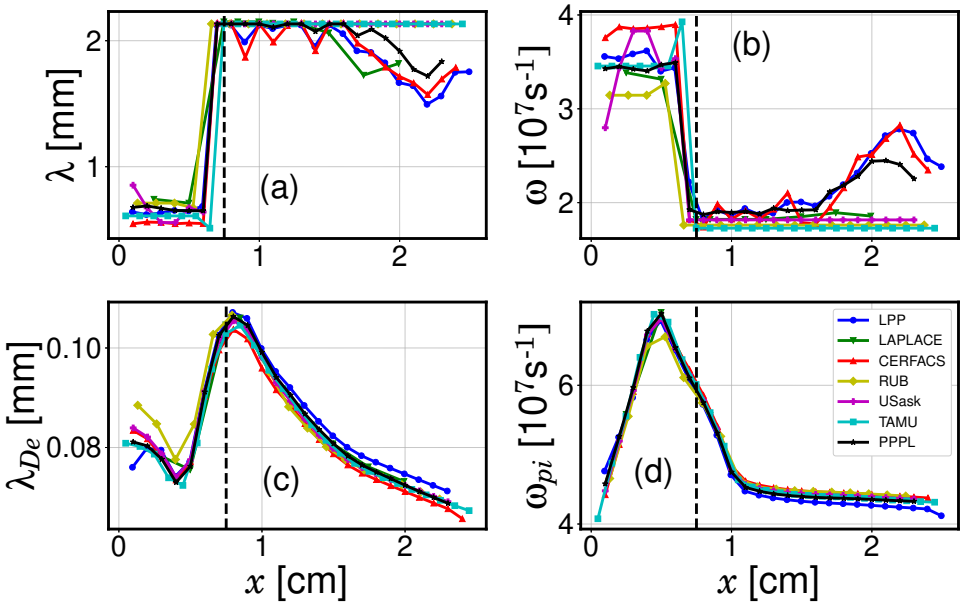

Figure B1: **Case 2**: Axial evolution of dominant mode characteristics for azimuthal electric field (azimuthal instabilities). (a) Wavelength. (b) Frequency. (c) Debye length. (d) Ion plasma frequency. Dashed line corresponds to the position of maximum magnetic field.

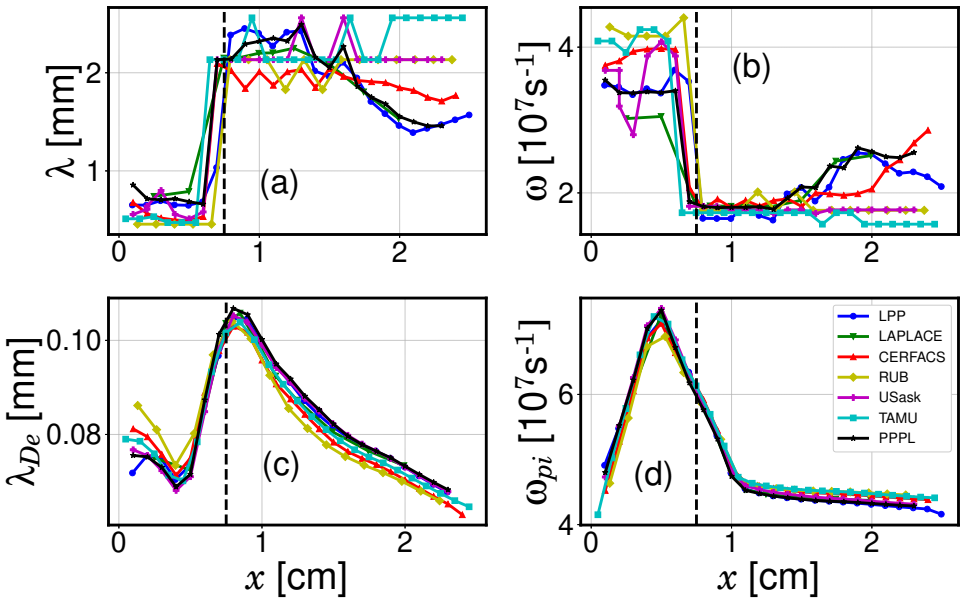

Figure B2: **Case 3**: Axial evolution of dominant mode characteristics for azimuthal electric field (azimuthal instabilities). (a) Wavelength. (b) Frequency. (c) Debye length. (d) Ion plasma frequency. Dashed line corresponds to the position of maximum magnetic field.

Appendix C. Supplementary data files

The averaged axial profiles of axial electric field, ion density and electron temperatures for the 3 benchmark cases displayed in section 4.1 can be found in an output file, along with the wavelength and frequency of the instabilities dominant mode displayed in section 4.2 and Appendix B, for the 3 benchmark cases. The authors would like to make this data available on the journal website.

References

[1] Adam J, Boeuf J P, Dubuit N, Dudeck M, Garrigues L, Gresillon D, Heron A, Hagelaar G, Kulaev V, Lemoine N, Mazouffre S, Luna J P, Pisarev V and Tsikata S 2008 *Plasma Phys. Control. Fusion* **50** 124041

[2] Boeuf J 2017 *J. Appl. Phys.* **121** 011101

[3] Anders A 2017 *J. Appl. Phys.* **121** 171101

[4] Gudmundsson J T, Brenning N, Lundin D and Helmersson U 2012 *Journal of Vacuum Science & Technology A* **30** 030801

[5] Smolyakov A, Chapurin O, Frias Pombo W, Koshkarov O, Romadanov I, Tang T, Umansky M, Raitses Y, Kaganovich I and Lakhin V 2017 *Plasma Physics and Controlled Fusion* **59** 014041

[6] Choueiri E 2001 *Phys. Plasmas* **8** 1411

[7] Gary S P and Sanderson J J 1970 *J. Plasma Phys.* **4** 739–751

[8] Adam J C, Heron A and Laval G 2004 *Phys. Plasmas* **11** 295–305

[9] Cavalier J, Lemoine N, Bonhomme G, Tsikata S, Honore C and Gresillon D 2013 *Phys. Plasmas* **20** 082107

[10] Ducrocq A, Adam J C, Heron A and Laval G 2006 *Phys. Plasmas* **13** 102111

[11] Lafleur T, Baalrud S D and Chabert P 2016 *Phys. Plasmas* **23** 053502

[12] Mikellides I G, Jorns B, Katz I and Lopez Ortega A *in 52nd AIAA/SAE/ASEE Joint Propulsion Conference* (American Institute of Aeronautics and Astronautics, 2016)

[13] Lafleur T and Chabert P 2018 *Plasma Sources Sci. Technol.* **27** 015003

[14] Boeuf J P and Chaudhury B 2013 *Phys. Rev. Lett.* **111** 155005

[15] Tsikata S and Minea T 2015 *Phys. Rev. Lett.* **114** 185001

[16] Hara K 2019 *Plasma Sources Sci. Technol.* **28** 044001

[17] Turner M 2016 *Plasma Sources Sci. Technol.* **25** 054007

[18] Surendra M 1995 *Plasma Sources Sci. Technol.* **4** 56

[19] Turner M, Derzsi A, Donkó Z, Eremin D, Kelly S, Lafleur T and Mussenbrock T 2013 *Phys. Plasmas* **20** 013507

[20] Carlsson J, Khrabrov A, Kaganovich I, Sommerer T and Keating D 2017 *Plasma Sources Sci. Technol.* **26** 014003

[21] Bagheri B, Teunissen J, Ebert U, Becker M, Chen S, Ducasse O, Eichwald O, Loffhagen D, Luque A, Mihailova D, Plewa J, van Dijk J and Yousfi M 2018 *Plasma Sources Sci. Technol.* **27** 095002

[22] Janhunen S, Smolyakov A, Chapurin O, Sydorenko D, Kaganovich I and Raitses Y 2018 *Phys. Plasmas* **25** 011608

[23] Janhunen S, Smolyakov A, Sydorenko D, Jimenez M, Kaganovich I and Raitses Y 2018 *Phys. Plasmas* **25** 082308

[24] Boeuf J P and Garrigues L 2018 *Phys. Plasmas.* **25** 061204

[25] Adam J C, Serveniere A G and Langdon A B 1982 *J. Comp. Phys.* **47** 229–244

[26] Falgout R D and Yang U M 2002 *Computational Science — ICCS 2002* (Springer Berlin Heidelberg) pp 632–641

[27] Boris J P and Shanny R A 1970 *Proc. 4th Conf. on Numerical Simulation of Plasmas, pp 3-67* (Naval Research Laboratory, Washington DC)

[28] Croes V, Lafleur T, Bonaventura Z, Bourdon A and Chabert P 2017 *Plasma Sources Sci. Technol.* **26** 034001
[29] Croes V 2018 Ph.D. thesis Université Paris-Saclay, France
[30] Croes V, Tavant A, Lucken R, Martorelli R, Lafleur T, Bourdon A and Chabert P 2018 *Phys. Plasmas* **25** 063522
[31] Tavant A, Croes V, Lucken R, Lafleur T, Bourdon A and Chabert P 2018 *Plasma Sources Sci. Technol.* **27** 12
[32] Boeuf J P, Chaudhury B and Garrigues L 2012 *Phys. Plasmas* **19** 113509
[33] Boeuf J P, Claustre J, Chaudhury B and Fubiani G 2012 *Phys. Plasmas* **19** 113510
[34] Boeuf J P and Chaudhury B 2013 *Phys. Rev. Lett.* **111** 155005
[35] Boeuf J P, Fubiani G and Garrigues L 2016 *Plasma Sources Sci. Technol.* **25** 045010
[36] Garrigues L, Fubiani G and Boeuf J P 2016 *J. Appl. Phys.* **120** 213303
[37] Garrigues L, Fubiani G and Boeuf J P 2017 *Nucl. Fusion* **57** 014003
[38] Coche P and Garrigues L 2014 *Phys. Plasmas* **21** 023503
[39] Fubiani G and Boeuf J P 2015 *Plasma Sources Sci. Technol.* **24** 055001
[40] Fubiani G, Garrigues L, Hagelaar G, Kohen N and Boeuf J P 2017 *New J. Phys.* **19** 015002
[41] Knuth D E 1998 *The Art of Computer Programming, Volume 2: Seminumerical Algorithms*
[42] Schonfeld T and Rudgyard M 1999 *AIAA Journal* **37** 1378–1385
[43] Gourdain N, Gicquel L, Montagnac M, Vermorel O, Gazaix M, Staffelbach G, Garcia M, Boussuge J F and Poinsot T 2009 *Computational Science & Discovery* **2** 015003
[44] Joncquieres V 2019 Ph.D. thesis Institut National Polytechnique de Toulouse, France
[45] Joncquieres V, Pechereau F, Laguna A A, Bourdon A, Vermorel O and Cuenot B 2018 *Joint Propulsion Conference, AIAA 2018-4905, July 9-11, 2018 Cincinnati, Ohio*
[46] Agullo E, Giraud L and Poirel L 2017 *International conference on domain decomposition methods, DD24*
[47] Poirel L 2018 Ph.D. thesis Université de Bordeaux, France
[48] Karypis G and Kumar V 2009 MeTis: Unstructured Graph Partitioning and Sparse Matrix Ordering System, Version 4.0
[49] Chen G, Chacón L and Barnes D C 2011 *Journal of Computational Physics* **230** 7018–7036
[50] Marsaglia G 2003 *Journal of Statistical Software, Articles* **8** 1–6
[51] Sydorenko D Y 2006 Ph.D. thesis University of Saskatchewan, Canada
[52] Harase S 2014 *Mathematics and Computers in Simulation* **100** 103–113
[53] Panneton F, L'Ecuyer P and Matsumoto M 2006 *ACM Trans. Math. Softw.* **32** 1–16
[54] Baker A H, Falgout R D, Kolev T V and Yang U M 2012 *High-Performance Scientific Computing*
[55] Saito M and Matsumoto M 2009 *Monte Carlo and Quasi-Monte Carlo Methods 2008* (Berlin, Heidelberg: Springer Berlin Heidelberg) pp 589–602
[56] Lafleur T, Baalrud S D and Chabert P 2017 *Plasma Sources Sci. Technol.* **26** 024008
[57] Lafleur T, Martorelli R, Chabert P and Bourdon A 2018 *Phys. Plasmas* **25** 061202
[58] Lampe M, Manheimer W, B McBride J, H Orens J, Shanny R and N Sudan R 1971 *Phys. Rev. Lett.* **26** 1221–1225
[59] Tsikata S, Lemoine N, Pisarev V and Grésillon D M 2009 *Phys. Plasmas* **16** 033506
[60] Okuda H and Birdsall C 1970 *Phys. Fluids* **13** 2123
[61] Turner M 2006 *Phys. Plasmas* **13** 033506

Bibliography

(1992). *Aspects of unstructured grids and finite-volume solvers for the Euler and Navier-Stokes equations*. 63

(2010). LXCat database. https://nl.lxcat.net/home/, accessed on 04-01-2020. 60

(2018). Landmark project (Low temperature magNetizeD plasMA benchmaRKs). https://www.landmark-plasma.com, accessed on 04-01-2020. 92

Adam, J., Gourdin Serveniere, A., and Langdon, A. (1982). Electron sub-cycling in particle simulation of plasma. *Journal of Computational Physics*, 47(2):229–244. 85, 93, 128

Adam, J., Héron, A., and Laval, G. (2004a). Study of stationary plasma thrusters using two-dimensional fully kinetic simulations. *Physics of Plasmas*, 11(1):295–305. 42

Adam, J., Héron, A., and Laval, G. (2004b). Study of stationary plasma thrusters using two-dimensional fully kinetic simulations. *Physics of Plasmas*, 11(1):295–305. 49, 117

Adams, J. C., Swarztrauber, P. N., and Sweet, R. (2016). Fishpack90: Efficient fortran subprograms for the solution of separable elliptic partial differential equations. *Astrophysics Source Code Library*, pages ascl–1609. 129

Aerospace Security (2020). Space Launch to Low Earth Orbit: How Much Does It Cost? https://aerospace.csis.org/data/space-launch-to-low-earth-orbit-how-much-does-it-cost/. Accessed: 2021-05-24. 28

Agullo, E., Giraud, L., and Poirel, L. (2017). Robust coarse spaces for abstract Schwarz preconditioners via generalized eigenproblems. In *International conference on domain decomposition methods, DD24*, Svalbard, Norway. 127

Agullo, E., Giraud, L., and Poirel, L. (2019). Robust preconditioners via generalized eigenproblems for hybrid sparse linear solvers. *SIAM Journal on Matrix Analysis and Applications*, 40(2):417–439. 72

Agullo, E.and Giraud, L., Joncquieres, V., Marait, G., Poirel, L., Vermorel, O., and Villafana, W. (2021). A note on the strong parallel scalability of numerically scalable poisson linear solvers. Technical report, INRIA CERFACS. 87

Ahedo, E. (1997). Structure of the plasma-wall interaction in an oblique magnetic field. *Physics of Plasmas*, 4(12):4419–4430. 49, 177

Ahedo, E. and De Pablo, V. (2007). Combined effects of electron partial thermalization and secondary emission in Hall thruster discharges. *Physics of Plasmas*, 14(8):083501. 48, 49, 82

Ahedo, E., Gallardo, J., and Martınez-Sánchez, M. (2003). Effects of the radial plasma-wall interaction on the Hall thruster discharge. *Physics of Plasmas*, 10(8):3397–3409. 48

Ahedo, E., Martınez-Cerezo, P., and Martınez-Sánchez, M. (2001). One-dimensional model of the plasma flow in a Hall thruster. *Physics of Plasmas*, 8(6):3058–3068. 48

Alvarez-Laguna, A., Magin, T., Massot, M., Bourdon, A., and Chabert, P. (2020). Plasma-sheath transition in multi-fluid models with inertial terms under low pressure conditions: Comparison with the classical and kinetic theory. *Plasma Sources Science and Technology*, 29(2):025003. 48

Amdahl, G. M. (1967). Validity of the single processor approach to achieving large scale computing capabilities. In *Proceedings of the April 18-20, 1967, spring joint computer conference*, pages 483–485. 89

Amestoy, P., Duff, I., and L'Excellent, J.-Y. (2000). Multifrontal parallel distributed symmetric and unsymmetric solvers. *Computer Methods in Applied Mechanics and Engineering*, 184(2):501–520. 73

Antares Development Team (2020). Antares Documentation Release 1.17.0. 156

Araki, S. and Wirz, R. E. (2014). Magnetic field aligned mesh for ring-cusp discharge chambers. In *50th AIAA/ASME/SAE/ASEE Joint Propulsion Conference*, page 3830. 50

Asadi, Z., Taccogna, F., and Sharifian, M. (2019). Numerical study of electron cyclotron drift instability: Application to Hall thruster. *Frontiers in Physics*, 7:140. 118, 121, 129, 166

Auffray, V. (2007). *Étude comparative de schémas numériques pour la modélisation de phénomènes diffusifs sur maillages multiéléments*. PhD thesis. These de doctorat dirigee par Poinsot, Thierry Dynamique des fluides Toulouse, INPT 2007. 58, 67

Bakunin, O. G. (2018). Quasilinear theory of plasma turbulence. origins, ideas, and evolution of the method. *Physics-Uspekhi*, 61(1):52. 41

Balay, S., Abhyankar, S., Adams, M. F., Brown, J., Brune, P., Buschelman, K., Dalcin, L., Dener, A., Eijkhout, V., Gropp, W. D., Karpeyev, D., Kaushik, D., Knepley, M. G., May, D. A., McInnes, L. C., Mills, R. T., Munson, T., Rupp, K., Sanan, P., Smith, B. F., Zampini, S., Zhang, H., and Zhang, H. (2019). PETSc Web page. https://www.mcs.anl.gov/petsc. 73, 74

Balay, S., Abhyankar, S., Adams, M. F., Brown, J., Brune, P., Buschelman, K., Dalcin, L., Dener, A., Eijkhout, V., Gropp, W. D., Karpeyev, D., Kaushik, D., Knepley, M. G., May, D. A., McInnes, L. C., Mills, R. T., Munson, T., Rupp, K., Sanan, P., Smith, B. F., Zampini, S., Zhang, H., and Zhang, H. (2020). PETSc users manual. Technical Report ANL-95/11 - Revision 3.14, Argonne National Laboratory. 73

Bareilles, J., Hagelaar, G., Garrigues, L., Boniface, C., Boeuf, J., and Gascon, N. (2004). Critical assessment of a two-dimensional hybrid Hall thruster model: Comparisons with experiments. *Physics of Plasmas*, 11(6):3035–3046. 50

Barral, S. and Ahedo, E. (2009). Low-frequency model of breathing oscillations in Hall discharges. *Physical Review E*, 79(4):046401. 41, 48

Barral, S., Makowski, K., Peradzyński, Z., and Dudeck, M. (2005). Transit-time instability in Hall thrusters. *Physics of Plasmas*, 12(7):073504. 41

Barral, S., Makowski, K., Peradzynski, Z., Gascon, N., and Dudeck, M. (2003). Wall material effects in stationary plasma thrusters. ii. near-wall and in-wall conductivity. *Physics of Plasmas*, 10(10):4137–4152. 37, 82

Barral, S. and Miedzik, J. (2011). Numerical investigation of closed-loop control for Hall accelerators. *Journal of Applied Physics*, 109(1):013302. 41

Barrett, P. J., Fried, B. D., Kennel, C. F., Sellen, J. M., and Taylor, R. J. (1972). Cross-field current-driven ion acoustic instability. *Phys. Rev. Lett.*, 28:337–340. 125, 161

Becker, M. M., Kählert, H., Sun, A., Bonitz, M., and Loffhagen, D. (2017). Advanced fluid modeling and PIC/MCC simulations of low-pressure ccrf discharges. *Plasma Sources Science and Technology*, 26(4):044001. 75

Benilov, M. S. (1996). Momentum and energy exchange between species of a multicomponent gas mixture due to inelastic and reactive collisions. *Physics of Plasmas*, 3(7):2805–2812. 47

Birdsall, C. K. (1991). Particle-in-cell charged-particle simulations, plus monte carlo collisions with neutral atoms, pic-mcc. *IEEE Transactions on Plasma Science*, 19(2):65–85. 56, 74, 119

Birdsall, C. K. and Langdon, A. B. (2004). *Plasma physics via computer simulation*. CRC press. 48

Bittencourt, J. (2004). *Fundamentals of Plasma Physics*. Springer New York. 5, 46

Black, D. L. and Gunn, S. V. (2003). Space nuclear propulsion. In Meyers, R. A., editor, *Encyclopedia of Physical Science and Technology (Third Edition)*, pages 555–575. Academic Press, New York, third edition edition. 32

Boccelli, S., Charoy, T., Alvarez Laguna, A., Chabert, P., Bourdon, A., and Magin, T. E. (2020). Collisionless ion modeling in Hall thrusters: Analytical axial velocity distribution function and heat flux closures. *Physics of Plasmas*, 27(7):073506. 48

Boeuf, J. and Garrigues, L. (1998). Low frequency oscillations in a stationary plasma thruster. *Journal of Applied Physics*, 84(7):3541–3554. 41

Boeuf, J.-P. (2017). Tutorial: Physics and modeling of Hall thrusters. *Journal of Applied Physics*, 121(1):011101. 4, 36, 44, 51, 118, 137, 142

Boeuf, J.-P. and Chaudhury, B. (2013). Rotating instability in low-temperature magnetized plasmas. *Phys. Rev. Lett.*, 111:155005. 117

Boeuf, J. P. and Garrigues, L. (2018). Exb electron drift instability in Hall thrusters: Particle-in-cell simulations vs. theory. *Physics of Plasmas*, 25(6):061204. 42, 48, 49, 80, 81, 92, 95, 99, 117, 122, 129, 135, 160, 175, 183

Boniface, C., Charbonnier, J.-M., Lefebvre, L., Leroi, V., and Lienart, T. (2017). An overview of electric propulsion activities at CNES. In *35th International Electric Propulsion Conference*. 33

Boniface, C., Garrigues, L., Hagelaar, G. J. M., Boeuf, J. P., Gawron, D., and Mazouffre, S. (2006). Anomalous cross field electron transport in a Hall effect thruster. *Applied Physics Letters*, 89(16):161503. 117

Boris, J. P. (1970). Relativistic plasma simulation-optimization of a hybrid code. In *Proc. Fourth Conf. Num. Sim. Plasmas*, pages 3–67. 74

Borras, P., Clement, D., Despeyroux, T., Incerpi, J., Kahn, G., Lang, B., and Pascual, V. (1988). Centaur: The system. *SIGSOFT Softw. Eng. Notes*, 13(5):14–24. 56

Bowers, K. (2001). Accelerating a particle-in-cell simulation using a hybrid counting sort. *Journal of Computational Physics*, 173(2):393–411. 85, 129

Box, G. E. P. and Muller, M. E. (1958). A note on the generation of random normal deviates. *Ann. Math. Statist.*, 29(2):610–611. 59

Brieda, L. (2012). *Multiscale modeling of Hall thrusters*. PhD thesis, The George Washington University. 50

Brown, N. P. and Walker, M. L. (2020). Review of plasma-induced Hall thruster erosion. *Applied Sciences*, 10(11):3775. 38

Brown, Z. A. and Jorns, B. A. (2019). Spatial evolution of small wavelength fluctuations in a Hall thruster. *Physics of Plasmas*, 26(11):113504. 37

Cavalier, J., Lemoine, N., Bonhomme, G., Tsikata, S., Honoré, C., and Grésillon, D. (2013). Hall thruster plasma fluctuations identified as the exb electron drift instability: Modeling and fitting on experimental data. *Physics of Plasmas*, 20(8):082107. 10, 42, 99, 125, 126, 138, 160, 161, 163, 185, 190, 193

Chabert, P. (2014). What is the size of a floating sheath? *Plasma Sources Science and Technology*, 23(6):065042. 122

Charoy, T. (2020). *Numerical study of electron transport in Hall Thrusters*. PhD thesis, Ecole Polytchnique. 41, 53, 79, 80, 81, 114, 138, 142, 152, 175

Charoy, T., Boeuf, J. P., Bourdon, A., Carlsson, J. A., Chabert, P., Cuenot, B., Eremin, D., Garrigues, L., Hara, K., Kaganovich, I. D., Powis, A. T., Smolyakov, A., Sydorenko, D., Tavant, A., Vermorel, O., and Villafana, W. (2019). 2d axial-azimuthal particle-in-cell benchmark for low-temperature partially magnetized plasmas. *Plasma Sources Science and Technology*, 28(10):105010. 13, 42, 49, 56, 85, 92, 95, 96, 97, 99, 101, 115, 119, 122, 128, 129, 135, 189

Charoy, T., Lafleur, T., Alvarez-Laguna, A., Bourdon, A., and Chabert, P. (2021). The interaction between ion transit-time and electron drift instabilities and their effect on anomalous electron transport in Hall thrusters. *Plasma Sources Science and Technology*. 41

Charoy, T., Lafleur, T., Tavant, A., Chabert, P., and Bourdon, A. (2020). A comparison between kinetic theory and particle-in-cell simulations of anomalous electron transport in e× b plasma discharges. *Physics of Plasmas*, 27(6):063510. 44, 48, 49

Chen, F. (1974). *Introduction to Plasma Physics and Controlled Fusion: Volume 1: Plasma Physics*. Introduction to Plasma Physics and Controlled Fusion. Springer US. 37, 39, 44, 46, 48, 177

Chen, F. F. (1965). Excitation of drift instabilities in thermionic plasmas. *Journal of Nuclear Energy. Part C, Plasma Physics, Accelerators, Thermonuclear Research*, 7(4):399–417. 125, 161

Cheng, L., Ajuria-Illarramendi, E., Bogopolsky, G., Bauerheim, M., and Cuenot, B. (2021). Using neural networks to solve the 2d poisson equation for electric field computation in plasma simulations. submitted. 192

Cho, S., Komurasaki, K., and Arakawa, Y. (2013). Kinetic particle simulation of discharge and wall erosion of a Hall thruster. *Physics of Plasmas*, 20(6):063501. 37, 49

Cho, S., Watanabe, H., Kubota, K., and Funaki, I. (2016). *The Effects of Cathode Boundary Condition on Particle Simulation of a SPT-100-like Hall Thruster*. 49, 81, 138, 142, 152

Cho, S., Watanabe, H., Kubota, K., Iihara, S., Fuchigami, K., Uematsu, K., and Funaki, I. (2015). Study of electron transport in a Hall thruster by axial–radial fully kinetic particle simulation. *Physics of Plasmas*, 22(10):103523. 49, 80, 138

Cho, S., Watanabe, H., Kubota, K., Iihara, S., Honda, K., Fuchigami, K., Uematsu, K., and Funaki, I. (2014). Parametric kinetic simulation of an ihi high specific impulse spt-type Hall thruster. In *50th AIAA/ASME/SAE/ASEE Joint Propulsion Conference*, page 3426. 49

Chodura, R. (1982). Plasma–wall transition in an oblique magnetic field. *The Physics of Fluids*, 25(9):1628–1633. 49, 177

Choueiri, E. Y. (2001a). Fundamental difference between the two Hall thruster variants. *Physics of Plasmas*, 8(11):5025–5033. 37

Choueiri, E. Y. (2001b). Plasma oscillations in Hall thrusters. *Physics of Plasmas*, 8(4):1411–1426. 41

Choueiri, E. Y. (2004). A critical history of electric propulsion: The first 50 years (1906-1956). *Journal of Propulsion and Power*, 20(2):193–203. 29

CNES (2020). Caracteristiques techniques. https://ariane5.cnes.fr/fr/caracteristiques-techniques. Accessed: 2021-05-24. 28

Coche, P. and Garrigues, L. (2014). A two-dimensional (azimuthal-axial) particle-in-cell model of a Hall thruster. *Physics of Plasmas*, 21(2):023503. 42, 49

Colella, P. and Norgaard, P. C. (2010). Controlling self-force errors at refinement boundaries for AMR-PIC. *Journal of Computational Physics*, 229(4):947–957. 140, 192

Commission, E. (2016). Space tech and services: Electric Propulsion. https://ec.europa.eu/growth/industry/policy/innovation/business-innovation-observatory/case-studies/grouped-by-trend_en. 29

Community, P., Everson, E., Stańczak, D., Murphy, N. A., Kozlowski, P. M., Malhotra, R., Langendorf, S. J., Leonard, A. J., Stansby, D., Haggerty, C. C., Mumford, S. J., Beckers, J. P., Bedmutha, M. S., Bergeron, J., Bessi, L., Bryant, K., Carroll, S., Chambers, S., Chattopadhyay, A., Choubey, A., Deal, J., Diaz, D., Díaz Pérez, R., Einhorn, L., Fan, T., Farid, S. I., Goudeau, G., Guidoni, S., Hansen, R. S., Heuer, P., Hillairet, J., How, P. Z., Huang, Y.-M., Humphrey, N., Isupova, M., Kent, J., Kulshrestha, S., Kuszaj, P., Lim, P. L., Magarde, A., Martinelli, J. V., Munn, J., Parashar, T., Patel, N., Polak, J., Rao, A., Raj, R., Rajashekar, V., Savcheva, A., Shen, C., Sherpa, D. N., Silva, F., Singh, A., Singh, A., Sipőcz, B., Tavant, A., Varnish, T., Vo, A., Xu, S., Zhang, C., Du, T., Qudsi, R., Richardson, S., Skinner, C., Modi, D., Drozdov, D., and Montes, K. (2021). Plasmapy. The development of PlasmaPy has been partially supported by the U.S. National Science Foundation, the U.S. Department of Energy, NASA, and the Smithsonian Institution. 160

Conversano, R. W., Goebel, D. M., Hofer, R. R., Mikellides, I. G., and Wirz, R. E. (2017). Performance analysis of a low-power magnetically shielded Hall thruster: experiments. *Journal of Propulsion and Power*, 33(4):975–983. 39

Croes, V. (2017). *Plasma discharge 2D modeling of a Hall thruster*. PhD thesis. Thèse de doctorat dirigée par Chabert, Pascal et Bourdon, Anne Physique des plasmas Université Paris-Saclay (ComUE) 2017. 49, 52, 82

Croes, V., Lafleur, T., Bonaventura, Z., Bourdon, A., and Chabert, P. (2017). 2d particle-in-cell simulations of the electron drift instability and associated anomalous electron transport in hall-effect thrusters. *Plasma Sources Science and Technology*, 26(3):034001. 42, 49, 118, 121

Crumpton, P. I. (1995). An efficient cell vertex method for unstructured tetrahedral grids. Technical report. 62

Dale, E., Jorns, B., and Gallimore, A. (2020). Future directions for electric propulsion research. *Aerospace*, 7(9):120. 33

Dale, E. T. and Jorns, B. A. (2019a). Non-invasive time-resolved measurements of anomalous collision frequency in a Hall thruster. *Physics of Plasmas*, 26(1):013516. 37

Dale, E. T. and Jorns, B. A. (2019b). Two-zone Hall thruster breathing mode mechanism, part i: Theory. In *36th International Electric Propulsion Conference, University of Vienna, Austria*. 41

Dale, E. T. and Jorns, B. A. (2019c). Two-zone Hall thruster breathing mode mechanism, part ii: Experiment. In *36th International Electric Propulsion Conference, University of Vienna, Austria*. 41

Dawson, P. (1966). Secondary electron emission yields of some ceramics. *Journal of Applied Physics*, 37(9):3644–3645. 82

De Lara, J., Pérez, F., Alfonseca, M., Galán, L., Montero, I., Román, E., and Garcia-Baquero, D. R. (2006). Multipactor prediction for on-board spacecraft rf equipment with the mest software tool. *IEEE Transactions on Plasma Science*, 34(2):476–484. 82

del Amo, J. G. (2015). European space agency (esa) electric propulsion activities. In *34th International Electric Propulsion Conference, Kobe*, pages 4–10. 33

DesJardin, I., Hara, K., and Tsikata, S. (2019). Self-organized standing waves generated by ac-driven electron cyclotron drift instabilities. *Applied Physics Letters*, 115(23):234103. 128

Dewar, R. L. (1973). Saturation of kinetic plasma instabilities by particle trapping. *The Physics of Fluids*, 16(3):431–435. 175, 190

Domínguez-Vázquez, A., Taccogna, F., and Ahedo, E. (2018). Particle modeling of radial electron dynamics in a controlled discharge of a Hall thruster. *Plasma Sources Science and Technology*, 27(6):064006. 129

Domínguez-Vázquez, A., Taccogna, F., Fajardo, P., and Ahedo, E. (2019). Parametric study of the radial plasma-wall interaction in a Hall thruster. *Journal of Physics D: Applied Physics*, 52(47):474003. 49, 82, 129

Ducrocq, A., Adam, J., Héron, A., and Laval, G. (2006). High-frequency electron drift instability in the cross-field configuration of Hall thrusters. *Physics of Plasmas*, 13(10):102111. 42, 99, 160, 193

Esclapez, L., Collin-Bastiani, F., Riber, E., and Cuenot, B. (2021). A statistical model to predict ignition probability. *Combustion and Flame*, 225:180 – 195. 53

Esipchuk, Y. B., Morozov, A., Tilinin, G., and Trofimov, A. (1974). Plasma oscillations in closed-drift accelerators with an extended acceleration zone. *Soviet Physics Technical Physics*, 18:928. 41

Euroconsult (2020). Satellites to be Built & Launched. https://digital-platform.euroconsult-ec.com/product/satellites-to-be-built-launched-new/?id_product=124&controller=product. Accessed: 2021-05-24. 27

F. Panneton, F., L Écuyer, P., and Matsumoto, M. (2006). Improved long-period generators based on linear recurrences modulo 2. *ACM Transactions on Mathematical Software*, 32:1–16. 128

Falgout, R. and Yang, U. (2002). *hypre: a Library of High Performance Preconditioners*. 128

Ferziger, J. and Kaper, H. (1973). Mathematical theory of transport processes in gases. *American Journal of Physics*, 41(4):601–603. 48

Fife, J. M. (1998). *Hybrid-PIC modeling and electrostatic probe survey of Hall thrusters*. PhD thesis, Massachusetts Institute of Technology. 41, 48, 50

Forslund, D., Morse, R., and Nielson, C. (1970). Electron cyclotron drift instability. *Physical Review Letters*, 25(18):1266. 42

French National Research Agency (2016). future Plasma thrusters for LOw earth orbit SatEllIte propulsiON systems – POSEIDON. https://anr.fr/Project-ANR-16-CHIN-0003. Accessed: 2021-05-24. 33

Furman, M. A. and Pivi, M. T. F. (2002). Probabilistic model for the simulation of secondary electron emission. *Phys. Rev. ST Accel. Beams*, 5:124404. 82

Garrigues, L., Fubiani, G., and Boeuf, J. (2016). Appropriate use of the particle-in-cell method in low temperature plasmas: Application to the simulation of negative ion extraction. *Journal of Applied Physics*, 120(21):213303. 129

Garrigues, L., Hagelaar, G., Bareilles, J., Boniface, C., and Boeuf, J. (2003). Model study of the influence of the magnetic field configuration on the performance and lifetime of a Hall thruster. *Physics of Plasmas*, 10(12):4886–4892. 35, 144

Garrigues, L., Hagelaar, G. J. M., Boniface, C., and Boeuf, J. P. (2006). Anomalous conductivity and secondary electron emission in Hall effect thrusters. *Journal of Applied Physics*, 100(12):123301. 117

Garrigues, L., Santhosh, S., Grimaud, L., and Mazouffre, S. (2019). Operation of a low-power Hall thruster: comparison between magnetically unshielded and shielded configuration. *Plasma Sources Science and Technology*, 28(3):034003. 4, 40

Garrison, T., Ince, M., Pizzicaroli, J., and Swan, P. (1997). Systems engineering trades for the iridium constellation. *Journal of Spacecraft and Rockets*, 34(5):675–680. 4, 28

Gary, S. P. (1970). Longitudinal waves in a perpendicular collisionless plasma shock: Ii. vlasov ions. *Journal of Plasma Physics*, 4(4):753–760. 42

Gary, S. P. and Sanderson, J. (1970). Longitudinal waves in a perpendicular collisionless plasma shock: I. cold ions. *Journal of Plasma Physics*, 4(4):739–751. 42, 99

Gascon, N., Dudeck, M., and Barral, S. (2003). Wall material effects in stationary plasma thrusters. i. parametric studies of an spt-100. *Physics of Plasmas*, 10(10):4123–4136. 37, 82

Giambusso, M., Squire, J. P., Chang Díaz, F. R., Corrigan, A., and Hardy, T. (2020). 120kw rf power processing unit in-vacuum testing for a vasimr® system. In *ASCEND 2020*, page 4020. 33

Gicquel, L. Y., Gourdain, N., Boussuge, J.-F., Deniau, H., Staffelbach, G., Wolf, P., and Poinsot, T. (2011). High performance parallel computing of flows in complex geometries. *Comptes Rendus Mécanique*, 339(2):104 – 124. High Performance Computing. 53, 127

Goebel, D. and Katz, I. (2008). *Fundamentals of Electric Propulsion: Ion and Hall Thrusters*. JPL Space Science and Technology Series. Wiley. 31, 32, 35, 48, 60, 69, 117

Gordeev G. V. (1952). *KETP*, page 660. 42, 160

Gourdain, N., Gicquel, L., Montagnac, M., Vermorel, O., Gazaix, M., Staffelbach, G., Garcia, M., Boussuge, J.-F., and Poinsot, T. (2009). High performance parallel computing of flows in complex geometries: I. methods. *Computational Science & Discovery*, 2(1):015003. 127

Graille, B., Magin, T., and Massot, M. (2009). Kinetic Theory of Plasmas: Translational Energy. *Mathematical Models and Methods in Applied Sciences*, 19(04):527–599. Preprint of an article accepted for publication in Mathematical Models and Methods in Applied Sciences © [2007] [copyright World Scientific Publishing Company] [http://www.worldscinet.com/m3as/m3as.shtml] Subject of a NASA Technical Memorandum NASA/TM-2008–214578 - June 2008. 48

Grimaud, L., Vaudolon, J., Mazouffre, S., and Boniface, C. (2016). Design and characterization of a 200w Hall thruster in" magnetic shielding"configuration. In *52nd AIAA/SAE/ASEE Joint Propulsion Conference*, page 4832. 39

Hackbusch, W. (1985). *Multi-Grid Methods and Applications*. Springer. 74

Hagelaar, G. (2015). Coulomb collisions in the boltzmann equation for electrons in low-temperature gas discharge plasmas. *Plasma Sources Science and Technology*, 25(1):015015. 48

Hagelaar, G., Bareilles, J., Garrigues, L., and Boeuf, J.-P. (2002). Two-dimensional model of a stationary plasma thruster. *Journal of Applied Physics*, 91(9):5592–5598. 48

Hagelaar, G. G. J. M. (2008). *MODELLING METHODS FOR LOW-TEMPERATURE PLASMAS*. Habilitation à diriger des recherches, Université Toulouse III Paul Sabatier (UT3 Paul Sabatier). 59, 81, 138

Hara, K. (2015). *Development of Grid-Based Direct Kinetic Method and Hybrid Kinetic-Continuum Modeling of Hall Thruster Discharge Plasmas.* PhD thesis. 50

Hara, K. (2019). An overview of discharge plasma modeling for Hall effect thrusters. *Plasma Sources Science and Technology*, 28(4):044001. 51, 118, 121

Hara, K., Sekerak, M. J., Boyd, I. D., and Gallimore, A. D. (2014). Perturbation analysis of ionization oscillations in Hall effect thrusters. *Physics of Plasmas*, 21(12):122103. 41

Hara, K. and Tsikata, S. (2020). Cross-field electron diffusion due to the coupling of drift-driven microinstabilities. *Phys. Rev. E*, 102:023202. 99, 122, 128, 160

Harase, S. (2009). Maximally equidistributed pseudorandom number generators via linear output transformations. *Mathematics and Computers in Simulation*, 79:1512–1519. 128

Harrison, T., Cooper, Z., Johnson, K., and Roberts, T. G. (2017). *Escalation and deterrence in the second space age*. Rowman & Littlefield. 4, 28

Haselbacher, A., Najjar, F., and Ferry, J. (2007). An efficient and robust particle-localization algorithm for unstructured grids. *Journal of Computational Physics*, 225:2198–2213. 6, 75, 76, 127

Hastings, D. E. and Niewood, E. (1989). Theory of the modified two stream instability in an mpd thruster. 117

Hendrickx, B. (2004). A history of soviet/russian meteorological satellites. *Journal of the British Interplanetary Society*, 57(1):56. 31

HiePaCS team (2020). MaPHyS user's guide. Technical Report 1.0.0, INRIA. 73

Hill, P. G. and Peterson, C. R. (1992). Mechanics and thermodynamics of propulsion. *Reading*. 25, 32

Hirakawa, M. and Arakawa, Y. (1995). Particle simulation of plasma phenomena in Hall thrusters. In *Proceedings of the 24th International Electric Propulsion Conference*, pages 95–164. 49, 52, 137, 138, 187, 190

Hirakawa, M. and Arakawa, Y. (1996). Numerical simulation of plasma particle behavior in a Hall thruster. In *32nd Joint Propulsion Conference and Exhibit*, page 3195. 49, 52, 137, 138, 187, 190

Hofer, R., Mikellides, I., Katz, I., and Goebel, D. (2007). Wall sheath and electron mobility modeling in hybrid-pic Hall thruster simulations. In *43rd AIAA/ASME/SAE/ASEE Joint Propulsion Conference & Exhibit*, page 5267. 50

Hofer, R. R., Goebel, D. M., Mikellides, I. G., and Katz, I. (2014). Magnetic shielding of a laboratory Hall thruster. ii. experiments. *Journal of Applied Physics*, 115(4):043304. 39

Hofer, R. R., Jankovsky, R. S., and Gallimore, A. D. (2006). High-specific impulse Hall thrusters, part 1: Influence of current density and magnetic field. *Journal of Propulsion and Power*, 22(4):721–731. 4, 36

Holste, K., Dietz, P., Scharmann, S., Keil, K., Henning, T., Zschätzsch, D., Reitemeyer, M., Nauschütt, B., Kiefer, F., Kunze, F., et al. (2020). Ion thrusters for electric propulsion: Scientific issues developing a niche technology into a game changer. *Review of Scientific Instruments*, 91(6):061101. 4, 29, 30, 31, 32

Hénon, P., Ramet, P., and Roman, J. (2002). Pastix: a high-performance parallel direct solver for sparse symmetric positive definite systems. *Parallel Computing*, 28(2):301–321. 73

Héron, A. and Adam, J. C. (2013). Anomalous conductivity in Hall thrusters: Effects of the non-linear coupling of the electron-cyclotron drift instability with secondary electron emission of the walls. *Physics of Plasmas*, 20(8):082313. 42, 49, 116, 117, 118, 121

Jablonski, A. (2013). Angular distribution of elastic electron backscattering from surfaces: determination of the electron inelastic mean free path. *Journal of Physics D: Applied Physics*, 47(5):055301. 82

Jackson, J., Allen, M., Myers, R., Hoskins, A., Soendker, E., Welander, B., Tolentino, A., and Hablitzel, S. (2017). 100 kw nested Hall thruster system development. In *35th International Electric Propulsion Conference, IEPC-2017-219, Electric Rocket Propulsion Society, Atlanta, GA*. 39

Janhunen, S., Smolyakov, A., Chapurin, O., Sydorenko, D., Kaganovich, I., and Raitses, Y. (2018a). Nonlinear structures and anomalous transport in partially magnetized ExB plasmas. *Physics of Plasmas*, 25(1):011608. 42, 43, 56, 125, 160

Janhunen, S., Smolyakov, A., Sydorenko, D., Jimenez, M., Kaganovich, I., and Raitses, Y. (2018b). Evolution of the electron cyclotron drift instability in two-dimensions. *Physics of Plasmas*, 25(8):082308. 43, 49, 116, 118, 119, 121, 123, 124, 125, 135, 191

Joncquieres, V. (2019). *Modélisation et simulation numérique des moteurs à effet Hall*. PhD thesis, Institut National Polytechnique de Toulouse. 48, 54, 127

Joncquieres, V., Pechereau, F., Alvarez Laguna, A., Bourdon, A., Vermorel, O., and Cuenot, B. (2018). chapter A 10-moment fluid numerical solver of plasma with sheaths in a Hall Effect Thruster. AIAA Propulsion and Energy Forum. American Institute of Aeronautics and Astronautics. 0. 48, 49, 54, 55, 127

Joncquieres, V., Vermorel, O., and Cuenot, B. (2020). A fluid formalism for low-temperature plasma flows dedicated to space propulsion in an unstructured high performance computing solver. *Plasma Sources Science and Technology*, 29(9):095005. 6, 48, 54, 88, 143

Jones, W. (2012). *An introduction to the linear theories and methods of electrostatic waves in plasmas*. Springer Science & Business Media. 41

Jules Vernes (1865). De la terre à la lune. 25

Kadomtsev, B. B. and Shafranov, V. D. (2012). *Reviews of Plasma Physics*, volume 21. Springer Science & Business Media. 41

Kaganovich, I. D., Smolyakov, A., Raitses, Y., Ahedo, E., Mikellides, I. G., Jorns, B., Taccogna, F., Gueroult, R., Tsikata, S., Bourdon, A., Boeuf, J.-P., Keidar, M., Powis, A. T., Merino, M., Cappelli, M., Hara, K., Carlsson, J. A., Fisch, N. J., Chabert, P., Schweigert, I., Lafleur, T., Matyash, K., Khrabrov, A. V., Boswell, R. W., and Fruchtman, A. (2020). Physics of ExB discharges relevant to plasma propulsion and similar technologies. *Physics of Plasmas*, 27(12):120601. 37, 39, 51, 117, 118

Karypis, G. and Kumar, V. (2009). MeTis: Unstructured Graph Partitioning and Sparse Matrix Ordering System, Version 4.0. http://www.cs.umn.edu/~metis. 53, 84, 127

Keidar, M. and Boyd, I. (2005). On the magnetic mirror effect in Hall thrusters. *Applied Physics Letters*, 87(12):121501. 177

Keidar, M., Boyd, I., and Beilis, I. (2001). Plasma flow and plasma–wall transition in Hall thruster channel. *Physics of Plasmas*, 8(12):5315–5322. 37

Komurasaki, K. and Kuninaka, H. (2007). Overview of electric propulsion activities in japan. In *43rd AIAA/ASME/SAE/ASEE Joint Propulsion Conference & Exhibit*, page 5166. 33

Koo, J. W. (2005). *Hybrid PIC-MCC computational modeling of Hall thrusters*. University of Michigan. 50

Koppel, C. R. and Estublier, D. (2005). The smart-1 Hall effect thruster around the moon: In flight experience. In *29th International electric propulsion conference*, page 119. 29

Krall, N. A. and Liewer, P. C. (1971). Low-frequency instabilities in magnetic pulses. *Phys. Rev. A*, 4:2094–2103. 117, 118

Lafleur, T., Baalrud, S. D., and Chabert, P. (2016a). Theory for the anomalous electron transport in Hall effect thrusters. i. insights from particle-in-cell simulations. *Physics of Plasmas*, 23(5):053502. 42, 44, 48, 49, 99, 115, 117, 118, 121, 166, 173, 175

Lafleur, T., Baalrud, S. D., and Chabert, P. (2016b). Theory for the anomalous electron transport in Hall effect thrusters. ii. kinetic model. *Physics of Plasmas*, 23(5):053503. 10, 43, 44, 48, 49, 99, 101, 115, 117, 118, 160, 161, 163, 173, 175, 186, 191, 193

Lafleur, T. and Chabert, P. (2017). The role of instability-enhanced friction on 'anomalous' electron and ion transport in hall-effect thrusters. *Plasma Sources Science and Technology*, 27(1):015003. 49, 114

Laguna, A. A., Pichard, T., Magin, T., Chabert, P., Bourdon, A., and Massot, M. (2020). An asymptotic preserving well-balanced scheme for the isothermal fluid equations in low-temperature plasmas at low-pressure. *Journal of Computational Physics*, 419:109634. 48

Lam, C., Fernández, E., and Cappelli, M. (2015). A 2-d hybrid Hall thruster simulation that resolves the electron drift direction. *IEEE Transactions on Plasma Science*, 43:86–94. 50

Lamarque, N. (2007). *Schémas numériques et conditions limites pour la simulation aux grandes échelles de la combustion diphasique dans les foyers d'hélicoptère.* PhD thesis, Institut National Polytechnique de Toulouse-INPT. 67

Lampe, M., Manheimer, W., McBride, J., Orens, J., Papadopoulos, K., Shanny, R., and Sudan, R. (1972). Theory and simulation of the beam cyclotron instability. *The Physics of Fluids*, 15(4):662–675. 42, 43, 99, 160, 175, 190

Lampe, M., Manheimer, W. M., McBride, J. B., Orens, J. H., Shanny, R., and Sudan, R. (1971a). Nonlinear development of the beam-cyclotron instability. *Physical Review Letters*, 26(20):1221. 42, 43, 99, 160, 175, 190

Lampe, M., McBride, J. B., Orens, J. H., and Sudan, R. N. (1971b). Theory of beam cyclotron instability in plasmas. *Physics Letters A*, A 35(2):131. 42, 99, 125

Lashmore-Davies, C. N. and Martin, T. J. (1973). Electrostatic instabilities driven by an electric-current perpendicular to a magnetic-field. *Nuclear Fusion*, 13(2):193–203. 99, 125

Laturia, A., Van de Put, M. L., and Vandenberghe, W. G. (2018). Dielectric properties of hexagonal boron nitride and transition metal dichalcogenides: from monolayer to bulk. *npj 2D Materials and Applications*, 2(1):6. 69

Le, H. P. and Cambier, J.-L. (2016). Modeling of inelastic collisions in a multifluid plasma: Ionization and recombination. *Physics of Plasmas*, 23(6):063505. 47

Liang, H., Yongjie, D., Xu, Z., Liqiu, W., and Daren, Y. (2017). Magnetic field deformation due to electron drift in a Hall thruster. *AIP Advances*, 7(1):015008. 45

Liang, R. (2013). *The Combination of Two Concentric Discharge Channels into a Nested Hall-Effect Thruster.* PhD thesis. 4, 30, 34

Lieberman, M. A. and Lichtenberg, A. J. (2005). *Principles of plasma discharges and materials processing; 2nd ed.* Wiley, Newark, NJ. 5, 46

Luu, P. T., Tückmantel, T., and Pukhov, A. (2016). Voronoi particle merging algorithm for pic codes. *Computer Physics Communications*, 202:165 – 174. 86, 102, 105, 110

Malé, Q., Vermorel, O., Ravet, F., and Poinsot, T. (2021). Direct numerical simulations and models for hot burnt gases jet ignition. *Combustion and Flame*, 223:407 – 422. 53

Marsaglia, G. (2003). Xorshift rngs. *Journal of Statistical Software*, 8(14):1 – 6. 129

Martin, R. S. and Cambier, J.-L. (2012). Moment preserving adaptive particle weights using octree velocity distributions for pic simulations. *AIP Conference Proceedings*, 1501(1):872–879. 86

Mavriplis, D. (2003). *Revisiting the Least-Squares Procedure for Gradient Reconstruction on Unstructured Meshes*. 74

Mazouffre, S. (2012). Laser-induced fluorescence diagnostics of the cross-field discharge of Hall thrusters. *Plasma Sources Science and Technology*, 22(1):013001. 37

Mazouffre, S. (2016). Electric propulsion for satellites and spacecraft: established technologies and novel approaches. *Plasma Sources Science and Technology*, 25(3):033002. 30

Mazouffre, S., Dubois, F., Albarede, L., Pagnon, D., Touzeau, M., and Dudeck, M. (2003). Plasma induced erosion phenomena in a Hall thruster. In *International Conference on Recent Advances in Space Technologies, 2003. RAST'03. Proceedings of*, pages 69–74. IEEE. 38

McBride, J. B., Ott, E., Boris, J. P., and Orens, J. H. (1972). Theory and simulation of turbulent heating by the modified two-stream instability. *The Physics of Fluids*, 15(12):2367–2383. 117

Meecker, D. (2000). Finite Element Method Magnetics. 144

Meezan, N., Hargus, W., and Cappelli, M. (2001). Anomalous electron mobility in a coaxial Hall discharge plasma. *Physical review. E, Statistical, nonlinear, and soft matter physics*, 63:026410. 4, 44, 48, 114, 117

Mertmann, P., Eremin, D., Mussenbrock, T., Brinkmann, R. P., and Awakowicz, P. (2011). Fine-sorting one-dimensional particle-in-cell algorithm with monte-carlo collisions on a graphics processing unit. *Computer Physics Communications*, 182(10):2161 – 2167. 61, 129

Mikellides, I. G., Katz, I., Hofer, R. R., and Goebel, D. M. (2014). Magnetic shielding of a laboratory Hall thruster. i. theory and validation. *Journal of Applied Physics*, 115(4):043303. 4, 39, 40

Mikellides, I. G. and Ortega, A. L. (2020). Growth of the modified two-stream instability in the plume of a magnetically shielded Hall thruster. *Physics of Plasmas*, 27(10):100701. 117

Minelli, P. and Taccogna, F. (2017). How to build pic-mcc models for Hall microthrusters. *IEEE Transactions on plasma science*, 46(2):219–224. 49, 52, 137, 138, 187, 190

Mishev, I. D. (1998). Finite volume methods on voronoi meshes. *Numerical Methods for Partial Differential Equations*, 14(2):193–212. 63

Moreland, K. and Oldfield, R. (2015). Formal metrics for large-scale parallel performance. In *International Conference on High Performance Computing*, pages 488–496. Springer. 89, 90

Moritz, J., Lesur, M., Faudot, E., Devaux, S., Heuraux, S., and Ledig, J. (2019). The plasma-wall transition with collisions and an oblique magnetic field: Reversal of potential drops at grazing incidences. *Physics of Plasmas*, 26(1):013507. 49, 177

Morozov, A. (2003). The conceptual development of stationary plasma thrusters. *Plasma Physics Reports*, 29(3):235–250. 31

Morozov, A. and Savelyev, V. (2000). Fundamentals of stationary plasma thruster theory. *Reviews of plasma physics*, pages 203–391. 35, 48, 87, 178, 186

Muschietti, L. and Lembege, B. (2013). Microturbulence in the electron cyclotron frequency range at perpendicular supercritical shocks. *Journal of Geophysical Research-Space Physics*, 118(5):2267–2285. 125

OECD (2019). *The Space Economy in Figures*. 27

Okuda, H. and Birdsall, C. K. (1970). Collisions in a plasma of finite size particles. *The Physics of Fluids*, 13(8):2123–2134. 56, 134

Oliphant, T. E. (2007). Python for scientific computing. *Computing in science & engineering*, 9(3):10–20. 160

Ortner, M. and Bandeira, L. G. C. (2020). Magpylib: A free python package for magnetic field computation. *SoftwareX*, 11:100466. 144

Panelli, M., Morfei, D., Milo, B., D'Aniello, F. A., and Battista, F. (2021). Axisymmetric hybrid plasma model for Hall effect thrusters. *Particles*, 4(2):296–324. 50

Parra, F., Ahedo, E., Fife, J., and Martinez-Sanchez, M. (2006). A two-dimensional hybrid model of the Hall thruster discharge. *Journal of Applied Physics*, 100(2):023304. 50

Peterson, P. Y., Gallimore, A. D., and Haas, J. M. (2002). An experimental investigation of the internal magnetic field topography of an operating Hall thruster. *Physics of Plasmas*, 9(10):4354–4362. 45

Petronio, F., Tavant, A., Charoy, T., Alvarez Laguna, A., Bourdon, A., and Chabert, P. (2021). Conditions of appearance and dynamics of the modified two-stream instability in ExB discharges. *Physics of Plasmas*, 28(4):043504. 11, 43, 49, 118, 160, 164, 165, 185

Pierron, J., Inguimbert, C., Belhaj, M., Gineste, T., Puech, J., and Raine, M. (2017). Electron emission yield for low energy electrons: Monte carlo simulation and experimental comparison for al, ag, and si. *Journal of Applied Physics*, 121(21):215107. 82

Pitchford, L., Alves, L., Bartschat, K., Biagi, S., Bordage, M., Bray, I., Brion, C., Brunger, M., Campbell, L., Chachereau, A., Chaudhury, B., Christophorou, L., Carbone, E., Dyatko, N., Franck, C., Fursa, D., Gangwar, R., Guerra, V., Haefliger, P., and Pancheshnyi, S. (2016). Lxcat: An open-access, web-based platform for data needed for modeling low temperature plasmas. *Plasma Processes and Polymers*. 60

Poirel, L. (2018). *Méthodes de décomposition de domaine algébriques pour solveurs hybrides (direct-iteratif)*. PhD thesis, Ecole doctorale de mathématiques et d'informatique de l'université de Bordeaux. 72, 84, 88, 127, 181

Press, W. H., Teukolsky, S. A., Vetterling, W. T., and Flannery, B. P. (2007). *Numerical Recipes 3rd Edition: The Art of Scientific Computing*. Cambridge University Press, USA, 3 edition. 128, 129

Queguineur, M., Bridel-Bertomeu, T., Gicquel, L., and Staffelbach, G. (2019). Large eddy simulations and global stability analyses of an annular and cylindrical rotor/stator cavity limit cycles. *Physics of Fluids*, 31(10):paper 104109. 53

Raisanen, A. (2020). *A Two-dimensional Hybrid-Direct Kinetic Model of a Hall Thruster*. PhD thesis. 50

Raitses, Y., Kaganovich, I. D., Khrabrov, A., Sydorenko, D., Fisch, N. J., and Smolyakov, A. (2011). Effect of secondary electron emission on electron cross-field current in ExB discharges. *IEEE Transactions on Plasma Science*, 39(4):995–1006. 44

Raitses, Y., Staack, D., Keidar, M., and Fisch, N. (2005a). Electron-wall interaction in Hall thrusters. *Physics of Plasmas*, 12(5):057104. 37

Raitses, Y., Staack, D., Smirnov, A., and Fisch, N. J. (2005b). Space charge saturated sheath regime and electron temperature saturation in Hall thrusters. *Physics of Plasmas*, 12(7):073507. 37

Ravaud, R., Lemarquand, G., Lemarquand, V., and Depollier, C. (2008). Analytical calculation of the magnetic field created by permanent-magnet rings. *IEEE Transactions on Magnetics*, 44(8):1982–1989. 143

Rayman, M. D., Fraschetti, T. C., Raymond, C. A., and Russell, C. T. (2006). Dawn: A mission in development for exploration of main belt asteroids vesta and ceres. *Acta Astronautica*, 58(11):605–616. 32

Romadanov, I., Raitses, Y., and Smolyakov, A. (2018). Hall thruster operation with externally driven breathing mode oscillations. *Plasma Sources Science and Technology*, 27(9):094006. 41

Saad, Y. (2003 - 2003). *Iterative methods for sparse linear systems / Yousef Saad*. Society for Industrial and Applied Mathematics, Philadelphia, PA, second edition. edition. 72

Salvat, F., Jablonski, A., and Powell, C. J. (2021). elsepa—dirac partial-wave calculation of elastic scattering of electrons and positrons by atoms, positive ions and molecules (new version announcement). *Computer Physics Communications*, 261:107704. 82

Schenk, O. and Gartner, K. (2004). Solving unsymmetric sparse systems of linear equations with pardiso. *Journal of Future Generation Computer Systems*, 20(3):475–487. 129

Schinder, A. M. (2016). *Investigation of Hall effect thruster channel wall erosion mechanisms*. PhD thesis, Georgia Institute of Technology. 37

Schmid, P. J. (2010). Dynamic mode decomposition of numerical and experimental data. *Journal of fluid mechanics*, 656:5–28. 156

Schmidt, G., Jacobson, D., Patterson, M., Ganapathi, G., Brophy, J., and Hofer, R. (2018). Electric propulsion research and development at nasa. 33

Schonfeld, T. and Rudgyard, M. (1999). Steady and unsteady flow simulations using the hybrid flow solver avbp. *AIAA Journal*, 37(11):1378–1385. 53, 127

Semenkin, A. (2007). Overview of electric propulsion activity in russia. In *Proceedings of 30th International Electric Propulsion Conference*, pages 1–16. 33

Sengupta, M. and Smolyakov, A. (2020). Mode transitions in nonlinear evolution of the electron drift instability in a 2d annular exb system. *Physics of Plasmas*, 27(2):022309. 39, 117

Shastry, R., Gallimore, A., and Hofer, R. (2009). Near-wall plasma properties and eedf measurements of a 6-kw Hall thruster. In *45th AIAA/ASME/SAE/ASEE Joint Propulsion Conference & Exhibit*, page 5356. 37

Shepard, D. (1968). A two-dimensional interpolation function for irregularly-spaced data. In *Proceedings of the 1968 23rd ACM National Conference*, ACM '68, page 517–524, New York, NY, USA. Association for Computing Machinery. 64

Smirnov, A., Raitses, Y., and Fisch, N. (2002). Parametric investigation of miniaturized cylindrical and annular Hall thrusters. *Journal of Applied Physics*, 92(10):5673–5679. 38

Smirnov, A., Raitses, Y., and Fisch, N. J. (2007). Experimental and theoretical studies of cylindrical Hall thrusters. *Physics of Plasmas*, 14(5):057106. 38

Smirnov, A. N., Raitses, Y., and Fisch, N. J. (2006). Electron cross-field transport in a miniaturized cylindrical Hall thruster. *IEEE Transactions on Plasma Science*, 34(2):132–141. 117

Smith, A. W. and Cappelli, M. A. (2009). Time and space-correlated plasma potential measurements in the near field of a coaxial Hall plasma discharge. *Physics of Plasmas*, 16(7):073504. 138

Smolyakov, A., Zintel, T., Couedel, L., Sydorenko, D., Umnov, A., Sorokina, E., and Marusov, N. (2020). Anomalous electron transport in one-dimensional electron cyclotron drift turbulence. *Plasma Physics Reports*, 46:496–505. 42, 43, 118, 166

Smolyakov, A. I., Chapurin, O., Frias, W., Koshkarov, O., Romadanov, I., Tang, T., Umansky, M., Raitses, Y., Kaganovich, I. D., and Lakhin, V. P. (2016). Fluid theory and simulations of instabilities, turbulent transport and coherent structures in partially-magnetized plasmas of $\mathbf{e}\times \mathbf{b}$ discharges. *Plasma Physics and Controlled Fusion*, 59(1):014041. 41

Song, S. and Yovanovich, M. (1987). Correlation of thermal accommodation coefficient for engineering surfaces. *ASME HTD*, 69:107–116. 78

Space News (2017). All-electric satellites halfway to becoming half of all satellites. https://spacenews.com/all-electric-satellites-halfway-to-becoming-half-of-all-satellites/. Accessed: 2021-05-24. 29

Spillane, N. (2014). *Méthodes de décomposition de domaine robustes pour les problèmes symétriques définis positifs*. PhD thesis. Thèse de doctorat dirigée par Nataf, Frédéric Mathématiques Appliquées Paris 6 2014. 73, 84

Spillane, N., Dolean, V., Hauret, P., Nataf, F., Pechstein, C., and Scheichl, R. (2014). Achieving robustness through coarse space enrichment in the two level Schwarz framework. In *Domain Decomposition Methods in Science and Engineering XXI*, pages 447–455. Springer. 84

Stix, T. H. (1992). *Waves in plasmas*. Springer Science & Business Media. 41

Sun, A., Becker, M. M., and Loffhagen, D. (2016). Pic/mcc simulation of capacitively coupled discharges: Effect of particle management and integration. *Computer Physics Communications*, 206:35–44. 75

Sutherland, O., Stramaccioni, D., Benkhoff, J., Wallace, N., Feili, D., Rocchi, A., and Jehn, R. (2019). Bepicolombo: Esa's interplanetary electric propulsion mission to mercury. In *36th International Electric Propulsion Conference, Vienna, Austria*. 32

Swope, W. C., Andersen, H. C., Berens, P. H., and Wilson, K. R. (1982). A computer simulation method for the calculation of equilibrium constants for the formation of physical clusters of molecules: Application to small water clusters. *The Journal of Chemical Physics*, 76(1):637–649. 75

Sydorenko, D., Kaganovich, I., Raitses, Y., and Smolyakov, A. (2009). Breakdown of a space charge limited regime of a sheath in a weakly collisional plasma bounded by walls with secondary electron emission. *Physical review letters*, 103(14):145004. 49

Sydorenko, D., Smolyakov, A., Kaganovich, I., and Raitses, Y. (2006). Kinetic simulation of secondary electron emission effects in Hall thrusters. *Physics of Plasmas*, 13(1):014501. 44

Sydorenko, D., Smolyakov, A., Kaganovich, I., and Raitses, Y. (2008). Plasma-sheath instability in Hall thrusters due to periodic modulation of the energy of secondary electrons in cyclotron motion. *Physics of Plasmas*, 15(5):053506. 117

Sydorenko, D. Y. (2006). *Particle-in-cell simulations of electron dynamics in low pressure discharges with magnetic fields*. Theses, University of Saskatchewa. 37, 52, 53, 62, 82

Szabo, J. J. (2001). *Fully Kinetic Numerical Modeling of a Plasma Thruster*. PhD thesis, Massachusetts Institute of Technology. 49, 79, 80, 81, 142, 152

Taccogna, F. (2003). *Plasma-Surface Interaction Inside a Hall Thruster*. Theses, Universitá degli Studi di Bari Facoltá di Scienze Matematiche, Fisiche a Naturali. 37, 82

Taccogna, F. and Garrigues, L. (2019). Latest progress in Hall thrusters plasma modelling. *Reviews of Modern Plasma Physics*, 3(1). 37, 43, 51

Taccogna, F., Longo, S., and Capitelli, M. (2005). Plasma sheaths in Hall discharge. *Physics of plasmas*, 12(9):093506. 49

Taccogna, F., Longo, S., Capitelli, M., and Schneider, R. (2007). Particle-in-cell simulation of stationary plasma thruster. *Contributions to Plasma Physics*, 47(8-9):635–656. 49

Taccogna, F., Longo, S., Capitelli, M., and Schneider, R. (2009). Anomalous transport induced by sheath instability in Hall effect thrusters. *Applied Physics Letters*, 94(25):251502. 44

Taccogna, F. and Minelli, P. (2018). Three-dimensional particle-in-cell model of Hall thruster: The discharge channel. *Physics of Plasmas*, 25(6):061208. 49, 52, 118, 137, 138, 144, 187, 190, 192

Taccogna, F., Minelli, P., Asadi, Z., and Bogopolsky, G. (2019). Numerical studies of the ExB electron drift instability in Hall thrusters. *Plasma Sources Science and Technology*, 28(6):064002. 42, 43, 49, 117, 121, 129

Taccogna, F., Schneider, R., Longo, S., and Capitelli, M. (2008). Kinetic simulations of a plasma thruster. *Plasma Sources Science and Technology*, 17(2):024003. 129

Tavant, A. (2019). *Study of the plasma/wall interaction and erosion on a plasma thruster of low power*. PhD thesis. ThÃšse de doctorat dirigÃ©e par Bourdon, Anne et Chabert, Pascal Physique des plasmas UniversitÃ© Paris-Saclay (ComUE) 2019. 62, 118, 166, 175, 191

Tavant, A., Croes, V., Lucken, R., Lafleur, T., Bourdon, A., and Chabert, P. (2018). The effects of secondary electron emission on plasma sheath characteristics and electron transport in an exb discharge via kinetic simulations. *Plasma Sources Science and Technology*, 27(12):124001. 44, 49, 117, 118, 121, 138

Tavant, A., Lucken, R., Bourdon, A., and Chabert, P. (2019). Non-isothermal sheath model for low pressure plasmas. *Plasma Sources Science and Technology*, 28(7):075007. 49

Tichý, M., Pétin, A., Kudrna, P., Horký, M., and Mazouffre, S. (2018). Electron energy distribution function in a low-power Hall thruster discharge and near-field plume. *Physics of Plasmas*, 25(6):061205. 37

Trottenberg, U., Oosterlee, C. W., and Schuller, A. (2001). *Multigrid*. Elsevier. 74

Tsikata, S. (2009). *Small-scale electron density fluctuations in the Hall thruster, investigated by collective light scattering*. PhD thesis, Citeseer. 42, 92

Tsikata, S., Honore, C., and Gresillon, D. (2013). Collective thomson scattering for studying plasma instabilities in electric thrusters. *Journal of Instrumentation*, 8(10):C10012. 42, 92

Tsikata, S., Honoré, C., Lemoine, N., and Grésillon, D. M. (2010). Three-dimensional structure of electron density fluctuations in the Hall thruster plasma: ExB mode. *Physics of Plasmas*, 17(11):112110. 42, 57, 92, 118, 136, 190

Tsikata, S., Lemoine, N., Pisarev, V., and Gresillon, D. (2009). Dispersion relations of electron density fluctuations in a Hall thruster plasma, observed by collective light scattering. *Physics of Plasmas*, 16(3):033506. 37, 42, 92

Tsikata, S. and Minea, T. (2015). Modulated electron cyclotron drift instability in a high-power pulsed magnetron discharge. *Physical review letters*, 114(18):185001. 37, 117

Tsiolkovsky, K. (1903). Issledovanie mirovykh prostransty reaktivnymi priborami (exploration of space with rocket devices). *Naootchnoye Obozreniye (Scientific Review)*, pages 12–13. 27

Tsuda, Y., Yoshikawa, M., Abe, M., Minamino, H., and Nakazawa, S. (2013). System design of the hayabusa 2—asteroid sample return mission to 1999 ju3. *Acta Astronautica*, 91:356–362. 32

Turner, M. M. (2006). Kinetic properties of particle-in-cell simulations compromised by monte carlo collisions. *Physics of Plasmas*, 13(3):033506. 134

Turner, M. M., Derzsi, A., Donko, Z., Eremin, D., Kelly, S. J., Lafleur, T., and Mussenbrock, T. (2013). Simulation benchmarks for low-pressure plasmas: Capacitive discharges. *Physics of Plasmas*, 20(1):013507. 7, 13, 92, 102, 103, 104, 106, 115, 128, 193

Vahedi, V. and Surendra, M. (1995). A monte carlo collision model for the particle-in-cell method: applications to argon and oxygen discharges. *Computer Physics Communications*, 87(1):179 – 198. Particle Simulation Methods. 60

Vaudolon, J. and Mazouffre, S. (2015). Observation of high-frequency ion instabilities in a cross-field plasma. *Plasma Sources Science and Technology*, 24(3):032003. 41

Vaudolon, J., Vial, V., Cornu, N., and Habbassi, I. (2019). Ppsr© x00 thruster development status at safran. In *Proceedings of the 36th International Electric Propulsion Conference, Vienna, Austria*, pages 15–20. 33, 193

Vaughan, J. R. M. (1989). A new formula for secondary emission yield. *IEEE Transactions on Electron Devices*, 36(9):1963–1967. 37, 82

Vazquez, A. D. (2019). *Axisymmetric simulation codes for Hall effect thrusters and plasma plumes*. Theses, Universidad Carlos III de Madrid. 50, 52, 53

Vedenov, A. (1963). Quasi-linear plasma theory (theory of a weakly turbulent plasma). *Journal of Nuclear Energy. Part C, Plasma Physics, Accelerators, Thermonuclear Research*, 5(3):169. 41

Villafana, W., Petronio, F., Denig, A. C., Jimenez, M. J., Eremin, D., Garrigues, L., Taccogna, F., Alvarez-Laguna, A., Boeuf, J.-P., Bourdon, A., Chabert, P., Charoy, T., Cuenot, B., Hara, K., Péchereau, F., Smolyakov, A. I., Sydorenko, D., Tavant, A., and Vermorel, O. (2021). 2d radial-azimuthal particle-in-cell benchmark for e x b discharges. *Plasma Sources Science and Technology*. 11, 43, 49, 101, 115, 116, 165, 189

Villemant, M. (2018). *Modelling and experimental characterisation of electron emission influence on Hall thrusters operation*. Theses, Institut supérieur de l'Aéronautique et de l'Espace (ISAE). 37, 81, 82, 83

Villemant, M., Sarrailh, P., Belhaj, M., Inguimbert, C., Garrigues, L., and Boniface, C. (2017). Electron emission model for Hall thruster plasma modelling. 81

Vincent, B., Tsikata, S., and Mazouffre, S. (2020). Incoherent thomson scattering measurements of electron properties in a conventional and magnetically-shielded Hall thruster. *Plasma Sources Science and Technology*, 29(3):035015. 37

Viozat, C., Held, C., Mer, K., and Dervieux, A. (2001). On vertex-centered unstructured finite-volume methods for stretched anisotropic triangulations. *Computer Methods in Applied Mechanics and Engineering*, 190(35):4733–4766. 63

Wauteleta, P. and Kestenera, P. (2011). Parallel io performance and scalability study on the prace curie supercomputer. *White paper, Prace*, 115. 180

Woodcock, G., Kos, L., and Eberle, B. (2002). Benefits of nuclear electric propulsion for outer planet exploration. *Earth*, 120:140. 32

Yokota, S., Komurasaki, K., and Arakawa, Y. (2006). Plasma density fluctuation inside a hollow anode in an anode-layer Hall thruster. In *42nd AIAA/ASME/SAE/ASEE Joint Propulsion Conference & Exhibit*, page 5170. 49

Zakari, M. (2013). *Modélisation Volumes-Finis en maillages non-structurés de décharges électriques à la pression atmosphérique*. Theses, Institut National Polytechnique de Toulouse - INPT. 53, 63, 74

Zurbach, S., Cornu, N., and Lasgorceix, P. (2011). Performance evaluation of a 20 kw Hall effect thruster. *Proc. IEPC 2011 (Kurhaus, Wiesbaden, Germany)*. 33